Fibre optic monitoring and finite element analysis of well integrity in methane hydrate reservoirs

Tsubasa Sasaki

Department of Engineering

University of Cambridge

This dissertation is submitted for the degree of

Doctor of Philosophy

Churchill College   January 2019

To my family

Declaration

This dissertation is the result of my own work and includes nothing which is the outcome of work done in collaboration except as declared in the Preface and specified in the text. It is not substantially the same as any that I have submitted, or, is being concurrently submitted for a degree or diploma or other qualification at the University of Cambridge or any other University or similar institution except as declared in the Preface and specified in the text. I further state that no substantial part of my dissertation has already been submitted, or, is being concurrently submitted for any such degree, diploma or other qualification at the University of Cambridge or any other University or similar institution except as declared in the Preface and specified in the text. It does not exceed the prescribed word limit for the relevant Degree Committee.

Tsubasa Sasaki

January 2019

Abstract

Fibre optic monitoring and finite element analysis of well integrity in methane hydrate reservoirs

Tsubasa Sasaki

Well integrity is crucial for sustainable hydrocarbon production from oil and gas reservoirs. The number of new wells can be minimized by maintaining the integrity of existing wells. Also, oil and gas leakage due to compromised well integrity can be curtailed through proactive well integrity management.

The present research focuses on well integrity analysis and monitoring for methane hydrate reservoirs. Methane hydrate reservoirs are susceptible to large deformation due to their unconsolidated nature, which could substantially compromise well integrity during well construction as well as gas production periods. Therefore, in the present research, finite element analyses (FEA) and laboratory experiments of well integrity are carried out for the case of the Nankai Trough methane hydrate reservoir in Japan, in order to contribute to a better well integrity management. FEA on well construction and reservoir compaction processes as well as cement shrinkage process is conducted. Laboratory experiments are carried out with a distributed fibre optic monitoring technique called Brillouin optical time domain reflectometry/analysis (BOTDR/A) on the strain development of laboratory-scale well specimens subjected to tensile and bending loading.

The primary contributions of the present research are as follows. First, cement shrinkage volumes for the Nankai Trough formation case are estimated to be up to 0.7%. Second, cement shrinkage of 0.7% during well construction induces stress concentrations in the high hydrate saturation layers of the Nankai Trough formation. Third, the well is found to become most vulnerable to damage in the initial stages of hydrate dissociation under large depressurisation. Forth, fibre optic cables with minimal number of coating layers and tight interlayer buffering will be effective for accurate in-well integrity monitoring with BOTDR/A. Fifth, fibre optic cables should be attached on the casing rather than in the cement in the well to facilitate accurate bending curvature monitoring with BOTDR/A.

Acknowledgements

First and foremost, I would like to thank my two supervisors, Dr. Mohammed Elshafie and Prof. Kenichi Soga, for their continuous support on my research. Mohammed is my official supervisor and he has helped me with liaising with technicians and research staff to carry out laboratory experiments at Cambridge. I would like to thank him for leading me in the right directions. Prof. Kenichi Soga is my host faculty at the University of California, Berkeley (UC Berkeley) during my work away period in the States. He supervised me for two years since I came to California in February 2017. I feel extremely fortunate to have him as another supervisor not only because he is supportive of research activities but also because he is incredibly humble. His presence and warm support will always be missed no matter where I go in the future.

Second, I would like to thank staff members at Cambridge University and UC Berkeley who helped me with my research works. Dr. Cedric Kechavarzi is the Operations Manager at the Cambridge Centre for Smart Infrastructure and Construction (CSIC) and he advised me a great deal on my fibre optic monitoring experiments. His joyful personality always encouraged me to learn more from him and I would like to thank him for that. Peter Knott and Jason Shardelow are technical staff at CSIC who helped me to execute all my experiments at Cambridge. I believe they are the best technicians in the UK and it was always fun to work with them. So, I would like to sincerely thank them for their help. Martin Touhey, Phil McLaren, Lorna Roberts and David Layfield are technicians at the Structures Laboratory at Cambridge University. They helped me with my experiments along with Peter and Jason. Their sense of humour always made it enjoyable to work with them and I would like to thank them for that. Dr. Shakhzod Takhirov is the Engineering Manager at the Civil and Environmental Engineering (CEE) Department at UC Berkeley. Shakhzod actively helped me to organize laboratory experiments and I owe him a great deal of appreciation for this help. Llyr Griffith, Matt Cataleta, Phillip Wong and Cruz Carlos Jr. are technicians at the CEE Department at UC Berkeley. They helped me with everything in carrying out laboratory experiments. They are so professional and fun to work with, and I would like to thank them for helping me. Dr. Linqing Luo is a post-doctoral fellow of Prof. Soga and he specializes in fibre optic monitoring. His specialist advice and help were indispensable to successfully complete my experiments at UC Berkeley, so I feel grateful for his help.

Third, I would like to express my gratitude to my fellow Methane Hydrate Research Group members: Dr. Mingliang (Carter) Zhou, Dr. Ningjun Jiang, Dr. Amanda Murphy, Dr. Xiang Sun, Hao Luo and Marilena Papadopoulou. Carter introduced me to the ABAQUS finite element

Table of contents

II

List of figures

List of tables

Nomenclature

Roman symbols

A	Dilation enhancement constant 1
A_c	Cross-sectional area of the cement of the well specimen
A_i	Cross-sectional area of the inner pipe of the well specimen
A_o	Cross-sectional area of the outer pipe of the well specimen
B	Dilation enhancement constant 2
C	Cohesion enhancement constant 1
C_ε	Strain coefficient of a fibre optic cable
C_T	Temperature coefficient of a fibre optic cable
c	Specific heat capacity
c'	Interface cohesion
D	Cohesion enhancement constant 2
$\boldsymbol{D}^e_{hs}$	Isotropic elastic stiffness matrix of hydrate-bearing soil
E	Young's modulus
E_c	Young's modulus of the cement of the well specimen
E_i	Young's modulus of the inner pipe of the well specimen
E_o	Young's modulus of the outer pipe of the well specimen
f	Value of a yield function
f^{now}	Value of a yield function at the current stress state
f^{pred}	Value of a yield function at the prediction stress state
G_h	Shear modulus of methane hydrate
G_{hs}	Shear modulus of hydrate-bearing soil
G_s	Shear modulus of soil skeleton
g	Gravity acceleration
I	Second moment of inertia
J_2	Second variant of deviatoric stress tensor
K	Bulk modulus
K_0	Ratio of vertical to horizontal effective stresses
K_h	Bulk modulus of methane hydrate
K_{hs}	Bulk modulus of hydrate-bearing soil
K_s	Bulk modulus of soil skeleton
k	Interface shear stiffness
L	Length of a specimen

M	Bending moment
m_1	Hydrate degradation constant
m_2	Stiffness enhancement constant
n	Porosity
P	Point load
P_i	Pore pressure at the wellbore-formation interface
P_o	Hydrostatic pore pressure
p	Interface contact pressure
p'	Mean effective stress
p'_{cc}	Cohesion enhancement parameter
p'_{cd}	Dilation enhancement parameter
p'_{cs}	Preconsolidation effective stress
p_e	Effective photo-elastic coefficient
p_g	Pore gas pressure
p_l	Pore liquid pressure
q	Deviator stress
R	Ratio of the subloading to yield surfaces
R_o	Radius from the wellbore centre to a location where pore pressure reaches hydrostatic pore pressure
R_s	Radius of formation subsidence
r	Radius from the centre of wellbore
r_f	Radius of the hydrate dissociation front
r_0	Radius of wellbore
r_{co}	Radius of the cement-outer pipe interface in the well specimen
r_{ic}	Radius of the inner pipe-cement interface in the well specimen
S_h	Hydrate saturation
S_{max}	Maximum formation subsidence
T	Absolute temperature
t	Elapsed time
t_{set}	Time period between cement mixing and initial set
U	Subsurface constant
u	Pore pressure (single fluid phase, no gas phases)
v	Specific volume
x	Axial distance
y	Distance from the neutral axis of a beam
y_c	Axial displacement of the cement of the well specimen

y_i	Axial displacement of the inner pipe of the well specimen
y_o	Axial displacement of the outer pipe of the well specimen
z	Depth

Greek symbols

α_L	Linear thermal expansion coefficient
α_n	Thermo-optic coefficient
α_p	Ratio of the permeability values of dissociated and undissociated hydrate-bearing soil
δ_{max}	Maximum deflection of a beam
$\boldsymbol{\varepsilon}$	Strain vector
ε	Mechanical strain
$\boldsymbol{\varepsilon}^e$	Elastic strain vector
$\boldsymbol{\varepsilon}^p$	Plastic strain vector
ε^p_d	Plastic deviatoric strain
ε^p_v	Plastic volumetric strain
ε_{BOTDR}	Strain distribution along a fibre optic cable obtained from BOTDR measurements
ε_d	Deviatoric strain
ε_{real}	Actual Strain distribution along a fibre optic cable
ε_v	Volumetric strain
γ	Total tangential interface displacement
γ^e	Elastic tangential interface displacement
γ^p	Plastic tangential interface displacement
γ^e_{ult}	Ultimate elastic tangential interface displacement
κ	Gradient of swelling line
$\kappa^{'}$	Curvature
Λ	Plastic multiplier
λ	Gradient of compression line
$\lambda^{'}$	Wavelength of light wave
λ_0	Baseline wavelength of light wave
λ_T	Thermal conductivity
M	Critical state frictional constant
μ	Interface friction coefficient
ν	Poisson's ratio
ν_B	Brillouin frequency

π	Pi constant
ρ_c	Density of cement slurry
ρ_w	Density of water
$\boldsymbol{\sigma}$	Stress tensor
σ	Standard deviation of the Gaussian distribution
$\boldsymbol{\sigma}'$	Effective stress tensor
σ'	Effective stress
$\boldsymbol{\sigma}'_0$	Reference effective stress vector
σ'_h	Horizontal effective stress
σ'_v	Vertical effective stress
σ_a	Axial stress
σ_h	Horizontal total stress
σ_m	Mean total stress
σ_v	Vertical total stress
τ	Interface shear stress
τ_{ult}	Ultimate interface shear stress
ϕ'	Effective internal friction angle
χ	Shear-induced stiffness degradation constant for hydrate-bearing soil

1. Introduction

1.1. Background

Securing stable and reliable energy resources is crucial to nations' prosperity. Having reliable energy resources not only helps to meet the energy demand of countries but also boosts their economy, especially for those who do not possess domestic energy resources such as Japan.

In 2013, Japan completed world's first offshore gas production test from methane hydrate reservoirs at the Nankai Trough (Yamamoto et al. 2014) (Figure 1-1). Methane hydrate is an unconventional natural gas resource, in which methane gas is trapped in ice cages. Methane gas can be extracted by destabilizing the ice cage by increasing the temperature and/or decreasing the pressure. For example, in the Nankai Trough case, the depressurization method (i.e., pore pressure decrease by water pumping) was employed to dissociate methane hydrate into methane gas and water in the formation. The pump then extracted methane gas (and water) to the surface production platform. The gas production test continued for six days until well failure occurred with abrupt sand production. The mechanism of the well failure remains unknown.

(a)
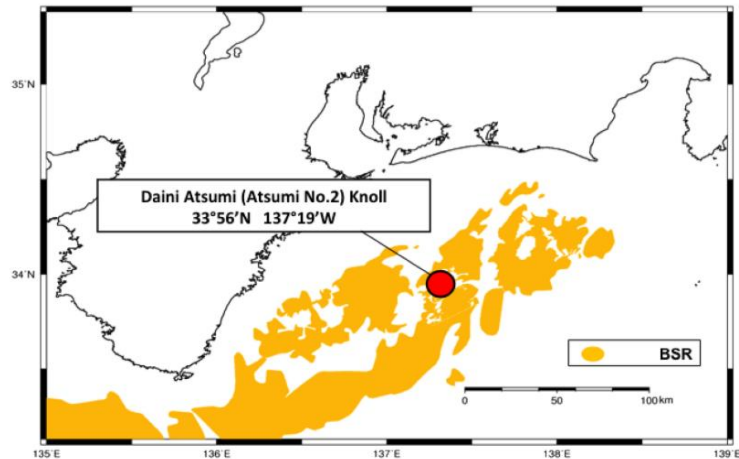
(b)
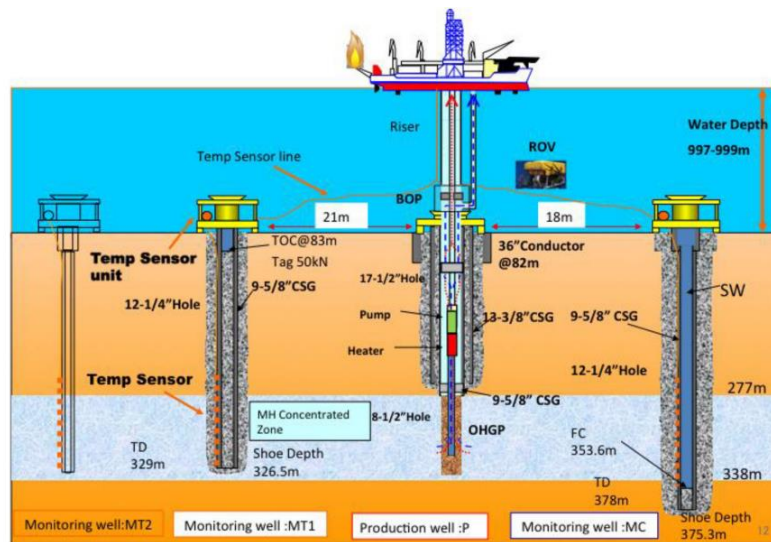
(c)

Figure 1-1 World's first offshore gas production from methane hydrate reservoirs at the Nankai Trough, Japan: (a) gas flare which signifies the successful gas production; (b) the location of the gas production test site; (c) the configuration of the production and monitoring wells [after Yamamoto et al. (2014)].

It is critical to maintain the integrity of wells, in order to achieve a sustainable long-term gas production from the Nankai Trough methane hydrate reservoir. As is mentioned earlier, the mechanism of the Nankai Trough well failure has not yet been discovered. One of the possible causes is reservoir compaction. If fact, reservoir compaction has induced numerous well failures in the conventional oil and gas reservoirs in the past (Nagel, 2001). Another possibility is formation damage incurred during well construction. The Nankai Trough formation is unconsolidated and is thus prone to significant stress/ strain changes due to external disturbances

2

(i.e., well construction processes). Cement shrinkage, which occurs during well construction processes, is often ignored because the level of cement shrinkage volume is believed to be negligible and to have no effect on well/formation integrity. However, cement shrinkage might have contributed to the Nankai Trough well failure by inducing loss of zonal isolation of the well from the formation. In order to mitigate well failure, it is also imperative to carry out real-time monitoring of well integrity to detect signs of impending well failure, in combination with numerical analysis of potential well failure mechanisms.

Finite element analyses are viable approach towards the modelling of well-formation interaction which is key to characterise the response of wells to reservoir compaction. Not only reservoir compaction but also well construction and cement shrinkage can be modelled in finite element analyses. For the real-time monitoring of well integrity, a distributed fibre optic strain and temperature monitoring technique called Brillouin optical time domain reflectometry/analysis (BOTDR/A) (Horiguchi & Tateda 1989; Kurashima et al. 1993) is an ideal candidate. This is because of BOTDR/A's long measurement distance (tens of kilometres), high spatial and temporal resolutions (e.g., 1 m and 5 min) and high strain and temperature precisions (e.g., ± 50 $\mu\varepsilon$ and ± 1 C$^\circ$). BOTDR/A will enable real-time diagnosis of well integrity, which will facilitate timely countermeasures for mitigating well damage.

It is envisaged that finite element modelling methodologies for simulating well integrity during the life of wells (i.e., well construction plus reservoir compaction processes) will be instrumental in interpreting the mechanism of well failures. Also, it is hoped that a careful evaluation of BOTDR/A's capability to carry out distributed strain sensing (DSS) of wells will be beneficial for well integrity management not only for unconventional methane hydrate reservoirs but also for conventional oil and gas reservoirs.

1.2. Scope and objectives
The aims of this research are as follows:

1. To assess a reasonable range of cement shrinkage volumes for the Nankai Trough case through finite element analysis. It is important to identify the range of possible shrinkage volume to evaluate formation integrity accurately during well construction. The mechanism of cement shrinkage is capillary pressure development during the cement hydration reaction and it is modelled as pore pressure decrease in a saturated porous material. A coupled hydro-mechanical simulation is performed to simulate the water flow from the formation to

hydrating cement during cement shrinkage.

2. To model the construction process of a well drilled at the Nankai Trough site through finite element analysis to assess formation integrity prior to gas production. The well construction process includes drilling, casing hanging, cementing, cement shrinkage and hardening and casing landing. The response of the formation is simulated through a calibrated constitutive model for methane hydrate-bearing soils.

3. To investigate the development of stresses and strains in the well during reservoir compaction for the Nankai Trough case. Different compaction profiles are simulated to assess their effect on well integrity. The casing-cement-formation interaction is modelled through a calibrated interface friction constitutive model which facilitates an accurate well integrity modelling during reservoir compaction.

4. To examine the effectiveness of BOTDR/A in monitoring the axial tensile deformation of wells through laboratory experiments. Fibre optic cables, which differ in the characteristics of coating layers, are employed to find key features of effective fibre optic cables for the strain monitoring. The development of axial tensile strain is also measured by a reference fibre Bragg grating (FBG) cable to evaluate the performance of the BOTDR/A measurement.

5. To evaluate the effectiveness of BOTDR/A in monitoring the bending deformation of wells through laboratory experiments. Fibre optic cables are embedded in the cement sheath as well as on the steel box section which constitute the well specimen. Curvature profiles at different load levels during a three-point bending test are derived from BOTDR/A measurements which are compared with analytical curvature profiles to assess the effectiveness of BOTDR/A and the effect of cable location on the accuracy of bending curvature measurement.

1.3. Thesis layout

The thesis consists of eight chapters. A brief summary of each chapter is provided below:

Chapter 2

The literature review of the research is presented. The characteristics and spatial distribution of methane hydrate in the world are provided, followed by a summary of the recent field gas production trials. Well failures observed at conventional oil and gas fields are introduced to show

the mechanisms of well failures during reservoir compaction. Existing numerical models in the literature for well integrity assessments are summarised to ascertain the necessity for detailed well construction modelling and well integrity analysis with calibrated interface and formation constitutive models. Fibre optic monitoring techniques for oil and gas wells are reviewed to show that the potential of BOTDR/A to carry out DSS has not been fully examined yet neither at the laboratory- nor field-scale.

Chapter 3

Finite element analysis of the shrinkage behaviour of different types of cement is provided. Hydro-mechanical coupled behaviours of early-age cement during hydration and its interaction with the formation are simulated under the wellbore configuration and conditions. Due to the uncertainty of the effective stress and pore pressure conditions of early-age cement during the phase shift from slurry to solid cement (i.e., initial set), two different scenarios (consolidated and underconsolidated cement cases) are simulated to estimate a range of possible cement shrinkage volumes for the Nankai Trough case.

Chapter 4

Finite element analysis of well construction process is presented. The development of the radial, vertical and circumferential effective stresses as well as plastic deviatoric strain in the formation around the well at each well construction stage is computed for the Nankai Trough case. The modelled Nankai Trough formation consists of an overburden clay layer, methane hydrate reservoir layer and underburden sand layer. The relative impact of each well construction stage, with a particular emphasis on the cement shrinkage stage, on formation integrity is investigated.

Chapter 5

Finite element analysis of well integrity during depressurization-induced reservoir compaction is presented. A variety of compaction profiles are created by specifying different pore pressure distributions in the reservoir layer. The casing-cement-formation interaction was modelled through an interface friction constitutive model calibrated against laboratory test data obtained from Chapter 6. Well construction process described earlier in Chapter 4 is incorporated to encompass the entire period of the life of the well for the modelling of well integrity.

Chapter 6

Laboratory experiments on the axial tensile deformation of well specimens are described. BOTDR is employed to carry out distributed fibre optic strain measurements. Different types of fibre optic cables (e.g., different cable outer diameter (OD), number of coating layers, tight buffer between

coating layers, etc.) are employed to examine their strain monitoring performance with BOTDR. The identified key characteristics of fibre optic cables for an accurate strain monitoring are incorporated in the suggested design of a new fibre optic cable for the monitoring of new wells to be drilled in methane hydrate reservoirs in Alaska, USA.

Chapter 7

Results of laboratory experiments on the distributed strain monitoring of the bending deformation of well specimens are presented. The effectiveness of BOTDR in measuring the curvature distributions of the well specimen at different load levels under three-point bending loading is examined through comparison with the analytical curvatures calculated from the central deflection values obtained from displacement transducers. Fibre optic cables are installed in the cement sheath as well as on the surface of the steel box section of the specimen to evaluate the effect of cable location on the accuracy of bending curvature measurement by BOTDR. Digital image correlation measurement is also performed to corroborate the result of the BOTDR measurement.

Chapter 8

The primary findings from the present research on the integrity of wells in methane hydrate reservoirs with particular emphasis for the Nankai Trough case are presented. Suggestions on the areas of further research are also provided to indicate potential future directions of the present work.

2. Literature review

2.1. Methane hydrate as an energy resource

2.1.1. Exploratory surveys

Figure 2-1 shows the distribution of methane hydrate around the world (Maslin et al. 2010). Methane hydrate is distributed over the continental margins under the ocean. This is because organic carbons, which supplies methane gas for methane hydrate generation, are readily available in the continental margins due to their proximity to the rivers with high plankton productivity (Maslin et al. 2010). It is also because methane hydrate is stable only under high-pressure and low-temperature conditions as shown in Figure 2-2 (Kvenvolden 1993). If pressure decreases and/or temperature increases, methane hydrate disintegrates into mathane gas and water. Methane hydrate also exists in onshore formation such as under permafrost due to its low-temperature and high overburden pressure environment.
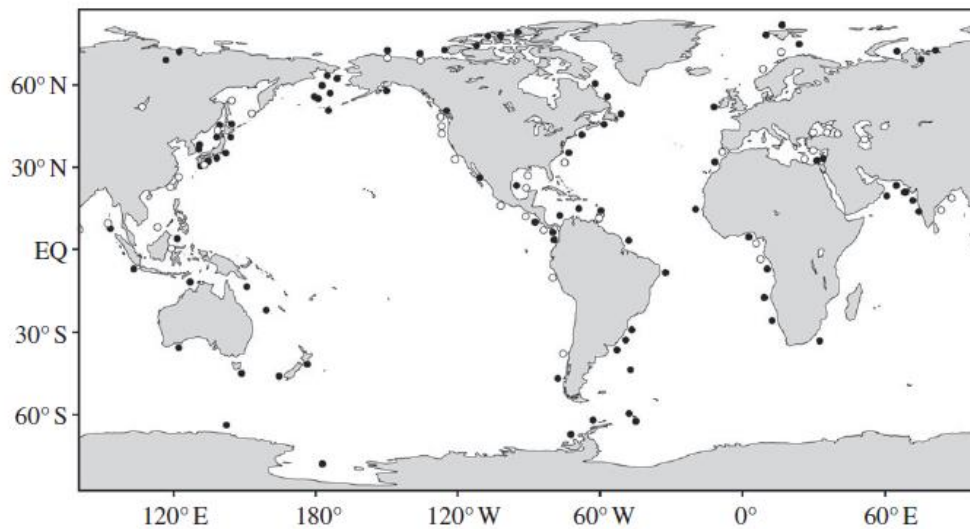
Figure 2-1 Confirmed (open dots) and inferred (solid dots) locations of methane hydrate [after Maslin et al. (2010)].

Maslin et al. (2010) estimated world's total amount of methane gas in methane hydrate to be at least 500 gigatonnes carbon, which is equivalent to 1.6×10^{15} m^3 of methane gas at 0 °C and 1 atm. This is more than 10 times the amount of world's undiscovered conventional technically recoverable gas (U.S. Geological Survey 2012). Moreover, the energy density of methane hydrate (i.e., ratio of gas to host sediment volumes under the standard conditions) is higher than that of

other conventional and unconventional gas resources. This suggests that methane hydrate is an attractive source of natural gas.
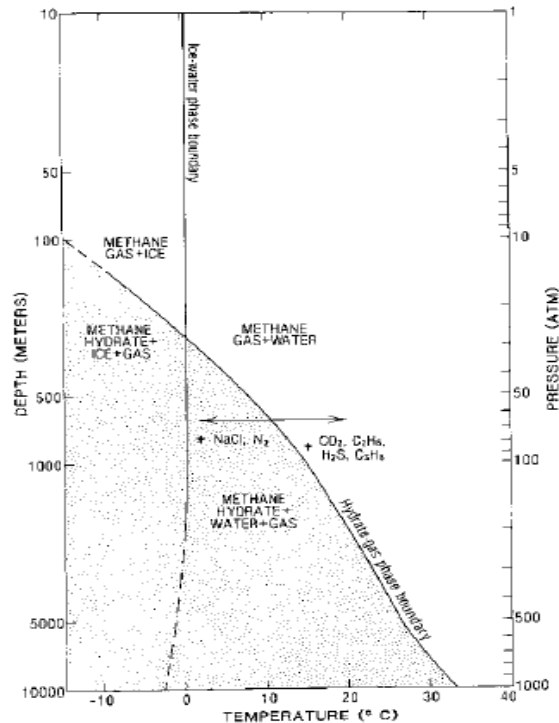
Figure 2-2 Pressure- and temperature-dependent stability curves of methane hydrate [after Kvenvolden (1993)].

2.1.2. Field gas production tests

Field gas production tests from methane hydrate reservoirs have been carried out in different countries. Table 2-1 shows the details of the past field gas production tests (Yamamoto & Dallimore 2008; Moridis et al. 2008; Farrell et al. 2012; Boswell 2013).

World's first field test was carried out in the Mackenzie Delta, Canada (i.e., onshore location). During the five-day gas production period, the test yielded a total of 470 m^3 of methane gas by the thermal stimulation method (i.e., hot fluid circulation). In the following test in the same location in 2007, the depressurization method (i.e., pore pressure decrease by pumping) was employed and the test generated 830 m^3 of methane gas over 2.5 days before it was terminated by sand production. One more test was conducted in the Mackenzie Delta a year later, which produced approximately 13,000 m^3 of methane gas in total over the 6-day production period. A similar field test was also conducted in Alaska, USA, in 2012 and a total amount of 28,000 m^3 of methane gas was produced during the 30-day gas production period (Farrell et al. 2012).

Japan carried out world's first offshore gas production test in the eastern Nankai Trough in 2013. The test continued for six days, yielding 120,000 m³ of methane gas in total, before the test was terminated by sand production. Another offshore field test was carried out at the Nankai Trough in 2017, in which two gas production wells were drilled (i.e., P2 and P3 wells). In the P2 well, the gas production continued for 24 days without sand production and generated a total of approximately 200,000 m³ of methane gas. In the P3 well, however, the test yielded only approximately 35,000 m³ of methane gas over 12 days before the test was discontinued due to sand production (Chen, Feng, Kogawa, et al. 2018).

The sand production issue indicates that well integrity was compromised during the filed tests. Therefore, the following sections discuss well integrity studies in the literature in order to gain a deeper insight into well failure patterns in methane hydrate reservoirs.

Table 2-1 Details of field gas production tests from methane hydrate reservoirs.

Test program	Test location	Test dates	Duration of gas production (day)	Total gas production (m³)	Gas production rate (m³/day)	Gas production method
Mallik-2002	Northwest Territories, Canada	March, 2002	5	470	1,500	Thermal stimulation
Mallik-2007	Northwest Territories, Canada	April, 2007	2.5	830	1,600	Depressurization
Mallik-2008	Northwest Territories, Canada	March, 2008	6	13,000	2,000-4,000	Depressurization
Ignik Sikumi	Alaska, USA	March-April, 2012	30	28,000	5,000	CO_2-CH_4 exchange, depressurization
Nankai Trough-2013	Eastern Nankai Trough, Japan	March, 2013	6	120,000	20,000	Depressurization
Nankai Trough-2017	Eastern Nankai Trough, Japan	May-June, 2017	24 (P2 well), 12 (P3 well)	200,000 (P2 well), 35,000 (P3 well)	8,000 (P2 well), 3,000 (P3 well)	Depressurization

2.2. Integrity of oil and gas wells

Well integrity is critical for long-term sustainable gas production from methane hydrate reservoirs. This is because methane hydrate reservoirs are usually unconsolidated (i.e., formation consists of soil particles that are not consolidated into rocks) and the gas production by depressurization results in reservoir compaction. Below are examples of well failures due to reservoir compaction in conventional oil and gas fields.

- The Wilmington field

  This oilfield is located near the city of Long Beach, California, USA. It was discovered in 1932 and the production was initiated in 1936. By the time the first subsidence measurement was carried out in 1940, the subsidence was clearly visible on the surface (Nagel, 2001). By 1969, the total subsidence reached 9 m, which cost approximately a hundred million dollars for remedial operations (Mayuga & Allen 1969). Figure 2-3 shows a damaged well in this field. In total, more than 300 wells were damaged and approximately 40 % of the wells were terminated (Roberts 1953).

Figure 2-3 Well damage at the Wilmington field [after Roberts (1953)].

- The Ekofisk field

  The Ekofisk field is located in the North Sea. Well failure was first noticed in 1978 in advance of subsidence which was detected later in 1984 (Yudovich et al. 1988). The total cost of remedial operations, such as jacking up the production platforms, reached nearly one billion dollars (Nagel 2001). The compaction of the weak reservoir chalk caused buckling failure of the wells. Tension and shear failures were also observed in the overburden layers (Schwall & Denney 1994).

- The Belridge field

  The Belridge field is located in Kern County, California, USA. Since hydraulic fracturing was introduced to increase the production in 1970's, the Belridge field experienced significant subsidence, which led to well damage of more than a thousand wells (Fredrich et al. 2000). The extensive well damage could be attributed to the high-porosity, low-strength reservoir layer. The observed well failure mechanisms were shear and compression failures (Dale et al. 1996).

2.2.1. Well failure mechanisms at the Nankai Trough

As is mentioned earlier, wells constructed in the Nankai Trough methane hydrate reservoir

became non-operational during gas production due to sand production, which could be caused by well failure. Figure 2-4 shows potential failure mechanisms of wells at the Nankai Trough: (i) well buckling due to uneven hydrate dissociation, (ii) axial tension and compression due to reservoir compaction, (iii) well bending due to deviation of the well and (iv) cement shrinkage-induced well buckling and/or loss of zonal isolation. Uneven hydrate dissociation around the well could occur because of heterogeneous hydrate distributions and/or permeability profiles of the reservoir. As a result, methane hydrate in the reservoir layer on one side of the well dissociates faster than the other side, which leads to uneven stress distribution around the well and it could buckle accordingly. Axial tension and compression of the well are developed in the well during reservoir compaction in the overburden and reservoir layers, respectively. This is because the well in the reservoir layer is dragged downward by reservoir compaction whilst the top and bottom parts of the well are fixated in the overburden and underburden layers. Bending of the well is also caused by reservoir compaction, but it occurs to deviated wells where not only axial but also transverse displacements are developed by reservoir compaction. Finally, cement shrinkage could cause well failure by creating void between the formation and well, thereby decreasing the pressure support from the formation against buckling. Cement shrinkage could also induce cracks within the cement itself, potentially leading to loss of zonal isolation. These hypotheses on the Nankai Trough well failure have not been addressed in detail. Hence, there is a need for numerical and/or experimental investigations into the abovementioned potential failure mechanisms of the Nankai Trough well.
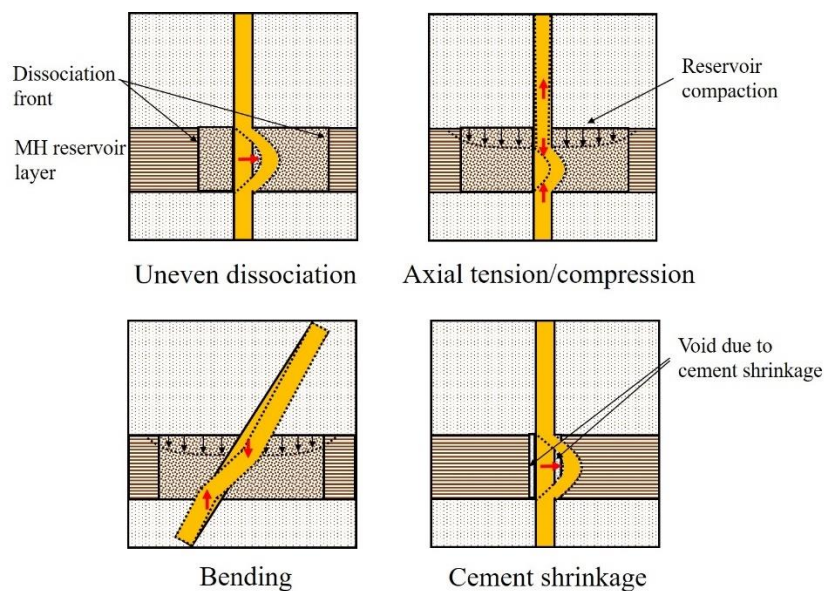
Figure 2-4 Potential failure mechanisms of wells in the Nankai Trough.

11

In the following section, modelling techniques for well integrity analyses during reservoir compaction as well as well construction processes are introduced.

2.3. Well integrity modelling

There are a number of studies on the modelling of well integrity in the literature. The emphasis of each model varies as some are focused on individual casing, cement or formation integrity whereas others incorporate the interaction among them. Modelled processes (i.e., well construction and reservoir compaction processes) also vary. In the following sections, the existing models are categorized into different groups and their details are provided.

2.3.1. No well construction and reservoir compaction modelling

Table 2-2 gives a list of studies in which the finite element and difference models are used without consideration of well construction or reservoir compaction process. Such models primarily focused on well integrity during well operations (e.g., pressure test, hydraulic fracturing, steam injection, etc.).

Table 2-2 Well integrity models with neither well construction nor compaction process.

Authors	Casing	Cement	Formation	Well construction	Reservoir Compaction
Badakhshan Raz & Ghassemi (2011)	No	No	Yes	No	No
Kalil & Mcspadden (2012)	Yes	Yes	No	No	No
Jammer et al. (2015)	Yes	Yes	No	No	No
Thiercelin et al. (1998)	Yes	Yes	Yes	No	No
Philippacopoulos & Berndt (2002)	Yes	Yes	Yes	No	No
Rodriguez et al. (2003)	Yes	Yes	Yes	No	No
Berger et al. (2004)	Yes	Yes	Yes	No	No
Heathman & Beck (2006)	Yes	Yes	Yes	No	No
Freij-Ayoub, Clennell, et al. (2007)	Yes	Yes	Yes	No	No
Bui & Tutuncu (2013)	Yes	Yes	Yes	No	No
Jandhyala et al. (2013)	Yes	Yes	Yes	No	No

Some models analyse casing integrity. Kalil & Mcspadden (2012) investigated casing burst strength and found that thinner cement sheath would lead to a greater risk of casing burst failure. Jammer et al. (2015) analysed casing collapse strength and showed that cement void would

decrease the collapse strength if continuous void is present in the cement sheath. Rodriguez et al. (2003) asserted the importance of cement mechanical properties by showing that the stress development in the casing was affected by them. Berger et al. (2004) also highlighted the negative effect of cement void on the casing stress development. In summary, modelling of cement is found to be important in order to assess casing integrity.

Some models assessed cement integrity. Thiercelin et al. (1998) found that cement would be more likely to suffer tensile failure during pressure change (i.e., hydraulic fracturing) than temperature change (i.e., steam injection). Pressure change-induced cement damage could be aggravated by well inclination and anisotropic horizontal stress field of the formation (Bui & Tutuncu 2013). In order to survive pressure and temperature changes, low-stiffness cement was found effective (Jandhyala et al. 2013; Philippacopoulos & Berndt 2002). In addition, low-shrinkage cement is also effective in preventing cement damage including interface debonding (Heathman & Beck 2006).

Some models simulated hydrate dissociation and well integrity. Freij-Ayoub, Clennell, et al. (2007) found that high-stiffness and high-interface bonding strength cement would increase the factor of safety of casing during hydrate dissociation in the formation. Badakhshan Raz & Ghassemi (2011) found that the tensile stress development of hydrate-bearing formation would increase with increasing gas production rate and period.

In summary, modelling of cement sheath was found to be important in assessing not only cement integrity but also casing and formation integrities. However, all of the abovementioned models are 2D plane-strain models, which limits the relevance of these findings in analysing the entire well and formation system. Therefore, a model which incorporates the whole well as well as the surrounding formation needs to be developed to be able to assess well integrity holistically.

2.3.2. Well construction modelling

Table 2-3 lists well integrity models that incorporate well construction process. Hodge et al. 2006; Freij-Ayoub, Tan, et al. 2007 examined drilling operation and its effect on formation integrity. It was found that the borehole would be more likely to fail during drilling if the formation stress field is anisotropic and/or formation permeability is high.

Table 2-3 Well integrity models with well construction process only.

Authors	Casing	Cement	Formation	Well construction	Reservoir compaction
Hodge et al. (2006)	No	No	Yes	Yes	No
Freij-Ayoub, Tan, et al. (2007)	No	No	Yes	Yes	No
Bosma et al. (1999)	Yes	Yes	Yes	Yes	No
Ravi et al. (2002a)	Yes	Yes	Yes	Yes	No
Ravi et al. (2002b)	Yes	Yes	Yes	Yes	No
Gray et al. (2007)	Yes	Yes	Yes	Yes	No
Saint-Marc et al. (2008)	Yes	Yes	Yes	Yes	No
Salehabadi et al. (2008)	Yes	Yes	Yes	Yes	No

Some models simulated cement volume change and its effect on well integrity. Results are mixed as some studies found that decreasing cement shrinkage is important to maintain cement integrity (Bosma et al. 1999; Ravi et al. 2002a; Ravi et al. 2002)) whereas others showed that slight cement expansion (e.g., 1.5%) would be beneficial to cement integrity (Saint-Marc et al. 2008). In addition, Gray et al. (2007) showed that the effect of cement volume change on well integrity is dependent on formation stiffness.

Some models show that thermal properties of cement are important in assessing well integrity in methane hydrate-bearing formation. Salehabadi et al. (2008) found that low-thermal diffusivity cement would curtail shear stress development in the casing during hydrate dissociation. They also found that low-thermal diffusivity cement could enhance casing shear stress development if voids were present in the cement.

In summary, it is found that the modelling of cement volume change is needed for well integrity analyses. Also, formation stress state might have significant impact on formation integrity during well construction processes. However, well construction processes simulated in these studies are rather oversimplified. The actual well construction processes include more than just drilling and/or cement shrinkage, which seem to be the only well construction stages modelled in these studies. Other essential well construction processes include, but are not limited to, casing hanging, cementing, cement hardening and casing landing. Unless the entire well construction processes are incorporated in the order of their implementation in the field, the effect of well construction processes on formation integrity cannot be assessed accurately. Therefore, more detailed construction processes need to be incorporated into the simulation to facilitate better formation integrity assessments.

2.3.3.   Reservoir compaction modelling

Table 2-4 lists finite element and difference models that simulate reservoir compaction process but not well construction process. Many well failures are caused by shear deformation of the overburden layer during reservoir compaction (Bruno & Bovberg 1992), especially in the form of weak layer slip (Hamilton et al. 1993; Furui et al. 2011). The overburden shear deformation could be enhanced by water injection (Fredrich et al. 2000), which is often implemented as a countermeasure against reservoir compaction.

Table 2-4 Well integrity models with reservoir compaction process only.

Authors	Casing	Cement	Formation	Well construction	Reservoir compaction
Bruno & Bovberg (1992)	No	No	Yes	No	Yes
Hamilton et al. (1993)	No	No	Yes	No	Yes
Fredrich et al. (2000)	No	No	Yes	No	Yes
Sayers et al. (2006)	No	No	Yes	No	Yes
Furui et al. (2011)	No	No	Yes	No	Yes
Shin & Santamarina (2016)	Yes	No	Yes	No	Yes
Chia & Bradley (1988)	Yes	Yes	Yes	No	Yes
Yudovich et al. (1988)	Yes	Yes	Yes	No	Yes
Chia & Bradley (1989)	Yes	Yes	Yes	No	Yes
Li et al. (2003)	Yes	Yes	Yes	No	Yes
Li et al. (2005)	Yes	Yes	Yes	No	Yes
Jinnai & Morita (2009)	Yes	Yes	Yes	No	Yes
Yoneda et al. (2018)	Yes	Yes	Yes	No	Yes

Well integrity could be compromised by compressive deformation as well. Yudovich et al. (1988) showed that 5% axial strain would be the threshold value for compressive casing failure. This threshold could be met sooner with higher depressurization rates (Chia & Bradley 1989) and/or insufficient mechanical support by cement sheath (Sayers et al. 2006). Also, the compressive failure could be localized at casing connections (Li et al. 2003). Moreover, not only casing but also gravel pack could also fail during reservoir compaction (Yoneda et al. 2018). As to cement, it could be damaged at lithology interfaces (e.g., shale-sand interface, overburden-reservoir interface) (Li et al. 2005; Jinnai & Morita 2009). The compressive stress/strain development of the well are found dependent on formation permeability change caused by porosity change (Shin & Santamarina 2016) and interface friction strength between cement and formation (Chia & Bradley 1988).

In summary, it is found that well failures are closely linked with formation deformation, e.g., well could fail in shear if the shear deformation of formation becomes significant. The compressive well failure is controlled by depressurization rates as well as whether sufficient cement mechanical support is present in the well. The modelling of interface friction seems also important. However, one of the shortcomings of these studies is that well construction processes are not included prior to reservoir compaction process. As well construction precedes reservoir compaction, well construction processes could have critical effects on well/formation integrities during reservoir compaction. For example, reduction in the radial stress could occur due to cement shrinkage around the well, which affects shaft friction development of the well during reservoir compaction. Also, reduction in the formation stiffness due to plastic deformation of the formation during drilling could affect formation behaviour during reservoir compaction. Another limitation is that the interface friction constitutive model (i.e., Coulomb friction model) employed in these studies is not calibrated against laboratory test data. The deformation of the well during reservoir compaction is governed by shaft friction development between the well and formation, hence it is critical to model the interface friction behaviour accurately. Therefore, a model, which incorporates well construction processes prior to reservoir compaction process as well as a calibrated interface friction constitutive model, has to be developed, in order to assess well integrity accurately during reservoir compaction.

2.3.4. Combination of well construction and reservoir compaction modelling

Table 2-5 lists finite element and difference models that simulated both well construction and reservoir compaction processes. Klar et al. (2010) found that hydrate dissociation in a horizontal well could lead to the development of bending moment in the casing due to the stress relaxation in the formation in the horizontal direction, where hydrate initially bears part of the wellbore pressure (i.e., cement slurry pressure) prior to depressurization. Rutqvist et al. (2012) found that drilling pressure and quality of cement job (e.g., presence of void) are important in maintaining formation integrity. Qiu et al. (2015) found that the effect of methane hydrate on the mechanical properties of formation governs the timing of plastic strain development in the formation. In these simulations, however, only the drilling and/or completion stage is incorporated as the other well construction processes, such as cement shrinkage, which is found to have significant impact on well integrity from the literature introduced in the earlier sections, are ignored.

At present, the model developed by Xu (2014) seems to be the only model which simulates casing-cement-formation interaction during reservoir compaction process after detailed well construction processes. Xu (2014) conducted an axi-symmetric hydro-mechanical finite element analysis on well integrity in the Nankai Trough case. In his model, however, a realistic range of cement

shrinkage volume was not employed as it was unknown at that time. Also, the effect of different horizontal stress distributions of the formation on well integrity was not assessed. Moreover, the well-formation interface friction model was not calibrated through experimental data, as the simple Coulomb friction model was employed. Therefore, the work by Xu (2014) needs to be extended by new models which (i) quantify a reasonable range of cement shrinkage volume in the wellbore conditions, (ii) evaluate the effect of cement shrinkage and initial horizontal stress distributions of the formation on well integrity during well construction processes and (iii) assess the effect of reservoir compaction on well integrity by using a calibrated well-formation friction constitutive model. These extensions to the existing well integrity models will lead to an advancement of well integrity analysis in methane hydrate reservoirs in the Nankai Trough.

Table 2-5 Well integrity models with both well construction and reservoir compaction processes.

Authors	Casing	Cement	Formation	Well construction	Reservoir compaction
Klar et al. (2010)	Yes	No	Yes	Yes	Yes
Rutqvist et al. (2012)	Yes	No	Yes	Yes	Yes
Qiu et al. (2015)	Yes	Yes	Yes	Yes	Yes
Xu (2014)	Yes	Yes	Yes	Yes	Yes

2.3.5. Methane hydrate critical state model

Details of the methane hydrate critical state (MHCS) constitutive model (Uchida 2012; Uchida et al. 2012), which is used to model the hydrate-bearing formation behaviour in this thesis, are provided herein. In the MHCS model employed in this thesis, the temperature terms are omitted due to their insignificant effects on the geomechanical behaviour of hydrate-bearing soil. The essential components of any constitutive models are (i) elastic properties, (ii) yield criterion, (iii) flow rule and (iv) hardening rule (Wood 2004), hence each of these characteristics of the MHCS model adopted in this research are described below.

(i)   Elastic properties

The isotropic linear elastic stiffness matrix of hydrate-bearing soil (D_{hs}^e) is assumed to be composed of those of soil skeleton and methane hydrate. The effective stress increment relative to the initial effective stress level ($\sigma' - \sigma'_0$) is calculated as the product of the stiffness matrix of hydrate-bearing soil and elastic strain vector (ϵ^e) as follows:

$$\sigma' - \sigma'_0 = D_{hs}^e \epsilon^e \tag{2-1}$$

where σ' = effective stress, σ'_0 = initial (reference) effective stress, D_{hs}^e = stiffness matrix of

hydrate-bearing soil and ϵ^e = elastic strain. The initial effective stress level is considered because the stress state of hydrate-bearing soil changes not only with elastic strain increments but also with hydrate dissociation-induced softening. As a result, in order to calculate the effective stress increment ($d\boldsymbol{\sigma}'$), changes in the stiffness of hydrate-bearing soil due to hydrate dissociation ($d\boldsymbol{D}_{hs}^e = (\partial \boldsymbol{D}_{hs}^e/\partial S_h)dS_h$) need to be considered in addition to the elastic strain increment ($d\boldsymbol{\epsilon}^e$), which leads to the following equation:

$$d\boldsymbol{\sigma}' = \boldsymbol{D}_{hs}^e d\boldsymbol{\epsilon}^e + d\boldsymbol{D}_{hs}^e \boldsymbol{\epsilon}^e$$

$$\Leftrightarrow \qquad d\boldsymbol{\sigma}' = \boldsymbol{D}_{hs}^e (d\boldsymbol{\epsilon} - d\boldsymbol{\epsilon}^p) + d\boldsymbol{D}_{hs}^e \boldsymbol{\epsilon}^e \tag{2-2}$$

where $d\boldsymbol{\sigma}'$ = effective stress increment, $d\boldsymbol{\epsilon}^e$ = elastic strain increment, $d\boldsymbol{D}_{hs}^e$ ($=(\partial \boldsymbol{D}_{hs}^e/\partial S_h)dS_h$) = changes in stiffness matrix of hydrate-bearing soil due to hydrate dissociation and $d\boldsymbol{\epsilon}^p$ = plastic strain increment. The stiffness matrix of hydrate-bearing soil is defined as follows:

$$\boldsymbol{D}_{hs}^e = \begin{bmatrix} \frac{4}{3}G_{hs} + K_{hs} & -\frac{2}{3}G_{hs} + K_{hs} & -\frac{2}{3}G_{hs} + K_{hs} & 0 & 0 & 0 \\ -\frac{2}{3}G_{hs} + K_{hs} & \frac{4}{3}G_{hs} + K_{hs} & -\frac{2}{3}G_{hs} + K_{hs} & 0 & 0 & 0 \\ -\frac{2}{3}G_{hs} + K_{hs} & -\frac{2}{3}G_{hs} + K_{hs} & \frac{4}{3}G_{hs} + K_{hs} & 0 & 0 & 0 \\ 0 & 0 & 0 & G_{hs} & 0 & 0 \\ 0 & 0 & 0 & 0 & G_{hs} & 0 \\ 0 & 0 & 0 & 0 & 0 & G_{hs} \end{bmatrix} \tag{2-3}$$

where K_{hs} = bulk modulus of hydrate-bearing soil and G_{hs} = shear modulus of hydrate-bearing soil, which are calculated by the following equations:

$$K_{hs} = K_s + K_h \approx K_s = \frac{p'}{\kappa(1-n)} \tag{2-4}$$

$$G_{hs} = G_s + G_h = \frac{3(1-2\nu)}{2(1+\nu)}K_s + m_2 \chi S_h \tag{2-5}$$

where K_s = bulk modulus of the soil skeleton, K_h = enhancement of the bulk modulus of soil skeleton due to methane hydrate, p' ($= tr(\boldsymbol{\sigma}')/3$) = mean effective stress, κ = the gradient of swelling line as defined in Critical State Soil Mechanics (Schofield & Wroth 1968), n = porosity,

G_s = shear modulus of hydrate-bearing soil, G_h = enhancement of the shear modulus of hydrate-bearing soil due to methane hydrate, ν = Poisson's ratio of soil skeleton, m_2 = stiffness enhancement constant, χ = stiffness degradation constant and S_h = hydrate saturation. From the definitions of the stiffness matrix, bulk modulus and shear modulus of hydrate-bearing soil, changes in the stiffness matrix due to hydrate dissociation are derived as follows:

$$dD_{hs}^e = \frac{\partial D_{hs}^e}{\partial S_h} dS_h = \begin{bmatrix} \frac{4}{3}m_2 & -\frac{2}{3}m_2 & -\frac{2}{3}m_2 & 0 & 0 & 0 \\ -\frac{2}{3}m_2 & \frac{4}{3}m_2 & -\frac{2}{3}m_2 & 0 & 0 & 0 \\ -\frac{2}{3}m_2 & -\frac{2}{3}m_2 & \frac{4}{3}m_2 & 0 & 0 & 0 \\ 0 & 0 & 0 & m_2 & 0 & 0 \\ 0 & 0 & 0 & 0 & m_2 & 0 \\ 0 & 0 & 0 & 0 & 0 & m_2 \end{bmatrix} \chi dS_h \qquad (2\text{-}6)$$

The χ parameter ranges from 1 (initial value) to 0 (ultimate value) depending on the accumulated plastic deviatoric strain which induces shear degradation of the stiffness contributed by hydrate.

(ii)   Yield criterion

The yield surface of the MHCS model is defined as follows:

$$f(p', q, p'_{cs}, p'_{cd}, p'_{cc}, R) = q^2 + M^2(p' + p'_{cc})(p' - R(p'_{cs} + p'_{cd} + p'_{cc})) = 0 \qquad (2\text{-}7)$$

where $q\ (= q(\boldsymbol{\sigma}') = \sqrt{3J_2})$ = deviator stress (J_2= the second invariant of deviatoric stress tensor), $p'\ (= p'(\boldsymbol{\sigma}') = tr(\boldsymbol{\sigma}')/3)$ = mean effective stress, M = critical state frictional constant, p'_{cs} = preconsolidation stress, $p'_{cd}\ (= A(\chi dS_h)^B)$ = dilation enhancement parameter, $p'_{cc}\ (= C(\chi dS_h)^D)$ = cohesion enhancement parameter, R = Hashiguchi subloading surface ratio. The subloading surface ratio, R, can take a positive value between 0 and 1, which indicates that when $R = 1$ the soil has reached the yield condition. The Hashiguchi subloading surface (Hashiguchi 1989) is an auxiliary yield surface within the yield surface which is designed to produce small plastic strains prior to yielding. The subloading surface thus helps introduce smooth transition from elastic constitutive behaviours to plastic ones. A schematic diagram of an MHCS yield surface and subloading surfaces is shown in Figure 2-5.

The consistency condition adopted in this thesis is shown below:

$$f(\boldsymbol{\sigma}' + d\boldsymbol{\sigma}', p'_{cs} + dp'_{cs}, p'_{cd} + dp'_{cd}, p'_{cc} + dp'_{cc}, R + dR) = 0$$

$$\Leftrightarrow \quad f(\boldsymbol{\sigma'} + \boldsymbol{D}^e_{hs}d\boldsymbol{\epsilon} + d\boldsymbol{D}^e_{hs}\boldsymbol{\epsilon}^e, p'_{cs}, p'_{cd}, p'_{cc}, R) - \left(\frac{\partial f}{\partial \boldsymbol{\sigma'}}\right)^T \boldsymbol{D}^e_{hs}d\boldsymbol{\epsilon}^p + \left(\frac{\partial f}{\partial p'_{cs}}\right)dp'_{cs}$$

$$+ \left(\frac{\partial f}{\partial p'_{cd}}\right)dp'_{cd} + \left(\frac{\partial f}{\partial p'_{cc}}\right)dp'_{cc} + \left(\frac{\partial f}{\partial R}\right)dR = 0$$

$$\Leftrightarrow \quad f^{pred} - \left(\frac{\partial f}{\partial \boldsymbol{\sigma'}}\right)^T \boldsymbol{D}^e_{hs}d\boldsymbol{\epsilon}^p + \left(\frac{\partial f}{\partial p'_{cs}}\right)dp'_{cs} + \left(\frac{\partial f}{\partial p'_{cd}}\right)dp'_{cd} + \left(\frac{\partial f}{\partial p'_{cc}}\right)dp'_{cc}$$

$$+ \left(\frac{\partial f}{\partial R}\right)dR = 0 \tag{2-8}$$

where f^{pred} = the value of the yield function at prediction stress state.
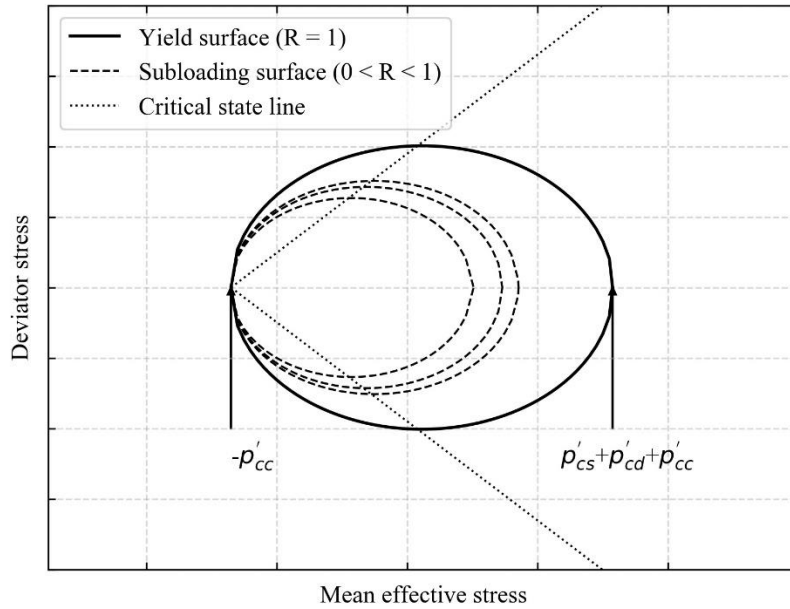
Figure 2-5 A schematic diagram of an MHCS yield surface (R = 1) and subloading surfaces (0 < R < 1), which have a symmetric elliptic shape.

(iii)   Flow rule

Associated flow rule (i.e. plastic potential function (g) = yield criterion (f)) is employed in the MHCS model. Hence, the plastic strain increment is calculated as follows:

$$d\boldsymbol{\epsilon}^p = \Lambda \frac{\partial g}{\partial \boldsymbol{\sigma'}} = \Lambda \frac{\partial f}{\partial \boldsymbol{\sigma'}} \tag{2-9}$$

where Λ = plastic multiplier. Plastic volumetric and deviatoric strain increments are calculated as below:

20

$$d\epsilon_v^p = \Lambda \frac{\partial f}{\partial p'} \tag{2-10}$$

$$d\epsilon_d^p = \Lambda \frac{\partial f}{\partial q} \tag{2-11}$$

(iv)   Hardening rule

There are four hardening parameters in the MHCS model (p'_{cs}, p'_{cd}, p'_{cc}, R). Plastic volumetric hardening is used for the hardening of preconsolidation stress (p'_{cs}) as follows:

$$dp'_{cs} = \frac{p'_{cs}}{(\lambda - \kappa)(1 - n)} d\epsilon_v^p \tag{2-12}$$

where p'_{cs} = preconsolidation stress, dp'_{cs} = preconsolidation stress increment, λ, κ = the gradient of compression line and swelling line as defined in Critical State Soil Mechanics, respectively (Schofield & Wroth 1968), n = porosity, $d\epsilon_v^p$ = plastic volumetric strain increment.

Plastic deviatoric hardening along with hydrate dissociation-induced hardening are employed for the dilation enhancement parameter (p'_{cd}) and cohesion enhancement parameter (p'_{cc}) as follows:

$$dp'_{cd} = AB(\chi S_h)^{B-1}\left(-m_1 \chi S_h d\epsilon_d^p + \chi dS_h\right) \tag{2-13}$$

$$dp'_{cc} = CD(\chi S_h)^{D-1}\left(-m_1 \chi S_h d\epsilon_d^p + \chi dS_h\right) \tag{2-14}$$

where A, B = constants for the dilation enhancement parameter, C, D = constants for the cohesion enhancement parameter, S_h = hydrate saturation, χ = a parameter for shear degradation of hydrate, m_1 = a constant for shear degradation of hydrate, $d\epsilon_d^p$ = plastic deviatoric strain increment. A combination of plastic volumetric and deviatoric hardening (i.e., the L^2 norm of plastic strain increments ($|d\epsilon^p|$)) is employed for the hardening of the subloading surface ratio (R) as shown in the equation below:

$$dR = -U\left(1 + \frac{p'_{cd} + p'_{cc}}{p'_{cs}}\right) \ln R \, |d\epsilon^p| \tag{2-15}$$

where U = subsurface constant and $|d\epsilon^p|$ = the L^2 norm of the plastic strain increment vector.

By substituting Equation 2-9, 2-10, 2-11, 2-12, 2-13, 2-14 and 2-15 into Equation 2-8, the plastic multiplier (Λ) is calculated as below:

$$\Lambda = \frac{f^{pred} + \frac{\partial f}{\partial S_h} dS_h}{\left(\frac{\partial f}{\partial \boldsymbol{\sigma'}}\right)^T \boldsymbol{D}_{hs}^e \left(\frac{\partial f}{\partial \boldsymbol{\sigma'}}\right) - \left(\frac{\partial f}{\partial \epsilon_v^p}\right)\left(\frac{\partial f}{\partial p'}\right) - \left(\frac{\partial f}{\partial \epsilon_d^p}\right)\left(\frac{\partial f}{\partial q}\right) - \left(\frac{\partial f}{\partial R}\frac{dR}{|d\epsilon^p|}\right)\left|\frac{\partial f}{\partial \boldsymbol{\sigma'}}\right|} \qquad (2\text{-}16)$$

It is noted that all the derivatives are evaluated at the stress level = $\boldsymbol{\sigma'} + \boldsymbol{D}_{hs}^e d\boldsymbol{\epsilon} + d\boldsymbol{D}_{hs}^e \boldsymbol{\epsilon}^e$. The advantage of calculating Λ using f^{pred} is that iterations can be implemented to ensure $f = 0$ at the updated values of the parameters (i.e., $p' + dp', q + dq, p'_{cs} + dp'_{cs}, p'_{cd} + dp'_{cd}, p'_{cc} + dp'_{cc}, R + dR$). For example, if $f_i \neq 0$ ($i = 1,2, \dots$) after i-th iteration, another iteration can be conducted to calculate Λ_{i+1} by substituting $f^{pred} = f_i$ (and $dS_h = 0$ if dS_h for the increment is already applied in a previous iteration) in Equation 2-16. Also, all the partial derivatives have to be re-evaluated with the updated values of the parameters to obtain Λ_{i+1}. Consequently, the stress increment that satisfies $f = 0$ is obtained as follows:

$$
\begin{aligned}
d\boldsymbol{\sigma'} &= \boldsymbol{D}_{hs}^e \left(d\boldsymbol{\epsilon} - \sum_i d\boldsymbol{\epsilon}_i^p\right) + d\boldsymbol{D}_{hs}^e \boldsymbol{\epsilon}^e \\
&= \boldsymbol{D}_{hs}^e d\boldsymbol{\epsilon} + d\boldsymbol{D}_{hs}^e \boldsymbol{\epsilon}^e - \sum_i \boldsymbol{D}_{hs}^e \Lambda_i \left(\frac{\partial f}{\partial \boldsymbol{\sigma'}}\right)_i
\end{aligned}
\qquad (2\text{-}17)
$$

Finally, the constitutive Jacobian ($\partial d\boldsymbol{\sigma'}/\partial d\boldsymbol{\epsilon}$) is calculated through the substitution of Equation 2-9, 2-16 and 2-17 into Equation 2-2:

$$
\begin{aligned}
d\boldsymbol{\sigma'} &= \boldsymbol{D}_{hs}^e d\boldsymbol{\epsilon} - \frac{\boldsymbol{D}_{hs}^e \frac{\partial f}{\partial \boldsymbol{\sigma'}} f^{pred}}{\left(\frac{\partial f}{\partial \boldsymbol{\sigma'}}\right)^T \boldsymbol{D}_{hs}^e \left(\frac{\partial f}{\partial \boldsymbol{\sigma'}}\right) - \left(\frac{\partial f}{\partial \epsilon_v^p}\frac{\partial f}{\partial p'}\right) - \left(\frac{\partial f}{\partial \epsilon_d^p}\frac{\partial f}{\partial q}\right) - \left(\frac{\partial f}{\partial R}\frac{dR}{|d\epsilon^p|}\right)\left|\frac{\partial f}{\partial \boldsymbol{\sigma'}}\right|} \\
&\quad + \left(\left(\frac{\partial \boldsymbol{D}_{hs}^e}{\partial S_h}\right)\boldsymbol{\epsilon}^e - \frac{\boldsymbol{D}_{hs}^e \frac{\partial f}{\partial \boldsymbol{\sigma'}}\frac{\partial f}{\partial S_h}}{\left(\frac{\partial f}{\partial \boldsymbol{\sigma'}}\right)^T \boldsymbol{D}_{hs}^e \left(\frac{\partial f}{\partial \boldsymbol{\sigma'}}\right) - \left(\frac{\partial f}{\partial \epsilon_v^p}\frac{\partial f}{\partial p'}\right) - \left(\frac{\partial f}{\partial \epsilon_d^p}\frac{\partial f}{\partial q}\right) - \left(\frac{\partial f}{\partial R}\frac{dR}{|d\epsilon^p|}\right)\left|\frac{\partial f}{\partial \boldsymbol{\sigma'}}\right|}\right) dS_h \\
&= \boldsymbol{D}_{hs}^e d\boldsymbol{\epsilon} - \frac{\boldsymbol{D}_{hs}^e \frac{\partial f}{\partial \boldsymbol{\sigma'}}\left(f(p', q, p'_{cs}, p'_{cd}, p'_{cc}, R) + \left(\frac{\partial f}{\partial \boldsymbol{\sigma'}}\right)^T \left(\boldsymbol{D}_{hs}^e(d\boldsymbol{\epsilon} - \sum_i d\boldsymbol{\epsilon}_i^p) + d\boldsymbol{D}_{hs}^e \boldsymbol{\epsilon}^e\right)\right)}{\left(\frac{\partial f}{\partial \boldsymbol{\sigma'}}\right)^T \boldsymbol{D}_{hs}^e \left(\frac{\partial f}{\partial \boldsymbol{\sigma'}}\right) - \left(\frac{\partial f}{\partial \epsilon_v^p}\frac{\partial f}{\partial p'}\right) - \left(\frac{\partial f}{\partial \epsilon_d^p}\frac{\partial f}{\partial q}\right) - \left(\frac{\partial f}{\partial R}\frac{dR}{|d\epsilon^p|}\right)\left|\frac{\partial f}{\partial \boldsymbol{\sigma'}}\right|}
\end{aligned}
$$

$$+\left(\left(\frac{\partial \boldsymbol{D}_{hs}^e}{\partial S_h}\right)\boldsymbol{\epsilon}^e - \frac{\boldsymbol{D}_{hs}^e\frac{\partial f}{\partial \boldsymbol{\sigma'}}\frac{\partial f}{\partial S_h}}{\left(\frac{\partial f}{\partial \boldsymbol{\sigma'}}\right)^T \boldsymbol{D}_{hs}^e\left(\frac{\partial f}{\partial \boldsymbol{\sigma'}}\right) - \left(\frac{\partial f}{\partial \epsilon_v^p}\frac{\partial f}{\partial p'}\right) - \left(\frac{\partial f}{\partial \epsilon_d^p}\frac{\partial f}{\partial q}\right) - \left(\frac{\partial f}{\partial R}\frac{dR}{|d\boldsymbol{\epsilon}^p|}\right)\left|\frac{\partial f}{\partial \boldsymbol{\sigma'}}\right|}\right)dS_h$$

$$=\left(\boldsymbol{D}_{hs}^e - \frac{\boldsymbol{D}_{hs}^e\left(\frac{\partial f}{\partial \boldsymbol{\sigma'}}\right)\left(\frac{\partial f}{\partial \boldsymbol{\sigma'}}\right)^T \boldsymbol{D}_{hs}^e}{\left(\frac{\partial f}{\partial \boldsymbol{\sigma'}}\right)^T \boldsymbol{D}_{hs}^e\left(\frac{\partial f}{\partial \boldsymbol{\sigma'}}\right) - \left(\frac{\partial f}{\partial \epsilon_v^p}\frac{\partial f}{\partial p'}\right) - \left(\frac{\partial f}{\partial \epsilon_d^p}\frac{\partial f}{\partial q}\right) - \left(\frac{\partial f}{\partial R}\frac{dR}{|d\boldsymbol{\epsilon}^p|}\right)\left|\frac{\partial f}{\partial \boldsymbol{\sigma'}}\right|}\right)d\boldsymbol{\epsilon}$$

$$+\left(\left(\frac{\partial \boldsymbol{D}_{hs}^e}{\partial S_h}\right)\boldsymbol{\epsilon}^e - \frac{\boldsymbol{D}_{hs}^e\frac{\partial f}{\partial \boldsymbol{\sigma'}}\left(\left(\frac{\partial f}{\partial \boldsymbol{\sigma'}}\right)^T\left(\frac{\partial \boldsymbol{D}_{hs}^e}{\partial S_h}\right)\boldsymbol{\epsilon}^e + \left(\frac{\partial f}{\partial S_h}\right)\right)}{\left(\frac{\partial f}{\partial \boldsymbol{\sigma'}}\right)^T \boldsymbol{D}_{hs}^e\left(\frac{\partial f}{\partial \boldsymbol{\sigma'}}\right) - \left(\frac{\partial f}{\partial \epsilon_v^p}\frac{\partial f}{\partial p'}\right) - \left(\frac{\partial f}{\partial \epsilon_d^p}\frac{\partial f}{\partial q}\right) - \left(\frac{\partial f}{\partial R}\frac{dR}{|d\boldsymbol{\epsilon}^p|}\right)\left|\frac{\partial f}{\partial \boldsymbol{\sigma'}}\right|}\right)dS_h$$

$$+\frac{\boldsymbol{D}_{hs}^e\frac{\partial f}{\partial \boldsymbol{\sigma'}}\left(\frac{\partial f}{\partial \boldsymbol{\sigma'}}\right)^T \boldsymbol{D}_{hs}^e\sum_i d\epsilon_i^p}{\left(\frac{\partial f}{\partial \boldsymbol{\sigma'}}\right)^T \boldsymbol{D}_{hs}^e\left(\frac{\partial f}{\partial \boldsymbol{\sigma'}}\right) - \left(\frac{\partial f}{\partial \epsilon_v^p}\frac{\partial f}{\partial p'}\right) - \left(\frac{\partial f}{\partial \epsilon_d^p}\frac{\partial f}{\partial q}\right) - \left(\frac{\partial f}{\partial R}\frac{dR}{|d\boldsymbol{\epsilon}^p|}\right)\left|\frac{\partial f}{\partial \boldsymbol{\sigma'}}\right|}$$

As a result,

$$\therefore \quad \frac{\partial d\boldsymbol{\sigma'}}{\partial d\boldsymbol{\epsilon}} = \boldsymbol{D}_{hs}^e - \frac{\boldsymbol{D}_{hs}^e\left(\frac{\partial f}{\partial \boldsymbol{\sigma'}}\right)\left(\frac{\partial f}{\partial \boldsymbol{\sigma'}}\right)^T \boldsymbol{D}_{hs}^e}{\left(\frac{\partial f}{\partial \boldsymbol{\sigma'}}\right)^T \boldsymbol{D}_{hs}^e\left(\frac{\partial f}{\partial \boldsymbol{\sigma'}}\right) - \left(\frac{\partial f}{\partial \epsilon_v^p}\frac{\partial f}{\partial p'}\right) - \left(\frac{\partial f}{\partial \epsilon_d^p}\frac{\partial f}{\partial q}\right) - \left(\frac{\partial f}{\partial R}\frac{dR}{|d\boldsymbol{\epsilon}^p|}\right)\left|\frac{\partial f}{\partial \boldsymbol{\sigma'}}\right|} \quad (2\text{-}18)$$

It is noted again that all the derivatives should be evaluated with updated values of the model parameters at the end of the final iteration where the convergence ($f = 0$) is considered to be established.

2.4. Annular cement shrinkage

In most well integrity models introduced in the preceding section, cement shrinkage was not incorporated because it was assumed insignificant for well integrity. However, if the cement is surrounded by low-permeability formation, significant cement shrinkage could occur due to insufficient water supply to the cement during its hydration reaction from the formation. Therefore, it is critical to investigate the shrinkage behaviour of cement in the wellbore conditions, especially

at its early age (i.e., a few days since the mixing of cement with water) as the majority of cement shrinkage occurs during this time period. In the following sections, the physics of cement shrinkage as well as laboratory tests and numerical simulations for the shrinkage behaviour of early-age cement are presented.

2.4.1. The physics of cement shrinkage

Cement shrinkage is characterized by the development of capillary suction pressure in the pores of cement during its hydration period where water is consumed by the cement particles. Hua et al. (1995) showed that the shrinkage volume of early-age cement after the initial set (i.e., phase shift from liquid to solid cement) could be estimated by applying capillary suction pressure change as confining pressure on a porous elastic material with time-varying stiffness. Lura et al. (2003) modelled capillary suction pressure development as a function of time-varying degree of water saturation, in order to calculate the confining pressure development and resulting cement shrinkage development accurately. By conducting a thermo-hydro-mechanical coupled finite element analysis, Zhen & Xiong (2013) found that the contribution of the thermal strain from cement hydration heat to cement shrinkage was pronounced only during the first 5 h since the initial set after which it decreased to a negligible level in 24 h. The capillary suction pressure concept for estimating the shrinkage volume of cement was found effective for post early-age cement as well (Coussy et al. 2004). Rougelot et al. (2009) also showed that the capillary suction pressure concept would be valid for hardened cement and argued that the effect of cement particle stiffness and cement bulk stiffness was significant.

Considering the abovementioned findings on the physics of the shrinkage of cement, it is more effective to carry out a hydro-mechanical coupled numerical analysis on a porous elastic material with the capillary suction pressure concept than to carry out an uncoupled mechanical analysis in which cement shrinkage is modelled by specifying a uniform volume change as a boundary condition, in order to accurately estimate the shrinkage behaviour of early-age cement. By adopting the former approach, water flow from the formation to hydrating cement can be modelled, which reflects the actual shrinkage behaviour of cement under the wellbore conditions. An earlier attempt of such modelling was performed by Thiercelin et al. (1998), who utilized the fluid sink term in the hydro-mechnical coupled equations to model the water consumption within the cement which was modelled as a porous material. Bois et al. (2011) and Bois et al. (2012) employed a simpler approach to model the shrinkage behaviour of cement in which the pore pressure of the porous material (i.e., cement) was specified as an input parameter that changes with time. It is noted that capillary suction pressure (p_g-p_l) reduces to pore liquid pressure (p_l) when the cement pore space is fully saturated (p_g=0) and cavitation is unlikely to occur due to

high liquid pressure (e.g., deepwater cementing).

Table 2-6 Shrinkage volume values of oil/gas well cements measured in laboratory.

	Cement type	Water-to-cement ratio	Additives	Temperature (°C)	Pressure (MPa)	Drainage	Test duration (h)	Shrinkage volume (%)
Backe et al. (1999)	Class G	0.44	Retarder	90	0.0025	Open	20	3.92
Chenevert & Shrestha (1991)	Class H	N/A	Retarder	37.8, 65.6, 93.3	8.27, 24.1, 35.9	Closed	70	4.3, 3.8, 3.4
Goboncan & Dillenbeck (2003)	Class G	N/A	Fluid loss control, dispersant	149	19.3	Open	110	0.1
Justnes et al. (1995)	Class G	0.3, 0.4, 0.5	None	20	Ambient pressure	Closed	48	2.2, 1.5, 1.1
Lyomov et al. (1997)	N/A	N/A	Retarder	25, 60,	0.6~1.6	Open	24	3.7, 3.5
Parcevaux & Sault (1984)	Class G	0.44	Dispersant, retarder	20	0.5, 4.0, 10.0	Closed	48	7.15, 6.30, 4.30
Reddy et al. (2009)	N/A	N/A	Defoamer	26.7	0, 6.89, 13.8, 20.7	Closed	70	1.3, 3.1, 3.6, 3.8

2.4.2. Laboratory tests on cement shrinkage

Various shrinkage volume values of typical oil well cements are reported in the literature. As shown in Table 2-6, a wide range of shrinkage volume between 0.1% and 7.15% is reported. The shrinkage behaviour of cement is affected by many factors, including temperature and pressure conditions as well as test equipment and procedure (Reddy et al. 2009). For example, high-temperature conditions cause the double-peak hydration temperature evolution of cement, which results in the S-shaped shrinkage development curves (Lyomov et al. 1997). Goboncan & Dillenbeck (2003) showed that under high-pressure and high-temperature conditions (20 MPa and 150 °C) the shrinkage volume of Class G cement was 0.1% at 100 h since the mixing of cement powder with water. The shrinkage volume of Class G cement decreased with decreasing water-to-cement ratio as well as increasing amount of calcium carbonate and polyvinyl alcohol (PVA) (Justnes et al. 1995). Also, lower cement powder contents (Backe et al. 1999) and higher bonding agent contents (Parcevaux & Sault 1984) resulted in smaller cement shrinkage volume. As for Class H cement, it was shown that the shrinkage volume decreased with increasing pressure and temperature as well as increasing amount of sodium chloride, silica flour, bentonite or sodium silicate (Chenevert & Shrestha 1991). This is because the amount of water available for cement

hydration was decreased by those conditions and additives. The shrinkage volume of Class H cement cured under 8.3 MPa and 38 °C reached its asymptotic value of 3.8% in 70 h (Chenevert & Shrestha 1987).

Although a significant amount of studies on cement shrinkage in laboratory have accumulated in the literature, measured cement shrinkage volumes may not be representative under the wellbore conditions. It is not realistic to conduct a laboratory test in which the wellbore conditions are realized because casing and formation would have to be included to create the annulus for curing cement under high-pressure and/or high-temperature conditions. Therefore, it is more effective to carry out a numerical simulation which incorporates the aforementioned coupled hydro-mechanical modelling framework on a porous material with the capillary pressure concept, in order to estimate the shrinkage volume of early-age cement.

2.4.3. Cement shrinkage and well integrity

Despite the uncertainty in the shrinkage behaviour of early-age cement in the actual wellbore conditions, the effect of cement shrinkage on well integrity has been examined in the literature. For example, Ravi et al. (2002) showed that, the smaller the cement shrinkage is, the smaller the risk of cement failure (i.e., cracking, plastic deformation and debonding) becomes. Oyarhossein & Dusseault (2015) reported that the shrinkage of cement surrounded by stiff formation would increase the risk of casing-cement interface debonding because stiff formation could not deform with the shrinking cement. They argued that cement shrinkage data under the wellbore conditions would be necessary, in order to conduct more accurate assessment. Gray et al. (2007) carried out a three-dimensional finite element analysis and showed that cement shrinkage could cause debonding at the casing-cement interface if anisotropic horizontal plastic strain development occurs in the formation.

In these studies, however, a uniform shrinkage volume was specified in the cement as a boundary condition. Moreover, the values of cement shrinkage were radically different among the studies (i.e., 0% and 4% (Ravi et al. 2002), 0.5% (Oyarhossein & Dusseault 2015) and 5% (Gray et al. 2007)). Saint-Marc et al. (2008) modelled cement shrinkage with more accurate underlining physics of cement shrinkage by incorporating a volumetric strain term in the constitutive equations which was correlated with change in the degree of cement hydration. However, pore fluid flow was not considered in their simulation. Therefore, there is a need for a coupled hydro-mechanical simulation which incorporates the underlining physics of early-age cement shrinkage (i.e., capillary pressure decrease), in order to investigate the effect of cement shrinkage on well integrity under the actual wellbore conditions.

2.5. Well integrity monitoring

The importance of numerical modelling of well integrity during well construction and reservoir compaction processes, as well as that of cement shrinkage, have been highlighted in the earlier sections. However, in order to make the best use of numerical models, it is necessary to provide feedback from field monitoring. Monitoring data can be used to calibrate model parameters and/or to verify/reject assumptions incorporated in numerical models, in order to gain deeper understanding of the phenomena that the models are attempting to capture. Monitoring data could also be used for judging the effectiveness of well operations (e.g., hydraulic fracturing) and/or the locations and timing of remedial operations against well failures. Therefore, it is crucial to carry out field monitoring of well integrity. In the following sections, conventional monitoring techniques and novel distributed fibre optic monitoring techniques are introduced.

2.5.1. Conventional monitoring techniques

Herein, conventional monitoring techniques for the assessment of well integrity are introduced. For the monitoring of formation compaction, radioactive bullets are used. Radioactive bullets, in which low-strength yet high-longevity radioactive material such as caesium is contained, are shot into the formation at known intervals (usually 10 m). Wireline logging tools are then lowered into the well to measure the change in the position of the bullets to estimate the compaction/elongation of the formation (Figure 2-6). A disadvantage of this monitoring technique is that it is applicable only to vertical wells as shooting bullets in deviated wells increases the uncertainty of bullet positions. Also, radioactive bullets may not be used in production wells either because bullet shooting might enhance sand production.

Another monitoring technique is field seismic survey, in which seismic waves are transmitted through the formation and are then reflected back to receiver arrays installed on the formation surface. The seismic data taken at different times are analysed to calculate changes in the seismic velocities of the formation, which are correlated with formation compaction (i.e., seismic velocity increase) and elongation (i.e., seismic velocity decrease) (Figure 2-7).

For the assessment of cement integrity, cement-bond-log (CBL) tools are used. CBL tools represent a small-diameter tubing equipped with acoustic or ultrasonic wave sources and receivers. The generated acoustic and ultrasonic waves respectively propagate through the bulk cement and casing-cement interface before they are detected by the receivers. Measured acoustic and

27

ultrasonic energy losses are correlated with the bulk cement and casing-cement bond quality, respectively. A drawback of CBL tools is that data interpretation is not straightforward as many factors including microannulus at the casing-cement interface, casing eccentricity and CBL tool eccentricity affect CBL measurements. As to casing integrity, callipers can be used to measure the diameter and shape of casing, from which casing deformation can be visualized.
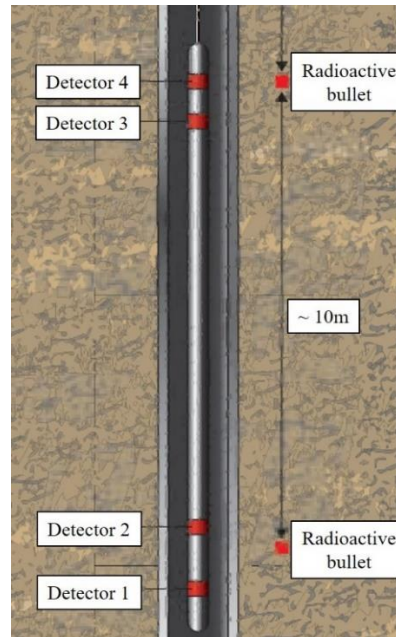
Figure 2-6 Formation compaction monitoring with the radioactive bullet technique [after Doornhof et al. (2006)].
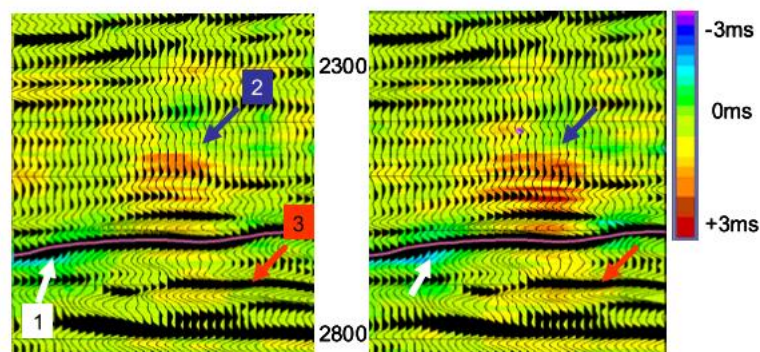
Figure 2-7 An example of formation compaction monitoring by seismic survey in which seismic velocity changes are correlated with formation compaction [after Kristiansen et al. (2005)].

The primary limitation of the conventional monitoring techniques is that they require well intervention (i.e., temporary termination of oil/gas production to allow the entry of logging tools). Because well intervention is extremely expensive, measurements can only be taken once in

several years. However, such low temporal resolution may not be acceptable for the well integrity monitoring in unconsolidated formation, which could develop compaction in a short period of time. Also, the spatial resolution of the conventional techniques is also low (e.g., 10 m for the radioactive bullet technique), which might not capture localized well damage. Moreover, real-time diagnosis of well integrity is difficult with the conventional techniques as time-consuming post-processing is necessary to convert raw data into relevant information, in addition to the fact that the measurement itself takes some time to complete.

Therefore, new monitoring techniques with high spatial and temporal resolutions, which do not require well intervention, are needed to facilitate real-time well integrity assessment. Distributed fibre optic monitoring techniques are a promising candidate for achieving this goal. Hence, in the following sections, distributed fibre optic monitoring techniques are discussed in detail.

2.5.2. Fibre optic monitoring techniques

Fibre optic sensors are effective for oil and gas well monitoring due to their immunity to electromagnetic interreference and high resistance to harsh environments. There are two main fibre optic monitoring techniques: fibre Bragg grating (FBG)-based and backscatter-based techniques.

The FBG-based technique is a semi-distributed monitoring technique as strain and/or temperature change is measured at discrete locations along fibre optic cables where FBG is imprinted. FBG is a periodic modulation of the refractive index of optical fibre core (i.e., red lines in Figure 2-8), which works as a mirror to reflect the input light. The wavelength of reflected light changes with strain and temperature changes, which is utilized to obtain semi-distributed strain and temperature profiles along fibre optic cables.

The backscatter-based technique is a fully distributed monitoring technique. The basic principle of backscatter-based techniques is shown in Figure 2-9. There are three types of backscatters in optical fibres: Rayleigh, Raman and Brillouin backscatters. Rayleigh backscatter occurs due to the interaction of input light with microscopic random fluctuations of the refractive index of optical fibres. The frequency of backscattered Rayleigh light is identical to that of the input light. Raman backscatter is caused by the interaction of input light with molecules which consist optical fibres. The molecules absorb energy from the input light to shift their vibrational state to higher levels. The molecules then emit part of the absorbed energy via backscatter to shift back to lower vibrational states. The frequency of the backscattered Raman light is constant whereas the power changes with the temperature of fibre optic cables. Brillouin backscatter occurs due to the

interaction of input light with the acoustic wave generated by the thermal vibration of the fibre material (Zhang et al. 2015). The frequency of the backscattered Brillouin light changes with strain and temperature changes of fibre optic cables. In the following sections, details about the FBG- and backscatter-based fibre optic monitoring techniques are introduced.
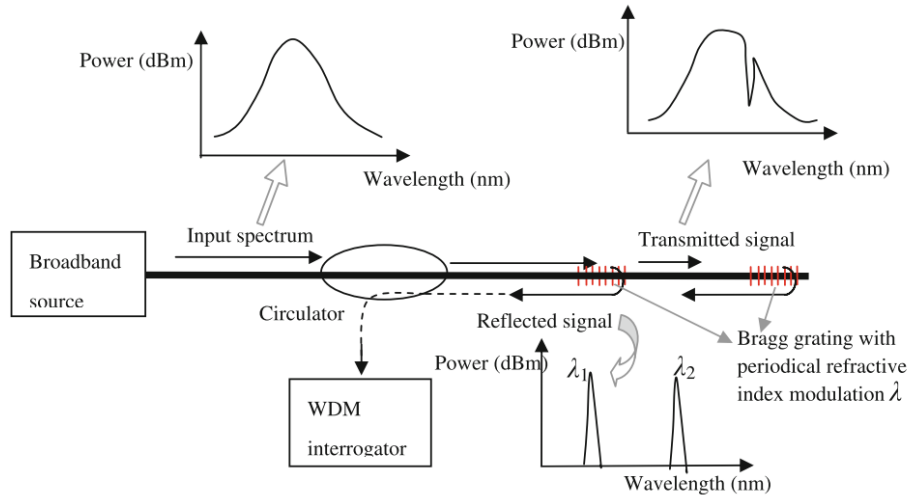
Figure 2-8 The principle of the FBG-based fibre optic monitoring technique [after Xu et al. (2013)].
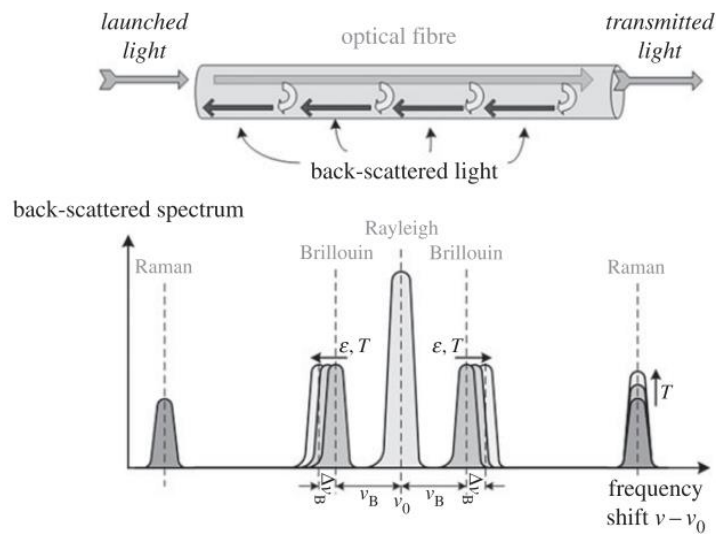
Figure 2-9 The principle of the backscatter-based fibre optic monitoring technique [after Soga & Schooling (2016)].

2.5.3. FBG-based technique

The photosensitivity in optical fibres, which is the cornerstone for realizing the FBG-based techniques, was discovered in late 1970's (Othonos 1997). Fabrication of FBG in optical fibres started to develop rapidly since late 1980's and many studies on the FBG-based technique for

(semi-)distributed sensing purposes have been conducted. For example, the FBG-based technique was found applicable for the monitoring of strain and temperature (Liu et al. 2003) and humidity (Yeo et al. 2005). Due to its semi-distributed nature, the FBG-based technique was found particularly useful for the monitoring of large-scale structures such as civil infrastructure. For the monitoring of bridges, Maaskant et al. (1997) used the FBG-based technique to measure dynamic strain development due to traffic load as well as relaxation of prestresses in tendons. Schulz et al. (2000) measured macroscale strain distributions caused by traffic loading with the FBG-based technique. Gebremichael et al. (2005) utilized strain measurements from the FBG-based technique to facilitate the validation of the design codes for bridges. The FBG-based technique has also been used for other applications such as beam and pile monitoring as well acoustic and ultrasonic monitoring of rock mass (Majumder et al. 2008).

(a)

(b)
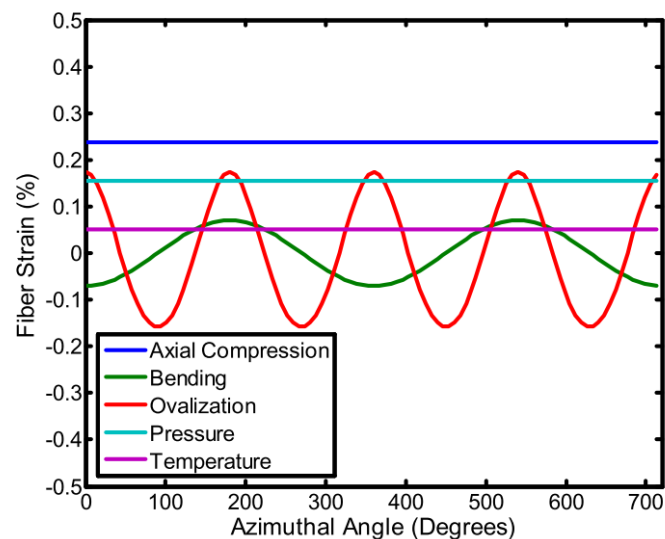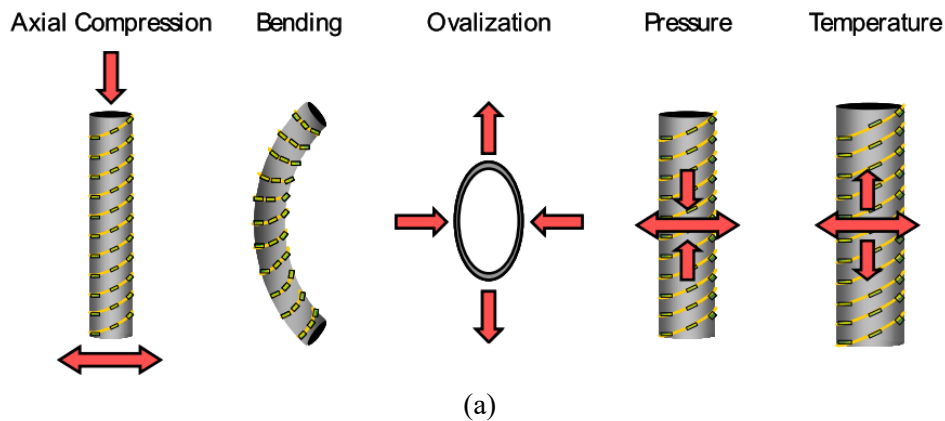
Figure 2-10 (a) different deformation modes of the screen; (b) manifestations of these deformation modes in the RTCI measurement [after Pearce & Rambow (2009)].

31

The FBG-based technique is also utilized for the monitoring of oil and gas wells. Pearce & Legrand (2009) developed an FBG-based strain sensing system called Real-Time Compaction Imager (RTCI) where thousands of FBG were imprinted on a single optical fibre with a small spacing (~ 2 cm). The FBG optical fibres are helically wrapped around the screen (i.e., a type of casing) for deployment. The helical wrap configuration could identify different deformation modes of the screen such as tension, compression, bending and ovalization (Figure 2-10) through laboratory experiments (Earles et al. 2010). RTCI was employed for the monitoring of an actual gas well (Pearce & Rambow 2009). The strain development of casings during cementing, cement cure, hydraulic fracturing and gas production was captured by RTCI. A drawback of RTCI is that the measurement distance is limited up to 250 m per channel. This means that the maximum monitoring distance of RTCI is 1 km (i.e., the RTCI analyzer has four channels). Also, dynamic strain sensing with RTCI is currently difficult as scanning thousands of FBG is time-consuming.

Therefore, it may be more advantageous to employ backscatter-based fibre optic monitoring techniques. In the following sections, the three different backscatter-based distributed fibre optic monitoring techniques are discussed.

2.5.4. Rayleigh backscatter-based techniques

Rayleigh backscatter-based techniques are mainly utilized for distributed acoustic sensing (DAS). However, it can also be used to detect strain/temperature changes by using a system called optical frequency domain reflectometry (i.e., OFDR) or another system called phase-sensitive optical time domain reflectometry (ϕOTDR).

Froggatt & Moore (1998) hypothesized that random fluctuations of the refractive index of optical fibres form distributed FBGs and they employed OFDR to detect the strain development in optical fibres. The temperature development in a harsh environment (i.e., a nuclear reactor) was also captured by the Rayleigh backscatter-based OFDR system (Sang et al. 2007). In addition, FBG cables can be used with the OFDR system to obtain high-precision strain data (Kreger et al. 2016). As to ϕOTDR, which was first proposed by Choi & Taylor (2003), it has been utilized for the DAS measurement of broadband acoustic vibration such as pencil break at 1 kHz (Lu et al. 2010) as well as dynamic strain measurement at 5 kHz with the strain precision of better than 1 $\mu\varepsilon$ (Masoudi et al. 2013). However, the main disadvantage of these systems is that the measurement distance is typically limited below a hundred metres.

Specific to oil and gas well applications, the first DAS measurement was conducted by Molenaar

et al. (2012) in 2009 in tight gas wells for the monitoring of in-well operations such as perforations. DAS has also been shown applicable to well integrity monitoring. Hveding & Porturas (2015) employed DAS to detect gas leakage, in which the leakage was detected as acoustic noise from gas bubbles migrated upward in the well. Thiruvenkatanathan et al. (2016) employed DAS for sand production monitoring, where sand ingress log was created to identify the locations of sand production. Although the applicability of DAS to well integrity monitoring seems plausible, it is not suitable for well integrity monitoring at the Nankai Trough as the strain measurement range of DAS is limited to as low as just few micro strains, whereas significant static strain development (> 1,000 $\mu\varepsilon$) is expected to occur in the unconsolidated formation at the Nankai Trough.

2.5.5. Raman backscatter-based techniques

Raman backscatter is utilized for distributed temperature sensing (DTS) as it is only sensitive to the temperature change in optical fibres (i.e., insensitive to strains).

Applications of DTS (i.e., Raman backscatter-based technique) for oil and gas wells began in mid-1990's. Hurtig et al. (1994) employed DTS to derive the flow rate of injection fluid and the location of fractures in the borehole. Großwig et al. (1996) found that DTS was as precise in mesuring temperature change as a high-precision temperature logging tool. For high-temperautre DTS monitoring, it was found that special protection has to be implemented on optical fibres to mitigate hydragen darkening (i.e., optical power attenuation) and coating errosion (Williams et al. 2000). Moreover, DTS has also been employed for pipeline leak detection, in-well monitoring of liquid flow and the optimization of gas lift operations (Baldwin 2018).

Although the Raman backscatter-based technique (i.e., DTS) could supplement well integrity monitoring by providing potential oil/gas leakage locations, it cannot be used as the primary or standalone monitoring technique for well integrity assessment. Therefore, another fibre optic monitoring technique is needed, which is discussed in the following section.

2.5.6. Brillouin backscatter-based techniques

Brillouin backscatter-based techniques are primarily used for distributed strain sensing (DSS) as they are capable of measuring a wide range of strain levels of up to 1 ~ 2% for a distance of tens of kilometres.
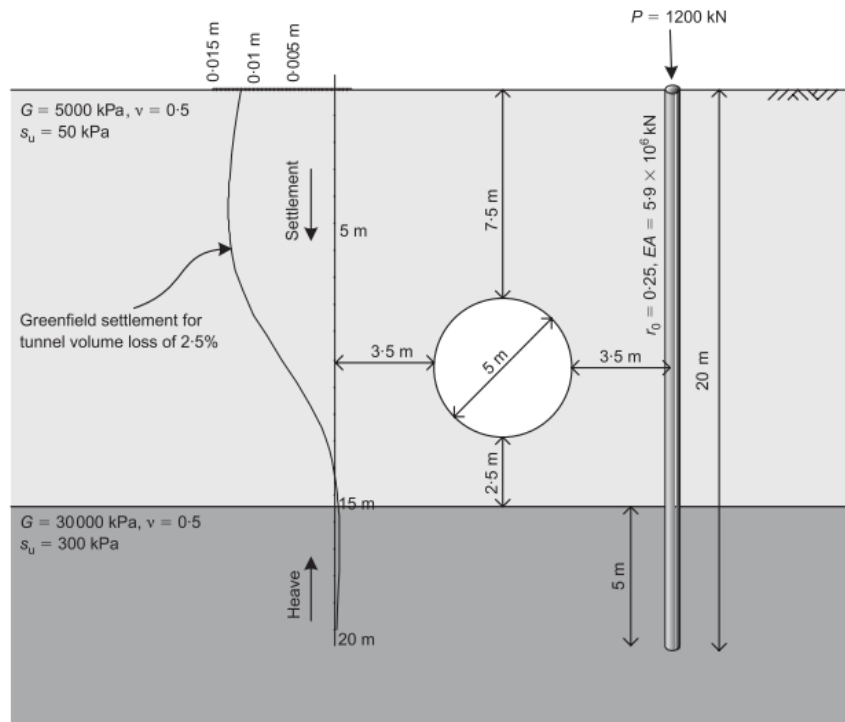
(a)
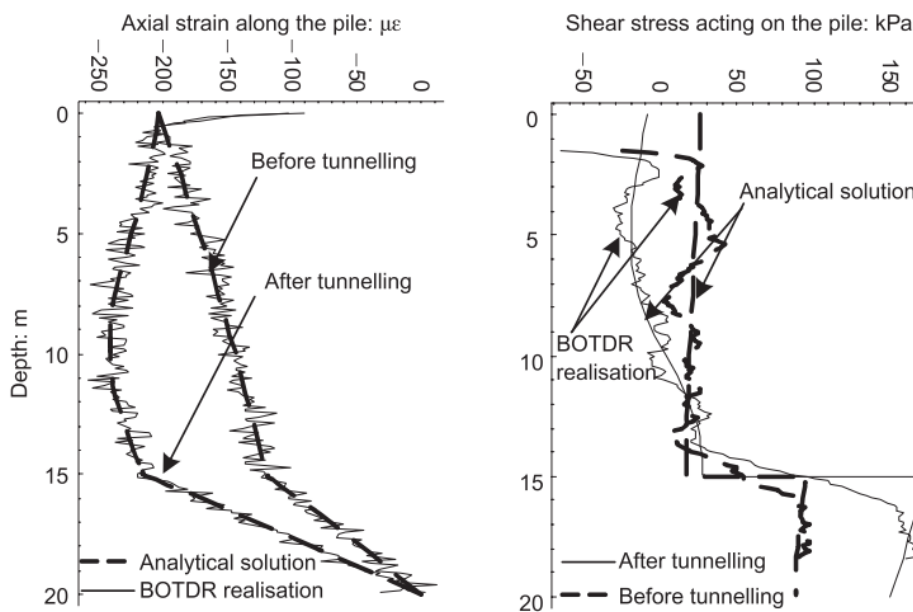
(b)

Figure 2-11 BOTDR monitoring of a pile foundation: (a) the geometry of the pile, a tunnel to be constructed and soil strata; (b) the development of axial strain in the pile measured by BOTDR (left) and estimated shear stress development in the pile (right) before and after the tunnel construction [after Klar et al. (2006)].

The first Brillouin backscattering-based technique, which was termed Brillouin optical time domain analysis (BOTDA), was proposed as a non-destructive method to investigate the attenuation characteristics of optical fibres (Horiguchi & Tateda 1989). Horiguchi et al. (1989) first used BOTDA for DSS and measured the tensile strain development of optical fibres up to 5,000 $\mu\epsilon$. BOTDA requires both ends of an optical fibre to be connected to the analyser, which is inconvenient if the optical fibre breaks in the middle of measurement. This is resolved by another Brillouin backscatter-based technique called Brillouin optical time domain reflectometry (BOTDR), which requires only one end of an optical fibre to be connected to the analyser to take measurement.

BOTDR/A was initially utilized for the detection of strain development in telecommunication optical fibres (Horiguchi et al. 1995). The potential of BOTDR/A to monitor the integrity of structures such as a cantilever beam (DeMerchant et al. 1999), pipeline leakage (Nikles et al. 2004), pipe inner-wall defects (Zou et al. 2004) and pipe buckling (Zou et al. 2006) was later investigated. The application of BODTR/A then advanced to the field monitoring of civil infrastructure such as tunnels (Gue et al. 2015), piles (Klar et al. 2006; Pelecanos et al. 2018; Pelecanos et al. 2017), concrete bridge girders (Butler et al. 2016), concrete beams (Klar, Goldfeld, et al. 2010) and ground settlement during tunnelling (Hauswirth et al. 2014). BOTDR/A was also used for the feasibility study of the detection of the construction of smuggling tunnels across borders (Klar & Linker 2010) and sink hole formation (Linker & Klar 2015).

Figure 2-11 shows an example of BODTR monitoring of a pile foundation (Klar et al. 2006). The axial strain and shear stress development of the pile before and after the construction of a nearby tunnel was measured accurately by BOTDR. Another example is the monitoring of secant-piled wall (Mohamad et al. 2011) where the development of deflection and bending moment of the secant-piled wall in response to ground excavation was measured successfully. BOTDR was also applied for the monitoring of energy piles (i.e., a ground-source heat-pump system) constructed in London (Bourne-Webb et al. 2009), in which the development of mechanical and thermal strains in the piles during their cooling and heating cycles was accurately measured. Although these field implementations of BOTDR/A for the monitoring of pile integrity are relevant to the distributed fibre optic monitoring of oil and gas wells, the depth of oil and gas wells (~ 10,000 m) is considerably greater than that of piles (~ 100 m). As a result, oil and gas wells are often subjected to unique deformations such as shear/bending at geologic faults deep in the formation. Therefore, the feasibility of BOTDR/A for the monitoring of oil and gas wells needs to be assessed separately from that of pile foundations.

According to the latest literature on the fibre optic monitoring of oil and gas wells (Hveding et al. 2018; Baldwin 2018; Baldwin 2015), BOTDR/A is employed only for pipeline monitoring in the field. This is because the advantage of BOTDR/A is considered to be merely the long measurement distance. However, a recent report from the MIGRATE project in Europe (Klar et al. 2019) summarises the potential of BOTDR/A to be employed for the monitoring of well integrity in methane hydrate reservoirs in both static and dynamic manners. In fact, it is advantageous to utilize BOTDR/A for well integrity monitoring during reservoir compaction considering BOTDR/A's wide strain measurement range and long measurement distance. Moreover, oil and gas wells are drilled in challenging locations these days due to the depletion of conventional resources. The assessment of the integrity of such expensive wells will become critical to ensure their functionality over their lifetime and BOTDR/A will be instrumental in achieving this goal. Therefore, there is a need for investigating the potential of BOTDR/A to conduct well integrity monitoring.

2.5.7. Principles of BOTDR/A and FBG measurements

A schematic diagram of the principal of BOTDR measurements are illustrated in Figure 2-12. Incident light pulses at a certain wavelength (typically 1550 nm) are sent into a single-mode optical fibre. A fraction of the incident light pulses is backscattered due to the refractive diffraction grating induced by the acoustic wave generated within the fibre material (Zhang et al. 2015). The shift in the frequency of the backscattered light (i.e., Brillouin frequency shift) is linearly proportional to the external strain and temperature changes applied to the fibre, as shown in Equation 2-19:

$$\Delta v_B = C_\epsilon \, \Delta \epsilon + C_T \, \Delta T \qquad (2\text{-}19)$$

where Δv_B = Brillouin frequency shift; $\Delta \epsilon$ = change in mechanical strain; ΔT = change in temperature; C_ϵ = strain coefficient; C_T = temperature coefficient.

Regarding the FBG measurement, incident light pulses with broadband wavelengths are shot into such an optical fibre and a fraction of the incident light at a certain wavelength is reflected at the gratings. The wavelength shift of the reflected light is linearly related to changes in the mechanical strain and temperature along the FBG optical fibre as shown in Equation 2-20:

$$\Delta \lambda' \, / \, \lambda_0 = (1 - p_e \,)\Delta \epsilon + (\alpha_n + \alpha_L)\Delta T \qquad (2\text{-}20)$$

where $\Delta \lambda'$ = change in wavelength; λ_0 = baseline wavelength; $\Delta \epsilon$ = change in mechanical

strain; ΔT = change in temperature; p_e = effective photo-elastic coefficient; α_n = thermo-optic coefficient; α_L = linear thermal expansion coefficient.
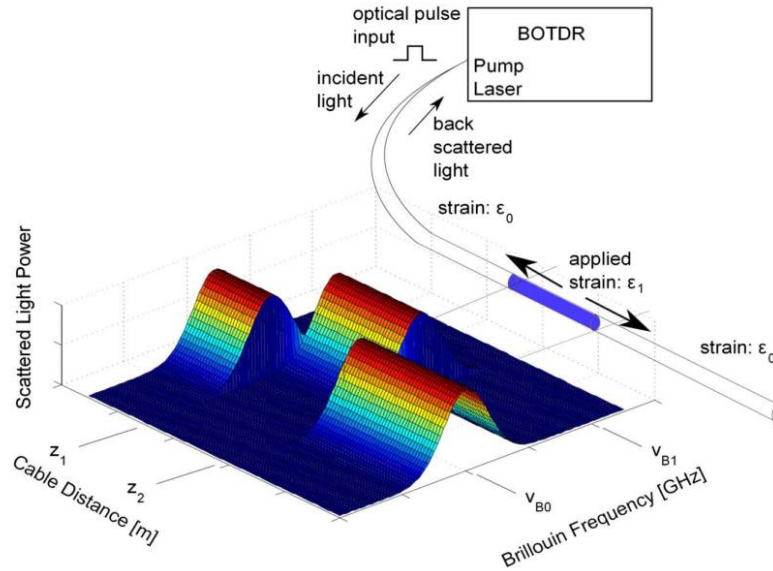
Figure 2-12 The principle of the BOTDR measurement [after Pelecanos et al. (2017)].

As shown in Equation 2-19 and 2-20, the frequency/wavelength shift in the BOTDR/A and FBG measurements is affected by both strain and temperature changes. Hence, the temperature term has to be compensated for to calculate strain changes from the measurement data. This can be performed by employing a temperature fibre optic cable, in which the fibre core is encased in an air- or gel-filled tube which helps isolate the fibre core from external strains, alongside a strain fibre optic cable in which the fibre core is tightly buffered to the outer layers of the cable. As a result, the entire frequency/wavelength shift measured along the temperature cable is converted into temperature change (i.e., $\Delta T = \Delta v_B / C_T$ for BOTDR/A and $\Delta T = (\Delta \lambda' / \lambda_0)/(\alpha_n + \alpha_L)$ for FBG). This temperature change is then used to calculate the temperature term in the measurement data obtained from the strain cable to extract strain changes.

2.6. Summary

Methane hydrate reservoirs are potentially promising sources of unconventional natural gas. The uniqueness of offshore methane hydrate reservoirs at the Nankai Trough is that the formation is unconsolidated, which could cause significant reservoir compaction. Despite the fact that reservoir compaction has led to well failures in conventional oil and gas fields, sufficient

investigations into the effect of reservoir compaction on well integrity at the Nankai Trough have not been provided. The primary findings from the present literature review are presented below.

(i)   The mechanism of cement shrinkage is the development of capillary suction pressure in the pores of the cement. In the wellbore conditions, cement absorbs water from the formation due to the capillary pressure development, which results in complex interactions among casing, cement and formation. It is more effective to carry out hydromechanical simulations than laboratory experiments to model this process.

(ii)   Due to the unconsolidated nature of the Nankai Trough formation, formation integrity could be significantly affected by well construction process. The effect of cement shrinkage and horizontal stresses of the formation have been disregarded for the Nankai Trough case, although existing studies show these factors could affect well integrity significantly.

(iii)   There are only limited number of numerical models for well integrity analysis which incorporate all well components and simulate well construction and reservoir compaction processes. Detailed well construction process is not simulated in those models. Also, different reservoir compaction scenarios and their effect on well integrity are not modelled either.

(iv)   Currently, distributed strain sensing by BOTDR/A has been conducted solely for pipeline monitoring. However, due to the inability of Rayleigh and Raman backscatter-based distributed fibre optic monitoring techniques to obtain strain profiles over a wide dynamic range, BOTDR/A is best suited for well integrity monitoring during reservoir compaction. The effectiveness of BOTDR/A for in-well monitoring can be evaluated through laboratory experiments and/or field tests.

These issues listed above are addressed in the following chapters. Finite element modelling of the interaction between early-age cement and formation in the well annulus is presented in Chapter 3, in order to estimate realistic values of cement shrinkage volume for the Nankai Trough case. In Chapter 4, a finite element analysis of well construction process in the Nankai Trough formation is presented. Cement shrinkage volumes obtained in Chapter 3 are incorporated into the well construction finite element analysis to assess the effect of cement shrinkage on well integrity during well construction. In Chapter 5, another finite element modelling work is presented in which a parametric study on the effect of different reservoir compaction scenarios

on well integrity for the Nankai Trough case is carried out. In Chapter 6 and 7, the effectiveness of BOTDR/A in monitoring well integrity is evaluated through laboratory experiments. In Chapter 6, BOTDR/A is used to measure the development of axial strain of a well specimen subjected to tensile loading, whereas in Chapter 7, BOTDR/A is used for the monitoring of bending deformation of another well specimen.

3. Water absorption and shrinkage behaviour of early-age cement in wellbore annulus

3.1. Introduction

Annular cement in oil and gas wells plays a crucial role in maintaining well integrity as the cement supports casing to enhance their mechanical stability as well as the zonal isolation of the formation by sealing the borehole. In the Nankai Trough methane hydrate reservoirs, the optimized particle size distribution (OPSD) cement was employed, which is characterised by its light weight compared to conventional cement such as Class G cement, to minimize formation disturbance during the cementing operation. Little attention was paid, however, to the shrinkage characteristics of the OPSD cement as the cement was considered to be zero-shrinkage cement by the cement manufacturer. However, it is not clear whether the zero-shrinkage actually means 0% shrinkage, i.e., 0.5% maybe considered zero-shrinkage by some and not by the others. In addition, such small cement shrinkage might still have an impact on formation integrity during well construction. The accurate estimation of cement shrinkage volume is crucial as the potential cement defects, such as shrinkage-induced cracks and debonding at the cement-formation interface, might have induced well failure at the Nankai Trough. Hence, it is important to investigate the volume shrinkage behaviour of cement in the well annulus.

In this study, a coupled hydro-mechanical finite element analysis is conducted to simulate the water migration, absorption and volume shrinkage behaviour of early-age cement in a wellbore configuration. The primary objectives of this study are as follows:

(i)   to determine the threshold permeability value of the formation below which the cement cannot absorb adequate water from the formation to compensate for the water consumption by the hydration reaction and

(ii)   to estimate a reasonable range of cement shrinkage volume in downhole conditions.

The wellbore is modelled to be placed in the overburden of the Nankai Trough in Japan (Yamamoto et al. 2014), where the cement is surrounded by the low permeability clay formation on the outer boundary and by impermeable casing on the inner boundary. The mechanical and hydrological parameters of hardening cement paste are calibrated by utilizing laboratory test data on three different types of cement: Class G cement, rapid setting (RS) cement and OPSD cement.

3.2. Mechanism of cement shrinkage

The bulk shrinkage of cement can occur by three different mechanisms: (i) capillary depression effect, (ii) surface tension effect, and (iii) disjoining pressure effect (Hua et al. 1995). One or more of these mechanisms are dominant over the others depending on the relative humidity of the cement. For example, the capillary depression effect is the dominant mechanism at high relative humidity (i.e. over 80%) whereas the other two mechanisms are activated at lower relative humidity levels (i.e. below 45%) (Rougelot et al. 2009; Lura et al. 2003; Hua et al. 1995). The relative humidity of early-age cement paste is known not to decease below 75% even though it is left in contact with the air (Lura et al. 2003). Therefore, in the wellbore condition where the cement is surrounded by water-saturated formation, the primary mechanism of cement bulk shrinkage volume is the depression of capillary suction pressure (i.e. pore pressure). Such phenomena can be simulated by the coupled hydro-mechanical equations for porous materials; the hydraulic part of the equations is derived from the conservation of fluid mass in a porous media, whereas the mechanical part is derived from the force equilibrium.

The poromechanical approach to simulate the behaviours of cement paste has been found valid by Ulm et al. (2004). Unlike soils in which the bulk stiffness values of both soil grains and pore water are assumed to be very large relative to the stiffness of soil skeleton, the cement skeleton after hardening can be as stiff as the cement particles and pore water (Vu et al. 2012). Thus, the stiffness values of cement particles and pore water must be included in the constitutive equation. The modelling of cement bulk shrinkage is analogous to that of rocks, in which the stiffness of the solid phase in addition to that of the bulk porous material must be considered in the constitutive equations (Biot 1962; Nur & Byerlee 1971; Garg & Nur 1973). In addition, since the stiffness of early-age cement evolves with time, the volumetric shrinkage strain needs to be calculated in increments using Equation 3-1:

$$d\varepsilon_v = \int \frac{(d\sigma_m - \alpha du)}{K} \qquad (3\text{-}1)$$

where $d\varepsilon_v$ is the volumetric strain increment, $d\sigma_m$ is the mean stress increment, du is the pore pressure increment, K is the time (or hardening) dependent bulk modulus of cement skeleton and α is the Biot-Willis coefficient (Biot & Willis 1957). The cement placed in wellbore annulus is often surrounded by a water-saturated formation under high hydrostatic pressure, which prevents the cavitation of the pore water and keeps the cement fully saturated. Hence, the effect

of degree of saturation on the stress increment is not considered in this study.

The incremental form of constitutive equation for the cement skeleton is also employed in Hua et al. (1995) and Zhen & Xiong (2013) to calculate the volumetric shrinkage strain. Experimental observations (Maharidge et al. 2016; Teodoriu et al. 2012) indicate that the stiffness of early-age cement increases significantly with time. In this study, the incremental stress-strain constitutive model with time-varying stiffness is employed to model the observed cement shrinkage behaviour. This allows the calculation of irreversible strains due to the evolution of the skeleton stiffness of the cement. Plasticity models could also be used to simulate the volumetric shrinkage behaviour (Thiercelin et al. 1998). However, the determination of plasticity model parameters for early-age cement is very difficult.

The main model input is the sink term (i.e. volumetric strain of the pore fluid) in the fluid mass conservation equation. This term governs the loss of pore water due to the hydration reaction of cement particles, which leads to the depression of pore pressure and hence shrinkage volume. The stiffness and permeability of the cement are assumed to be time-dependent. Their time dependency changes are evaluated by laboratory test data available in literature, which is discussed in the next section.

3.3. Modelling of laboratory tests on cement shrinkage

3.3.1. Model dimensions and material parameters

The poromechanical framework for modelling the shrinkage behaviour of early-age cement is validated against laboratory test data on three different cement types: Class G cement, rapid setting (RS) cement (Appleby & Wilson 1996) and OPSD cement (Thomas et al. 2015). These experiments are chosen for the model calibration because the bulk volume shrinkage and absorbed water volumes are measured in these experiments, which are essential for the model calibration. In the experiment on the Class G and RS cement, pore pressure data is also available. The material composition of RS cement is identical to that of Class G except for the extra amount of gypsum replacing cement particles to accelerate the initial set (i.e. the thickening time). OPSD cement is a light weight cement containing hollow fly ash particles and is designed for the cementing of shallow unconsolidated formation. OPSD cement was employed for the cementing operation of wellbores in the Nankai Trough in Japan (Taoutaou et al. 2014; Qiu et al. 2015).
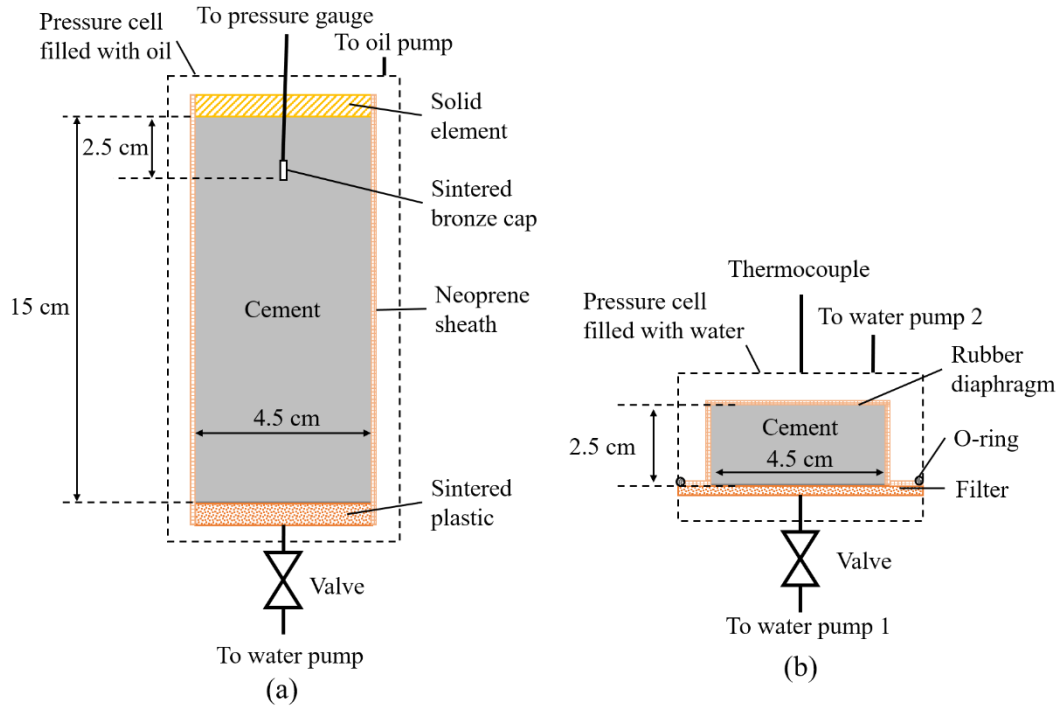
Figure 3-1 Test setups of the laboratory tests on cement shrinkage: (a) Class G cement and RS cement [after Appleby & Wilson (1996)]; (b) OPSD cement [after Thomas et al. (2015)].

In this study, the experimental work of Appleby & Wilson (1996) and Thomas et al. (2015) are simulated. The test setups of the cement specimens simulated in this study are shown in Figure 3-1. Two types of tests are usually conducted to examine the shrinkage behaviour of early-age cement; (i) drainage valve open (drained) and (ii) drainage value closed (undrained). In the former test, water is provided from the bottom port to the specimen and the amount of water absorbed into the specimen is recorded. In the latter test, the bulk shrinkage volume of the specimens is recorded instead of the absorbed water volume. The pore pressure data were available only for the Class G and RS cement tests. The applied pressure for the Class G and RS cement tests was 2 MPa whereas that for the OPSD cement test was 10 MPa. The temperature was maintained at approximately 20°C for the Class G and RS tests and 12°C for the OPSD cement test.

The ABAQUS finite element (FE) analysis software package is employed to carry out the coupled transient fluid flow and stress analysis. Since the geometry of the cement specimen is cylindrical (i.e. ϕ45 mm $\times$ 150 mm for the Class G and RS cement tests and ϕ45 mm $\times$ 25 mm for the OPSD cement test), axi-symmetric analysis is conducted. The finite element models (FEM) are shown in Figure 3-2. The models are discretized into 2250 axi-symmetric eight-node biquadratic displacement, bilinear pore pressure elements. For the boundary conditions, the constant pore

pressure equal to the initial pore pressure is specified at the bottom boundary nodes to simulate the open valve tests, whereas no fluid flux is specified to simulate the closed valve tests.
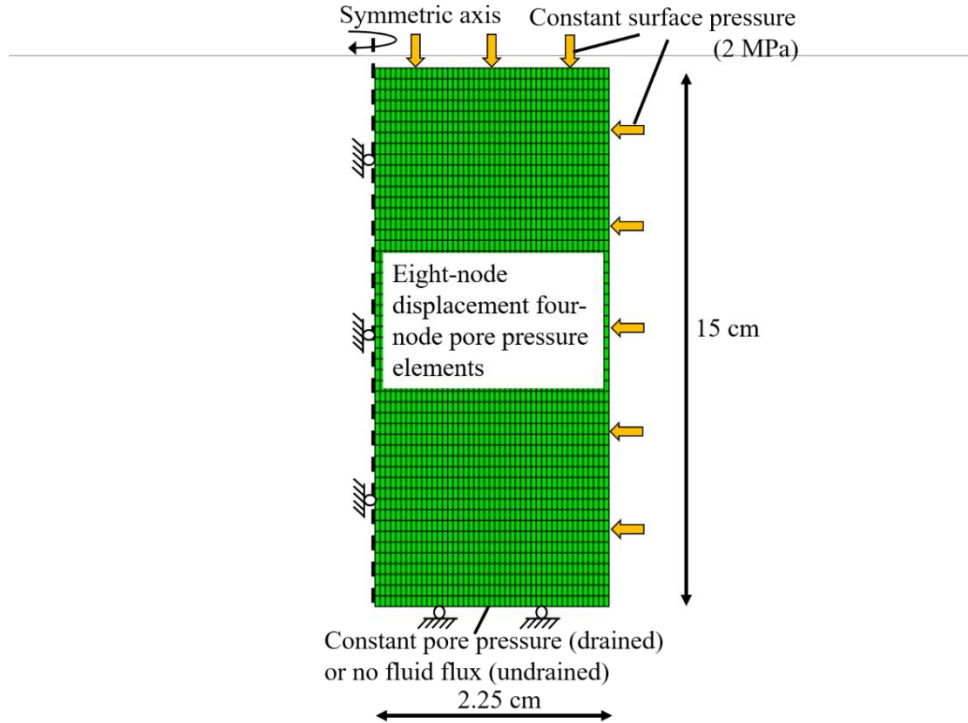
(a)
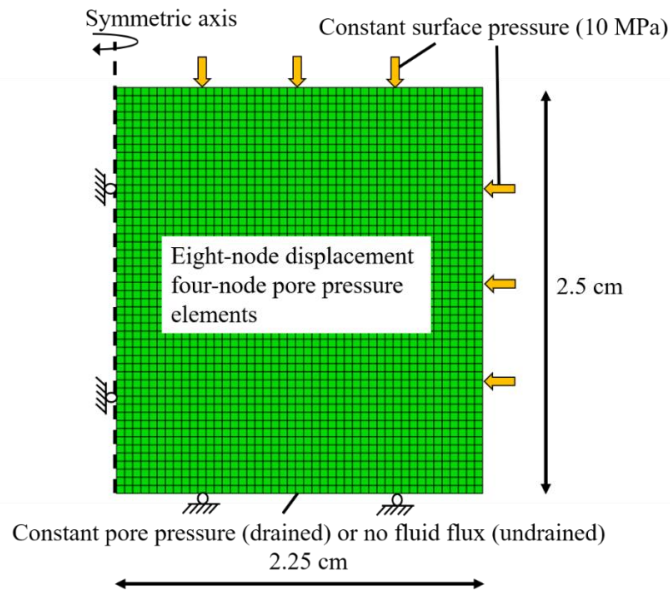
(b)

Figure 3-2 Finite element models (FEM) for the laboratory tests on cement shrinkage: (a) Class G cement and RS cement tests (enlarged three times in the horizontal direction); (b) OPSD cement test (to scale).

The bulk modulus of cement particles and water are 21 GPa, and 2.2 GPa, respectively. As described earlier, the calibrated model parameters are the time-dependent values of sink rate (i.e. the rate of volumetric strain change of the pore water), permeability and Young's modulus. A constant Poisson's ratio of 0.20 is adopted. Although it may be argued that the cement at its fluid-like stage is in close to incompressible condition, it is assumed that the shear resistance develops rapidly prior to the initial set. The porosity is set to be constant at 0.25. This assumption is employed because the porosity parameter in the simulation does not affect the amount of water consumption by the cement; the sink rate determines it. Porosity does not affect the mechanical behaviour, either, because Young's modulus and Poisson's ratio are specified independently of porosity in this study. These input parameters for the FEM for laboratory cement shirnkage tests are summarized in Table 3-1.

Table 3-1 Hydromechanical input parameters for the FEM for the laboratory tests on cement shrinkage.

Bulk modulus of cement particles	21 GPa
Bulk modulus of water	2.2 GPa
Poisson's ratio	0.2
Porosity	0.25
Sink rate	Figure 3-3a
Permeability	Figure 3-3b
Young's modulus	Figure 3-3c

3.3.2. Calibrated time-dependent sink rate, permeability and stiffness

The calibrated time-dependent sink rate, permeability and Young's modulus are shown in Figure 3-3a, 3b and 3c, respectively. An exponential function is employed to model the time variations of these parameters. The origin of the time corresponds to the time of the initial set of cement. The equations used to model the time-dependent sink rate, permeability and Young's modulus are shown in Equation 3-2, 3-3 and 3-4, respectively.

$$s(t) = (s_{ini} - s_{ult})e^{-\delta_s t} + s_{ult} \tag{3-2}$$

$$E(t) = \begin{cases} E_{ini} & (0 \leq t \leq t_0) \\ (E_{ini} - E_{ult})e^{-\delta_E (t-t_0)} + E_{ult} & (t > t_0) \end{cases} \tag{3-3}$$

$$k(t) = \begin{cases} k_{ini} & (0 \leq t \leq t_0) \\ (k_{ini} - k_{ult})e^{-\delta_k\,(t-t_0)} + k_{ult} & (t > t_0) \end{cases} \tag{3-4}$$

where s_{ini} = initial sink rate, s_{ult} = ultimate sink rate at $t \to \infty$, δ_s = time constant for sink rate, E_{ini} = initial Young's modulus, E_{ult} = ultimate Young's modulus at $t \to \infty$, δ_E = time constant for Young's modulus, k_{ini} = initial permeability, k_{ult} = ultimate permeability at $t \to \infty$, δ_k = time constant for permeability, t = elapsed time since the initial set of cement, t_0 = elapsed time since the initial set of cement where cement hydration reaction accelerates. The exponential function is chosen because the experimental data on the OPSD cement shows exponential decay/increase of absorbed water volume and ultrasonic transit time (i.e., stiffness). Although the change in permeability was not measured, it is reasonable to assume that it follows the trend of sink rate and stiffness and decreases exponentially with time. Note that the t_0 parameter is relevant only to the RS cement in which the initial ettringite formation hinders the hydration reaction until a certain time since the initial set of cement. The sink rate is defined as the rate of volumetric strain increment of pore water in this simulation, as shown in Equation 3-5:

$$s = \frac{\Delta\varepsilon_{v,water}}{\Delta t} \tag{3-5}$$

where $\Delta\varepsilon_{v,water}$ = volumetric strain increment of pore water (positive values for compression). The value of Δt is set to 1,800 seconds. The calibrated values of the parameters for the sink rate, Young's modulus and permeability are listed in Table 3-2.

Table 3-2 The calibrated values of the model parameters for Class G, RS and OPSD cements.

	Class G cement	RS cement	OPSD cement
s_{ini} (με/h)	6580	21200 ($t \leq 18$ h) 6580 ($t > 18$ h)	2070
s_{ult} (με/h)	80	1200 ($t \leq 18$ h) 80 ($t > 18$ h)	110
δ_s	0.1	1.0 ($t \leq 18$ h) 0.1 ($t > 18$ h)	0.075
E_{ini} (GPa)	0.05	0.05	0.02
E_{ult} (GPa)	16	16	3.81
δ_E	0.005	0.005	0.02
k_{ini} (mD)	1	0.1	1
k_{ult} (mD)	0.001	0.001	0.004
δ_k	0.5	0.25	0.4
t_0 (h)	0	15	0

The sink rate is assumed to monotonically decrease from its maximum value at $t = 0$ to an asymptote value at $t \to \infty$. A large initial sink rate is assigned for RS cement reflecting the fast reaction of gypsum. The sink rate of RS cement intersects with that of Class G cement at $t = 18$ h, after which the sink rates of Class G and RS cements are set to be identical. OPSD cement has an initial sink rate smaller than that of Class G and RS cements because OPSD cement has less amount of cement clinkers in the mix. The asymptotic sink rate of OPSD cement is larger than those of the other two cements because of the slow reaction of fly ash particles included in the mix. It is noted that the values of s_{ini} and s_{ult} are dependent on the initial porosity of the cement (i.e., set to 0.25 in this simulation). For instance, if the initial porosity doubles, the values of the initial and ultimate sink rates need to be reduced by half, in order to achieve the same amount of water consumption in the cement pore space.

The initial permeability is set to 1 mD for Class G cement and OPSD cement, whereas it is set to 0.1 mD for RS cement to reflect the early ettringite formation. The final permeability is 1 μD for Class G and RS cements and 4 μD for OPSD cement.

Due to limited data on the initial Young's modulus measurement of early-age cement, the initial values are set to be roughly one hundredth of the final values for all cements. The Young's modulus values of Class G and RS cements change from the initial value of 50 MPa to the final value of 16 GPa, whereas the Young's modulus value of OPSD cement changes from 20 MPa to 3.81 GPa. The development of permeability and Young's modulus for RS cement is assumed to be delayed until $t = 15$ h due to the delayed hydration reaction of cement clinkers caused by the early formation of ettringite (Appleby & Wilson 1996).

The calibration of these model parameters was carried out in the following manner. First, the time-dependent sink rate was calibrated to match the computed absorbed water volume to the experimental result, as the change in the permeability and Young's modulus had little effect on the computed absorbed water volume. Next, time-dependent Young's modulus was calibrated to match the computed bulk shrinkage volume (OPSD cement) or pore pressure change (Class G and RS cements) under the undrained condition (i.e., closed valve) with the experimental result due to the insensitivity of the permeability on the computed bulk shrinkage volume and pore pressure change under the undrained condition. Finally, the time-dependent permeability was calibrated to match the computed pore pressure change under the drained condition (i.e., open valve) with the experiment data. Since pore pressure data were not available for the OPSD cement test, a reasonable initial value and the rate of permeability decrease were assumed for OPSD cement. The ultimate permeability value of OPSD cement (0.04 mD) was taken from Thomas et

al. (2015).
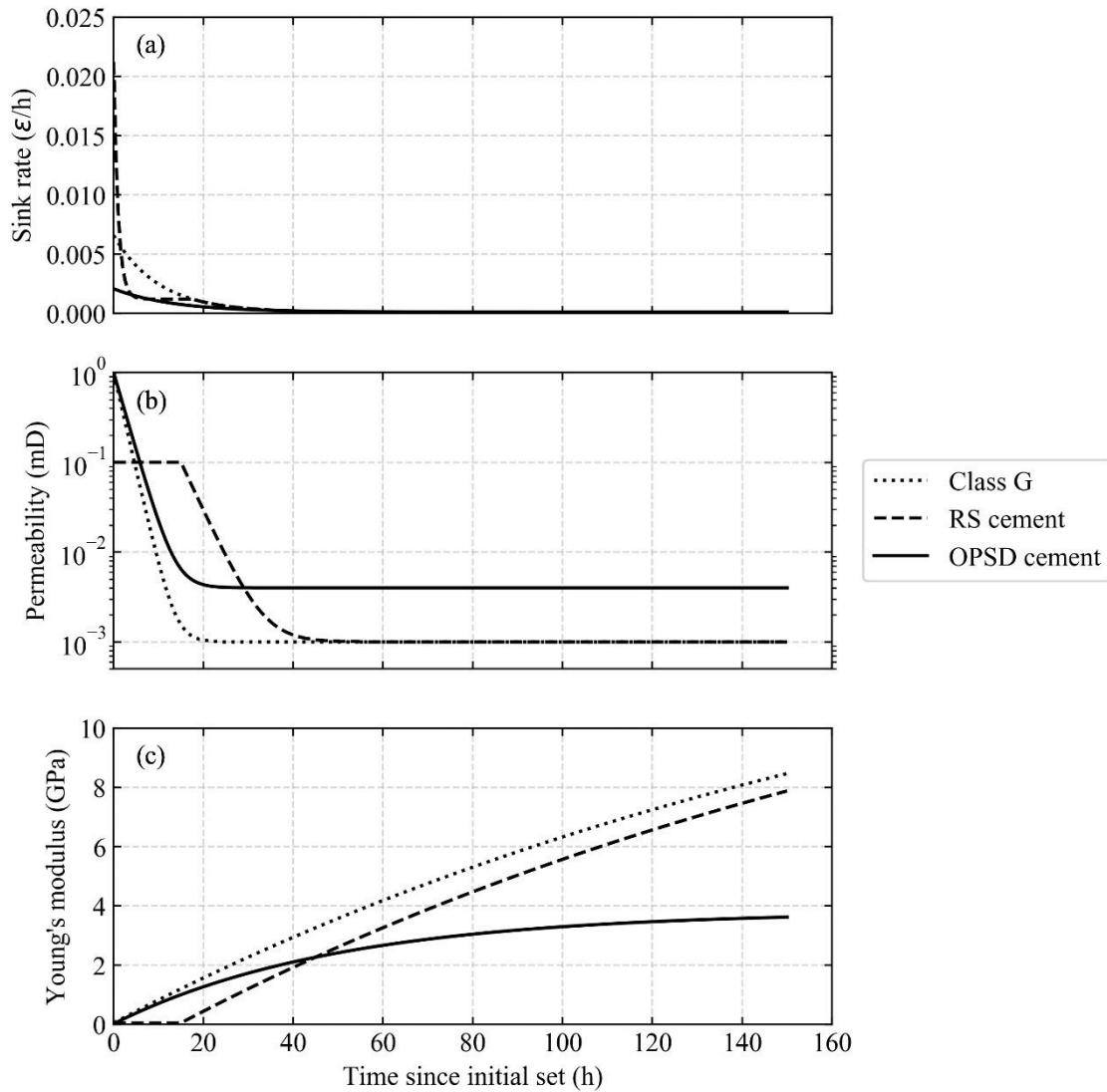
Figure 3-3 Calibrated changes of the (a) sink rate, (b) permeability and (c) Young's modulus of each cement with time.

3.3.3. Sensitivity analysis of the calibrated parameters

The calibrated values of the parameters for the sink rate, Young's modulus and permeability are not determined through rigorous optimisation (e.g., least square method), but they are rather obtained through trial and error until satisfactory match between the experimental and computational results are obtained by visual inspection. Therefore, there could be other combinations of parameter values that achieve a satisfactory match. In this section, a sensitivity analysis of the model parameters on the computed absorbed water volume and pore pressure

changes for RS cement is carried out, in order to evaluate how the computed outputs change with increasing or decreasing input parameter values.
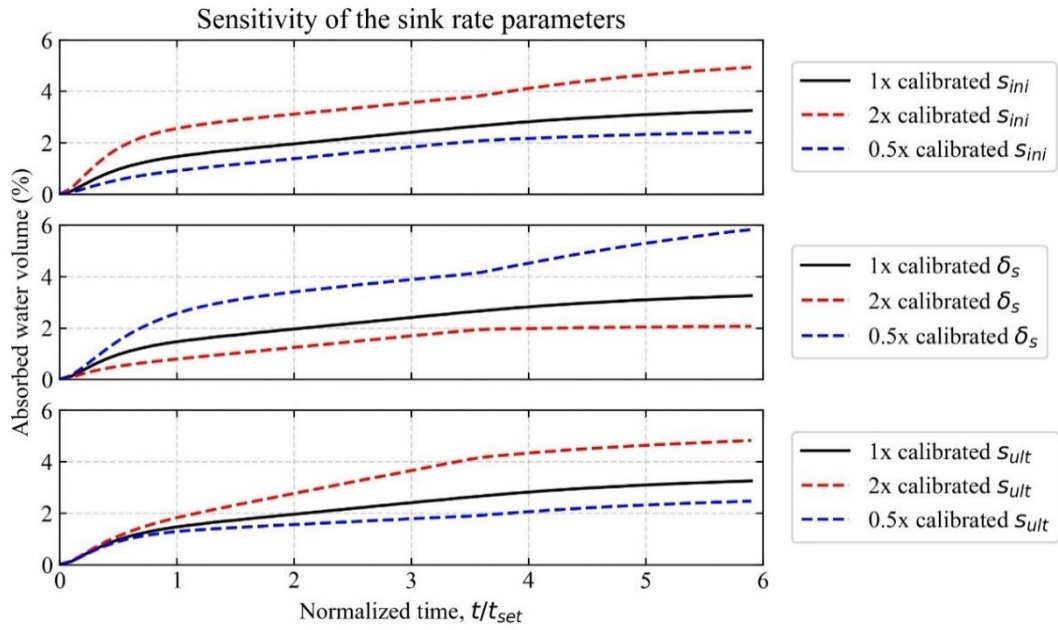
(a)
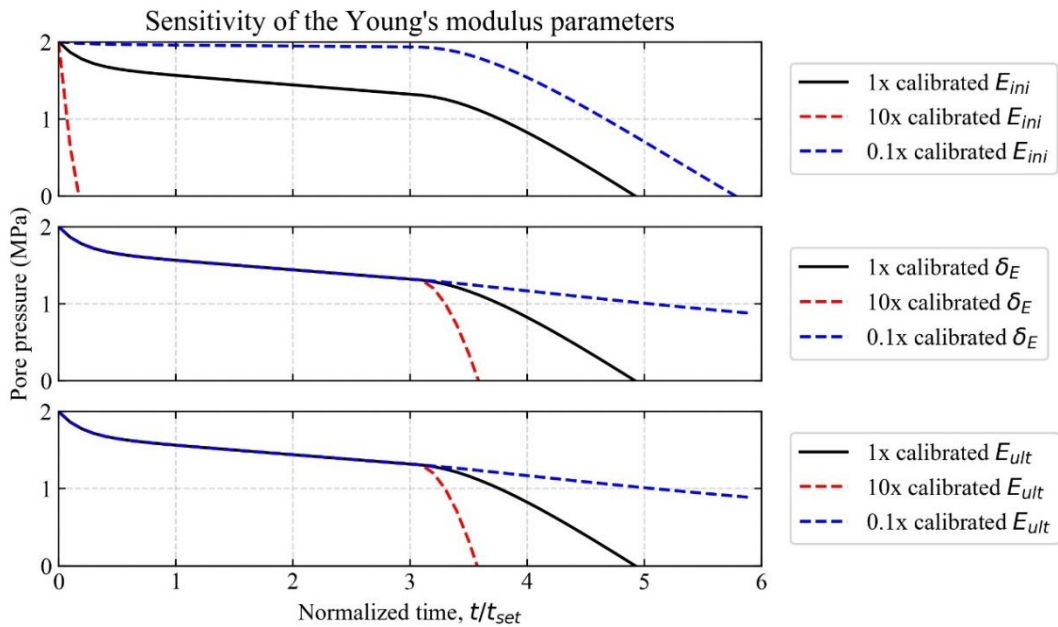
(b)
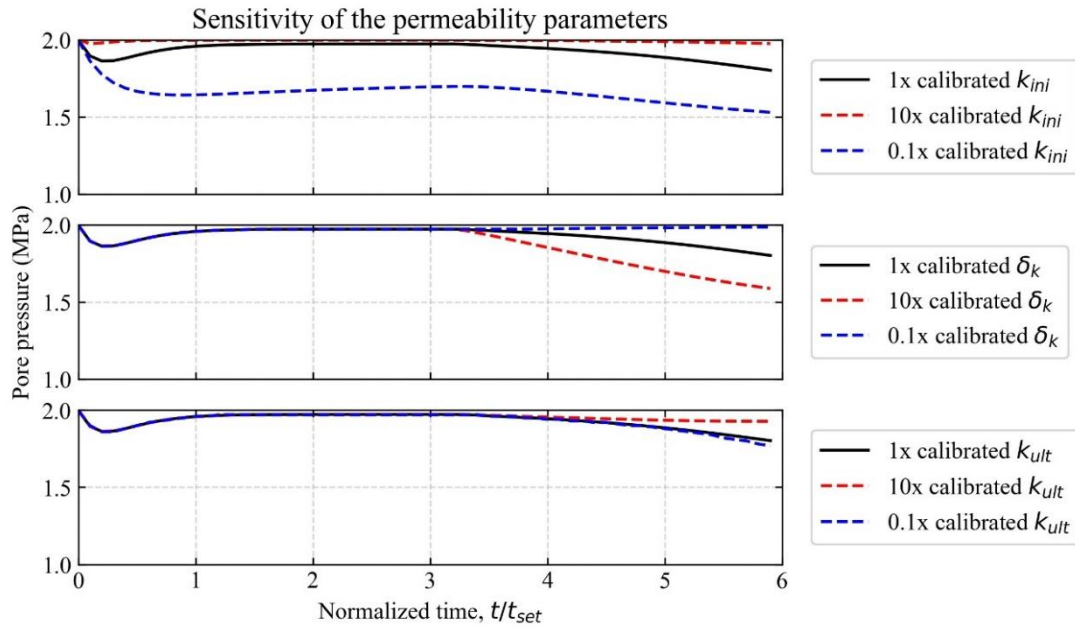
(c)

Figure 3-4 The sensitivity analysis of the cement model parameters (RS cement): (a) sensitivity
of absorbed water volume to the sink rate parameter values; (b) sensitivity of pore pressure
under the undrained (closed valve) condition to the Young's modulus parameter values; (c)
sensitivity of pore pressure under the drained (open valve) condition to the permeability
parameter values.

Figure 3-4a shows the effect of the sink rate parameters (s_{ini}, δ_s and s_{ult}) on the computed absorbed
water volume. The value of one parameter is changed by either twice or half of the calibrated
values listed in Table 3-2 (shown as 2x and 0.5x) while the values of the other two parameters are
fixed at the calibrated values. It is found that the increase in the initial sink rate (s_{ini}) and the
decrease in the time constant (δ_s) has a similar effect as they both increase the absorbed water
volume by approximately 2%. The increase in the ultimate sink rate (s_{ult}) also increases the
absorbed water volume, but the initial slope of the curve ($0 < t/t_{set} < 0.5$) remains unchanged.
Therefore, the values of the initial sink rate and time constant should be adjusted to match the
initial slope, whereas the ultimate sink rate should be adjusted to match the rest of the curve.

Figure 3-4b shows the effect of the Young's modulus parameters (E_{ini}, δ_E and E_{ult}) on the computed
pore pressure change under the undrained (closed valve) condition. It is found that the match in
the first half of the curve ($0 < t/t_{set} \leq 3$) is governed by the initial Young's modulus, whereas the
time constant (δ_E) and the ultimate Young's modulus (E_{ult}) only affect the second half of the curve
($3 < t/t_{set} < 6$). This is because the Young's modulus of RS cement is fixed at the initial Young's

modulus until t/t_{set} = 3 to reflect the early ettringite formation. Therefore, it is the initial Young's modulus that should be adjusted to match the first half of the curve. To match the second half of the curve, the values of the time constant and ultimate Young's modulus could be modified interchangeably. However, the value of the ultimate Young's modulus of cement can be constrained by experimental data in the literature (e.g., Teodoriu et al. 2012). Hence, the time constant should primarily be adjusted to match the second half of the curve.

Figure 3-4c shows the effect of the permeability parameters (k_{ini}, δ_k and k_{ult}) on the computed pore pressure change under the drained (open valve) condition. Similar to the Young's modulus calibration process, the permeability of RS cement is fixed at the initial permeability (k_{ini}) until t/t_{set} = 3 to take into account the ettringite formation. As a result, the first half of the curve is not affected by changes in the values of the time constant (δ_k) or ultimate permeability (k_{ult}). The time constant and ultimate permeability start to have an effect in the second half of the curve but in slightly different ways, as the former affects the entire second half of the curve ($3 < t/t_{set} < 6$) whereas the latter alters only the end part of the second half of the curve ($4.5 < t/t_{set} < 6$). Therefore, the first half of the permeability curve can be matched by adjusting the initial permeability value, whereas the early and late second halves of the curve should be matched by changing the time constant and ultimate permeability values, respectively.

3.3.4. Results

The model calibration results for the three cement tests are shown in Figure 3-5. The time axis indicates the time after the initial set of the cement. The data from the period from the mixing of the cement to the initial set, t_{set}, (i.e. the thickening time) are removed. The shrinkage before the initial set is compensated for by the drop of the cement slurry column in the annulus (Thiercelin et al. 1998; Backe et al. 1999). Hence, the shrinkage after the initial set is relevant in this study.

As shown in Figure 3-5, there is good agreement between the experiments and simulations. The time-dependent behaviours of the absorbed water and shrinkage volumes are captured adequately for all cement types. The time scale of the Class G cement data is limited to a short period of several hours after the initial cement set. Hence it is not possible to calibrate beyond this time. As a result, the calculated bulk shrinkage volume of Class G cement seems to slightly overestimate its typical shrinkage volume (Reddy et al. 2009) (see Figure 3-5a). The agreement in the pore pressure curves (Figure 3-5c) is satisfactory until the simulation calculates pore water pressure much smaller than the experiment near the end of the time scale. This is probably due to the formation of air bubbles in the cement pores in the experiment which decreases pore pressure levels. The produced air is initially dissolved in the pore water under high pore pressure. Also, the

rebound of the computed pore pressure of Class G cement at the normalised time of approximately 2.6 (Figure 3-5d) is calculated because the sink rate of Class G cement decreases to the asymptote value and the permeability decrease due to cement hydration also stops by this time, allowing external water to migrate into the pores of cement to increase the pore pressure.
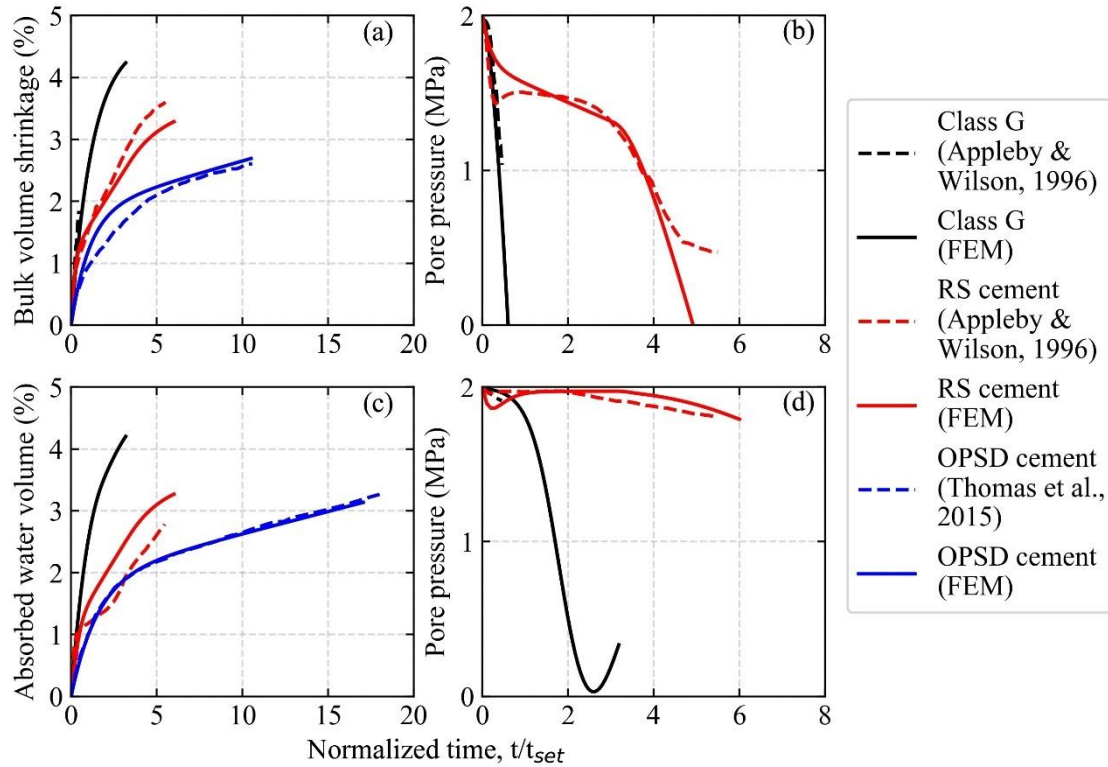
Figure 3-5 Finite element model (FEM) calibration results of the laboratory tests on cement shrinkage: (a) bulk shrinkage volume; (b) absorbed water volume; (c) pore pressure (drainage valve closed); (d) pore pressure (drainage valve open). t_{set} = 7.85 h and 5.0 h for the Class G and RS cement tests, respectively, while t_{set} = 12.0 h and 8.8 h for the bulk shrinkage volume and absorbed water volume of the OPSD cement test, respectively.

3.3.5. Effect of temperature

The temperature change of cement during hydration may have affected the experimental results through the thermal expansion of cement particles and pore water. To investigate this issue, a semi-coupled thermo-hydro-mechanical simulation was conducted with the FE model shown in Figure 3-2b. In this simulation, the temperature of cement was calculated by an independent thermal conduction analysis using the laboratory measured heat rate of OPSD slurry as shown in Figure 3-6.
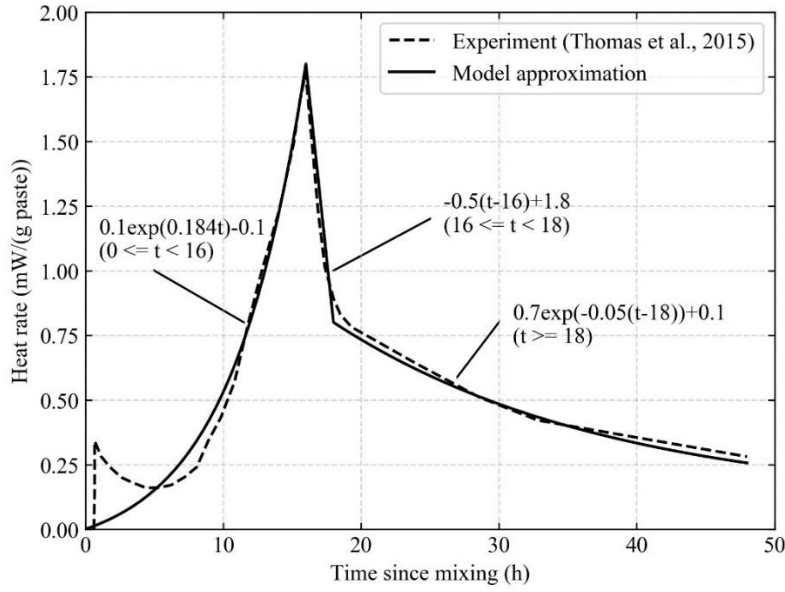
Figure 3-6 Hydration heat rate of OPSD slurry measured at 12°C and ambient pressure (Thomas et al. 2015) and its numerical approximation by three curves.

The experimental heat rate curve is approximated by a series of equations shown below:

$$\text{Heat rate (mW/g paste)} = \begin{cases} 0.1e^{0.184t} - 0.1 \ (0 \text{ h} \leq t < 16 \text{ h}) \\ -0.5(t - 16) + 1.8 \ (16 \text{ h} \leq t < 18 \text{ h}) \\ 0.7e^{-0.05(t-18)} + 0.1 \ (18 \text{ h} \leq t) \end{cases} \quad (3\text{-}6)$$

where t = time since cement mixing in hours. The axi-symmetric eight-node biquadratic displacement, bilinear temperature element was used. The employed thermal properties are shown in Table 3-3. Because thermal properties of OPSD slurry are not reported, two different values of thermal conductivity were assigned. A reasonable value of the thermal conductivity of Portland cement would be 1.0W/m/K (Zhen & Xiong 2013) (the upper bound). However, OPSD cement contains hollow fly ash particles, which may decrease the bulk thermal conductivity by a couple of orders of magnitude. As the thermal conductivity of air is about 0.025 W/m/K at 12°C, this value is used as the lower bound. The specific heat capacity was assigned as 1.0 J/g/K because the values for Portland cement (Zhen & Xiong 2013) and air are similar to this input value. The thermal expansion coefficient of early-age cement varies with moisture content (Sellevold & Bjøntegaard 2006) and temperature (Cruz & Gillen 1980). In this study, a constant value of 10 $\mu\varepsilon$/°C, which is the mean value of oil well cements (Loiseau 2014), was employed. The model also considered the temperature-dependent thermal expansion coefficient of pore water (13.41T-3717)/10^6 (1/K)). Because the laboratory test was conducted at a constant temperature of 12°C,

the initial temperature was set to 12°C and the temperature on the model boundaries was specified to a constant value of 12°C. The simulation period was 160 h.

Table 3-3 Thermal properties of cement, formation and pore water assigned to the FEM.

Thermal conductivity of cement	1.0, 0.025 W/m/K
Thermal conductivity of formation	2.0 W/m/K
Specific heat capacity of cement	1.0 J/g/K
Specific heat capacity of formation	2.0 J/g/K
Thermal expansion coefficient of cement	10 με/K
Thermal expansion coefficient of formation	1.77 με /K
Thermal expansion coefficient of pore water	13.41T-3717 με /K

Results from the thermal analysis of the OPSD cement test are shown in Figure 3-7. The maximum average temperature increase is 2.3°C with the lower bound thermal conduction coefficient (i.e. 0.025W/m/K) and is less than 0.1°C with the upper bound value (i.e. 1.0W/m/K). The computed temperature distributions are fed into the coupled hydro-mechanical simulation. Figure 3-8 shows that the effect of temperature change (up to 2°C increase) on the water absorption and shrinkage behaviour of OPSD cement is negligible. During the Class G and RS cement tests (Appleby & Wilson 1996), the maximum temperature changes were measured to be roughly 2°C, which is similar to the value computed for this OPSD cement case. Based on this finding, the effect of temperature change on water absorption and shrinkage behaviour is assumed to be insignificant.

(a)

(b)
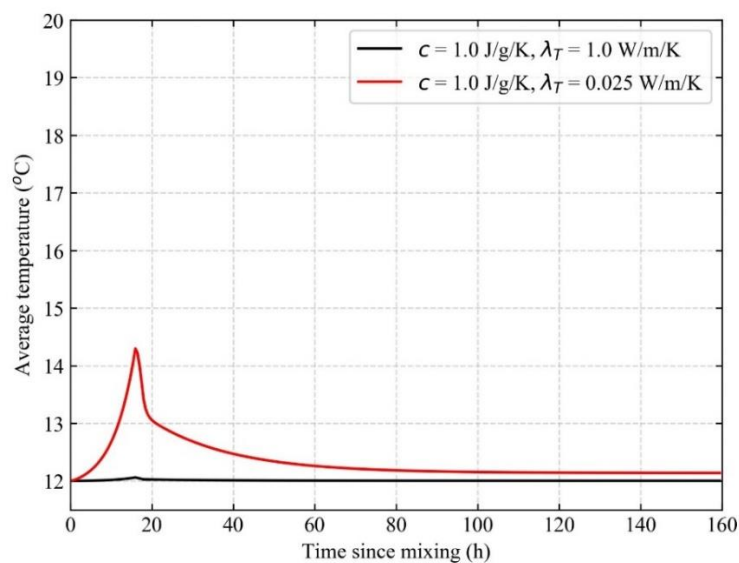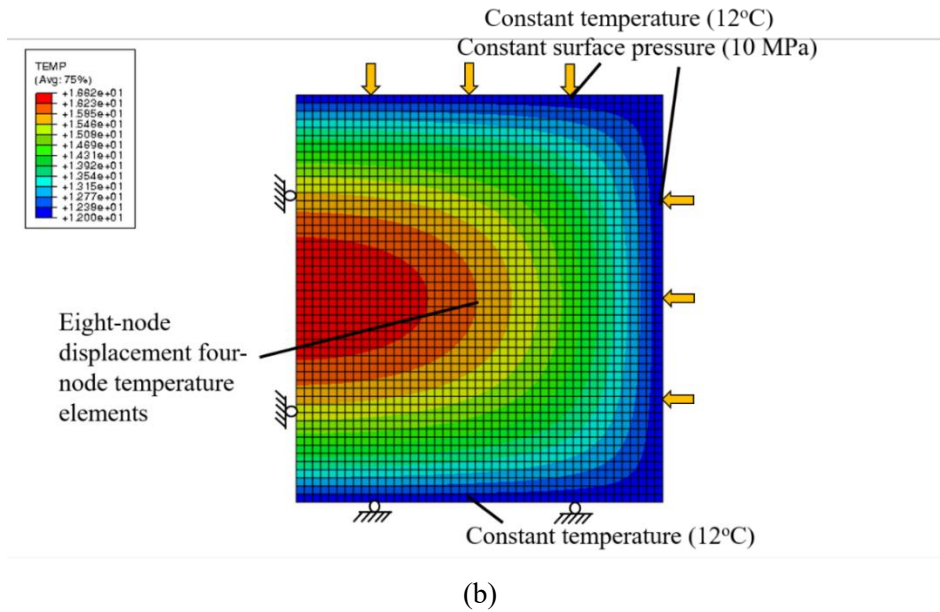
Figure 3-7 Results of the thermal analysis on OPSD slurry: (a) average cement temperatures; (b) spatial distribution of cement temperature at 16 h (c = 1.0 J/g/K and λ_T = 0.025 W/m/K).
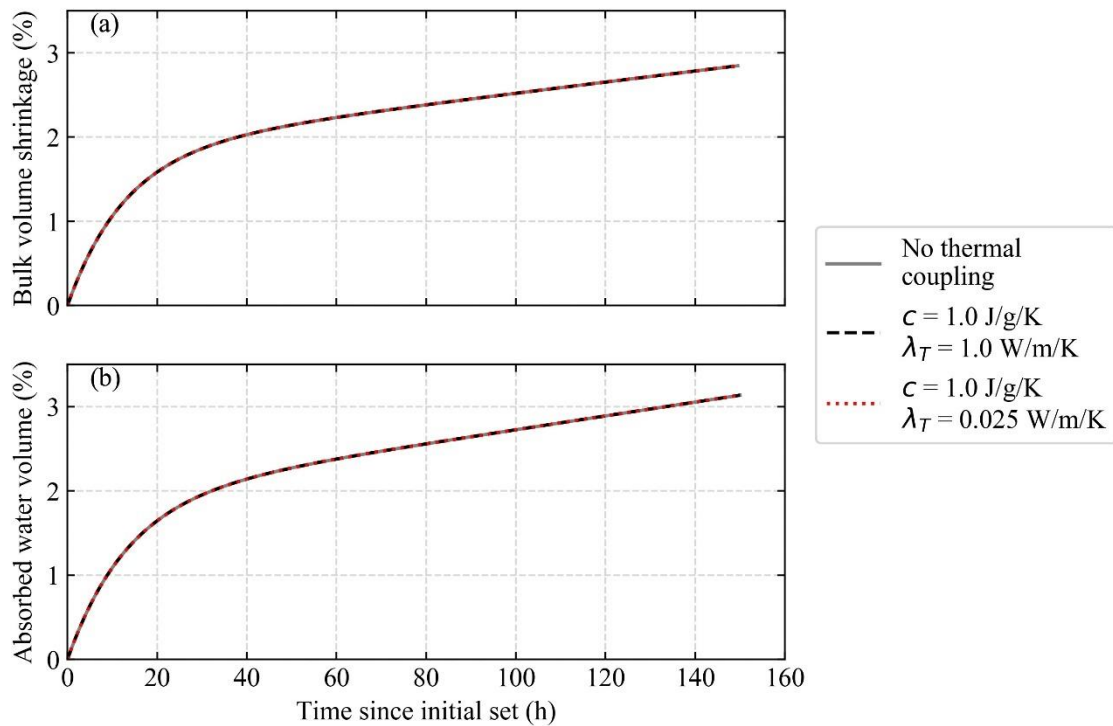
Figure 3-8 Results of the coupled hydro-mechanical cement shrinkage analysis of the OPSD cement with different temperature inputs from the thermal analysis: (a) bulk shrinkage volume; (b) absorbed water volume.

3.4. Modelling of cement shrinkage in a wellbore annulus

3.4.1. Model dimensions and material parameters

The dimensions of the axi-symmetric FEM are shown in Figure 3-9. The model represents a thin layer of cement and formation, which are assumed to be located at 100 m below the seafloor at the Nankai Trough in Japan (Yamamoto et al. 2014). The water depth of the seafloor is 1002 m. The inner and outer radius of the cement is set to 0.122 m and 0.156 m, corresponding to the outer diameter of the 9 5/8-in. casing and the diameter of a 12 1/4-in. borehole, respectively. The radial length of the formation model is set to 10 m. For both cement and formation, no vertical displacement is allowed (i.e., plane strain condition), assuming radial deformation is dominant.
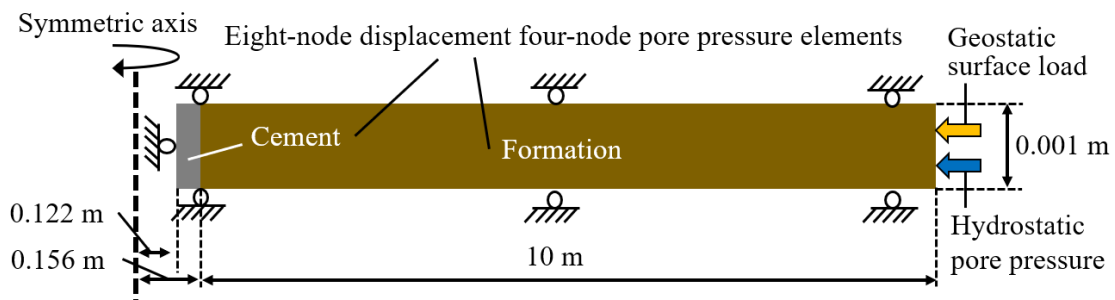
Figure 3-9 The dimensions of the axi-symmetric FEM for the wellbore model simulation.

Table 3-4 Material properties of the cement and formation.

	Cement	Formation
Sink rate	Figure 3-3a	N/A
Permeability	Figure 3-3b	1 mD-0.1 μD
Young's modulus	Figure 3-3c	N/A
Swelling gradient	N/A	0.03
Poisson's ratio	0.20	0.25
Porosity	0.25	0.57
Bulk modulus of solid phase	21 GPa	Incompressible
Bulk modulus of fluid phase	2.2 GPa	Incompressible

The ABAQUS finite element software package was employed to carry out the coupled transient fluid flow and stress analysis. The cement and formation are discretised into 20 and 5000 axi-symmetric eight-node biquadratic displacement, bilinear pore pressure elements, respectively.

The length and height of each cement element are 1.67 mm and 1 mm, whereas those of each formation element are 2 mm and 1 mm, respectively.

The model properties for the cement and formation are listed in Table 3-4. For the cement, the incremental stress-strain constitutive model with time-dependent properties evaluated earlier are adopted. The calibrated sink rate, permeability, and Young's modulus (Figure 3-3) are employed. For the formation, the pressure-dependent elastic bulk modulus K as shown in Equation 3-7 is used to calculate the stiffness of the unconsolidated formation at a given depth:

$$K = vp'/\kappa \qquad (3\text{-}7)$$

where p' is the mean effective stress, v is the specific volume ($=1+e$), e is the void ratio and κ is the swelling gradient. A value of $\kappa = 0.03$ is used based on the calibration results for this formation (Uchida 2012; Zhou 2015). It is noted that as the formation is assumed to be elastic, the mean effective stress does not change during cement shrinkage (i.e., cavity contraction). The pressure-dependent bulk modulus is used not for taking into account effective stress changes during cement shrinkage but for assigning the initial stiffness value appropriate to the depth (i.e., effective stress level) of the unconsolidated formation. A constant permeability is assigned to the formation within the range of 1 mD to 0.1 μD as part of parametric study.

3.4.2. Simulation process

The simulation process was divided into three stages: drilling stage, cement pumping stage, and cement shrinkage stage. The formation and cement were separately modelled in the first two stages, whereas the two were interacting in the final stage.

In the initial state (Figure 3-10a), the cement elements are not active. For the formation, the initial pore pressure and effective stresses are applied to reach geostatic equilibrium. The total vertical stress at a given depth of the Nankai Trough is given by the sum of the weight per unit area of the seawater with the density of 1.030 g/cm^3 and that of the formation with the bulk density of 1.750 g/cm^3 (Suzuki et al. 2015). The vertical effective stress is then calculated by subtracting the hydrostatic pore pressure from the total vertical stress. The initial horizontal effective stress is calculated using Equation 3-8:

$$\sigma'_h = (1 - \sin\phi')\mathrm{OCR}^{\sin\phi'}\sigma'_v \qquad (3\text{-}8)$$

where σ'_h is the horizontal effective stress; σ'_v is the vertical effective stress; ϕ' is the

internal effective friction angle of the formation and OCR is the ratio of the past maximum vertical effective stress to the current vertical effective stress. This formula for calculating the horizontal effective stresses is employed in soil mechanics. Because the modelled formation is unconsolidated clayey overburden at the Nankai Trough, this equation is suitable. The internal effective friction angle and OCR value of the Nankai Trough formation is obtained from Nishio et al. (2011). The horizontal pressure corresponding to the initial total horizontal stress of the formation is applied onto the right-hand side boundary of the formation. The pore pressure is fixed to the hydrostatic pressure on the right-hand side boundary, whereas it is free (zero-flux) on the left-hand side boundary.
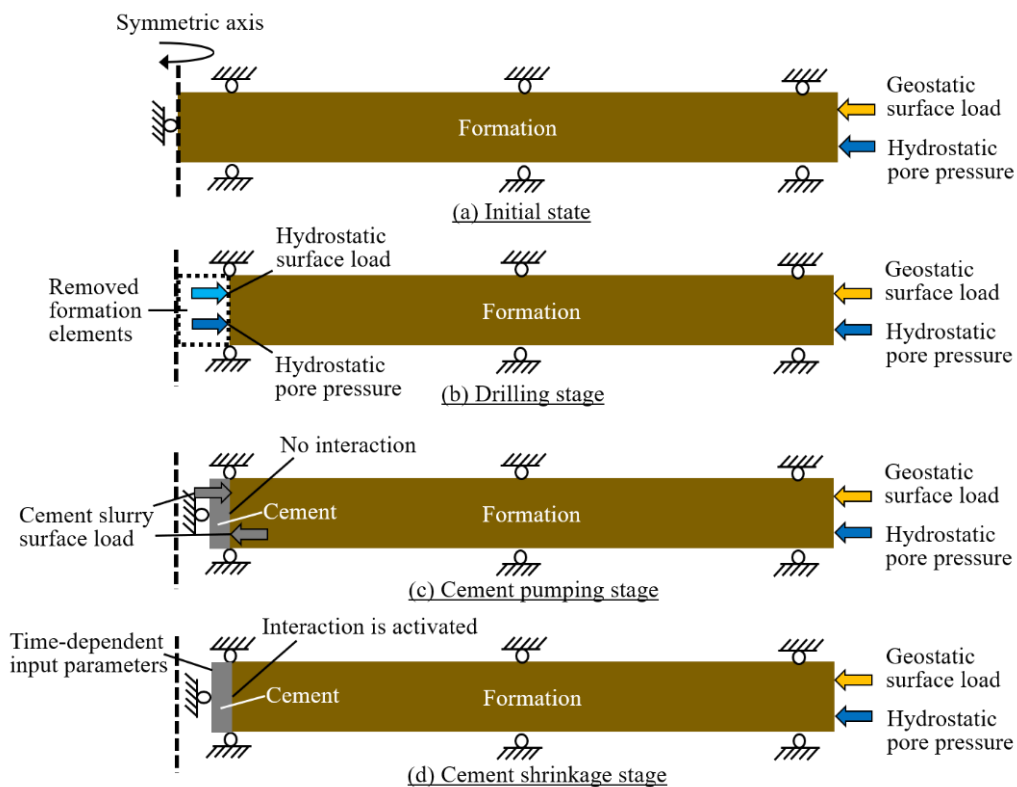
Figure 3-10 The three-stage process of the wellbore model simulation: (a) initial state; (b) drilling stage; (c) cement pumping stage; (d) cement shrinkage stage

In the drilling stage (Figure 3-10b), the formation elements located inside the borehole radius are removed to simulate the drilling process. The surface pressure corresponding to the hydrostatic pressure of seawater is applied on the left-hand side boundary surface. The pore pressure on the left-hand side boundary nodes is specified to hydrostatic seawater pressure to simulate drilling with seawater (i.e. drained condition).

In the cement pumping stage (Figure 3-10c), the cement elements are activated. The radial

displacement on the left-hand side boundary of the cement is constrained to simulate the casing wall. The slurry pressure is applied on the right-hand side surface of the cement. The slurry pressure is evaluated by the weight per unit area of the seawater (1002 m) and cement (100 m). The slurry density used to calculate the slurry pressure is 1900 kg/m³ for Class G and RS cements and 1200 kg/m³ for OPSD cement. Two possible scenarios are considered for the initial effective stress and pore pressure. Figure 3-11a shows one scenario where the effective stress (i.e. interparticle stress) of the cement is zero ($\sigma' = 0$) and the entire slurry pressure is converted into pore pressure ($u = \rho_c gz + p_w$) (i.e. underconsolidated cement case). Figure 3-11b shows the other scenario where pore pressure becomes the hydrostatic pressure of the formation ($u = \rho_w gz + p_w$) and the effective stress is generated as the difference between the weight of the cement slurry and formation water ($\sigma' = (\rho_c - \rho_w)gz$) (i.e. consolidated cement case). In both cases, the total stress of the cement remains identical to the slurry pressure ($\sigma = \sigma' + u = \rho_c gz + p_w$). These two cases for the initial effective stress and pore pressure levels at the onset of cement initial set are two extreme scenarios and the reality should lie somewhere in between them.
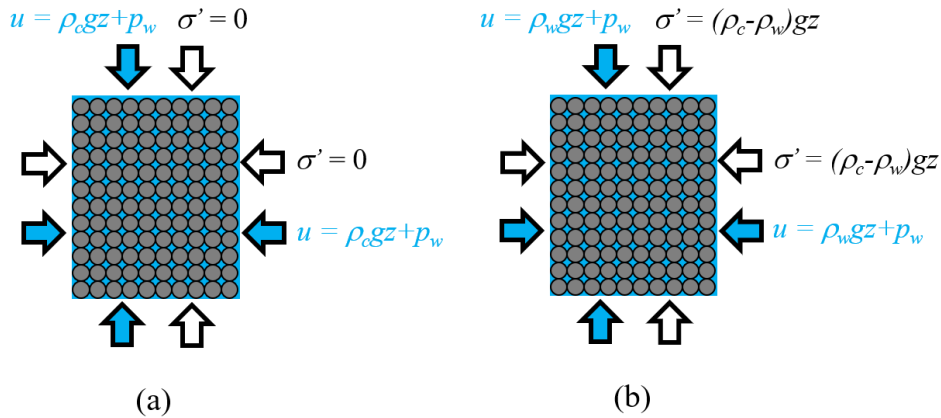
Figure 3-11 Assumed effective stress and pore pressure levels of the cement at the onset of cement initial set: (a) underconsolidated cement case; (b) consolidated cement case (σ'=effective stress, u=pore pressure, ρ_c=cement slurry density, ρ_w=water density, g=gravity acceleration, z=depth below seabed, p_w=seawater pressure at seabed).

For the formation, the cement slurry pressure is applied at the left-hand side boundary of the formation, resulting in radial deformation. Zero fluid flux condition is also applied. In response to the total radial stress change, the radial effective stress changes due to the cavity expansion process. The excess pore pressure is zero because the formation is modelled as an isotropic elastic material. Hence the pore pressure remains the same as the initial condition.

In the shrinkage stage (Figure 3-10d), the surface pressures on the contacting boundaries of the cement and formation are removed and the contact interaction between the right-hand side boundary surface of the cement and the left-hand side boundary surface of the formation is activated. The positions of the corresponding cement and formation nodes are adjusted before the simulation is submitted such that at the onset of the shrinkage stage these nodes are just in contact with each other without penetration or separation. The augmented Lagrange method in ABAQUS is used to enforce the contact interaction between the surfaces. In this contact model, the contact pressure is augmented in direct proportion to the penetration of the surfaces so as to prevent excessive penetration. No tangential friction is assumed as the vertical displacements of the cement and formation are both specified to be zero. Fluid flow across the contact interface is allowed and pore water moves between the formation and cement. The cement shrinkage is initiated by applying the calibrated time-varying sink rate (Figure 3-3a), permeability (Figure 3-3b), and Young's modulus (Figure 3-3c) to the cement. The period of this stage is set to 150 h with the time increment of 0.5 h.

3.4.3. Results from the consolidated cement case

When the cement is assumed to be consolidated at the onset of the initial set of cement (i.e. consolidated cement case), the pore pressure in the cement is the same as that of the formation. The pore water movement is therefore governed by the suction pressure development within the cement as well as the permeability contrast between the cement and formation during the hardening process. Figure 3-12 shows the changes in the absorbed water volume with time for the three cements. The largest absorbed water volume is calculated for Class G cement, whereas it is the lowest for OPSD cement. This trend can be explained by the water-to-cement ratio of each cement, i.e., the lower the ratio the larger the amount of cement particles that reacts and absorbs water. Although the ratios used for Class G and RS cement are not disclosed in Appleby & Wilson (1996), the standard water-to-cement ratio of Class G cement is 0.44. A higher water-to-cement ratio is usually adopted for RS cement as a portion of cement particles is replaced by gypsum to accelerate the initial set (i.e. thickening time). The water-to-cement ratio of OPSD cement is not disclosed in Thomas et al. (2015). However, since hollow fly ash particles represent 50% of the mass of dry ingredients and 41% of total slurry volume, a higher water-to-cement ratio than the other two cements is expected.
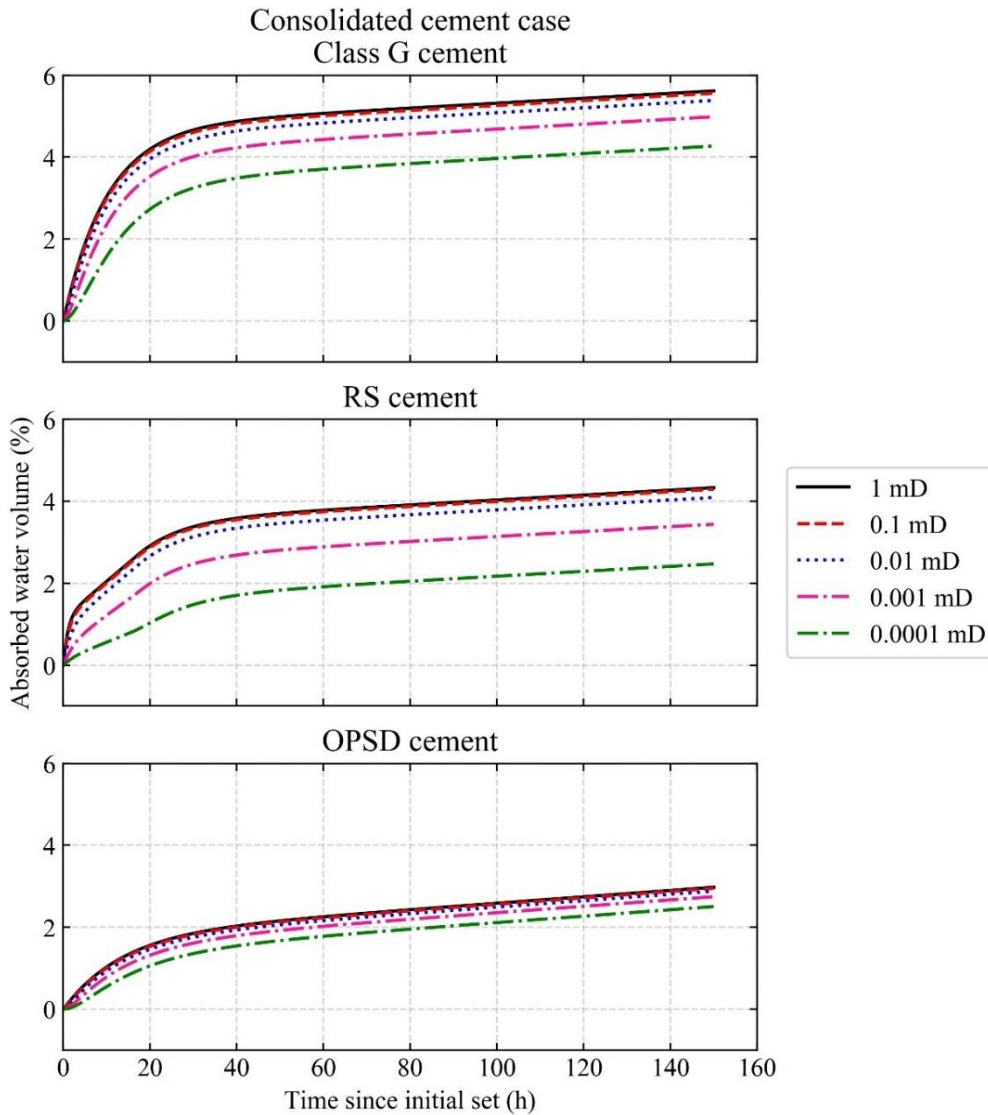
Figure 3-12 Absorbed water volume of cements since the initial set in the consolidated cement case.

For a given cement, the absorbed water volume is in direct proportion to the formation permeability as expected. When the formation permeability is greater than 0.1 mD, the absorbed water volume is the maximum (5.6% for Class G, 4.4% for RS cement and 3.0% for OPSD cement at 150 h). As the formation permeability decreases below 0.1 mD, the absorbed water volume becomes smaller due to limited water supply from the low permeability formation. The absorbed water volume still increases toward the end of the simulated period (150 h) because the asymptotic values of the calibrated sink rates are not zero. Under this condition, the absorbed water volume will keep increasing at a constant rate beyond the simulation period, which is unrealistic. Experimental data sets for longer periods of cement hydration are necessary, with which the sink

rate is calibrated to reach zero, to model long-term water absorption behaviours.
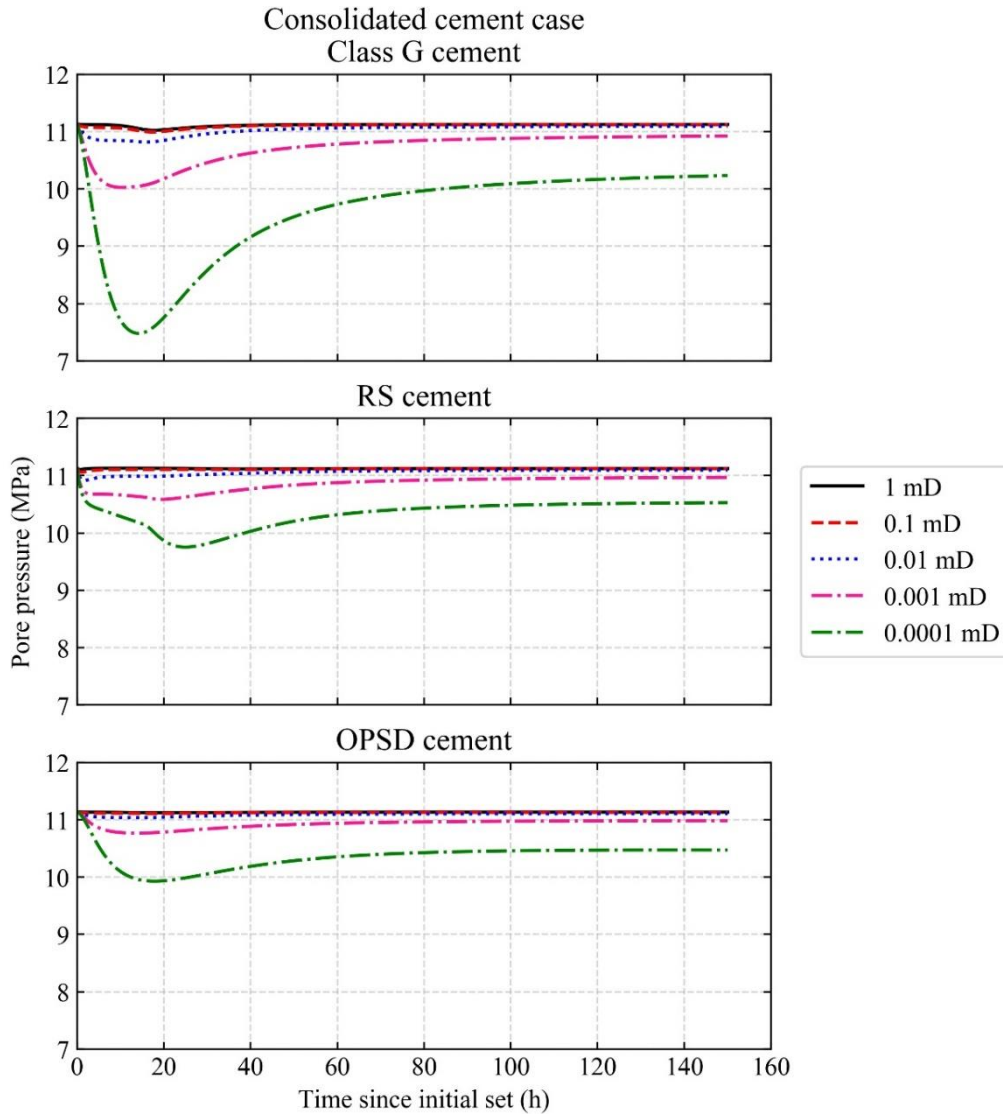
Figure 3-13 Pore pressure decrease in cements in the consolidated cement case at the contact surface with casing since the initial set.

The computed time-dependent pore pressure in the cement at the contact surface with casing is given in Figure 3-13 for different formation permeability values and different cements. When the formation permeability is greater than 0.1 mD, the pore pressure remains close to hydrostatic. However, as the formation permeability decreases, the pore pressure reduces due to suction pressure developing in the cement during the initial hydration process. The suction development is greater when water supply from the formation is more restricted. As the hydration continues, the suction pressure development decreases and the cement stiffness increases. Consequently, the

pore pressure recovers back to the hydrostatic condition. The pore pressure does not recover to hydrostatic when the formation permeability is lower than 0.01 mD. This is because the cement hydration process continues under restricted water supply from the formation. Pore pressure is stabilized below hydrostatic as the cement suction pressure is balanced with the limited water supply from the formation. In a long term, it is expected that pore pressure will go back to the hydrostatic pressure. To model such pore pressure change, experimental data sets for longer periods of cement hydration are necessary.
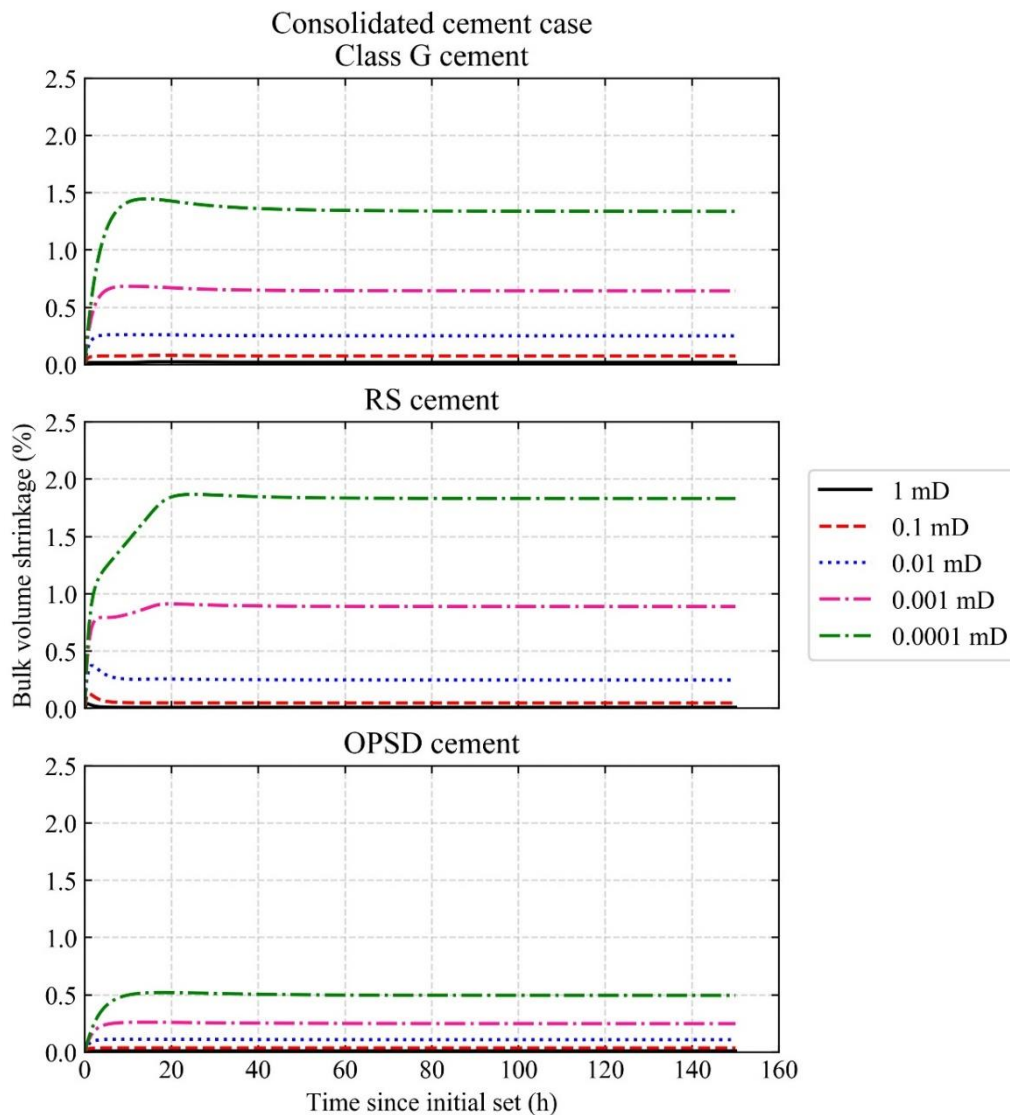
Figure 3-14 Bulk shrinkage volume of cements since the initial set in the consolidated cement case.

The bulk shrinkage behaviour with time is shown in Figure 3-14. When the formation permeability is greater than the threshold value of 0.1 mD, the amount of shrinkage is very small

because the cement is absorbing water from the surrounding formation during hydration. The amount of shrinkage increases as the formation permeability decreases and the amount of absorbed water during hydration decreases. The total shrinkage volume under the formation permeability of 0.1 μD is 1.3%, 1.8%, and 0.5% for Class G cement, RS cement, and OPSD cement, respectively. The behaviour of RS cement shows initial shrinkage immediately after the initial set but then swells back with time when the formation permeability is greater than 0.01 mD. This is because of the large initial sink rate of RS cement, which generates large temporal pore pressure decrease. However, the pore pressure quickly recovers by the flow of formation pore water into the cement. When the permeability is less than 0.01 mD, the flow from the formation is not fast enough and shrinkage increases with time. In all cases, the shrinkage process completes after certain time even though the absorbed water volume and pore pressure keep changing. This is because stiffness values of the cements become high enough that any additional cement volume change by any pore pressure change is negligible.

3.4.4. Results from the underconsolidated cement case

It is possible that the cement is not consolidated when the initial set of cement occurs. In this section, an extreme case of underconsolidated cement with zero effective stress is considered. Because the pore water in the cement is greater than that of the formation, the water flows from the cement to the formation initially. However, as the cement hydrates, water then starts to flow back into the cement as is observed in the consolidated cement case. Hence, complex water movement is expected in this case.

The computed absorbed water volume changes with time are shown in Figure 3-15 for the three cements. Different from the consolidated cement case, the amount of absorbed water volume is not in direct proportion to formation permeability. This is because the pressure difference across the cement-formation interface causes the outflux of cement pore water, resulting in negative values of absorbed water volume. As the formation permeability increases, the outflux becomes greater. However, as the hydration progress, the cement starts to absorb water from the formation. The water influx to the cement increases with increasing formation permeability. This competing water movement causes complex absorbed water volume changes. For example, in case of Class G cement, the absorbed water volume in the 0.1 mD case is the largest compared to the other cases with the formation permeability greater or less than 0.1 mD. In case of OPSD cement, the differences in absorbed water volume are small within the cases of different formation permeability values. In reality, the cement would be partially consolidated or the pore pressure of the formation around the cement would be greater than the hydrostatic condition due to infiltration of the slurry into the formation. Thus, the calculated cement pore water outflux may be somewhat

exaggerated.
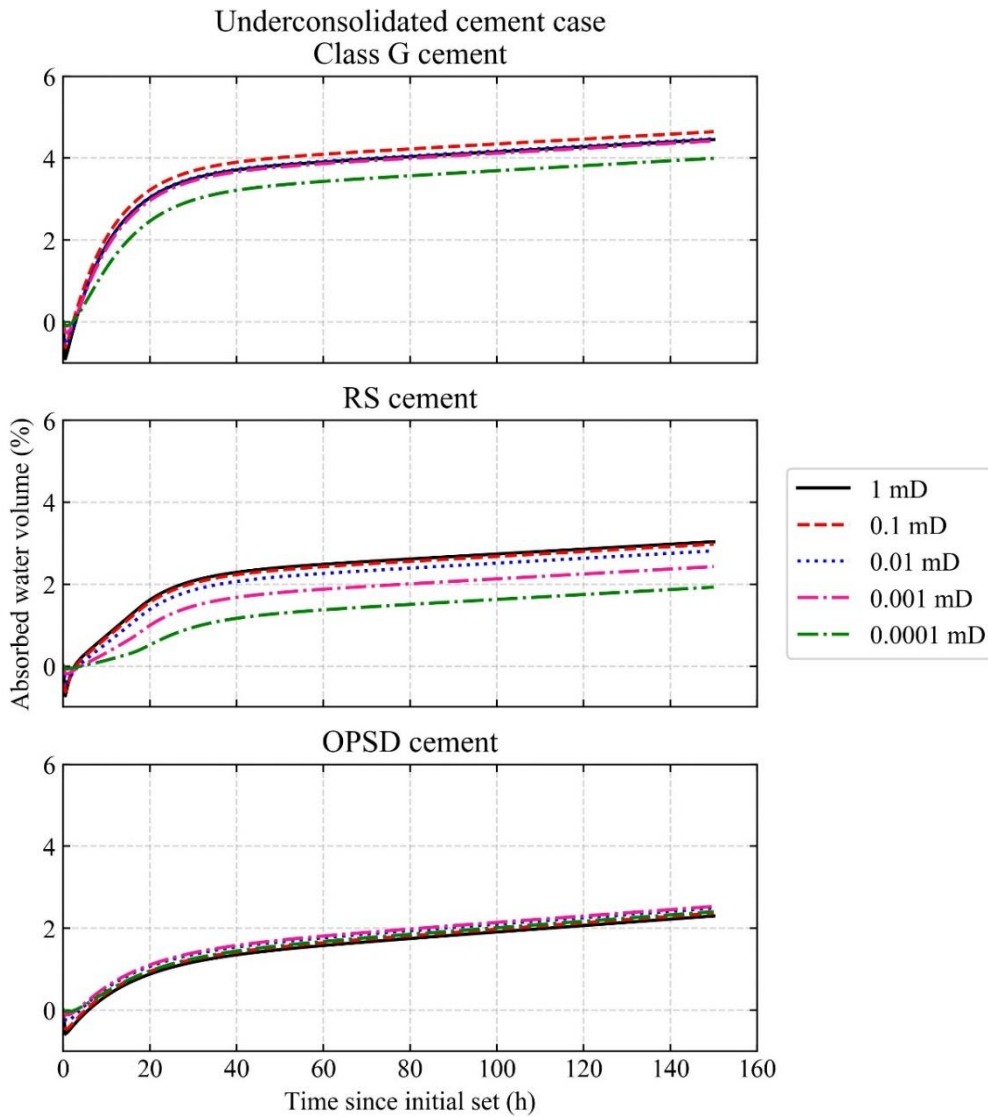
Figure 3-15 Absorbed water volume of cements since the initial set in the underconsolidated cement case.

The changes in the cement pore pressure at the interface with casing are shown in Figure 3-16. When the formation permeability is greater than 0.1 mD, the pore pressure decreases to the formation pressure of 11.14 MPa at the initial stage of hydration. When the formation permeability is less than 0.1 mD, the pore pressure decreases further with decrease in formation permeability as capillary suction pressure increases. However, pore pressure recovers back to the hydrostatic state with time as the hydration process progresses. A similar trend is observed in the consolidated cement case.
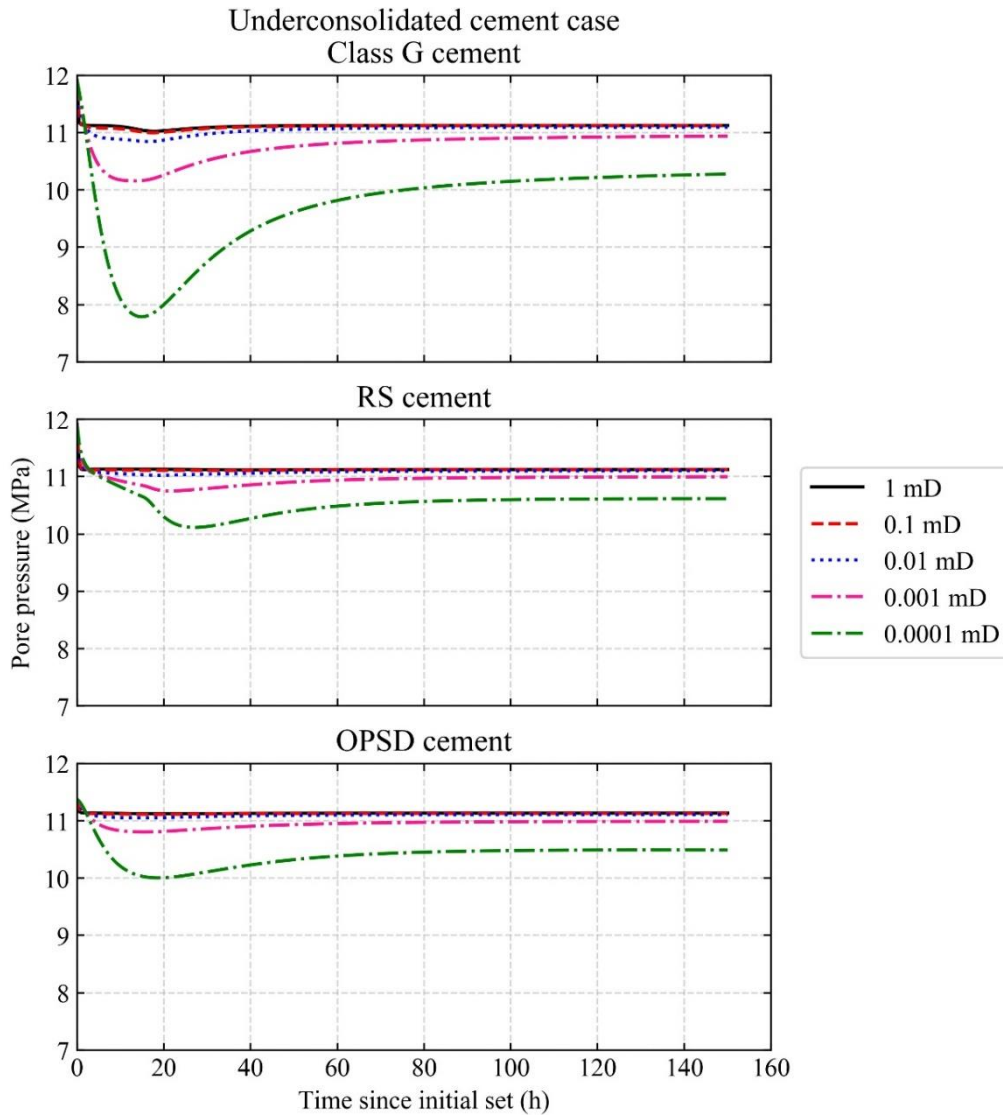
Figure 3-16 Pore pressure decrease in the cement at the contact surface with casing since the initial set in the underconsolidated cement case.

Figure 3-17 shows the bulk shrinkage behaviour of Class G cement, RS cement and OPSD cement, respectively. The trend observed here is inverse to what is observed in absorbed water volume. The total bulk shrinkage volume can be divided into two parts: (i) initial shrinkage due to the outflux of cement pore water and (ii) primary shrinkage due to cement water absorption. The initial shrinkage increases with increasing formation permeability, whereas the primary shrinkage decreases with increasing formation permeability. Because of the opposite trends of the initial shrinkage and primary shrinkage with respect to formation permeability, the total shrinkage does not correlate well with formation permeability.
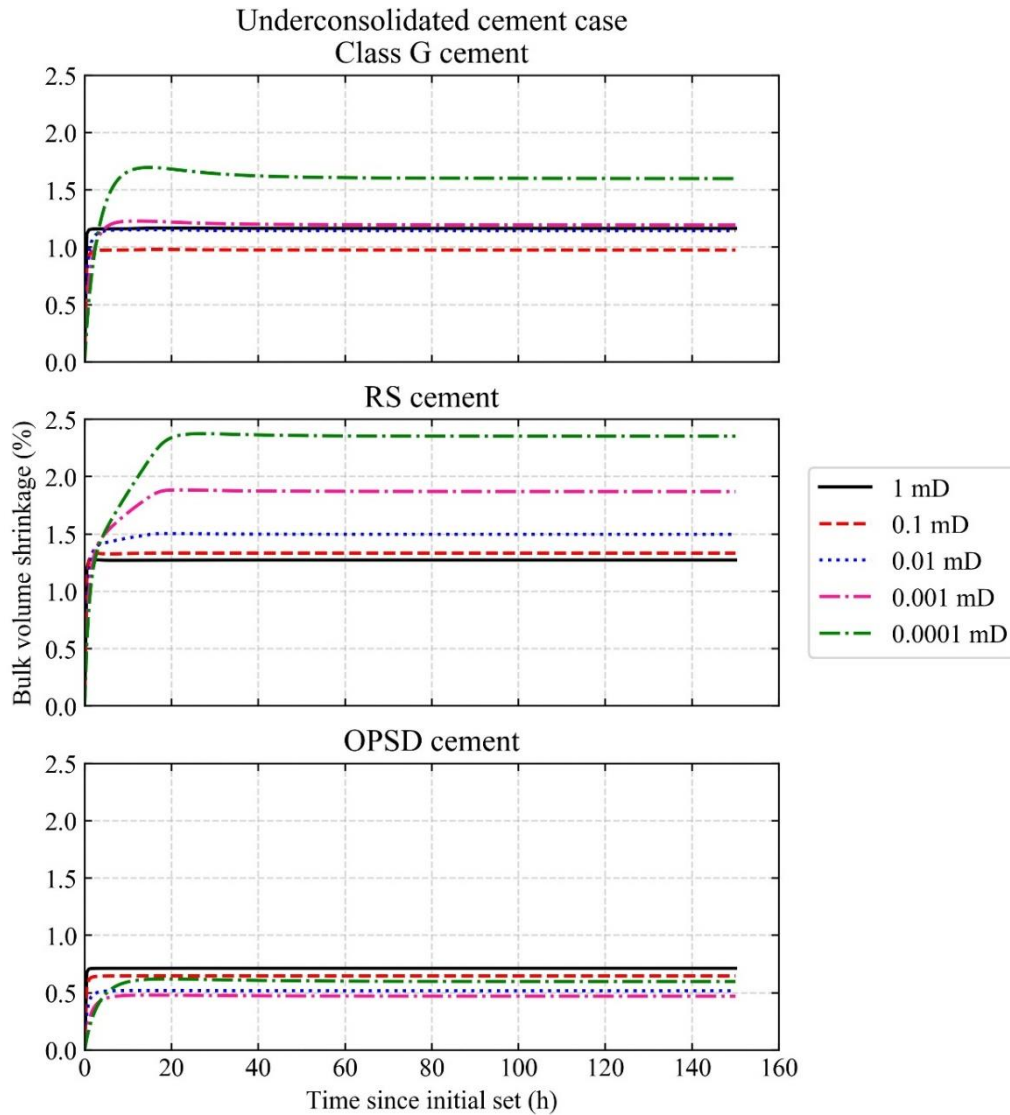
Figure 3-17 Bulk shrinkage volume of cements since the initial set in the underconsolidated cement case.

3.4.5. Effect of cement hydration heat

As was performed for the calibration simulation, a semi-coupled thermo-hydro-mechanical analysis on the water absorption and shrinkage behaviour of the annular cement was carried out to assess the effect of temperature change. First, a thermal analysis was conducted to compute the temperature distribution of the cement. The axi-symmetric eight-node biquadratic displacement, bilinear temperature element was assigned to the identical FEM shown in Figure 3-9. The thermal properties of the cement (i.e., OPSD cement) and formation are listed in Table 3-3. The initial temperature was set to 12°C. The model boundary was specified with a constant temperature of 12°C. The simulation period was set to 160 h. The computed average temperatures within the

cement with time are shown in Figure 3-18 for two different thermal conductivity values. The temperature increase of the cement is greater in the wellbore configuration compared to the laboratory test configuration. This is because in the wellbore configuration the radial dimension of the cement is larger than that in the laboratory test configuration, and it is also because no thermal conduction in the vertical direction is allowed in the wellbore configuration.

The computed temperatures were applied to the coupled hydro-mechanical simulations. The formation permeability was set to 0.1 µD. The results shown in Figure 3-19 indicate that the effect of temperature changes on the hydration of OPSD cement on the absorbed water and bulk shrinkage behaviour is found to be insignificant for this wellbore geometry, similar to what was found in the laboratory cases.
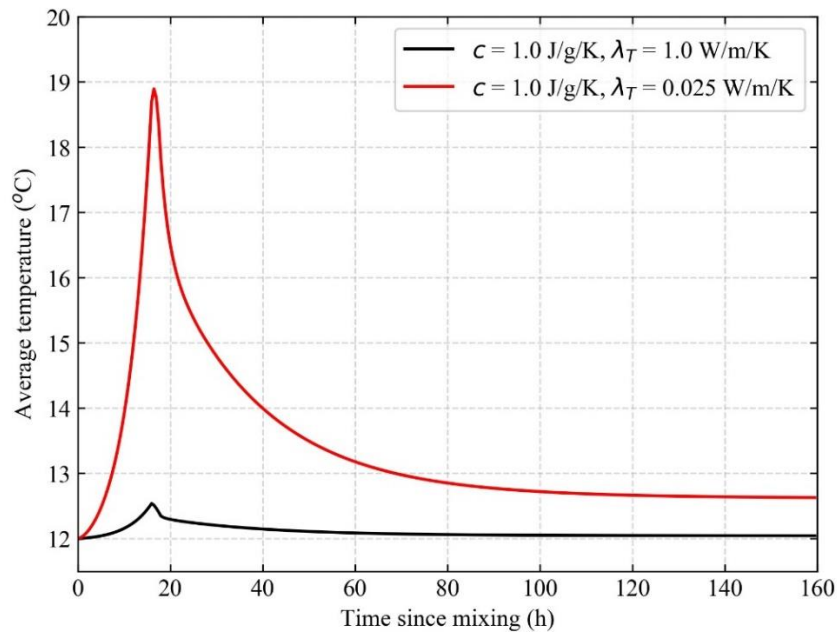
Figure 3-18 Changes in the average cement temperature of OPSD slurry computed in the thermal analysis in the wellbore configuration.
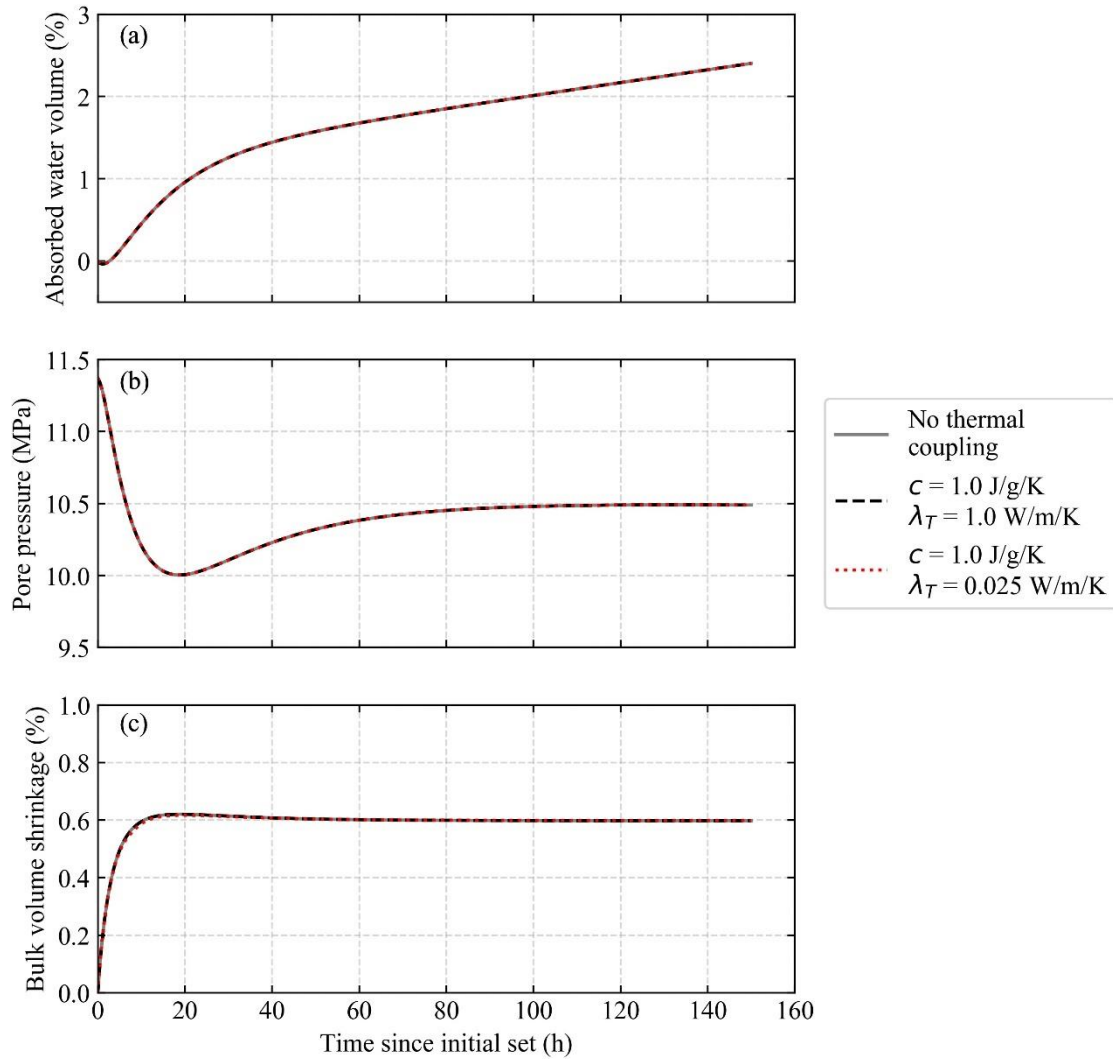
Figure 3-19 Result of the semi-coupled thermo-hydro-mechanical analysis on OPSD cement in the wellbore configuration: (a) absorbed water volume; (b) pore pressure; (c) bulk shrinkage volume.

3.5. Discussion

Figure 3-20 shows the correlation between cement bulk shrinkage volume at the end of the simulation period (150 h) and formation permeability for both consolidated and underconsolidated cement cases. The shaded area shows the uncertainty of bulk shrinkage volume due to the uncertainty in the initial pore pressure and effective stress levels of cement at its initial set. It is found that larger shrinkage values are calculated for the underconsolidated cement case than for the consolidated cement case in the formation permeability range examined in this study.

This is due to the initial outflux of cement pore water into the formation (i.e. initial shrinkage), which occurs because the initial pore pressure is assumed to be equal to the slurry pressure (> formation pore pressure) in the underconsolidated cement case. As a result, the uncertainty of bulk shrinkage volume increases with increasing formation permeability. At the formation permeability of 1 mD, for example, the bulk shrinkage volume could vary between 0.02% and 1.16% (Class G cement), 0.01% and 1.27% (RS cement) and 0.01% and 0.71% (OPSD cement). The uncertainty decreases with decreasing formation permeability. Whilst the uncertainty of bulk shrinkage volume decreases with decreasing formation permeability, the value of bulk shrinkage volume itself increases with decreasing formation permeability, as the formation water could not migrate to the cement pores to compensate for the shrinkage at lower formation permeability.
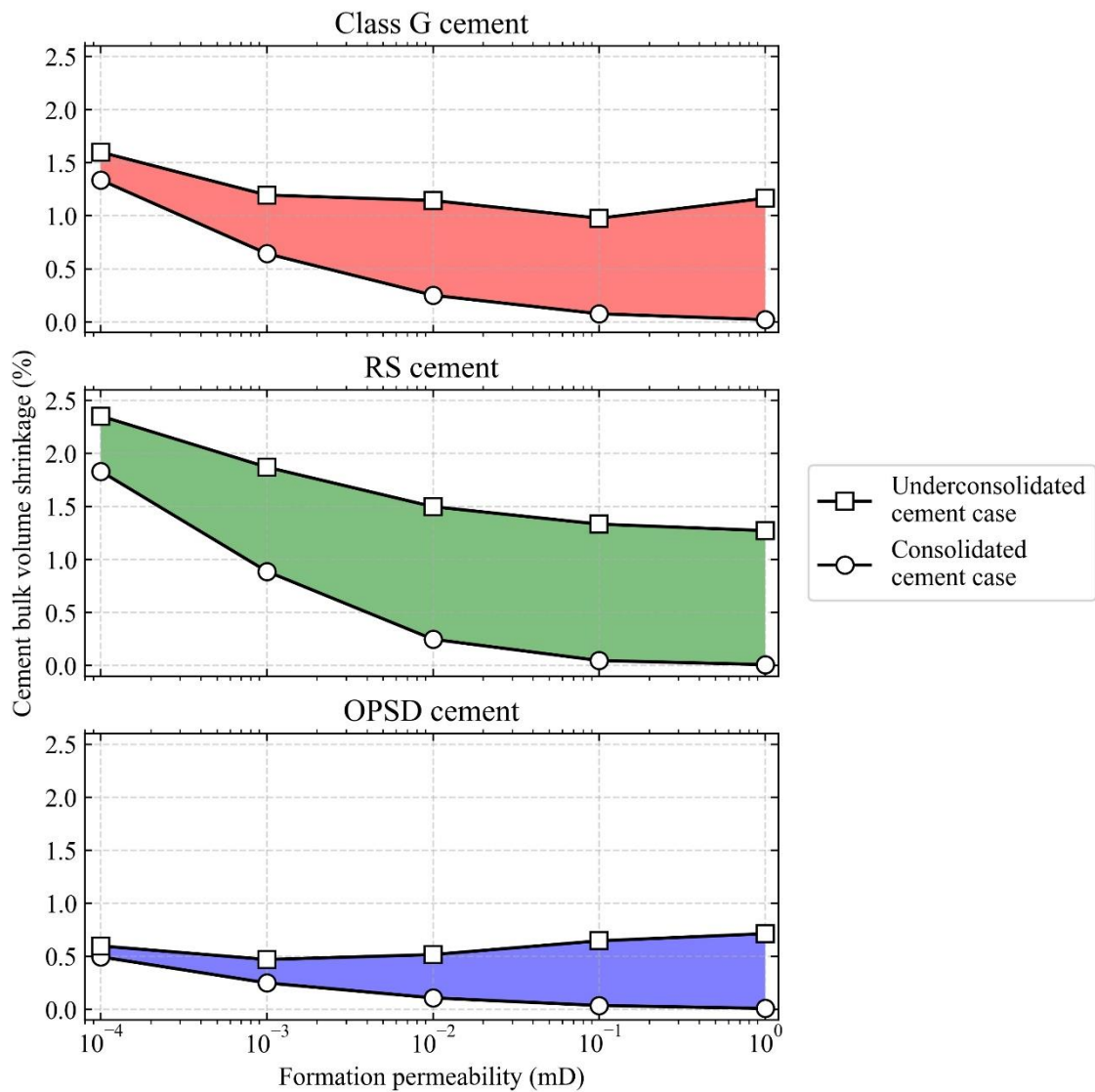
Figure 3-20 Correlations between bulk shrinkage volume of cements at 150 h and formation permeability.

Based on the pore pressure changes of the cements (see Figure 3-13 and Figure 3-16), the threshold formation permeability, above which the provision of sufficient formation water into the cement is guaranteed, appears to be between 0.01 mD and 0.1 mD for the cement types examined in this study under both consolidated and underconsolidated cases. The minimum permeability in the methane hydrate concentrated layer in the Nankai Trough seems to be 0.01 mD based on the formation core analysis (Konno et al. 2015) and wireline logging data (Fujii et al. 2015). Therefore, water provision to the hardening cement could be limited in the reservoir layer. In addition, the overburden layer is composed of clayey material, which is likely to have permeability values lower than 0.01 mD. In this case, insufficient water provision to the cement could cause larger-than-expected cement shrinkage volume. At the formation permeability value of 0.01 mD, the computed bulk shrinkage volume at 150 h varies between 0.25% and 1.14% (Class G cement), 0.25% and 1.50% (RS cement) and 0.11% and 0.52% (OPSD cement), respectively.

It is noted that the temperature and pressure conditions in the actual wellbore are different from those of the laboratory shrinkage test performed for Class G and RS cements. In the actual wellbore, typical temperature and pressure values are approximately 12°C and 12 MPa (Yamamoto et al. 2017), whereas the laboratory shrinkage test was conducted at approximately 20°C and 2 MPa. The literature shows that cement shrinkage volume increases with increasing temperature and pressure levels (Backe et al. 1998; Reddy et al. 2009). Hence, the shrinkage volume measured for Class G and RS cements might have been underestimated. Moreover, one of the modelling assumptions is that the formation remains poro-elastic during cement shrinkage. In reality, the stress distribution in the formation around the wellbore could change in a complex manner due to potential plastic strain development in the formation. Shear stress could also be generated at the cement-formation interface due to cement shrinkage, which was not considered in this study. The cement permeability could increase significantly if cracks are generated in the cement due to shrinkage. In this case, cracks would predominantly form radially from the casing-cement interface (Bois et al. 2012). These points may have to be addressed to improve the accuracy of the simulation of the annular cement shrinkage volume.

3.6. Summary

In this study, the coupled hydro-mechanical finite element analysis was carried out to simulate the migration and absorption of water and the bulk shrinkage behaviour of early-age cement in

the wellbore annulus. The main objectives of this study are (i) to assess the threshold value of formation permeability, below which the water supply to the hardening cement becomes important, and (ii) to estimate the bulk shrinkage volume of cements in the wellbore annulus for such cases. The water absorption characteristics of cements were calibrated based on the laboratory shrinkage test data on three different cement types found in the literature: Class G cement, rapid setting (RS) cement, and OPSD cement. The calibrated cement shrinkage parameters were incorporated into the wellbore cement shrinkage simulation where the interaction between the hardening cement and the formation was simulated. The simulation of the wellbore cement shrinkage yielded the following findings.

(i)   The threshold permeability value of the formation for providing sufficient water to hardening early-age cements is found to be between 0.01 mD and 0.1 mD for the Nankai Trough scenario. Since the formation permeability near the reservoir layer at this site could be as low as 0.01 mD, the formation might not be capable of providing sufficient water to hydrating early-age cements.

(ii) The bulk shrinkage volume of OPSD cement at the Nankai Trough case could be in a range of 0.01% to 0.71%, if formation permeability varies between 1 mD and 0.01 mD. If Class G or RS cement were used, the bulk shrinkage volume could vary from 0.02% to 1.16% (Class G cement) and from 0.01% to 1.50% (RS cement) in the same formation permeability range.

(iii) Whether the cement is consolidated or underconsolidated at the onset of cement initial set has a significant impact on the bulk shrinkage volume of the cements. In the underconsolidated cement case, the outflux of cement pore water into the formation occurs in the initial stage which increases the bulk shrinkage volume.

This study identified a reasonable range of cement bulk shrinkage volumes expected at the Nankai Trough, owing to the availability of the shrinkage test data of OPSD cement, which was actually used for the cementing operation at the Nankai Trough. The simulation cases of Class G and RS cements are carried out for comparison purposes. To extend the applicability of the proposed methodology to estimate the water migration/absorption and the bulk shrinkage behaviour of early-age cements to be used in different formation conditions, cement shrinkage tests need to be conducted under pressure and temperature conditions tailored to those at the target depths of the formation such that the model parameters are calibrated accurately.

4. Simulation of wellbore construction in offshore unconsolidated methane hydrate-bearing formation

4.1. Introduction

Field trials of gas production from methane hydrate reservoirs in the Mackenzie Delta in Canada (Yamamoto & Dallimore 2008) and in the Nankai Trough in Japan (Boswell 2013; Yamamoto et al. 2014) have shown that the control of formation integrity is crucial for sustainable gas production. For instance, the sand production issue was encountered in the Nankai Trough field trial (Yamamoto 2015) due to the unconsolidated nature of the methane hydrate-bearing formation, which terminated gas production by clogging the well.

During well construction, the integrity of unconsolidated formation is affected significantly near the wellbore, which in turn complicates the interpretation of downhole tests. For example, at the A1-E1 well in the Nankai Trough site, mini-frac tests were conducted to estimate the minimum horizontal stress after well construction, but it was found difficult to interpret the result (Matsuzawa et al. 2006; Yamamoto et al. 2005; Yamamoto et al. 2006). Figure 4-1a shows the estimated minimum horizontal stress values of the formation at the Nankai Trough site. The symbols indicate the estimations by the mini-frac tests (i.e., closure pressure and propagation pressure) whereas the lines show theoretical estimations calculated with the formation density of 1.75 g/cm^3 and seawater density of 1.027 g/cm^3 by Equation 4-1:

$$\sigma_h = K_0(\sigma_v - u) + u \qquad (4\text{-}1)$$

where σ_h = horizontal total stress; σ_v = vertical total stress; u = pore pressure; K_0 = ratio between the vertical and horizontal effective stresses (as in K_0 consolidation test). Figure 4-1a shows that the estimated values of the minimum horizontal stress from the mini-frac tests are scattered over a larger error range.

Figure 4-1b shows a borehole radius measurement of the A1-W well (Takahashi & Tsuji 2005), which was located approximately 50 m in the north from the A1-E1 well. The borehole radius is normalized by the radius of the drill bit. Considerable borehole enlargement was observed in the overburden and underburden layers of the unconsolidated Nankai Trough formation. This indicates that the formation was significantly disturbed by well construction process.

Therefore, it is hypothesized in this study that well construction process has an impact on formation integrity in a way that well construction-induced formation disturbance could potentially cause subsequent formation and/or well failures during hydrate dissociation. A finite element analysis was carried out to assess the effect of wellbore construction on the integrity of the unconsolidated Nankai Trough formation in Japan. The main objectives are as follows:

(i)   to assess the zone and magnitude of well construction-induced disturbance in the formation and

(ii)   to evaluate relative impact of each well construction stage on the integrity of the formation.
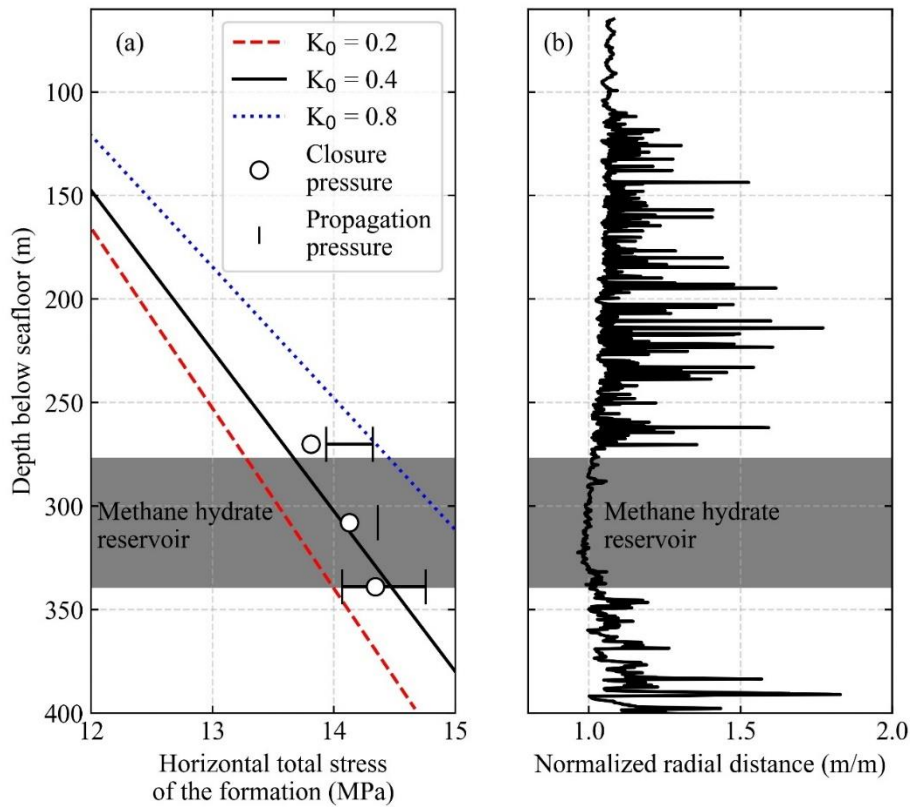
Figure 4-1 *In situ* measurements of wellbores at the Nankai Trough: (a) Estimated values of the minimum horizontal stress; (b) borehole enlargement after the drilling.

The geometry of the axi-symmetric finite element model was based on that of an experimental wellbore (i.e., the A1-E1 well) constructed in 2004 in the Nankai Trough. The methane hydrate critical state (MHCS) model (Uchida et al. 2012), which incorporates the effect of methane hydrate on the formation mechanical properties, such as strength, stiffness and dilation

74

enhancement (Hyodo et al. 2014; Hyodo et al. 2013; Masui et al. 2005; Masui et al. 2007; Yoneda et al. 2015; Miyazaki et al. 2011), was employed. The MHCS model was calibrated against triaxial test data of *in situ* formation samples recovered from the Nankai Trough (Yoneda et al. 2015; Nishio et al. 2011).

4.2. Finite element modelling

4.2.1. Model geometry

A two-dimensional axi-symmetric finite element model was constructed. The model geometry was designed by Xu (2014) and it was based on the A1-E1 well drilled in 2004 at the Atsumi No.2 knoll in the Nankai Trough (Takahashi & Tsuji 2005). The A1-E1 well was constructed as part of the multi-well exploration program implemented in 2004 at the Nankai Trough and it was organized by Japan Oil, Gas and Metals National Corporation (JOGMEC). In total, 32 wells were drilled at 16 locations by the drill ship "JOIDES Resolution" over a 122-day period. The main objectives of the exploration program were (i) to assess suitable drilling technologies for future exploration and (ii) to obtain accurate temperature profiles of the formation.

Figure 4-2 shows the dimensions of the two-dimensional axi-symmetric model with the boundary conditions. The seafloor was 1,002 m below the sea surface and the depth of the well was 404 m from the seafloor. The depth of the formation in the model was set to 430 m from the seafloor. The methane hydrate-bearing interval (i.e., 277 m-339 m) was overlaid by a clayey layer (0 m-277 m) and was underlain by a sandy layer (i.e., 339 m-430 m). In order to avoid any boundary effects, the radial length of the formation was set to 50 m, which was greater than 200 times the radius of the 17 1/2-in. borehole for the conductor casing. The wellbore was comprised of a conductor casing (0 m-53 m) and a surface casing (0 m-404 m) with cement in the annuli. The outer diameter of the conductor was 0.340 m (13 3/8-in.) which was placed in a 0.445 m (17 1/2-in.) diameter borehole. The diameter of the surface casing was 0.244 m (9 5/8-in.) and it was placed in a 0.311 m (12 1/4-in.) diameter borehole. The wall thicknesses of the conductor and surface casing were 0.00965 m and 0.0100 m, respectively. A constant formation/water pressure boundary was applied on the outer radial boundary of the model.

A finite element code, ABAQUS, was used for the simulations. The model was discretized into eight-node quadratic-displacement elements (casing and cement) and eight-node quadratic-displacement bilinear-pore pressure elements (formation). In total, the model was discretized into 37,051 elements and 112,250 nodes. The spatially-varying mesh size of the elements (Figure 4-3)

was designed by Xu (2014). The vertical mesh size of the methane hydrate-bearing interval was set to be finer (0.400 m) than that of the overburden and underburden layer (1.17 m). The radial mesh size of the formation was gradually varied from fine mesh near the symmetric axis (2.32 mm) to coarse mesh at the outer radial boundary of the model (4.72 m).
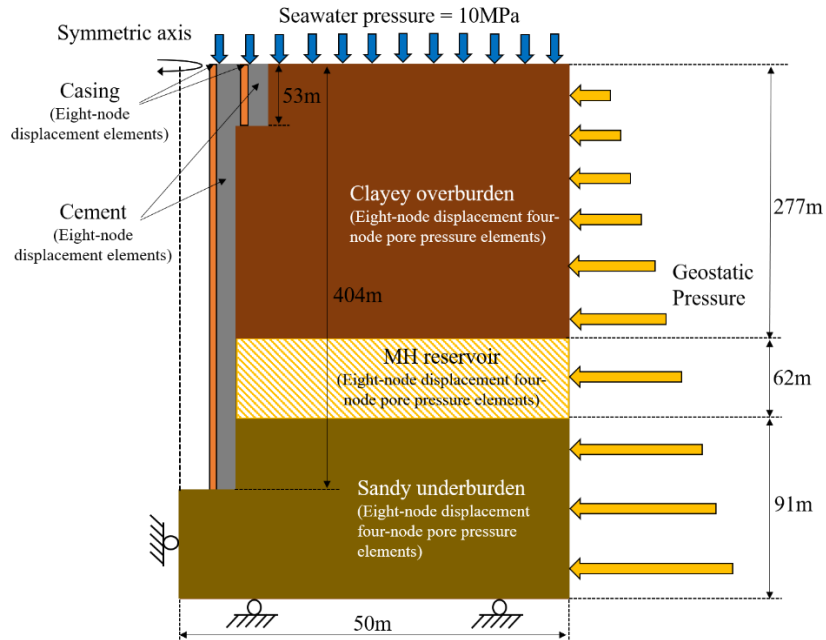
Figure 4-2 Geometry of the 2D axi-symmetric finite element model [after Xu (2014)].
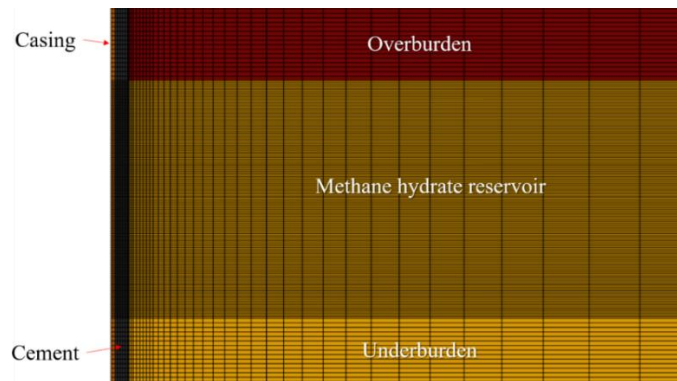
Figure 4-3 Mesh of the 2D axi-symmetric model around the wellbore and reservoir layer [after Xu (2014)].

4.2.2. Constitutive models

Methane hydrate critical state (MHCS) model (Uchida et al. 2012) was employed to simulate the behavior of the formation. The MHCS model is selected for the modelling of the formation behaviour because it is capable of simulating the enhancement of stiffness, strength and dilation of the formation due to the presence of methane hydrate in the soil pores (Miyazaki et al. 2007;

Masui et al. 2007; Masui et al. 2005). Also, in order to estimate formation damage during well construction process, it is critical to use a constitutive model which can simulate the plastic strain development of formation accurately. As the strength of the MHCS model is the accurate computation of plastic volumetric deformation of methane hydrate-bearing soil, the MHCS model is chosen to model the formation behaviour in this study. The subloading surface (Hashiguchi 1989) is incorporated to facilitate a smooth transition from the elastic to plastic behaviour. The model parameters of the MHCS model were calibrated against the triaxial test data on the core samples recovered from the Nankai Trough (Nishio et al. 2011; Yoneda et al. 2015).

Table 4-1 Calibrated MHCS model parameters for the formation.

	Overburden clay	Methane hydrate reservoir	Underburden sand
Depth (m)	0~277	277~339	339~430
Saturated bulk density (kg/m^3)	1750	1750~2000	2000
Initial void ratio	1.31	1.31~0.717	0.717
Gradient of compression line, λ	0.18	0.10	0.10
Gradient of swelling line, κ	0.03	0.02	0.02
Critical state frictional constant, M	1.30	1.37	1.37
Poisson's ratio, ν	0.25	0.35	0.35
Subsurface constant, U	15	8	8
Stiffness enhancement constant, m_2	0	200	0
Hydrate degradation constant, m_1	0	2.0	0
Dilation enhancement constant, A	0	20	0
Dilation enhancement constant, B	0	1.4	0
Cohesion enhancement constant, C	0	0.5	0
Cohesion enhancement constant, D	0	1.4	0

The values of the bulk density, initial void ratio and critical state frictional constant (i.e., internal friction angle) are taken from the literature (Yoneda et al. 2015; Suzuki et al. 2015; Nishio et al. 2009), whilst the values of the other parameters are calibrated to match the experimental results. For example, the initial slope of the deviator stress-axial strain curve is matched by adjusting the value of κ; while the magnitude of plastic strains (i.e., strain hardening/softening and dilation/compaction) is controlled by adjusting the value of λ. The rate of transition from elastic to plastic deformations is adjusted by changing the value of U. Typical values of Poisson's ratio for clay and sand are assumed. After matching the clay and sand with zero hydrate saturation data, the values of m_1, m_2, A, B, C and D are adjusted from the values provided in Uchida (2012) to match the computed results for the sand with non-zero hydrate saturation values with the experimental data. The match is judged visually and no optimisations of the parameter values (e.g., least square method) are carried out. The calibration results are demonstrated in Figure 4-4.

The calibration error for the excess pore pressure of the clayey overburden (Figure 4-4b) at the depth of 115.2 m and 240.1 m seems relatively large at large axial strain levels. However, this might be due to the poor quality of the samples taken at depths below 40 m as Nishio et al. (2011) pointed out in his paper. The calibrated parameters for the clayey overburden layer, methane hydrate reservoir and sandy underburden layer are shown in Table 4-1. The density and void ratio of the formation were determined from the logging data given in Suzuki et al. (2015). The hydrate saturation and permeability distributions were also obtained from the logging data (Figure 4-5). Details of the MHCS model and its parameters are provided in the Appendix of this paper.
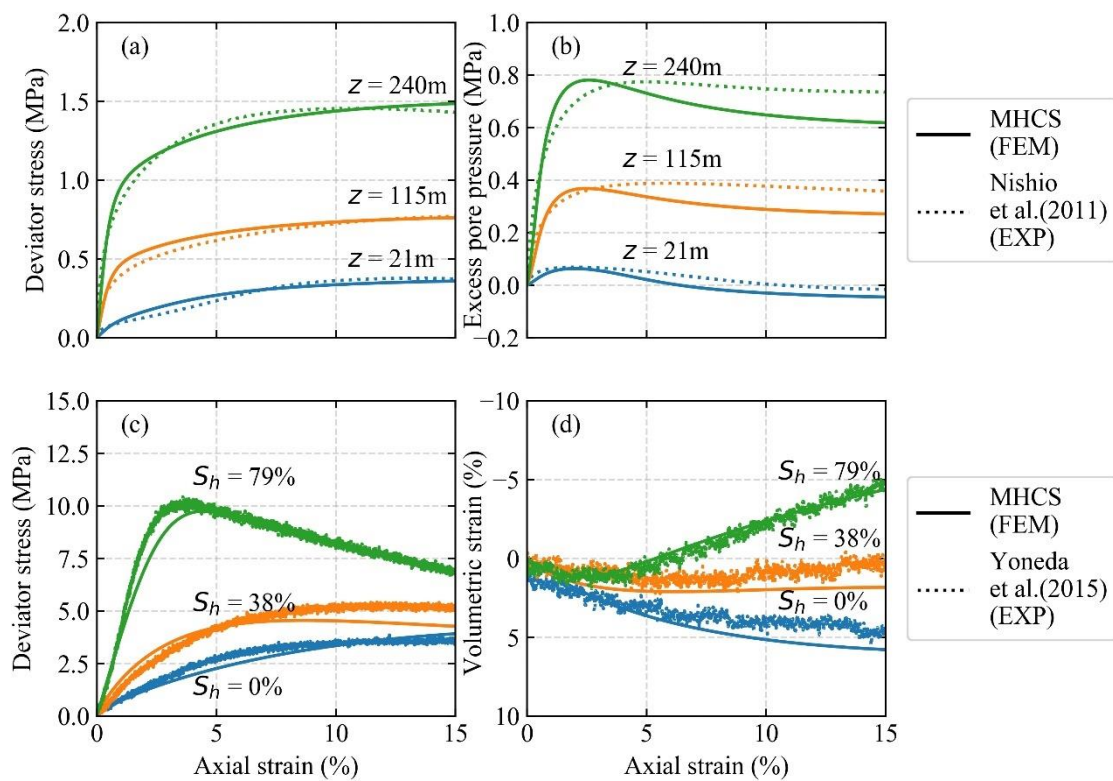
Figure 4-4: Calibration result of the MHCS model: (a) deviatoric stress vs. axial strain(clay); (b) excess pore pressure vs. axial strain (clay); (c) deviatoric stress vs. axial strain (sand); (d) volumetric strain vs. axial strain (sand).

The casings and cement were assumed to be isotropic linear elastic materials. The Young's modulus and Poisson's ratio of the casings are set to 200 GPa and 0.27, respectively. For the cement, the model parameters were varied with time during the hardening stage. The transition from slurry to hardened cement was modeled by linearly changing the Young's modulus and Poisson's ratio with time. The Young's modulus and Poisson's ratio for the slurry cement were 0.131 GPa and 0.49, while they were 3.81 GPa and 0.21 for the hardened state. The densities of

the casing and cement were set to 8000 kg/m^3 and 1370 kg/m^3, respectively.
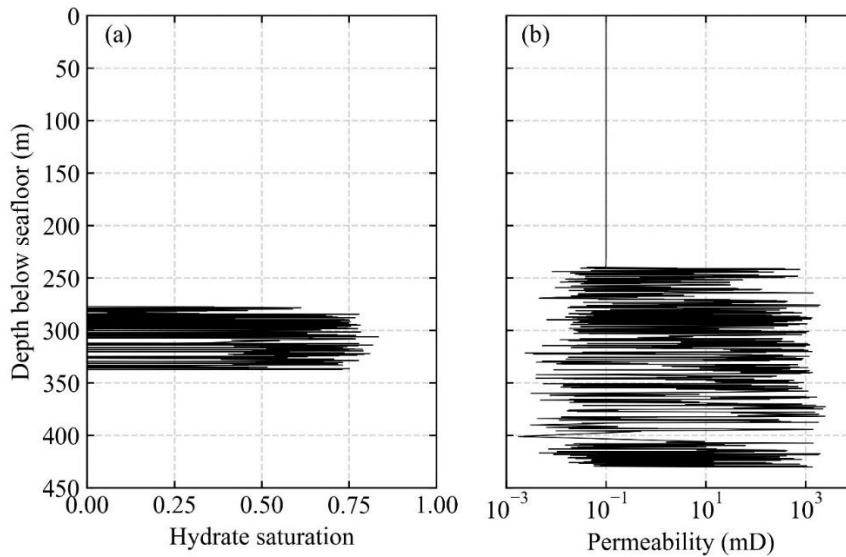
Figure 4-5: Distributions of (a) hydrate saturation and (b) permeability in the formation.

Table 4-2 The modeled construction stages.

	Construction activity	Duration (hour)
1.	Drilling (17 1/2-in.)	14.4
2.	Casing hanging (13 3/8-in.)	Immediate
3.	Cementing	Immediate
4.	Cement hardening/shrinkage	40.8
5.	Casing landing (13 3/8-in.)	Immediate
6.	Drilling (12 1/4-in.)	30.2
7.	Casing hanging (9 5/8-in.)	Immediate
8.	Cementing	Immediate
9.	Cement hardening/shrinkage	40.8
10.	Casing landing (9 5/8-in.)	Immediate

4.2.3. Construction processes of the wellbore

The construction process of the A1-E1 well was modelled in ten separate stages. The schematic diagrams of the construction stages are shown in Figure 4-6. Table 4-2 illustrates the modeled construction stages and their durations. It starts from (i) drilling, followed by (ii) casing hanging, (iii) cementing, (iv) cement hardening/shrinkage and finishes with (v) casing landing. These five stages were applied first for the conductor casing placement and then repeated for the surface casing placement. It is noted that hydrate dissociation or reformation was not simulated in this study as the pressure and temperature conditions of the A1-E1 well was maintained during well construction process by using in situ seawater as drilling fluid. Also, any thermal stress development in the formation was not considered for the same reason. The details of each

construction stage are described below.
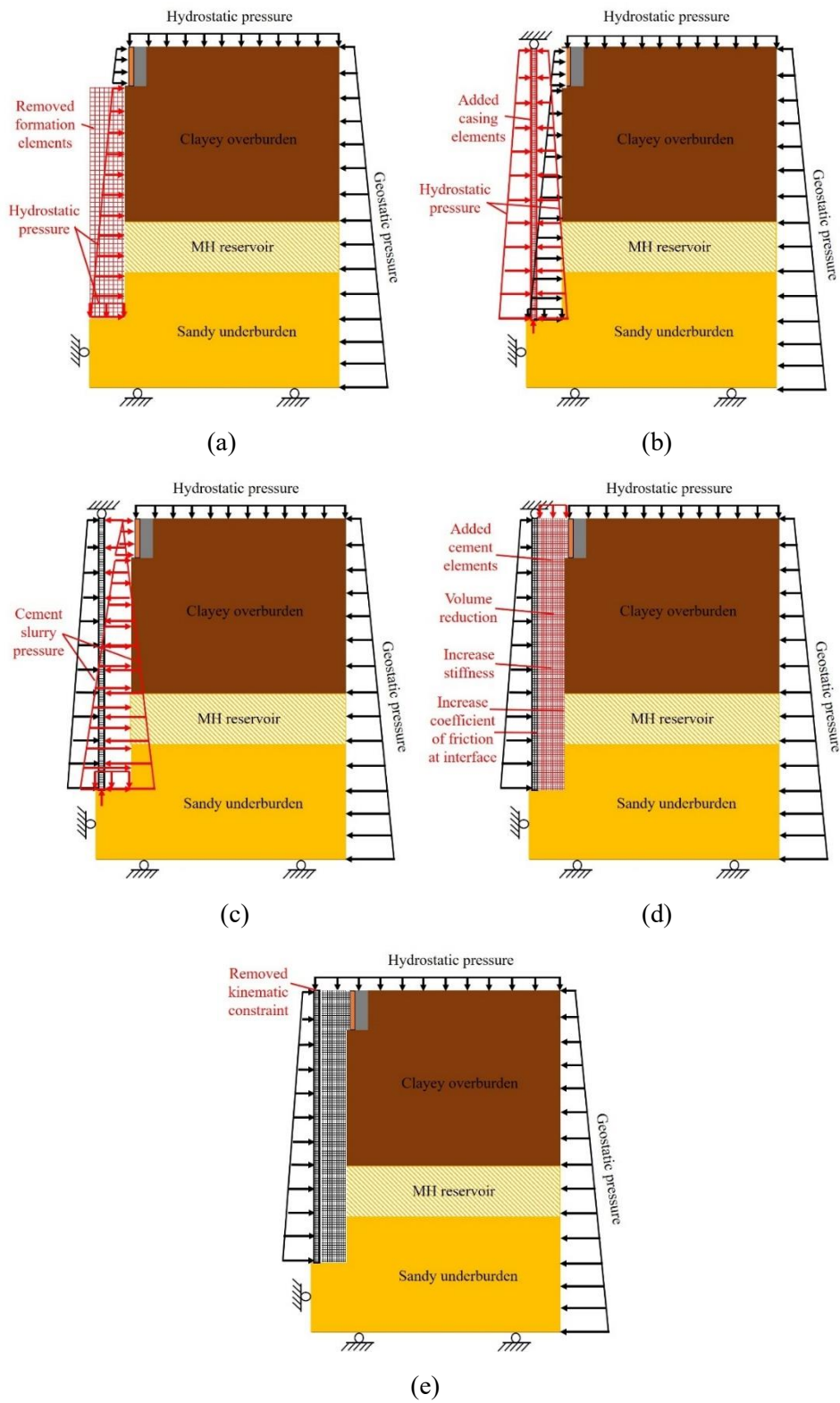
Figure 4-6 The simulated construction processes of wellbore: (a) drilling; (b) casing hanging; (c) cementing; (d) cement hardening/shrinkage; (e) casing landing.

(i) Drilling

The drilling process was modelled by removing the formation elements located inside the borehole. Upon the removal of the elements, the forces on the nodes of the neighboring elements along the borehole were linearly decreased with time from the values before the element removal to zero. The hydrostatic pore fluid pressure boundary condition was specified on the nodes of the borehole surface to model the drilling with seawater, which was actually performed for the A1-E1 well. Also, hydrostatic surface pressure boundary condition was implemented on the surface of the borehole. Figure 4-6a shows the modelling process of the drilling stage.

The load due to weight on bit (WOB) at the bottom of the borehole was not considered in this study by assuming that WOB was not significant during the drilling of the unconsolidated formation. This assumption could be validated by the speed of drilling which was 197 ft/h (60 m/h) for the overburden and underburden layer and 66 ft/h (20 m/h) for the methane hydrate-bearing layer (Takahashi & Tsuji 2005). Such a high drilling speed indicates the ease of drilling the unconsolidated formation. Also, the nozzle hydraulic jet during drilling and potential shaft friction between the drilling string and borehole wall were not considered. Thus, results of the simulation would indicate a lower-bound estimate for the disturbance of the formation during drilling.

(ii) Casing hanging

The casing elements, which had been deactivated at the start of the simulation, were activated in this stage. Zero vertical displacement boundary condition was enforced at the top nodes of the casing to simulate the hanging operation. Hydrostatic surface pressure boundary condition was applied on the surface of the casing. The hydrostatic surface pressure and pore pressure boundary condition on the borehole surface and nodes were maintained in this stage. The details of the casing hanging stage are illustrated in Figure 4-6b.

(iii) Cementing

To simulate the cementing stage, the hydrostatic surface pressure boundary condition on the casing outer surface and borehole surface was replaced by a new surface pressure boundary condition whose magnitude corresponded to the density of the cement slurry. The density of cement slurry employed for the A1-E1 well was 1370 kg/m^3 (Takahashi & Tsuji 2005). The hydrostatic surface pressure boundary condition was maintained on the inner surface of the casing to simulate the pressure from the drilling fluid (i.e., seawater), whereas the hydrostatic pore pressure boundary condition on the borehole surface was removed (i.e., pore pressure boundary

condition was left unspecified). Figure 4-6c depicts the boundary conditions of the cementing stage.

(iv) Cement hardening and shrinkage

The cement elements, which had been deactivated at the start of the simulation, were activated in the annulus and the surface interaction with the casing and formation were initiated. All the surface pressure boundary conditions in the wellbore were removed except for the hydrostatic surface pressure boundary condition on the inner surface of the casing.

To simulate cement hardening, the values of Young's modulus and Poisson's ratio were linearly varied with time from those of the slurry (0.131 GPa and 0.49) to those of the hardened cement (3.81 GPa and 0.21). In addition, the interface friction angle was linearly increased from 0º to 30º, which is an average friction angle of the cement interface to the casing and soil (Kakumoto et al. 2012; Yoneda et al. 2014). The interface friction stress was computed by the Coulomb friction model. To model cement shrinkage, the volume of the cement was linearly decreased with time through fictitious thermal contraction. Due to the simultaneous development of the cement interface friction and shrinkage, the compressive vertical stress in the cement decreases as the cement column was restrained from displacing downward.

The interface pressure was calculated by the penalty method with an augmentation iteration scheme (i.e., augmented Lagrange method). In this method, contact pressure is calculated by multiplying surface penetration distance by the stiffness of representative underlining elements. The contact pressure is then augmented through an iterative scheme to reduce the surface penetration below a limit value, which is based on a characteristic element length of the finite element model. Surface separation was allowed (i.e., zero contact stiffness in tension) even though surface separation never occurred in the simulation due to high initial contact pressure. Figure 4-6d shows the details of the cement hardening/shrinkage stage.

It is noted that the generation of cement hydration heat and resultant heat conduction was not simulated in this study. If the temperature increase due to cement hydration heat was large, methane hydrate would dissociate and the integrity of the formation would be affected. However, a cement hydration analysis in a well annulus at the Nankai Trough (Sasaki, Soga & Abuhaikal 2018) shows that the temperature increase due to cement hydration heat would be less than 0.5 ºC. As a result, the assumption of negligible cement hydration heat and no hydrate dissociation is valid for this study.

(v) Casing landing

The zero vertical displacement boundary condition at the top nodes of the casing was removed in this stage to release the casing from hanging. The hydrostatic surface pressure boundary condition on the inner surface of the casing was maintained. These procedures are illustrated in Figure 4-6e.

4.2.4. Cement volume shrinkage

Cement volume shrinkage occurs due to cement hydration process. The volumes of cement shrinkage reported in the literature varies from 0.1% to 4.5% (Goboncan & Dillenbeck 2003; Backe et al. 1998; Justnes et al. 1995; Chenevert & Shrestha 1991; Chenevert & Shrestha 1987). This large variance is not only because the cement volume shrinkage is significantly affected by the temperature and pressure conditions and the employed test method (Reddy et al. 2009), but also because the reported values often include shrinkage before the initial set of cement (i.e., shrinkage within the thickening time). In actual cementing operations, shrinkage before the initial set is usually compensated by the drop of slurry column in the annulus (Thiercelin et al. 1998; Backe et al. 1999). On the other hand, shrinkage after the initial set cannot be compensated in the same way due to the development of friction and cohesion at the cement interface to casing and formation (Chenevert & Jin 1989). Therefore, shrinkage after the initial set is the relevant parameter for the simulation. Also, due to the vertical frictional resistance, shrinkage after the initial set occurs predominantly in the radial direction (Zhou & Wojtanowicz 2000).

The shrinkage volume of a typical oil well cement after the initial set is smaller than 1% according to the laboratory cement shrinkage experiments (Reddy et al. 2009; Appleby & Wilson 1996). However, cement shrinkage in laboratory conditions may differ from that in downhole conditions where the cement is surrounded by casing and formation. A numerical simulation on cement shrinkage in the downhole condition at the Nankai Trough was conducted by Sasaki et al. (2018) and they found that the shrinkage volume of cement employed at the Nankai Trough could reach up to 0.75%. Therefore, the shrinkage volume was varied between 0 to 0.75% in the simulation.

4.2.5. Initial horizontal stress of the formation

The initial horizontal stress of the formation was calculated through the lateral earth pressure coefficient, K_0 as shown in Equation 4-2:

$$\sigma'_h = K_0 \sigma'_v \qquad (4\text{-}2)$$

where K_0 = lateral earth pressure coefficient; σ'_h = horizontal effective stress; σ'_v = vertical effective stress.

The effective stress in the equation refers to the Terzaghi effective stress, which is the total stress subtracted by pore fluid pressure ($\sigma' = \sigma - p$). Three different formulations for K_0 were used in this study. Equation 4-3 is the one frequently employed in the field of soil mechanics. This formulation takes into account the stress history of the formation on the current horizontal stress. The over-consolidation ratio (OCR) was calculated by dividing the maximum vertical effective stress experienced by the formation in the past by the current vertical effective stress. The past maximum vertical effective stress was estimated from the triaxial test data (Nishio et al. 2011; Yoneda et al. 2015) whereas the current vertical effective stress was obtained from the density data of the formation (Suzuki et al. 2015).

$$K_0 = (1 - \sin\phi')\text{OCR}^{\sin\phi'} \tag{4-3}$$

where ϕ' = internal friction angle of the formation; OCR = overconsolidation ratio, i.e., the ratio of the past maximum vertical effective stress to the current vertical effective stress.

Equation 4-4 is another formula for K_0 which is often employed in the field of rock mechanics. It calculates K_0 assuming that the formation is an elastic material.

$$K_0 = \frac{\nu}{1 - \nu} \tag{4-4}$$

where ν = Poisson's ratio of the formation.

A series of mini-frac test was performed at the Nankai Trough to estimate the minimum horizontal stress of the formation (Yamamoto et al. 2006; Yamamoto et al. 2005). The result suggested $K_0 =$ 0.40 at 310 m below seafloor, which is approaching the active pressure coefficient of the formation ($K_a = (1-\sin\phi')/(1+\sin\phi')$). It was also found through the anelastic strain recovery method that the difference between the maximum and minimum horizontal stress magnitudes would be small (Nagano et al. 2015). Accordingly, $K_0 = 0.40$ was also employed to calculate the initial horizontal stress of the formation. The three different K_0 profiles employed in this study are compared in Figure 4-7.
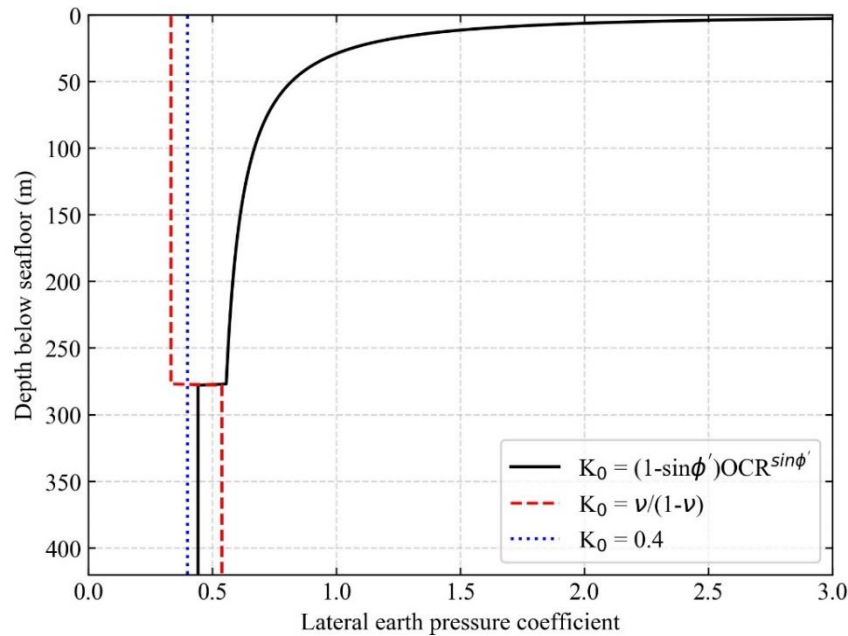
Figure 4-7 Three different distributions of the lateral earth pressure coefficient, K_0, employed to calculate the initial horizontal stress of the formation.

4.2.6. Initial conditions

The initial vertical effective stress was calculated based on the density distribution of the formation in the Nankai Trough (Suzuki et al. 2015). The initial horizontal effective stresses were assumed to have identical magnitudes. This assumption is considered to be valid for the formation in the Nankai Trough based on the anelastic strain recovery analysis on core samples (Nagano et al. 2015). The hydrostatic pore pressure was assigned as the initial pore pressure, which was calculated from the seawater density of 1027 kg/m^3. The initial porosities of the formation were determined from the in situ logging data (Suzuki et al. 2015).

4.2.7. Numerical solution scheme of the analysis

The simulation was performed by applying external load, which was induced by well construction process, as boundary conditions on the wellbore region of the model. In response to the input external load, displacement was calculated. Stress and strain were then calculated from the displacement through the constitutive model. Finally, internal load was calculated from the stress, which was then compared with the applied external load.

The solution was obtained iteratively by employing Newton's method. The convergence was considered to be satisfied if the load residual (i.e., difference between the external and internal load) at the end of an iteration in an increment was smaller than 0.5% of the time- and spatially-

85

averaged load of the entire model. If the load residual was greater than the tolerance value, another iteration was performed until the load residual was decreased below the tolerance value at all nodes in all degrees of freedom. In addition to the load convergence criterion, a displacement convergence criterion was specified such that the displacement calculated in the latest iteration (i.e., displacement correction) must be smaller than 1% of the total displacement calculated for the increment.

If the behavior of the model was found to be unstable due to material softening and/or buckling (i.e., negative stiffness), volume-proportional damping was applied to stabilize the model and to find a converged solution. The values of the damping factor were chosen in such a way that the incremental dissipated energy due to damping in an increment was smaller than 0.02% of the total strain energy of the model. Also, the cumulative dissipated energy due to damping was enforced to be smaller than 5% of the total strain energy of the model to make sure that the accuracy of the solution was not compromised due to damping.

4.3. Results and discussion

4.3.1. Effective stress and plastic strain in the formation during wellbore construction

The effective stresses, pore pressure and plastic deviatoric strain in the formation generated during the wellbore construction stages along the 12 1/4-in. dimeter borehole are presented in Figure 4-8. Positive effective stresses indicate compression using the traditional soil mechanics convention. The cement volume shrinkage was set to 0.75% while the initial horizontal stress of the formation was calculated with $K_0 = (1-\sin\phi')\text{OCR}^{\sin\phi'}$.

The formation behavior during wellbore construction was dictated by the cavity contraction/expansion mechanism around the wellbore, i.e., an increase in the radial effective stress is accompanied by a decrease in the circumferential effective stress, and vice versa. During the drilling stage, the radial effective stress at the wellbore surface decreased to zero (Figure 4-8b) because pore pressure and surface pressure are equal to each other at the hydrostatic pressure along the borehole, simulating the drilling with seawater as the drilling fluid. In the meantime, the circumferential effective stress increased according to the cavity contraction mechanism. The vertical effective stress decreased because the formation developed plastic strain during the drilling stage, causing stress redistribution around the wellbore.
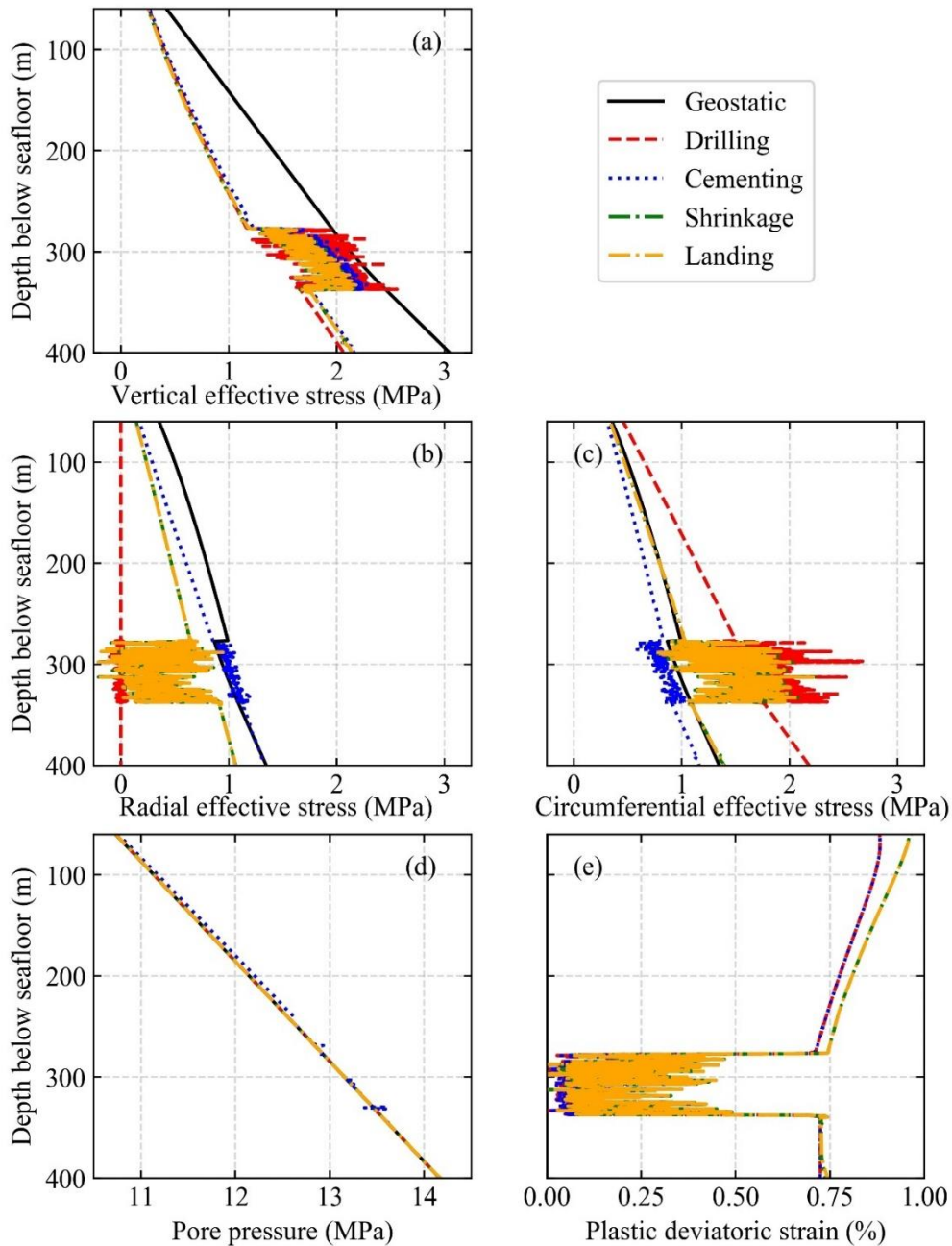
Figure 4-8: Changes in stress and strain levels of the formation along the 12 1/4-in. diameter borehole wall surface during well construction stages: (a) vertical effective stress; (b) radial effective stress; (c) circumferential effective stress; (d) pore pressure; (e) deviatoric plastic strain.

During the cementing stage, the borehole was enlarged because the pressure of the cement slurry was greater than that of seawater. As a result, the cavity expansion mechanism occurred. The radial effective stress increased while the circumferential effective stress decreased. The vertical

effective stress did not change significantly, which were consistent with the insignificant additional plastic strain development during this stage (Figure 4-8e).

During the cement hardening/shrinkage stage, the borehole contracted as the cement shrank in the radial direction, which rendered the formation to behave in the cavity contraction mechanism. At 0.75% shrinkage, the inward radial displacement of the borehole wall was calculated less than 1mm. Even at such small displacement the change in the radial and circumferential effective stress was approximately 0.2 MPa in the overburden/underburden and up to 1 MPa in the hydrate-bearing layer.

During the casing landing stage, the stresses along the borehole surface did not change substantially because the weight of the casing was primarily supported at the bottom of the borehole.

The pore pressure did not change significantly throughout the whole wellbore construction stages, even though small excess pore pressure was generated during the cementing stage. The majority of the plastic deviatoric strain was developed during the drilling stage, whereas the cement shrinkage stage developed minor additional plastic deformation. The oscillatory responses in the depths between 277 m and 339 m were due to steep changes in the formation mechanical properties arising from the highly heterogeneous distribution of hydrate saturation as shown in Figure 4-5a. Due to the bonding effect of methane hydrate, the formation in this interval can sustain tensile stress.

4.3.2.   Zone of stress disturbance in the formation

Figure 4-9, 4-10 and 4-11 show the effective stress contours at the end of wellbore construction near the 12 1/4-in. diameter borehole computed with different cement shrinkage volumes and initial horizontal stresses. The horizontal axes are denoted by the normalized radial distance, which was calculated by dividing the radius from the axi-symmetric axis by the radius of the 12 1/4-in. diameter borehole. For example, the normalized radial distance of seven corresponds to 1.09 m or 42.9 in. from the centre of the wellbore.
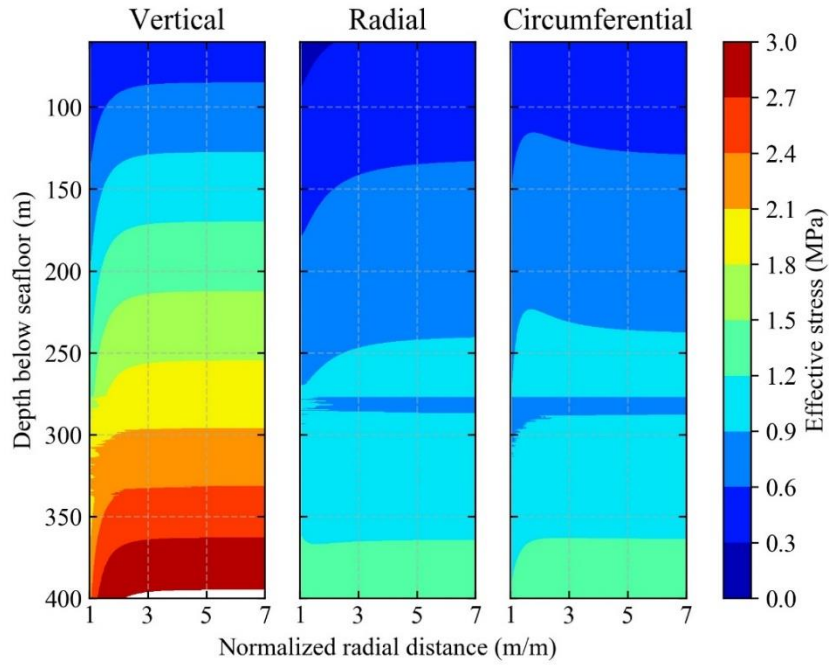
(a)
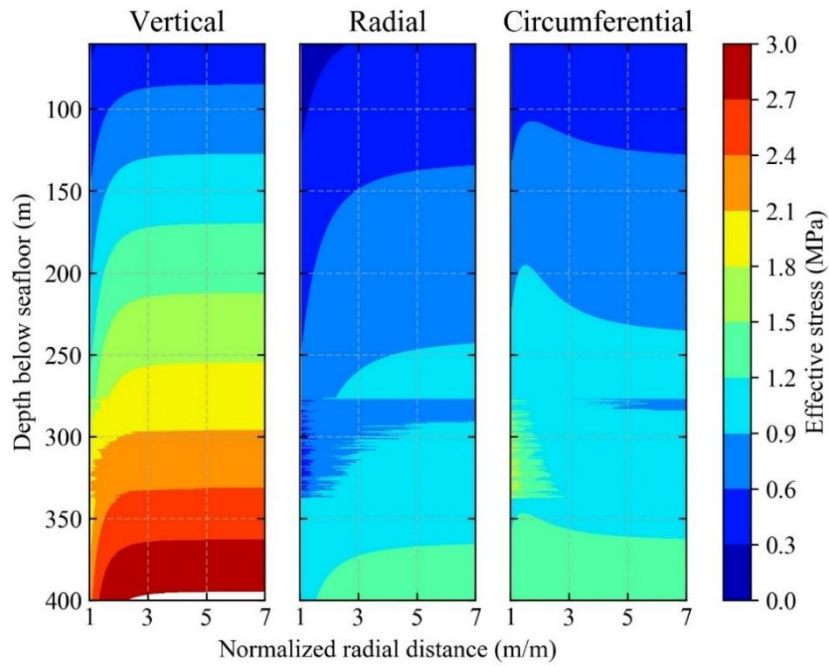
(b)

Figure 4-9 Effective stress distributions near the borehole: (a) $K_0 = (1-\sin\phi')\text{OCR}^{\sin\phi'}$, cement shrinkage = 0%; (b) $K_0 = (1-\sin\phi')\text{OCR}^{\sin\phi'}$, cement shrinkage = 0.75%.
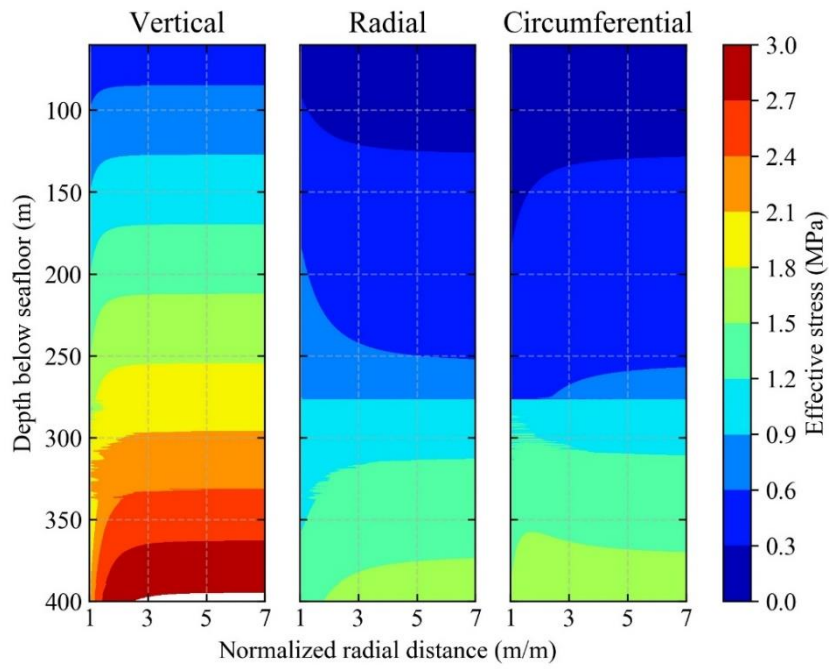
(a)
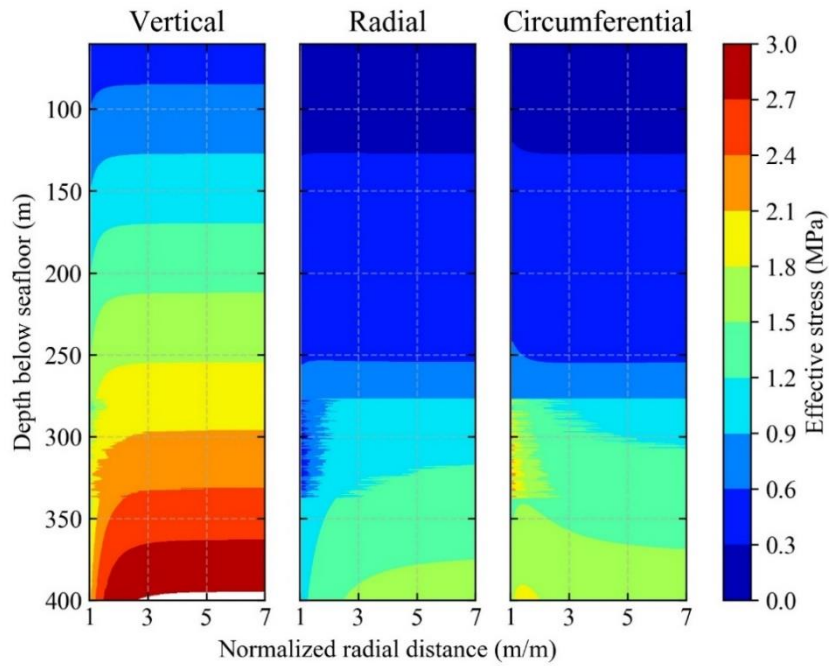
(b)

Figure 4-10 Effective stress distributions near the borehole: (a) $K_0 = v/(1-v)$, cement shrinkage = 0%; (b) $K_0 = v/(1-v)$, cement shrinkage = 0.75%.
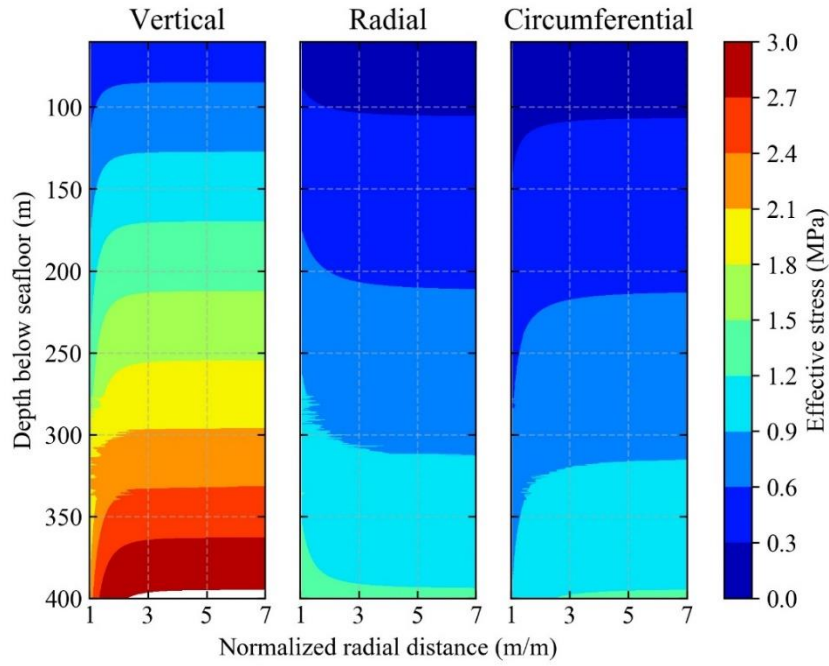
(a)
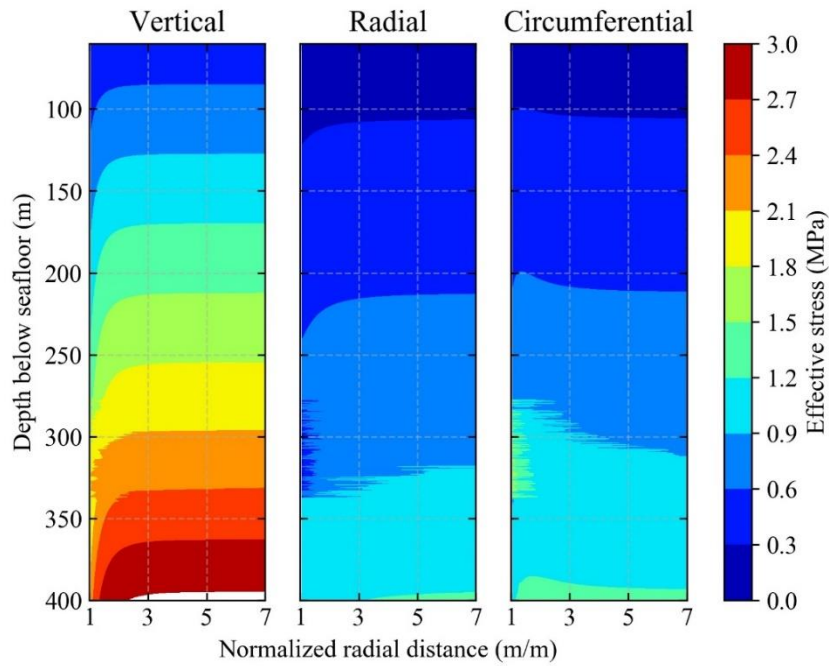
(b)

Figure 4-11 Effective stress distributions near the borehole: (a) K_0 = 0.40, cement shrinkage = 0%; (b) K_0 = 0.40, cement shrinkage = 0.75%.

Figure 4-9a and b show the effective stress contours with the cement shrinkage of 0% and 0.75%, respectively, with the initial horizontal stress calculated by $K_0 = (1\text{-}\sin\phi')OCR^{\sin\phi'}$. Although the vertical effective stress recovered to the geostatic levels within the normalized radial distance of two, the disturbance to the radial and circumferential stresses propagated much further. With the cement shrinkage of 0%, the horizontal stresses were affected up to the normalized radial distance of three. In the clayey overburden layer, the radial effective stress around the borehole decreased while the circumferential effective stress increased with respect to their geostatic levels. The decrease in the vertical effective stress near the borehole was due to the development of plastic strain which caused the redistribution of vertical effective stress levels in the formation.

When the cement shrinkage was set to 0.75%, the zone of horizontal stress disturbance did not change at the normalized radial distance of three but the magnitudes increased. The stress disturbance in the reservoir and sandy underburden layer was less pronounced than that in the clayey overburden layer. This was because in these layers the initial horizontal stress levels were similar to the cement slurry pressure levels, which recovered to the geostatic stress levels during the cementing stage after they were disturbed by the drilling. Also, the spiky stress response in the methane hydrate reservoir (i.e., 277 m to 339 m) became apparent during the cement shrinkage stage. This is caused by the difference in the stiffness values between the high and low hydrate saturation layers. A greater stress disturbance is incurred to the stiffer layer (i.e., high hydrate saturation layer) by the cement shrinkage-induced cylindrical cavity contraction of the wellbore.

Figure 4-10a and b show the effective stress contours with the initial horizontal stress calculated by $K_0 = \nu/(1\text{-}\nu)$, and with the cement shrinkage of 0% and 0.75%, respectively. Both the area and the magnitude of the vertical effective stress decrease in the clayey overburden layer were smaller than those calculated in the case of $K_0 = (1\text{-}\sin\phi')OCR^{\sin\phi'}$. This was because the initial horizontal stresses calculated by $K_0 = \nu/(1\text{-}\nu)$ were smaller than those by $K_0 = (1\text{-}\sin\phi')OCR^{\sin\phi'}$, resulting in smaller stress changes and hence less plastic deformation during drilling. In fact, in the reservoir and sandy underburden layers, where $K_0 = \nu/(1\text{-}\nu)$ resulted in larger initial horizontal stress levels than $K_0 = (1\text{-}\sin\phi')OCR^{\sin\phi'}$, the area and magnitude of the vertical effective stress decrease were greater than those calculated under $K_0 = (1\text{-}\sin\phi')OCR^{\sin\phi'}$. The disturbance in the radial and circumferential effective stresses was also affected by the initial horizontal stress levels. When the initial horizontal stresses in the overburden layer were calculated by $K_0 = (1\text{-}\sin\phi')OCR^{\sin\phi'}$, the radial effective stress decreased while the circumferential effective stress increased from their geostatic levels at the end of the entire construction processes. When $K_0 = \nu/(1\text{-}\nu)$ was employed, the opposite response was obtained, i.e., the radial effective stress increased while the circumferential effective stress decreased around the borehole. This was because the initial

horizontal stresses calculated by $K_0 = (1-\sin\phi')OCR^{\sin\phi'}$ were greater than the cement slurry pressure, leading to the cavity contraction of the wellbore after the installation of casing and cement, whereas the initial horizontal stress levels computed by $K_0 = v/(1-v)$ were smaller than the cement slurry pressure, resulting in the cavity expansion of the wellbore.

Figure 4-11a and b show the cases where the initial horizontal stresses were calculated by $K_0 = 0.40$ with the cement shrinkage of 0% and 0.75%, respectively. The area and the magnitude of the vertical effective stress decrease were comparable to those computed in the other two cases, while the disturbance in the radial and circumferential effective stresses was smaller. This was because the initial horizontal stresses calculated by $K_0 = 0.40$ were comparable to the cement slurry pressure. The horizontal stress levels, which were disturbed in the drilling stage, recovered to the geostatic levels during the cementing stage. In the methane hydrate layer, the horizontal stresses were significantly disturbed as was the case for the other initial horizontal stress cases.
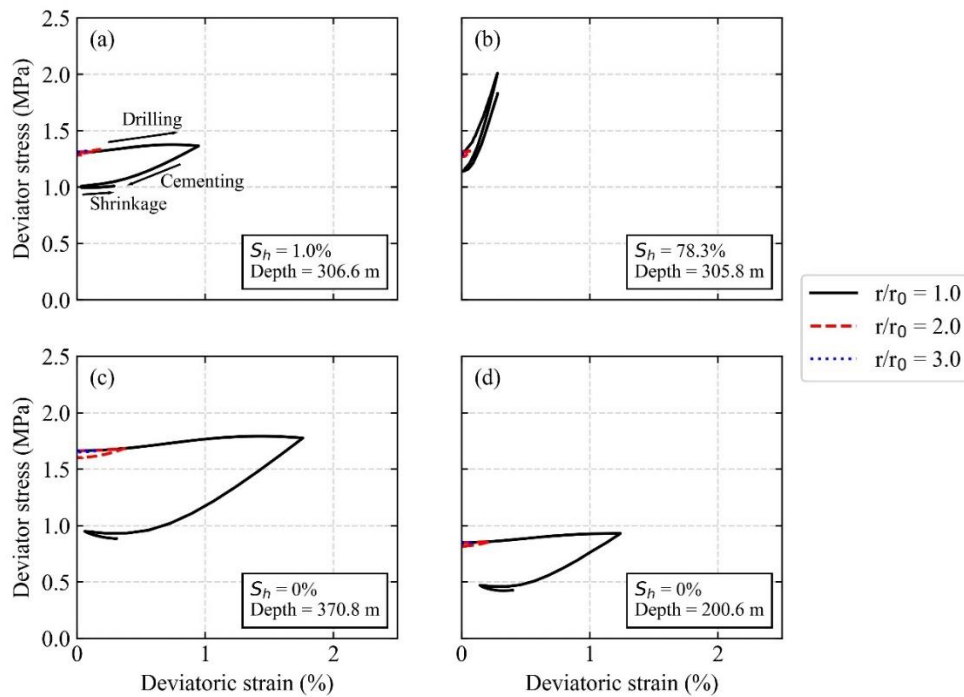
Figure 4-12 Deviatoric stress-strain changes in the formation (MHCS model, $K_0 = 0.4$, cement shrinkage = 0.75%): (a) low hydrate saturation layer; (b) high hydrate saturation layer; (c) underburden sand; (d) overburden clay.
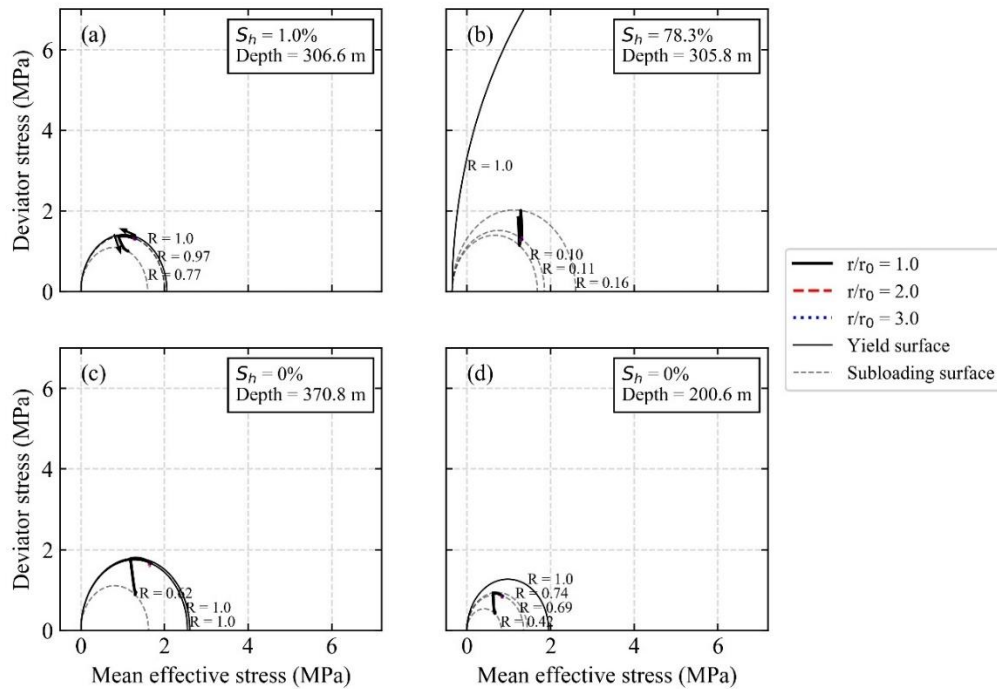
Figure 4-13 Stress paths in the formation (MHCS model, $K_0 = 0.4$, cement shrinkage = 0.75%): (a) low hydrate saturation layer; (b) high hydrate saturation layer; (c) underburden sand; (d) overburden clay.

Figure 4-12 and Figure 4-13 show the deviator stress-strain and deviator stress-mean effective stress changes (i.e., stress paths) of formation near the wellbore during well construction processes in the case of $K_0 = 0.4$ and cement shrinkage volume = 0.75%. The following four formation sections were selected: (i) methane hydrate reservoir layer with low hydrate saturation value ($S_h = 1.0\%$), (ii) methane hydrate reservoir layer with high hydrate saturation value ($S_h = 78.3\%$), (iii) underburden sand layer and (iv) overburden clay layer.

The changes in the deviator stress levels of the formation near the wellbore are found to be governed by the cement shrinkage stage, as the methane hydrate layer with a high hydrate saturation value (Figure 4-12b) exhibits stiffer response than the other layers with low or zero hydrate saturation values (Figure 4-12a, c and d) during the cement shrinkage stage, inducing the concentration of deviator stress in the reservoir layer with a high hydrate saturation value. This is because the reservoir layer with a high hydrate saturation value remains elastic during the entire well construction processes. In fact, the stress path of the high hydrate saturation layer (Figure 4-13b) shows that the stress level remains afar from the yield surface, whereas in the low or zero hydrate saturation layers (Figure 4-13a, c and d), the stress path is initially on or near the yield surface, which then approaches the yield surface during the drilling stage while accumulating

some plastic strains. The plastic strain development causes the vertical effective stress to decrease, which hinders the development of deviator stress in the low or zero hydrate saturation layers. The R values shown in Figure 4-13 indicate the ratio of the current stress to yield stress levels.

Also, it is found that changes in the deviator and mean effective stress levels due to the well construction processes are limited within the normalized radial distance of three, i.e. 0.467 m or 18.4 in. from the centre of the wellbore. Hence, the disturbance of these stresses due to well construction processes, which is primarily caused by the cylindrical cavity expansion/contraction of the wellbore, occurs only in limited areas just near the wellbore.

4.3.3. Effect of formation constitutive models

In order to validate the simulation results with the MHCS model, the simulation case for $K_0 = 0.4$ and cement shrinkage = 0.75% is re-run with the Mohr-Coulomb model with enhancement for soil strength, stiffness and dilation due to methane hydrate. ABAQUS' inbuilt Mohr-Coulomb model is used and its parameter values are correlated with hydrate saturation, to create a methane hydrate Mohr-Coulomb (MHMC) model.

The MHMC model was calibrated against the same experimental dataset that are used for the calibration of the MHCS model, and the calibration result is shown in Figure 4-14. The values of the model parameters determined through the calibration are listed in Table 4-3. It is evident that the MHCS model is a much simpler model than the MHCS model as the number of parameters are only five compared to eleven for the MHCS model. The bulk density and void ratio distributions in the formation are kept identical between the simulation cases with the MHCS and MHMC models. The well construction simulation results with the MHMC model are shown in Figure 4-15 and Figure 4-16, which are respectively deviatoric stress-strain changes and stress paths.

Table 4-3 The calibrated parameter values of the MHMC model.

	Overburden clay	Methane hydrate reservoir	Underburden sand
Young's modulus	$3(1-2\nu)(1+1.31)p'/0.03$	$360S_h +43.9$	$3(1-2\nu)(1+0.717)p'/0.02$
Poisson's ratio	0.25	0.30	0.30
Friction angle (°)	23	26	26
Dilation angle (°)	0.1	$12.6S_h$	0.1
Cohesion (MPa)	0.2	$2.54S_h +0.3$	0.3

NB: ν = Poisson's ratio and p' = mean effective stress.
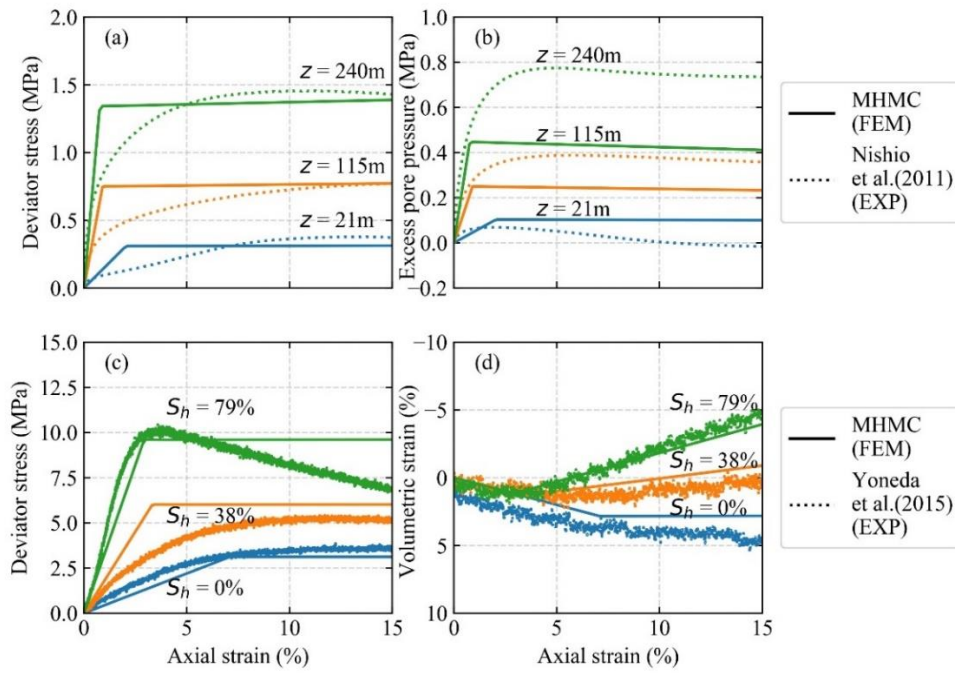
Figure 4-14 The calibration result of the methane hydrate Mohr-Coulomb (MHMC) model: (a) deviator stress-axial strain (clay); (b) excess pore pressure-axial strain (clay); (c) deviator stress-axial strain (sand); (d) volumetric strain-axial strain (sand).
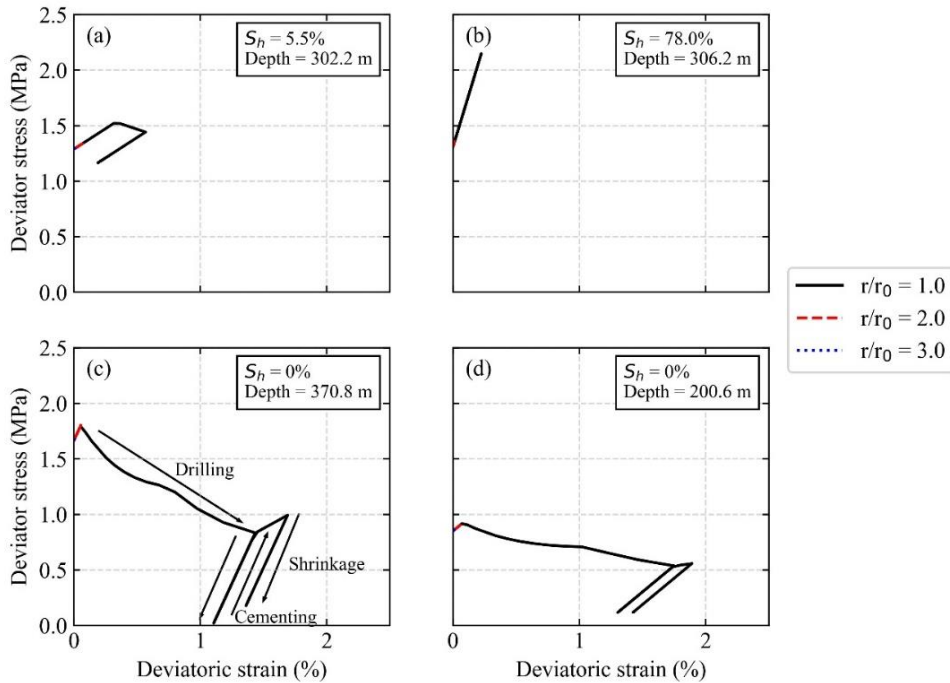
Figure 4-15 Deviatoric stress-strain changes in the formation (MHMC model, $K_0 = 0.4$, cement shrinkage = 0.75%): (a) low hydrate saturation layer; (b) high hydrate saturation layer; (c) underburden sand; (d) overburden clay.
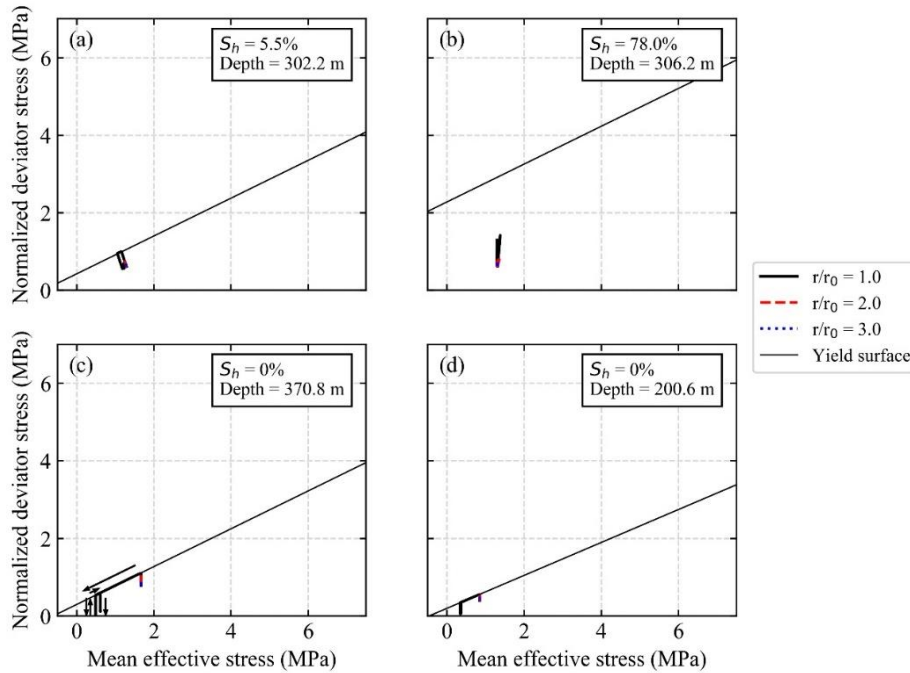
Figure 4-16 Stress paths in the formation (MHMC model, $K_0 = 0.4$, cement shrinkage = 0.75%): (a) low hydrate saturation layer; (b) high hydrate saturation layer; (c) underburden sand; (d) overburden clay. NB: deviator stress is normalised to take into account the Lode angle.

It is found that the deviator stress concentration in the high hydrate saturation reservoir layer is even more enhanced by the use of the MHMC model, as the high hydrate saturation layer remains fully elastic during the construction processes (Figure 4-15b and Figure 4-16b) whilst the other layers with low to zero hydrate saturation layers go through yielding and plastic softening. The magnitudes of accumulated plastic deviatoric strain are, however, on the same order with those calculated with the MHCS model (< 2%) (see Figure 4-12), which is relatively small to cause formation failure. This is consistent with the field observation at the Nankai Trough that the borehole after the drilling stage was stable, even though the drilling was carried out with seawater and no special stabilisation measure was implemented to protect the borehole. Therefore, the simulation results with the MHMC model validate those with the MHCS model in terms of the borehole behaviour during the construction processes.
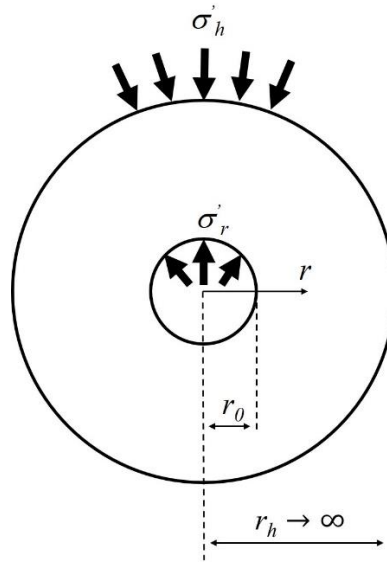
Figure 4-17 Cavity expansion/contraction of an elastic cylinder.

4.3.4. Elastic cylindrical cavity expansion/contraction analysis

In order to analyse the deviator stress changes calculated by the finite element analysis along the wellbore surface during well construction processes in the previous sections, an elastic cylindrical cavity expansion/contraction analysis is carried out. Assuming that the formation is originally in the isotropic horizontal stress state, the changes in the radial and circumferential effective stresses in response to cylindrical cavity expansion/contraction as shown in Figure 4-17 is calculated by Equation 4-5:

$$\sigma'_\theta = \sigma'_h - (\sigma'_r - \sigma'_h)\left(\frac{r_0}{r}\right)^2 \qquad (4\text{-}5)$$

where σ'_r = radial effective stress, σ'_θ = circumferential effective stress, σ'_h = horizontal (either radial or circumferential) effective stress in the geostatic state, r_0 = radius of the wellbore (=0.156 m) and r = radius from the centre of the wellbore. The corresponding deviator stress is calculated by Equation 4-6:

$$q = \sqrt{\frac{3}{2}}\sqrt{(\sigma'_r - p')^2 + (\sigma'_\theta - p')^2 + (\sigma'_v - p')^2} \qquad (4\text{-}6)$$

where σ'_v = vertical effective stress and p' = mean effective stress (= $(\sigma'_v + \sigma'_r + \sigma'_\theta)/3$). The change in the radial effective stress during cement shrinkage can be calculated by Equation

4-7:

$$\sigma'_r = \frac{2G}{r_0} \Delta r_{shrink} + \sigma'_h \qquad (4\text{-}7)$$

where G = shear modulus of the formation (calculated by Equation 2-5 in Chapter 2) and Δr_{shrink} = radial displacement of the wellbore perimeter during cement shrinkage, which is calculated by Equation 4-8:

$$\Delta r_{shrink} = \sqrt{(r_0^2 - r_c^2)\left(\frac{100 - \Delta V_{cement}}{100}\right) + r_c^2} - r_0 \qquad (4\text{-}8)$$

where r_c = radius of the casing (= 0.122 m) and ΔV_{cement} = cement shrinkage volume in percent (= 0.75%). This equation assumes that cement shrinkage occurs only in the radial direction and there is no shrinkage in the vertical direction.

Figure 4-18 shows deviator stress values of the formation, which are calculated from the elastic cylindrical cavity expansion/contraction theory described above, along the wellbore surface (i.e., $r = r_0$) at different depths and hydrate saturation values during well construction processes. The formation parameter values listed in Table 4-1 are used to calculate the values of initial vertical and horizontal effective stresses and shear modulus of the formation at different depths and hydrate saturation values. It is found that the deviator stress levels increase by more than 50% in all depth and hydrate saturation cases after the drilling stage but they decrease to approximately the initial geostatic deviator stress values after the cementing stage. The cement shrinkage stage does not change the deviator stress levels significantly in the low or zero hydrate saturation layers (i.e., the blue, red and pink bars in the figure). However, in the high-hydrate saturation layer (i.e., the green bars), the deviator stress level increases to approximately the same level generated after the drilling stage (2 MPa). This is because of the high stiffness of the high hydrate saturation layer. As a result, the deviator stress concentration is developed in the high-hydrate saturation layer relative to the low or zero hydrate saturation layers. This is consistent with the results of the finite element analysis shown in the previous sections. Therefore, the deviator stress concentration in the high hydrate saturation layer is found to be caused by the cylindrical cavity contraction of the wellbore induced by the cement shrinkage process.
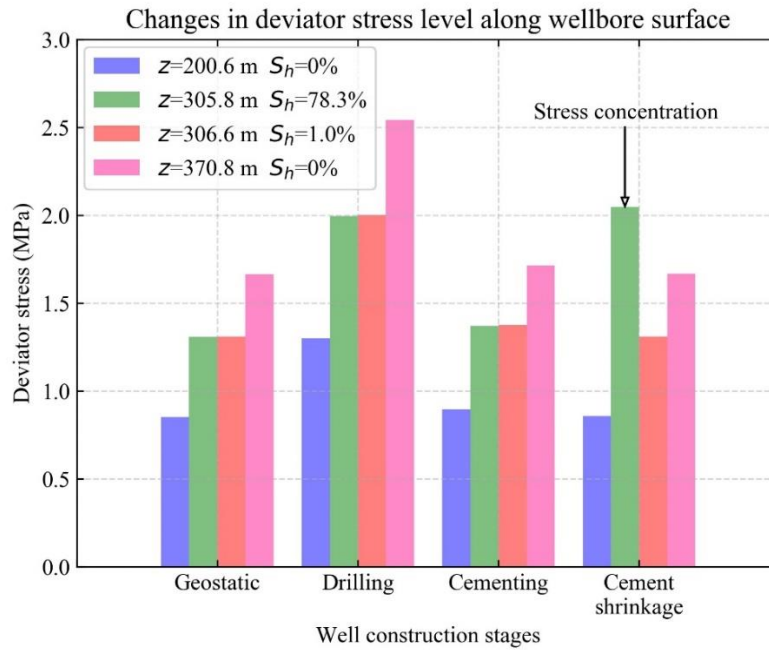
Figure 4-18 Elastic cylindrical cavity expansion/contraction analysis of the wellbore.

4.3.5. Zone of plastic deviatoric strain development in the formation

4.3.5.1. *Effect of cement volume shrinkage*

Figure 4-19 show the effect of cement shrinkage on the plastic deviatoric strain development in the formation near the 12 1/4-in. diameter borehole. Three cement volume shrinkage values (0%, 0.5% and 0.75%) are considered. The horizontal axis is the normalized radial distance, i.e., radial coordinates normalized by the radius of the 12 1/4-in. diameter borehole. The vertical coordinate covers the depths along the 12 1/4-in. diameter borehole. The initial horizontal stress was calculated by $K_0 = (1-\sin\phi')OCR^{\sin\phi'}$.

Results show that the cement shrinkage stage would have minor effects on the plastic deviatoric strain development in the formation compared to the drilling stage, as the variation of cement shrinkage volume between 0% and 0.75% only slightly increased the area and magnitude of the plastic deviatoric strain in the formation. This is in contrast with the cement shrinkage-induced stress changes in the formation described in the previous section. The stress changes were caused by the stiffness contrast between the high hydrate saturation layers (elastic) and low/zero hydrate saturation layers (plastic) induced during the drilling stage. In other words, cement shrinkage converted the stiffness contrast into stress contrast without accumulating extra plastic strain. This is why the stress state was significantly affected by cement shrinkage whereas the plastic strain development was not influenced by it. The maximum magnitude of plastic deviatoric strain was approximately 1% at 60 m below seafloor in the clayey overburden layer. A comparable

magnitude of plastic deviatoric strain was also developed in the sandy underburden layer. In the methane hydrate reservoir, however, the magnitude of plastic deviatoric strain was much smaller than in the overburden and underburden layers due to the reinforcement effect of methane hydrate.
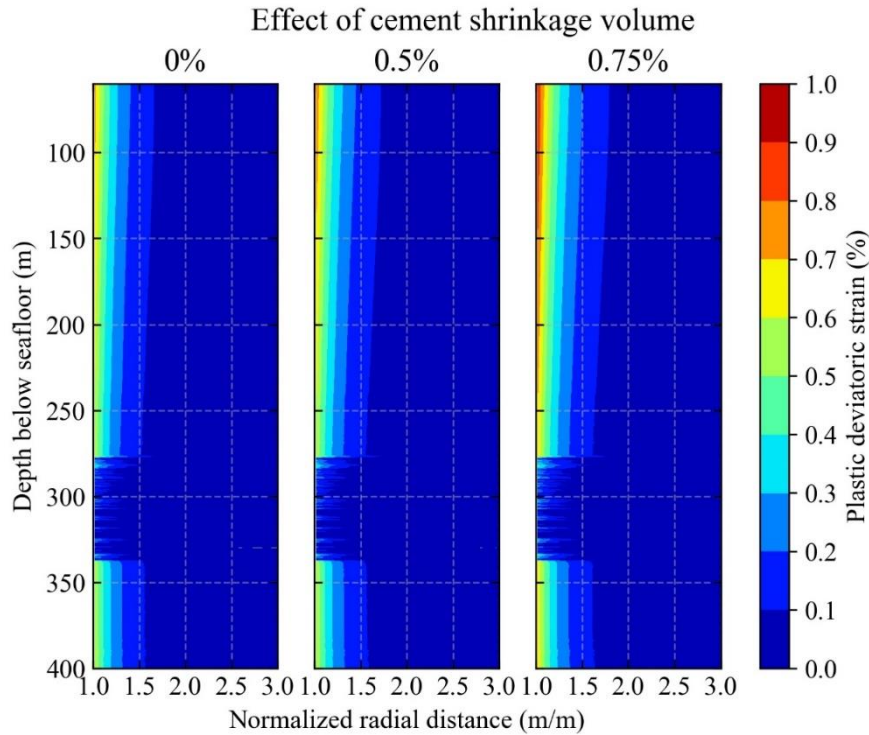
(c)

Figure 4-19 Effect of different volumes of cement shrinkage on the zone and magnitude of plastic deviatoric strain in the formation near the 12 1/4-in. diameter borehole.

The trend of plastic deviatoric strain development shown in Figure 4-19 could be related to the borehole radius measurement data obtained from wireline logging in the A1-W well (Figure 4-1b). The radial extent of the computed deviatoric plastic strain is in agreement with the borehole radius data. The small deviatoric plastic strain levels in the methane hydrate reservoir (277 m-339 m) coincide with the minimal borehole enlargement, while the large plastic strain magnitudes in the overburden and underburden layers match well with the significant borehole enlargement. Although this qualitative comparison between the computed plastic strain distribution and measured borehole enlargement does not directly demonstrate the accuracy of the simulation, it indicates that the essential aspects of the formation behavior during well construction are captured in the constitutive model. It is noted that the A1-W well was dedicated for wireline logging to probe formation properties, one of which was borehole radius, and was thus not constructed with casing and cement (Takahashi & Tsuji 2005). In fact, the A1-E1 well was the only vertical well that was constructed with casing and cement during the 2004 drilling campaign.
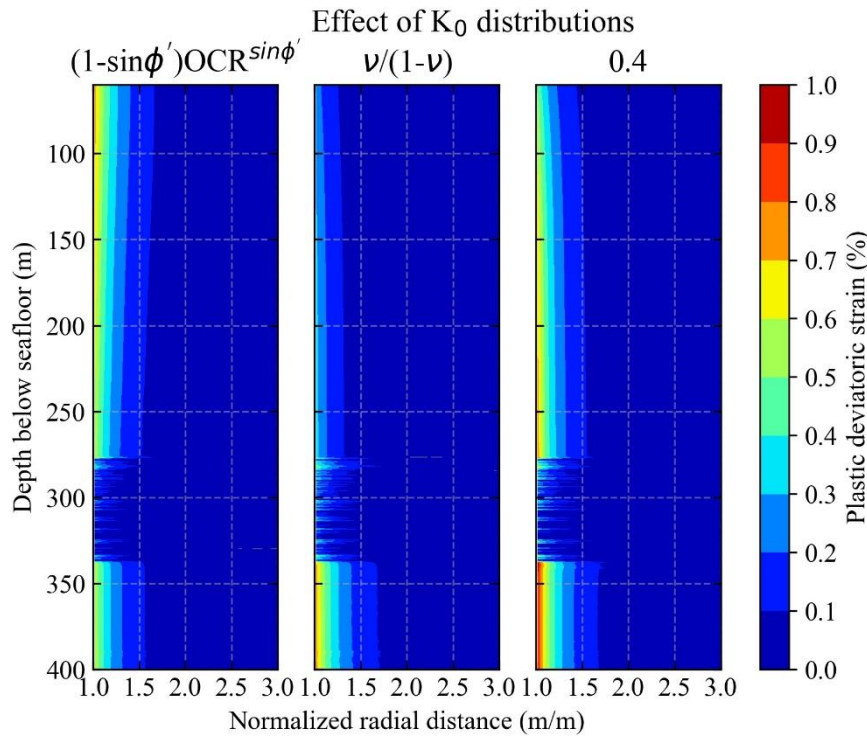
Figure 4-20 Effect of different initial horizontal stresses of the formation on the zone and magnitude of plastic deviatoric strain development in the formation near the 12 1/4-in. diameter borehole.

4.3.5.2. *Effect of initial horizontal stress of the formation*

Figure 4-20 shows the effect of different initial horizontal stress formula on the plastic deviatoric strain development in the formation around the 12 1/4-in. diameter borehole. The initial horizontal stress of the formation was found to have an impact on the plastic deviatoric strain development compared to the effect of cement volume shrinkage discussed earlier. When $K_0 = (1-\sin\phi')OCR^{\sin\phi'}$ was employed, the maximum plastic deviatoric strain was developed at approximately 60 m below seafloor in the overburden layer, while it was in the underburden layer when $K_0 = v/(1-v)$ was employed. When $K_0 = 0.40$ was used, the magnitude of the plastic deviatoric strain gradually increased with depth intermitted by the reservoir where the plasticity was minimal. The magnitude of plastic deviatoric strain can be related to the magnitude of initial horizontal effective stress. For instance, when $K_0 = v/(1-v)$ was employed, the largest initial horizonal effective stress occurred in the underburden layer. When $K_0 = 0.40$ was used, the initial horizontal effective stress linearly increased with depth. These trends of the initial horizontal effective stress corresponded well to those of the plastic deviatoric strain. This is because deviatoric stress development was proportional to the difference between the initial horizontal stress and drilling fluid (seawater) pressure (i.e., initial horizontal effective stress). The plastic deviatoric strain propagated to the

102

normalized radial distance of approximately one and a half among the examined simulation cases with different K_0 distributions.

Chen et al. (2018) showed that the change in hydrate saturation caused by well construction in the near-wellbore region would significantly affect the short-term gas production rate. The discrepancy between the simulation and field data on the short-term gas production rate at the Nankai Trough (Chen, Feng, Kogawa, et al. 2018) could also be due to well construction-induced complex initial permeability, gas and water saturation conditions around the wellbore prior to gas production. The result of this study on the plastic strain development in the methane hydrate-bearing layer in the near-wellbore region suggests that the effect of well construction-induced disturbance could indeed be complex yet limited within a very small radius from the centre of the well. Therefore, the discrepancy between the predicted and actual short-term gas production rate might be due to other factors such as hydrate reformation during initial gas production.

4.4. Summary

In this study, a finite element analysis of the effect of well construction on the integrity of the Nankai Trough offshore unconsolidated formation is presented. The modelled well construction processes are drilling, casing hanging, cementing, cement hardening/shrinkage and casing landing. The effects of key well construction stages, including the drilling and cement volume shrinkage stage, as well as the effect of initial horizontal stress of the formation on the formation integrity were assessed. The primary findings from the present study are provided below.

(i) In the Nankai Trough methane hydrate reservoir case, the well construction-induced stress disturbance in the formation extended to the normalized radial distance of approximately three, whereas plastic deviatoric strain development extended to that of one and a half. The volume of formation where plastic deviatoric strain develops might become vulnerable to sand production during gas production.

(ii) Because of the difference between the stiffness values of the high hydrate saturation layers (high stiffness) and the low to zero hydrate saturation layers (low stiffness), the decrease in the radial effective stress and the corresponding increase in the deviator stress occurrs in the high hydrate saturation layers during cement shrinkage-induced wellbore contraction (i.e., cylindrical cavity contraction). The radial stress relaxation during cement shrinkage in the high hydrate saturation layers could cause loss of confining pressure from the formation for the well, potentially leading to localised buckling of the

well.

(iii)   The key well construction process for estimating plastic strain development in the formation was found to be the drilling stage, whereas it was the cement shrinkage stage that was essential to predict formation stress changes.

From the above findings, it is recommended that the cement shrinkage during well construction is reduced below 0.75% so that radial effective stress relaxation, which is localised in the high hydrate saturation layers, can be minimised. Also, low to zero hydrate saturation layers in the reservoir, where plastic strain develops during the drilling stage, might have to be stabilised prior to hydrate dissociation to prevent potential sand production. It is noted, however, that the simulations results are dependent on the initial horizontal stress distributions of the formation, which have impact on both stress changes and plastic strain development in the formation during well construction processes. Hence, accurate estimation and/or measurement of the *in situ* horizontal stress distributions of the formation would have to be carried out to improve the accuracy of the well construction simulation.

5. Simulation of well integrity in offshore unconsolidated methane hydrate-bearing formation during reservoir compaction

5.1. Introduction

In this chapter, well integrity in methane hydrate reservoirs during reservoir compaction is analysed for the Nankai Trough case. Earlier attempts to investigate well integrity in methane hydrate-bearing formation was performed by Freij-Ayoub et al. (2007a&b). They assessed well integrity during heating-induced hydrate dissociation. However, well integrity against reservoir compaction was not assessed. Subsequently, well integrity in methane hydrate reservoirs during reservoir compaction were investigated by Rutqvist et al. (2012), Qiu et al. (2015), Shin & Santamarina (2016) and Yoneda et al. (2018). For example, Shin & Santamarina (2016) state that well integrity is affected by the change in formation permeability during compaction. However, the actual mechanism might be that different reservoir compaction profiles are developed depending on the parameter values for the coupling between permeability and volumetric compaction of the formation, and hence well integrity is affected differently.

In this study, it is hypothesized that different compaction profiles affect well integrity differently. To examine the effect of reservoir compaction characteristics on well integrity, a parametric study is carried out with an axi-symmetric finite element model for the case of the Nankai Trough methane hydrate reservoir. The cement sheath around the casing is incorporated into the model as the integrity of cement in the well annulus is crucial in maintaining zonal isolation of the formation as well as in preventing oil/gas leakage, even though the model developed by Shin & Santamarina (2016) does not include the cement. Also, well construction processes, especially cement shrinkage stage, are incorporated prior to reservoir compaction stages as it is found to affect formation stress state significantly in Chapter 4. The objectives of this study are as follows:

(i)   to evaluate the effect of different reservoir compaction cases on the stress and strain development of the casing and cement,

(ii)   to evaluate the effect of cement shrinkage volume and different horizontal stress states of the formation (i.e., overconsolidated or normally consolidated) on well integrity during reservoir compaction, and

(iii)   to assess the correlations between the stress and strain development of the casing and cement during reservoir compaction and depressurization/hydrate dissociation patterns

in the reservoir.

The Cambridge Methane Hydrate Critical State model (MHCS) model (Uchida et al. 2012) is employed as the formation constitutive model. The MHCS model parameters are calibrated against the triaxial test data on formation samples taken from the Nankai Trough (Nishio et al. 2011; Yoneda et al. 2015). Also, an interface friction model between the casing and cement is developed and verified against laboratory test data on well specimens which is presented in Chapter 6. The details of the methodology of the finite element analysis are provided in the following sections.

5.2. Finite element modelling

5.2.1. Model geometry

Figure 5-1 shows a schematic diagram of the axi-symmetric finite element model used in this study. The total depth and radius of the model are 650 m and 600 m, respectively. The thickness of the methane hydrate reservoir layer (MH reservoir layer) is 50 m, whereas the thicknesses of the overburden and underburden layers are 300 m. The well is drilled in the overburden layer and the borehole radius is 0.312 m (12 1/4 in.). The outer diameter and wall thickness of the casing are 0.122 m (9 5/8 in.) and 0.01 m (0.4 in.), respectively. The roller boundary constraint is applied at the left and bottom edges of the model whereas constant distributed pressure load is applied at the top (i.e., hydrostatic pore pressure) and right (i.e., total horizontal stress) edges. The model is assumed to be 1,000 m below sea surface at the top of the model.

The ground formation is discretized into 55,250 eight-node displacement four-node pore pressure elements, whereas the casing and cement are discretized into 600 and 1,800 eight-node displacement elements, respectively. Figure 5-2 shows the mesh of the model near the bottom of the wellbore. The vertical length of the mesh is set to 1 m throughout the model. The horizontal length of the casing and cement elements is set to be 5.0×10^{-3} m and 6.3×10^{-3} m, respectively. The horizontal length of the formation elements increases with increasing radius from the wellbore, i.e., 5.3×10^{-2} m at the cement-formation interface. The mesh size exponentially increases to 53 m at the right edge of the model.
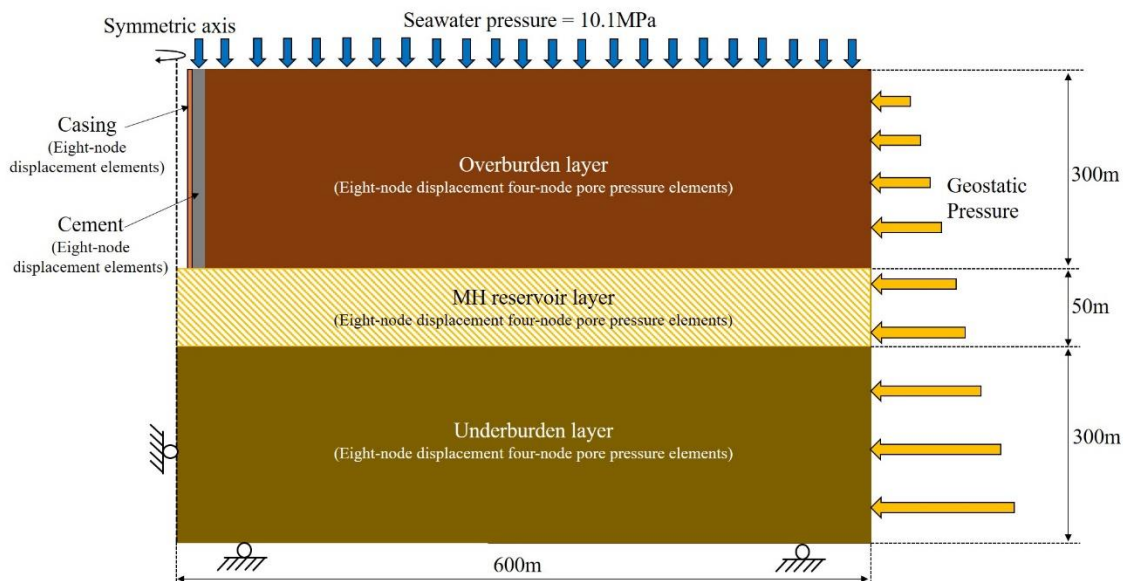
Figure 5-1 The geometry of the axi-symmetric finite element model.
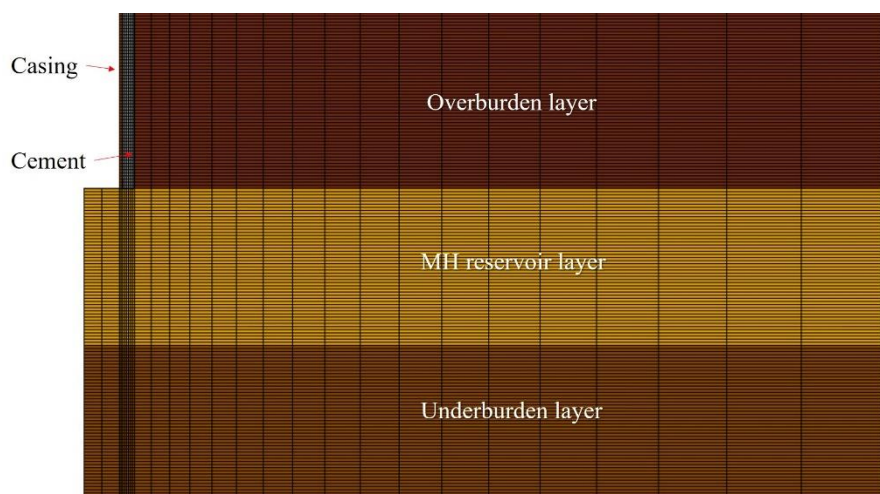
Figure 5-2 The mesh of the axi-symmetric finite element model near the bottom of the wellbore (horizontally enlarged a hundred times).

5.2.2. Constitutive models

The methane hydrate critical state model (MHCS model) (Uchida et al. 2012) is employed to simulate the mechanical behaviours of methane hydrate-bearing formation. The model parameters are calibrated against the triaxial test data of formation samples taken from the Nankai Trough (Yoneda et al. 2015; Nishio et al. 2009). The calibration results are presented in Figure 4-4 in Chapter 4. The values of the density and void ratio of each layer of the formation are chosen based on the in situ measurement data at the Nankai Trough (Suzuki et al. 2015).

Table 5-1 shows the values of the MHCS model parameters used in the simulation. The MHCS parameters for the hydrate effect (i.e., m_1, m_2, a, b, c, d) are set to zero in the MH reservoir layer. This is because it is assumed that methane hydrate is fully dissociated in the MH reservoir layer and the pore pressure distribution has reached the steady-state conditions.

For the casing and cement elements, a model of linear isotropic elasticity with a Mises yield surface with associated flow rule (casing) and with a Mohr-Coulomb yield surface with non-associated flow rule (cement) is employed to simulate their mechanical behaviours. The values of the constitutive mode parameters are shown in Table 5-2. These values are relevant to the casing and cement employed at the Nankai Trough (Qiu et al. 2015).

Table 5-1 The parameter values of the MHCS model for the formation.

	Overburden clay	Methane hydrate reservoir	Underburden sand
Depth from seafloor (m)	0~300	300~350	350~650
Saturated bulk density (kg/m³)	1,750	1,750~2,000	2,000
Initial void ratio	1.31	1.31~0.717	0.717
Gradient of compression line, λ	0.18	0.10	0.10
Gradient of swelling line, κ	0.03	0.02	0.02
Critical state frictional constant, M	1.30	1.37	1.37
Poisson's ratio, ν	0.25	0.35	0.35
Subsurface constant, U	15	8	8
Stiffness enhancement constant, m_2	0	0	0
Hydrate degradation constant, m_1	0	0	0
Dilation enhancement constant, A	0	0	0
Dilation enhancement constant, B	0	0	0
Cohesion enhancement constant, C	0	0	0
Cohesion enhancement constant, D	0	0	0

Table 5-2 The parameter values of the constitutive models for the casing (von Mises) and cement (Mohr-Coulomb).

	Casing	Cement
Density (kg/m³)	7,897	1,198
Young's modulus (GPa)	200	0.131 (slurry) 3.81 (solid)
Poisson's ratio (-)	0.28	0.49 (slurry) 0.20 (solid)
Yield stress (MPa)	379.5	NA
Friction angle (º)	NA	30
Dilation angle (º)	NA	0
Cohesion (MPa)	NA	2.72

5.2.3. Modelling of interface behaviours

Although the ABAQUS software does have a constitutive model for interface friction behaviour, it does not include the interface cohesion term, which is essential for the modelling of cement-steel (casing/pipes) interfaces. Therefore, an interface friction constitutive model incorporating the interface cohesion term is developed to simulate the interaction between cement and casing as well as between well and formation during reservoir compaction. Details of the interface friction model are described below.

(i)   Elastic properties

Recoverable (elastic) tangential interface displacement is allowed in the developed friction constitutive model as below:

$$\tau = k\gamma^e \tag{5-1}$$

where τ = interface shear stress, k = shear stiffness of the interface, γ^e = elastic tangential displacement of the interface. The incremental form of Equation 5-1 is shown below:

$$d\tau = k(d\gamma - d\gamma^p) \tag{5-2}$$

where $d\gamma$ = total tangential interface displacement increment and $d\gamma^p$ = plastic tangential interface displacement increment. The value of k is determined by the equation below:

$$k = \frac{\tau_{ult}}{\gamma^e_{ult}} \tag{5-3}$$

where γ^e_{ult} = ultimate elastic tangential displacement of the interface, τ_{ult} = ultimate interface shear stress, which is the shear stress level where irrecoverable tangential interface displacement starts to occur (i.e., yielding). Therefore, τ_{ult} is determined through a yield function which is described next.

(ii)   Yield criterion

The yield criterion for the tangential interface displacement is specified by the yield function, f, as shown below:

$$f = \tau - \mu p - c' \tag{5-4}$$

where p = interface contact pressure, μ = interface friction coefficient and c' = interface cohesion. Yielding is judged if the value of $f > 0$.

(iii)   Flow rule

The associated flow rule is employed to calculate the irrecoverable tangential interface displacement as follows:

$$d\gamma^p = \Lambda \frac{\partial f}{\partial \tau} \tag{5-5}$$

where $d\gamma^p$ = plastic tangential interface displacement increment and Λ = plastic multiplier.

(iv)   Hardening rule

The values of friction coefficient and cohesion in the yield function are set to constant values and no plastic hardening/softening was considered.

In order to obtain the interface shear stress increment, the plastic tangential interface displacement increment has to be calculated. This is done by satisfying the consistency condition shown below:

$$f(\tau + d\tau, p + dp, \mu, c) = 0$$

$$\Leftrightarrow \qquad f(\tau + k(d\gamma - d\gamma^p), p + dp, \mu, c) = 0$$

$$\Leftrightarrow \qquad f(\tau + kd\gamma, p + dp, \mu, c) - \frac{\partial f}{\partial \tau} kd\gamma^p = 0$$

$$\Leftrightarrow \qquad f^{pred} - \frac{\partial f}{\partial \tau} k\Lambda \frac{\partial f}{\partial \tau} = 0$$

$$\therefore \qquad \Lambda = \frac{f^{pred}}{\left(\frac{\partial f}{\partial \tau}\right) k \left(\frac{\partial f}{\partial \tau}\right)} \tag{5-6}$$

where $f^{pred} = f(\tau + kd\gamma, p + dp, \mu, c)$ is the value of the yield function at prediction stress state. Substituting Equation 5-5 and 5-6 into Equation 5-2 yields the following:

$$d\tau = k\left(d\gamma - \frac{f^{pred}\left(\frac{\partial f}{\partial \tau}\right)}{\left(\frac{\partial f}{\partial \tau}\right)k\left(\frac{\partial f}{\partial \tau}\right)}\right)$$

$$= k\left(d\gamma - \frac{\left(f(\tau,p,\mu,c) + \left(\frac{\partial f}{\partial \tau}\right)kd\gamma + \left(\frac{\partial f}{\partial p}\right)dp\right)\left(\frac{\partial f}{\partial \tau}\right)}{\left(\frac{\partial f}{\partial \tau}\right)k\left(\frac{\partial f}{\partial \tau}\right)}\right)$$

$$= k\left(\frac{-f^{now}\left(\frac{\partial f}{\partial \tau}\right) - \left(\frac{\partial f}{\partial p}\right)\left(\frac{\partial f}{\partial \tau}\right)dp}{\left(\frac{\partial f}{\partial \tau}\right)k\left(\frac{\partial f}{\partial \tau}\right)}\right) \tag{5-7}$$

Expanding the derivatives in Equation 5-7 by substituting the yield function shown in Equation 5-4 yields the interface shear stress increment as follows:

$$d\tau = \mu dp - f^{now} \tag{5-8}$$

where $f^{now} = f(\tau,p,\mu,c)$ is the value of the yield function at the current stress state. Equation 5-8 shows that the interface shear stress increment when yielding is judged is a combination of how much of an increase in the ultimate shear stress is obtained though dp and the difference between the current and yield stress levels (it is noted that $f \leq 0$ before yielding). It might be noteworthy that the constitutive Jacobian $\partial d\tau/\partial d\gamma = 0$ upon yielding because no plastic hardening is considered (i.e., perfectly plastic yielding). It is also noteworthy that no interface dilation or compaction due to plastic tangential interface displacement is taken into account in the developed friction constitutive model. Hence, caution should be exercised when applying this model to interfaces where interface dilation/compaction may become significant.

The ABAQUS subroutine, Fric, is employed to implement this interface friction model. As shown in the next section, the subroutine was verified through performance comparison with the ABAQUS inbuilt Coulomb friction model. The difference between the developed subroutine friction model and ABAQUS inbuilt friction model is that the latter does not incorporate the cohesion term. In order to model the interface cohesion (i.e., non-zero frictional resistance at zero interface confining pressure) between casing and cement, the abovementioned subroutine model, which incorporates the cohesion term, was developed.

The normal interface behaviour (i.e., interface pressure) is modelled by the augmented Lagrange method, which is a combination of the linear penalty method and an augmentation iteration

scheme. In the augmented Lagrange method, contact pressure is calculated by multiplying the stiffness of the representative underlying elements with the interface penetration distance. The interface penetration is maintained below 0.1% of the characteristic element length of the model by iteratively augmenting the contact pressure.

5.2.4. Verification of the interface model

In order to verify the performances of the developed interface friction model, a simulation that compares the model against the ABAQUS inbuilt interface function model is performed. Figure 5-3 shows the schematic diagram of the plane-strain finite element model created for the verification simulation. In this model, a cement block is pressed against a steel plate. The steel plate is then displaced downward while the cement block is fixed to induce interface slippage.
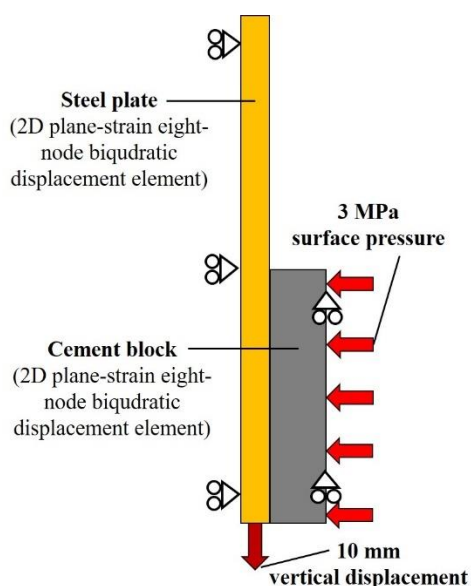
Figure 5-3 The plane-strain finite element model for the verification of the developed interface friction model.

The width and height of the steel plate are set to 5 mm and 100 mm, respectively, while those of the cement block are 9 mm and 50 mm. The steel plate is discretized into 20 eight-node biquadratic displacement elements (5 mm by 5 mm) and the cement into 75 eight-node biquadratic displacement elements (3 mm by 2 mm). The steel plate and cement block are both modelled as linear isotropic elastic material. The Young's modulus and Poisson's ratio are set to 200 GPa and 0.27 for the steel plate and 12 GPa and 0.21 for the cement block, respectively. For the interface, the friction coefficient, cohesion and ultimate elastic interface displacement are set to 0.55, 0 MPa and 0.25 mm, respectively, for both the ABAQUS inbuilt model and the

developed subroutine interface model.
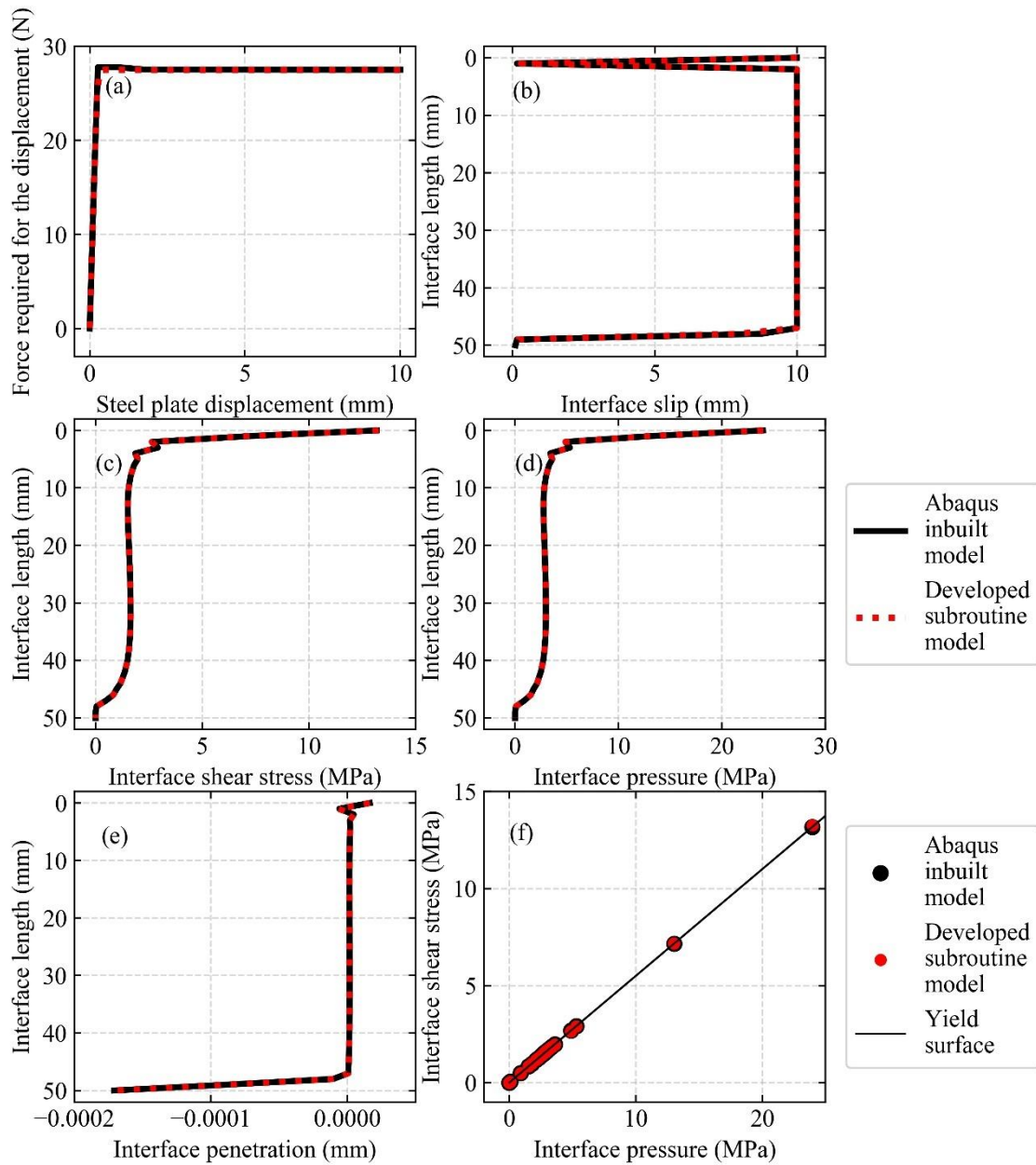
Figure 5-4 Comparison of the performances between the ABAQUS inbuilt and developed subroutine interface friction models: (a) force vs. displacement; (b) tangential interface displacement; (c) interface shear stress; (d) interface pressure; (e) interface penetration distance; (f) interface shear stress vs. interface pressure.

Figure 5-4 shows the results of the comparison simulation. Figure 5-4a shows the development of the force required to displace the steel plate. Figure 5-4b, c, d and e show the distribution of tangential interface displacement, shear stress, contact pressure and penetration distance,

respectively, along the steel plate-cement block interface at the end of the steel plate displacement (i.e., 10 mm). The performance of the developed subroutine model is in good agreement with that of the ABAQUS inbuilt model. Figure 5-4f shows that the computed interface shear stress and contact pressure values lie exactly on the yield surface. In the following section, the parameters of the verified interface model are calibrated for the casing-cement interface.

5.2.5. Calibration of the interface model and model parameter setting

To calibrate the parameters of the interface model, a finite element analysis of a laboratory experiment, where a well specimen is subjected to tensile loading (Figure 5-5a), is carried out. The simulated axial strain development of the well specimen during tensile loading is compared with the experimental data. The details of the experiments are given in Chapter 6.

(a)

(b)
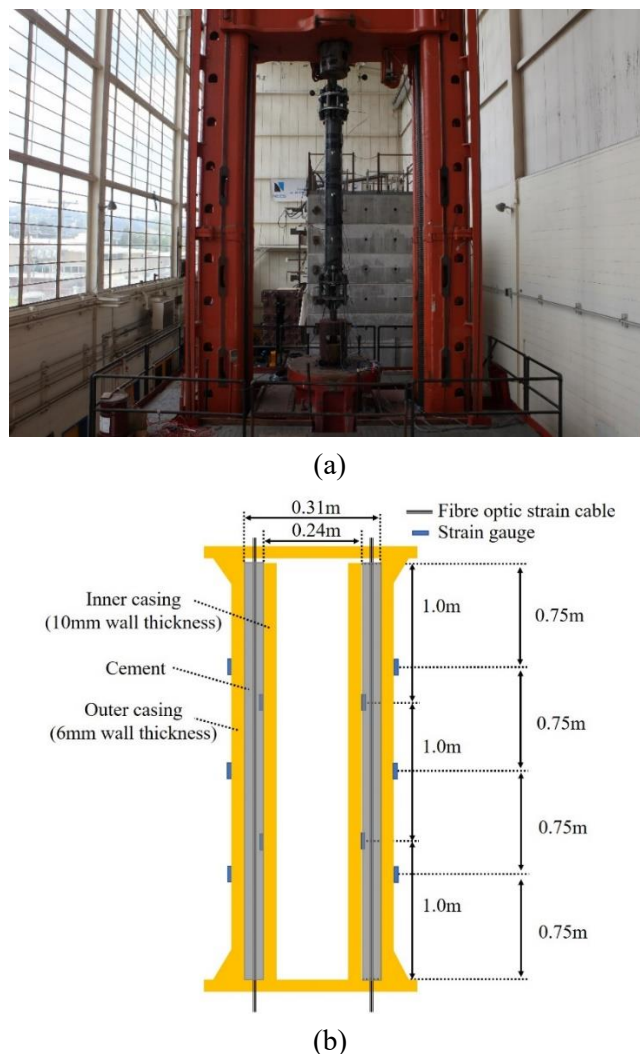
Figure 5-5 The laboratory experiment on the well specimen: (a) an overview of the specimen in

loading apparatus; (b) a cross section of the well specimen.

The cross-section of the well specimen is illustrated in Figure 5-5b. The specimen consists of inner casing, cement sheath and outer casing. Fibre optic cables for distributed axial strain monitoring are embedded in the cement, whereas strain gauges are attached the inner and outer casings.

Figure 5-6 shows the axi-symmetric finite element model used in this study. The inner casing, cement and outer casing are modelled with the eight-node biquadratic displacement element. The inner and outer casings are discretized into 600 elements each whereas the cement is discretized into 12,000 elements. To apply a tensile load, the displacements of the bottom nodes of the inner and outer casing are fixed and a distributed load is applied on the top nodes of the outer casing in the vertical direction.
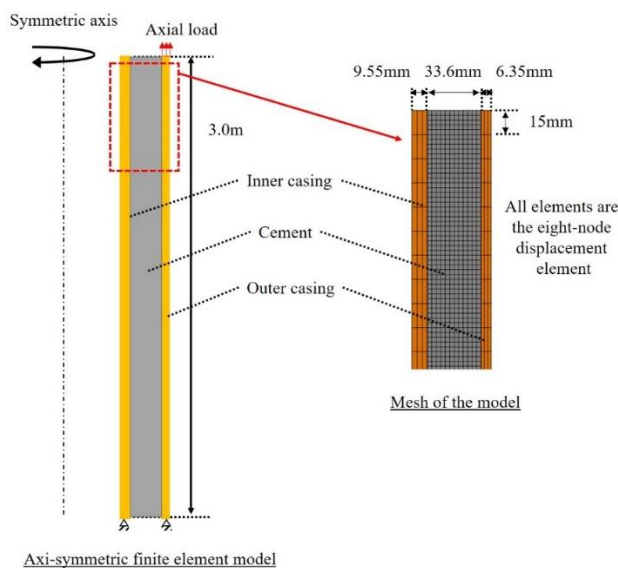
Figure 5-6 The axi-symmetric finite element model of the well specimen (left) and the model mesh (right).

The inner and outer casings are modelled isotropic linear elastic. The Young's modulus and Poisson's ratio are set to 200 GPa and 0.26, respectively, which correspond to the typical values of A36 steel which comprises the casings. The cement is modelled isotropic linear elastic with the Mohr-Coulomb yield surface. The Young's modulus and Poisson's ratio of the cement are set to 8.3 GPa and 0.10, which are taken from the literature (Bosma et al. 1999). The values of the internal friction angle and cohesion of the Mohr-Coulomb yield surface for the cement are also taken from the literature (Bosma et al. 1999) and are set to 17.1° and 21.6 MPa,

respectively. The dilation angle is assumed to be 0º. For the casing-cement interface, the values of the friction coefficient and cohesion are respectively set to 0.8 (i.e., friction angle of 38.7º) and 3.0 MPa. These values are based on the experimental result of the pushout test of a steel rod embedded in cylindrical cement sheath (Yoneda et al. 2014). The remaining parameter is the ultimate elastic interface displacement and a typical value for the casing-cement interface could not be obtained from the literature. Hence, this value is calibrated to match the simulation with the experimental data. The match between the simulation and experiment is judged visually and no proper optimisation such as the least square method is performed.

The model calibration result is shown in Figure 5-7. The numbers in the figures indicate the axial load increments (1 kips = 4.45 kN). It is found that a good match between the simulation and experiment is obtained with the value of ultimate elastic interface displacement = 0.5 mm. To validate the calibration result, an analytical solution for the casing-cement shaft friction problem is provided in Chapter 6 (Section 6.4.2.), which shows that the choice of 0.5 mm is appropriate as the numerical and analytical results match satisfactorily, including the gradient of axial strain at the top and bottom of the specimen, at small load levels (< 125 kips) where the cement is still elastic. Once the cement develops plastic strains after mid-load levels (> 175 kips), the gradient of axial strain increases significantly. The sharp strain gradient after the cement yield is dependent on the plastic parameters of the cement (i.e., friction angle, dilation angle and cohesion) and hence it could not be matched by changing solely the value of the ultimate elastic interface displacement.

For the cement-formation interface of the reservoir compaction simulation, it is assumed that the interface friction coefficient is identical to that of the underlying formation. The friction coefficient of the overburden layer is 0.67 (i.e., friction angle of 33.9º) whereas that of the MH reservoir and underburden layers is 0.63 (i.e., friction angle of 32.3º). As the difference is small, the mean value of 0.65 is used for the entire cement-formation interface. For the interface cohesion at the cement-formation interface, it is assumed negligible as soil particles of the unconsolidated formation do not resist friction at zero interface confining pressure, which is experimentally validated in the literature (Yoneda et al. 2014). The value of the ultimate elastic interface displacement is set to 0.25 mm for the cement-formation interface. This is determined by varying the value of ultimate elastic interface displacement between 0.25 mm and 2.5 mm and carrying out the reservoir compaction simulation which is presented in the following sections. Results show negligible differences in the development of stresses and strains of the casing and cement during reservoir compaction. Therefore, the value is set to 0.25 mm. To support this, an experimental study by Uesugi et al. (1990), where a sand specimen prepared

inside a stack of rectangular frames is sheared against a mortar plate placed beneath the sand while vertical confining pressure is maintained, shows that the value of ultimate elastic interface displacement between the sand and mortar is approximately 0.3 mm.
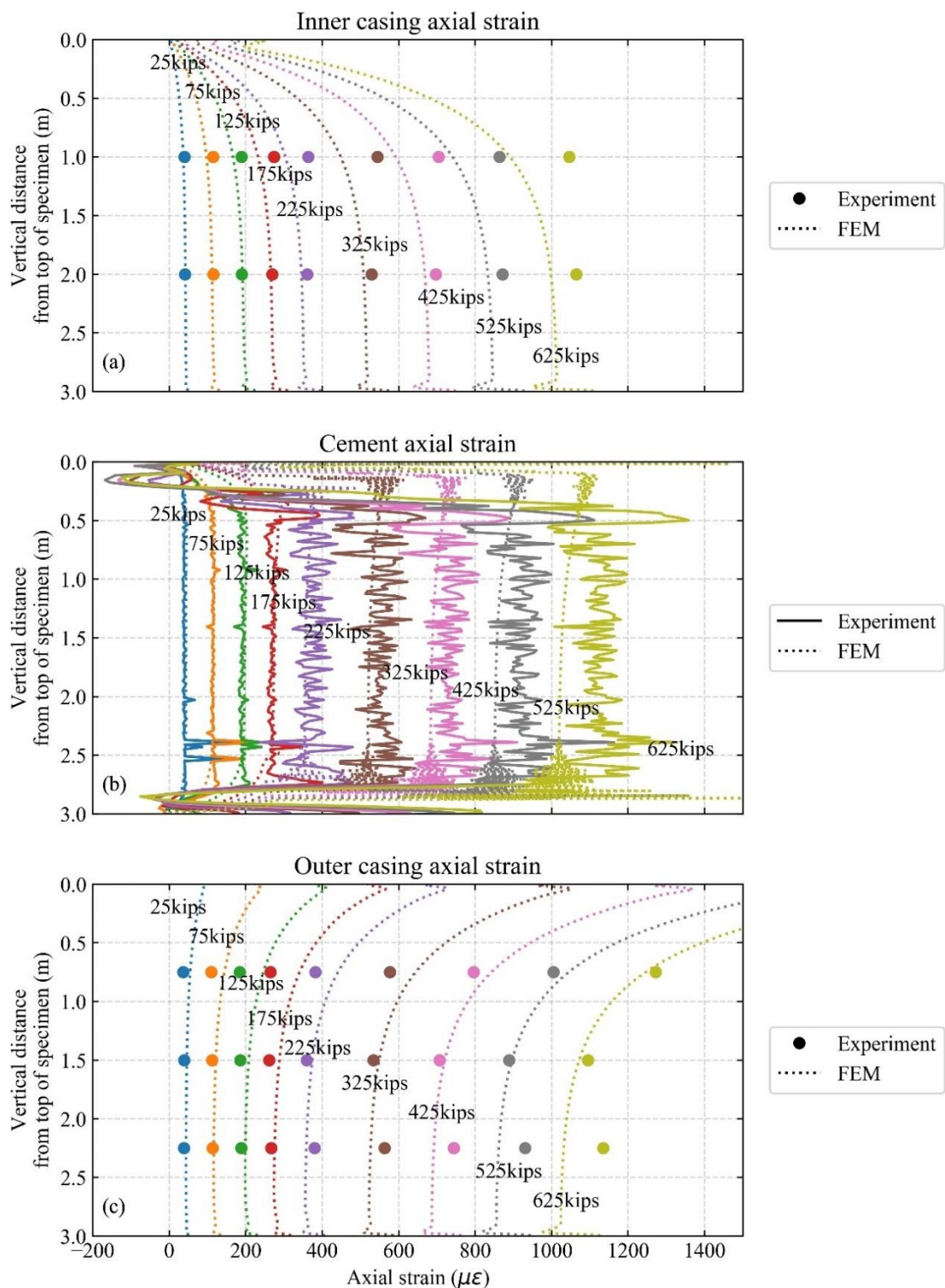
Figure 5-7 Comparisons of the axial strain development of the well specimen between the

simulation and experiment: (a) inner casing; (b) cement; (c) outer casing.

It is noted that the level of interface confining pressure between the laboratory experiment (Figure 5-5) (atmospheric pressure) and the actual wellbore in the Nankai Trough (~10 MPa) is significantly different. Although a better calibration of the friction model parameters could have been performed if the experiment had been conducted under the actual confining pressure conditions, the application of ~10 MPa confining pressure over the 3 m-long specimen was not feasible in the laboratory.

5.2.6.   Initial conditions

For the Nankai Trough case, the initial vertical stress distribution of the formation is derived from the in suit density measurement at the site (Suzuki et al. 2015). The initial void ratio distribution is also obtained from the same in situ density measurement. For the initial pore pressure distribution, the hydrostatic pore pressure distribution with the seawater density of 1.027 g/cm^3 is employed.
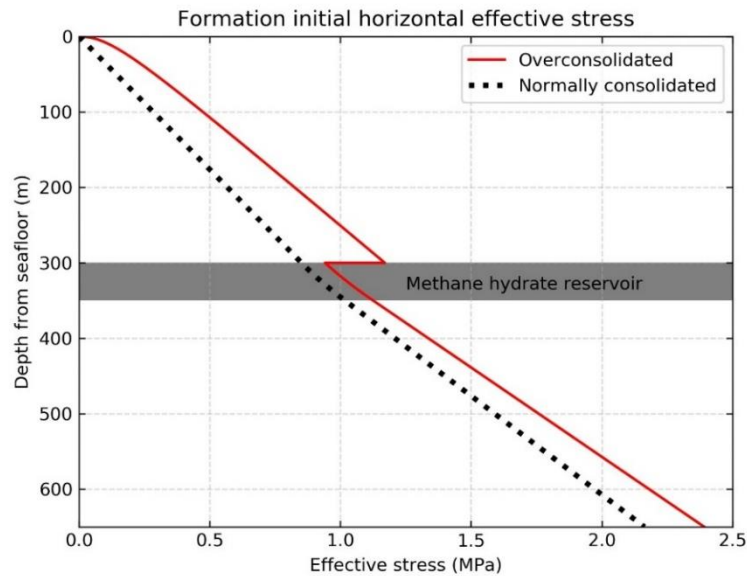
Figure 5-8 Initial horizontal effective stress distributions of the formation.

Two different initial horizontal effective stress distributions are employed as shown in Figure 5-8. The overconsolidated distribution is calculated via Equation 5-9:

$$\sigma'_h = (1 - \sin\phi')\text{OCR}^{\sin\phi'}\sigma'_v \qquad (5\text{-}9)$$

where σ'_h = horizontal effective stress, σ'_v = vertical effective stress, ϕ' = internal friction

118

angle, OCR = overconsolidation ratio. This formula is often employed in the soil mechanics. The OCR values of the overburden layer is derived from triaxial test data of formation core samples retrieved from the Nankai Trough (Nishio et al. 2011). Hence, the overconsolidated formation case is more representative of the actual Nankai Trough formation. For the normally consolidated case, the initial horizontal effective stress is calculated via $\sigma'_h = 0.4\sigma'_v$. The effect of initial lateral pressure will be examined in Section 5.3.6.

5.2.7. Well construction process

The construction process of the well is incorporated in the simulation. The modelling methodology of the well construction process is identical to the one employed in Sasaki et al. (2018a) and are described in Chapter 4. The modelled construction stages are presented in Table 5-3. The shrinkage volume of 0.75% is employed in the cement shrinkage stage for the Nankai Trough scenario (Sasaki et al. 2018b), which is determined through finite element modelling described in Chapter 3.

Table 5-3 The well construction processes incorporated in the simulation.

Construction process	Duration (hour)
1. Drilling	14.4
2. Casing hanging	Immediate
3. Cementing	Immediate
4. Cement hardening/shrinkage	40.8
5. Casing landing	Immediate

5.2.8. Depressurization and hydrate dissociation process

The depressurization stage is simulated by specifying the pore pressure distribution in the reservoir layer, rather than simulating the actual depressurization and dissociation processes. The analytical steady-state pore pressure distribution as shown below is employed to specify the pore pressure distribution in the reservoir layer:

$$u = C_1 \ln r + C_2 \qquad (5\text{-}10)$$

where u = pore pressure and r = radius from the centre of the well. It is assumed that the permeability of hydrate dissociated zone ($0 \leq r \leq r_f$) is higher than that of the undissociated zone ($r > r_f$). Therefore, the above equation is applied to each zone separately while satisfying that the radial flow velocities at the boundary between the dissociated and undissociated zones are equal. By applying the other boundary conditions ($u = P_i$ at $r = r_o$, $u = P_o$ at $r = R_o$), the values of the coefficients (C_1 and C_2) are obtained as follows:

$$C_1 = \begin{cases} (P_o - P_i)/\ln\left(r_f^{1-\alpha_p} R_o^{\alpha_p} / r_o\right) & (0 \leq r \leq r_f) \\ \alpha_p(P_o - P_i)/\ln\left(r_f^{1-\alpha_p} R_o^{\alpha_p} / r_o\right) & (r > r_f) \end{cases}$$

$$C_2 = \begin{cases} P_i - C_1 \ln r_o & (0 \leq r \leq r_f) \\ P_o - C_1 \ln R_o & (r > r_f) \end{cases}$$

where P_o = hydrostatic pore pressure, P_i = pore pressure at the well-formation interface, r_f = radius of the hydrate dissociation front, r_o = radius of the well-formation interface, R_o = radius where hydrostatic pore pressure is recovered and α_p = ratio of the permeability values of the dissociated and undissociated hydrate-bearing formation. According to the literature, the value of α_p is dependent on the hydrate saturation and it could be ~100 or greater (Kumar et al. 2010; Hou et al. 2018; Delli & Grozic 2014). In this study, it is set to a constant value of 100. As to the value of r_f, coupled simulations in the literature (Sun et al. 2016; Chen, Feng, Kogawa, et al. 2018; Klar, Soga, et al. 2010) suggest that it is a fraction of R_o and increases with increasing R_o. In this study, it is assumed that $R_0 = 2r_f$.

To model the progress of depressurization and hydrate dissociation, the values of P_i and r_f are linearly varied with time by $-\Delta P_i$ and Δr_f at each of the 14 depressurization and dissociation stages from the initial values of $P_i = P_o$ and $r_f = 0$. In the field, the rate of decrease in P_i depends on the speed of depressurization specified by the operator, whereas the rate of increase in r_f depends on the speed of hydrate dissociation, which is governed by the permeability field of the reservoir as well as heat supply from the far field. As changes of the formation permeability field in response to hydrate dissociation are complex, the rate of r_f increase may not be constant as assumed in this study. In order to estimate the rate of r_f increase more accurately, it would be necessary to carry out thermo-hydro-mechanical coupled simulations similar to the ones presented in the literature (Kimoto et al. 2007; Kakumoto et al. 2011; Klar et al. 2013; Gupta et al. 2017; Sun et al. 2005; Moridis et al. 2012; Sun et al. 2018; Uchida 2012). Figure 5-9 shows the simulated pore pressure profiles at the top of the reservoir layer in the case of localized (ΔP_i= -0.3 MPa and Δr_f = 0.5 m) and distributed (ΔP_i = -0.3 MPa and Δr_f = 3 m) hydrate dissociation cases. To create various depressurization and hydrate dissociation profiles, different combinations of ΔP_i and Δr_f values were employed (i.e., ΔP_i = -0.1, -0.2, -0.3, -0.4, -0.5, -0.6 MPa and Δr_f = 0.5, 1.0, 1.5, 2.0, 2.5, 3.0 m). In total, 36 different depressurization and hydrate dissociation cases are simulated, which are listed in Table 5-4.
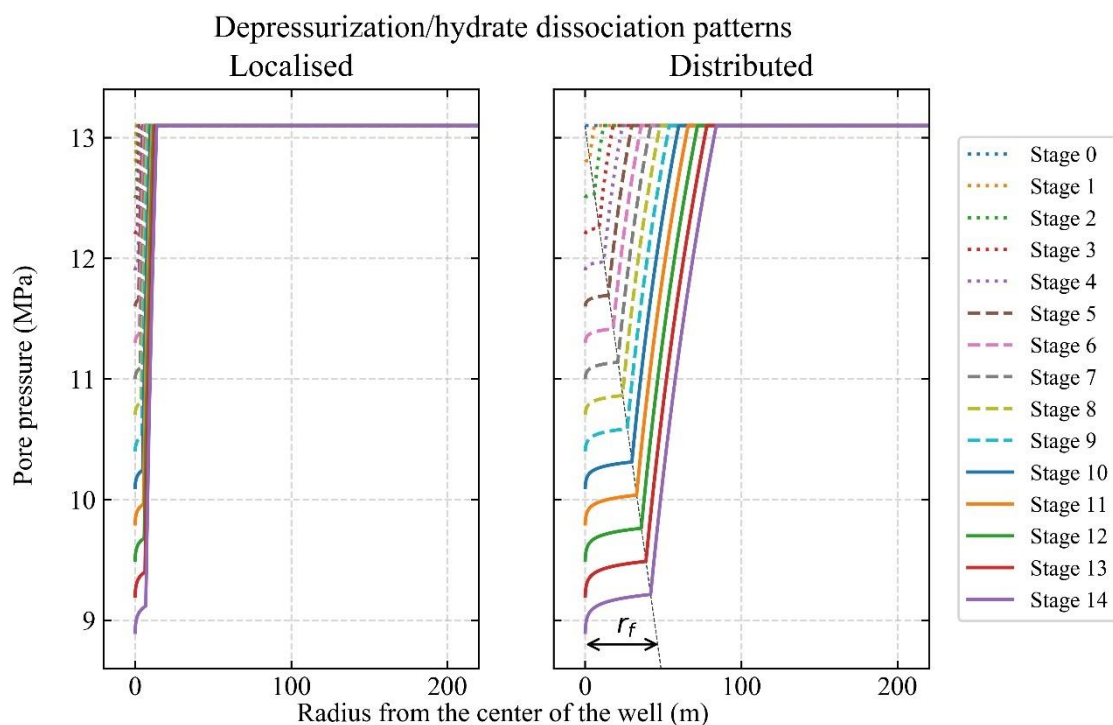
Figure 5-9 Simulated depressurization and hydrate dissociation (pore pressure) profiles in the MH reservoir layer (localized depressurization and dissociation case (ΔP_i = -0.3 MPa and Δr_f = 0.5 m) (left) and distributed depressurization and dissociation case (ΔP_i = -0.3 MPa and Δr_f = 3 m) (right)).

Table 5-4 The depressurization and hydrate dissociation cases simulated in this study.

Case#	ΔP_i (MPa)	Δr_f (m)	Case#	ΔP_i (MPa)	Δr_f (m)	Case#	ΔP_i (MPa)	Δr_f (m)
1		0.5	13		0.5	25		0.5
2		1.0	14		1.0	26		1.0
3	-0.1	1.5	15	-0.3	1.5	27	-0.5	1.5
4		2.0	16		2.0	28		2.0
5		2.5	17		2.5	29		2.5
6		3.0	18		3.0	30		3.0
7		0.5	19		0.5	31		0.5
8		1.0	20		1.0	32		1.0
9	-0.2	1.5	21	-0.4	1.5	33	-0.6	1.5
10		2.0	22		2.0	34		2.0
11		2.5	23		2.5	35		2.5
12		3.0	24		3.0	36		3.0

5.3. Results

5.3.1. Formation deformation patterns

Figure 5-10 shows the reservoir compaction profiles developed under the two different depressurization/hydrate dissociation patterns. The one on the left-hand side shows the localized dissociation case (Δr_f = 0.5 m), whereas the right-hand side one shows the distributed dissociation case (Δr_f = 3 m). It is noted that the depressurization level is identical between these two cases (ΔP_i = -0.3 MPa). The values of the maximum subsidence (S_{max}) and the subsidence radius (R_s), which is defined as a radial distance where the curvature of the subsidence distribution becomes maximum, are shown in the figures as circular and square dots, respectively. It is found that the more the depressurization/hydrate dissociation is localized, the smaller the maximum subsidence and subsidence radius values become.
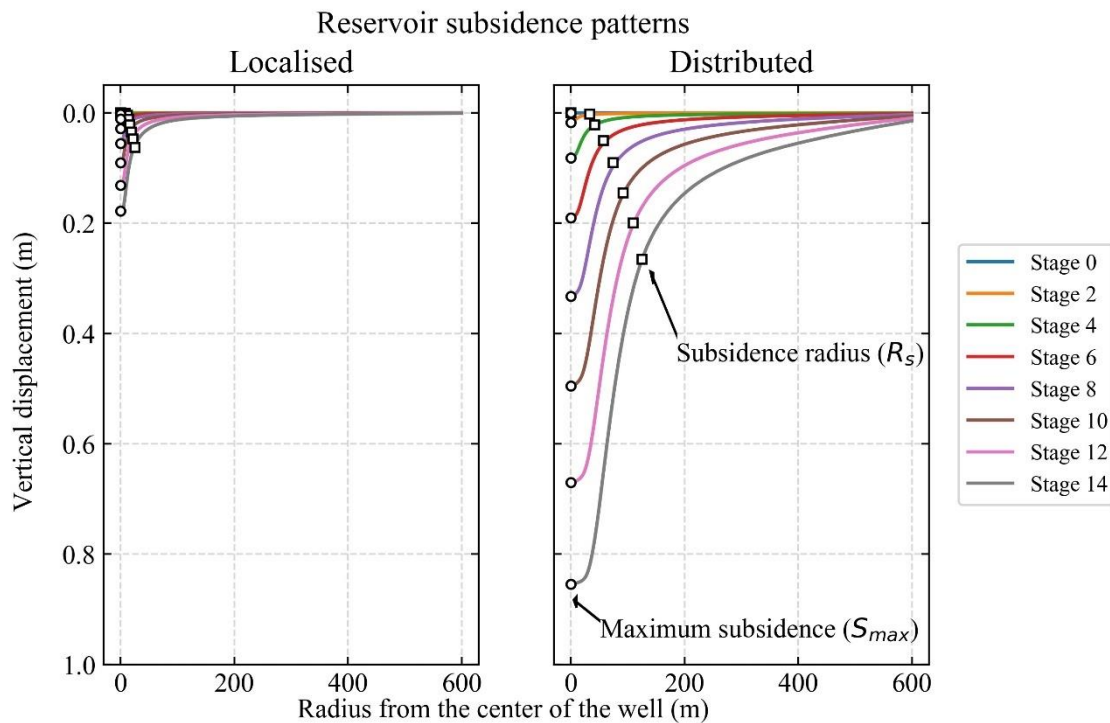
Figure 5-10 Reservoir subsidence along the top of the reservoir layer (localized dissociation case (ΔP_i = -0.3 MPa and Δr_f = 0.5 m) (left) and distributed dissociation case (ΔP_i = -0.3 MPa and Δr_f = 3 m) (right)).

Figure 5-11 shows the displacement patterns of the reservoir layer in the two different depressurization/hydrate dissociation cases mentioned above. It is noted that the magnitudes of the displacement vectors in these figures are normalised and scaled to increase their visibility. It is found that the reservoir layer deformation is concentrated near the wellbore in the localised dissociation case, whereas the reservoir layer deformation is radially distributed and developed primarily in the vertical direction in the distributed dissociation case.
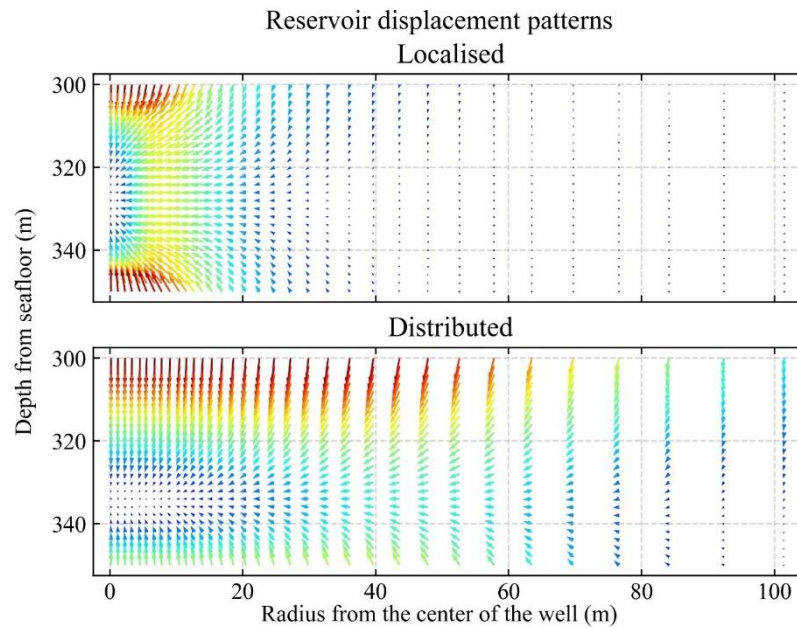
Figure 5-11 Deformation patterns of the reservoir layer (localized dissociation case (ΔP_i = -0.3 MPa and Δr_f = 0.5 m) (top) and distributed dissociation case (ΔP_i = -0.3 MPa and Δr_f = 3 m) (bottom)).
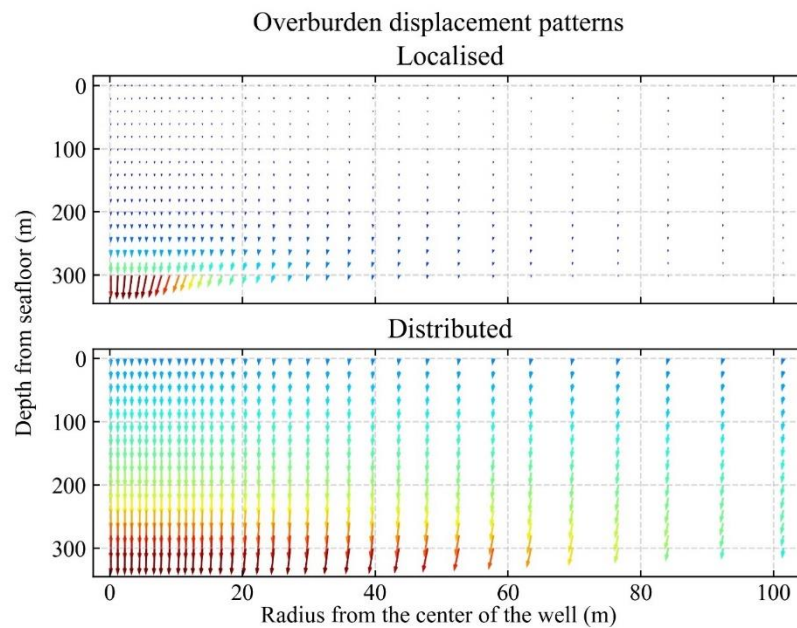
Figure 5-12 Deformation patterns of the overburden layer (localized dissociation case (ΔP_i = -0.3 MPa and Δr_f = 0.5 m) (top) and distributed dissociation case (ΔP_i = -0.3 MPa and Δr_f = 3 m) (bottom)).

Figure 5-12 shows the overburden layer deformation patterns corresponding to the reservoir layer

deformation patterns. It is evident that the overburden layer deformation is localised near the bottom of the overburden layer when the reservoir deformation is localised near the wellbore (i.e., localised dissociation case), whereas it is more evenly spread vertically and horizontally in the overburden layer when the reservoir deformation is likewise (i.e., distributed dissociation case). The difference in reservoir/overburden deformation patterns is found to have significant effects on well integrity during depressurization/hydrate dissociation, which is described in the following sections.
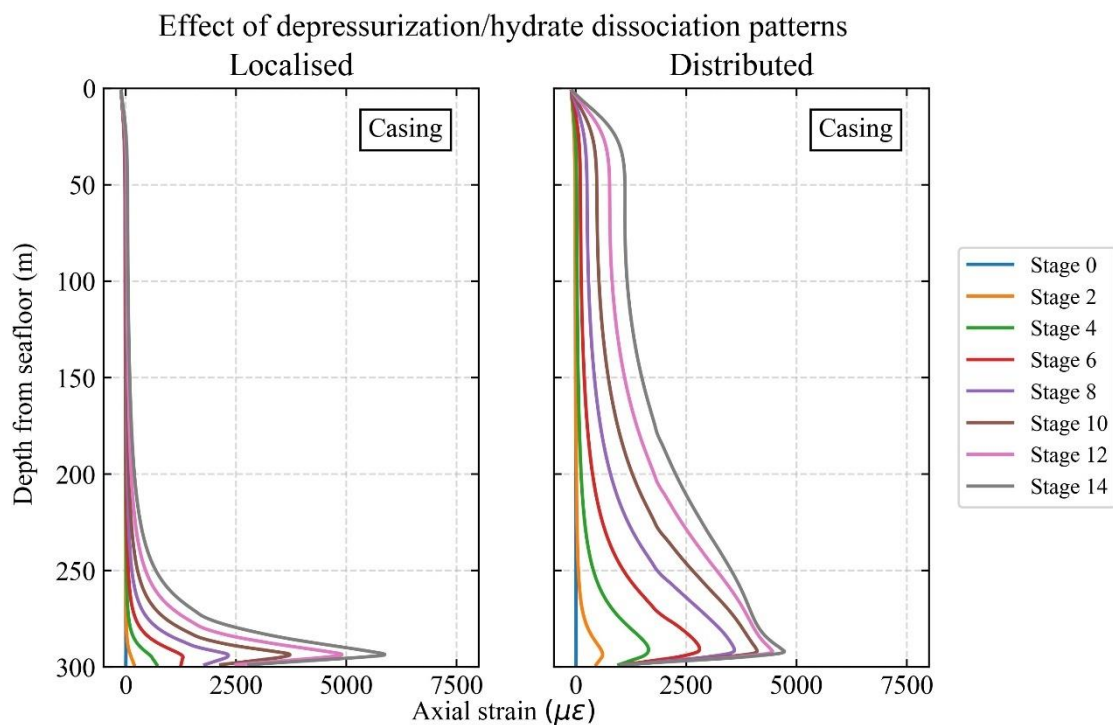
Figure 5-13 Axial strain profiles of the casing (localized dissociation (ΔP_i = -0.3 MPa and Δr_f = 0.5 m) (left) and distributed dissociation (ΔP_i = -0.3 MPa and Δr_f = 3 m) (right)).

5.3.2. Axial strain development

Figure 5-13 shows the axial strain development of the casing. It is found that in both cases the maximum axial strain level in the casing is developed near the bottom of the overburden layer (approximately 290 m) and the value is roughly 5,000 $\mu\varepsilon$ at the depressurization/hydrate dissociation stage 14. However, the average axial strain level along the depth of the casing is greater in the distributed dissociation case than in the localised dissociation case. This corresponds to the overburden layer deformation pattern where the vertical displacement is more evenly spread over the depth and radius of the overburden layer in the distributed dissociation case than in the localised dissociation case.
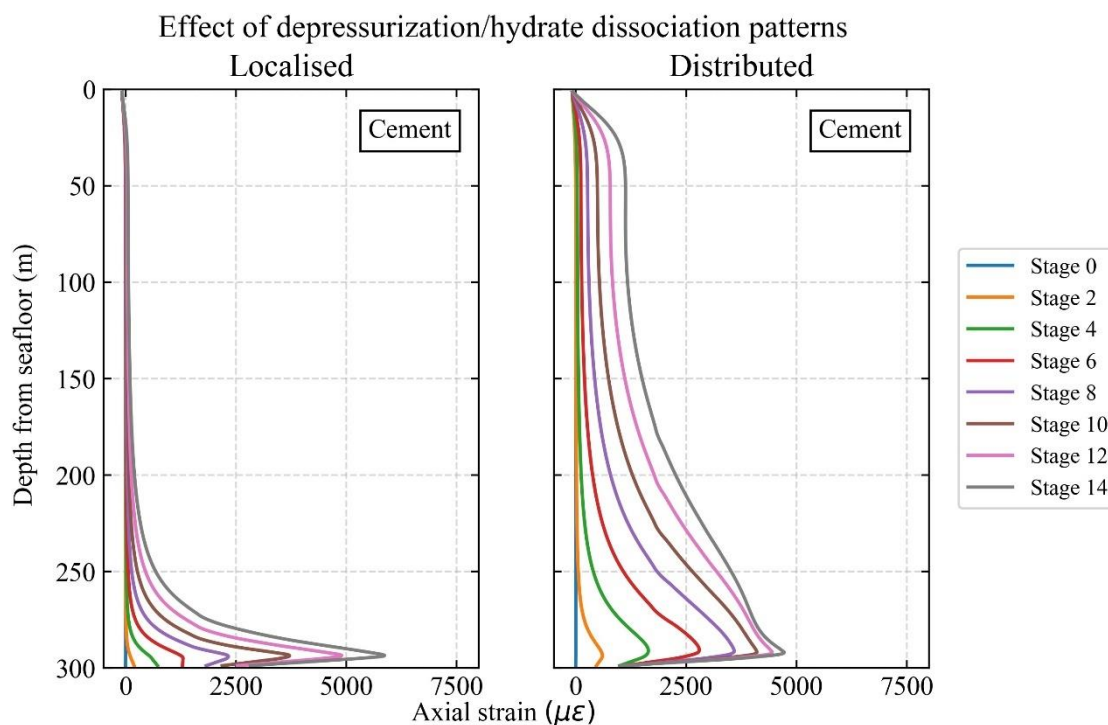
Figure 5-14 Axial strain profiles of the cement (localized dissociation (ΔP_i = -0.3 MPa and Δr_f = 0.5 m) (left) and distributed dissociation (ΔP_i = -0.3 MPa and Δr_f = 3 m) (right)).

Figure 5-14 shows the axial strain development of the cement. It is found that they are identical to those of the casing, which indicates that the interface slippage at the casing-cement interface does not occur under the simulated reservoir subsidence cases. This also suggests that the axial strain distribution of the casing could be estimated from that of the cement, which can be measured by strain sensors embedded in the cement. Distributed monitoring of the axial strain development of the well with fibre optic sensing techniques might be applicable for such measurement. Experimental studies on the potential of distributed fibre optic monitoring of well integrity are presented in Chapter 6 and 7 of this thesis.

It is noted that the small compressive strain (i.e., negative strain values) developed at the top of the well is caused by the casing landing stage, where the casing is released from hanging and compressed in the upper part of the well. In the experiments of fibre optic monitoring of well specimens described in Chapter 6 and 7, this compression effect is not incorporated during the specimen preparation. Hence, those test results are relevant to the middle and/or bottom depths of the well. Based on the depth of the initial compressive strain zone at depressurization/hydrate dissociation stage 0, the depth of the well affected by the casing landing stage is estimated to be approximately between 0 m and 30 m (approximately 10% of the well length).
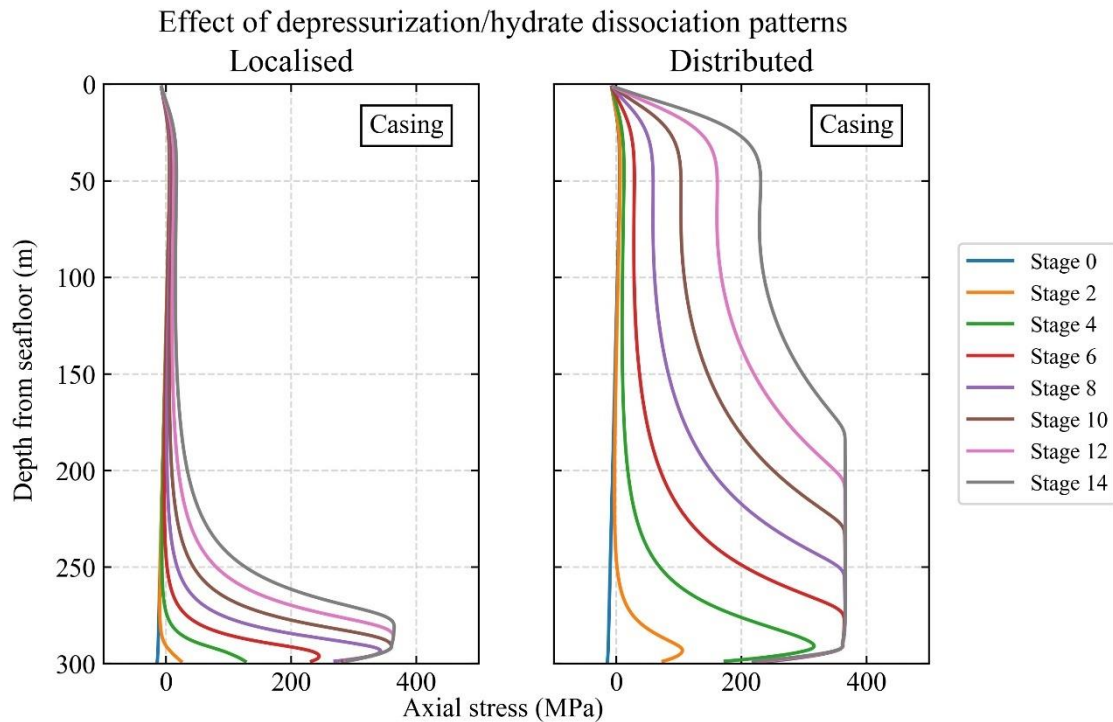
Figure 5-15 Axial stress profiles of the casing (localized dissociation (ΔP_i = -0.3 MPa and Δr_f = 0.5 m) (left) and distributed dissociation (ΔP_i = -0.3 MPa and Δr_f = 3 m) (right)).

5.3.3. Axial stress development

Figure 5-15 shows the axial stress development of the casing. The effect of depressurization/hydrate dissociation cases on the axial stress development of the casing is similar to that on the axial strain development of the casing: the average axial stress value of the casing is greater in the localised dissociation case than in the distributed dissociation case. The maximum axial strain level is developed near the bottom of the overburden layer, as it is the case for the maximum axial strain level. The difference, however, is that the axial stress level reaches its plateau once the deviator stress level exceeds the yield stress level of the casing (379.5 MPa) and the area of the axial stress plateau expands upward with the progress of depressurization/hydrate dissociation stages. The area of axial stress plateau indicates the area of plastic strain development and it covers the depths between 180 m and 290 m (i.e., 37% of the casing length) at the dissociation stage 14 in the distributed dissociation case. The plastic strain development is discussed later in the following section.
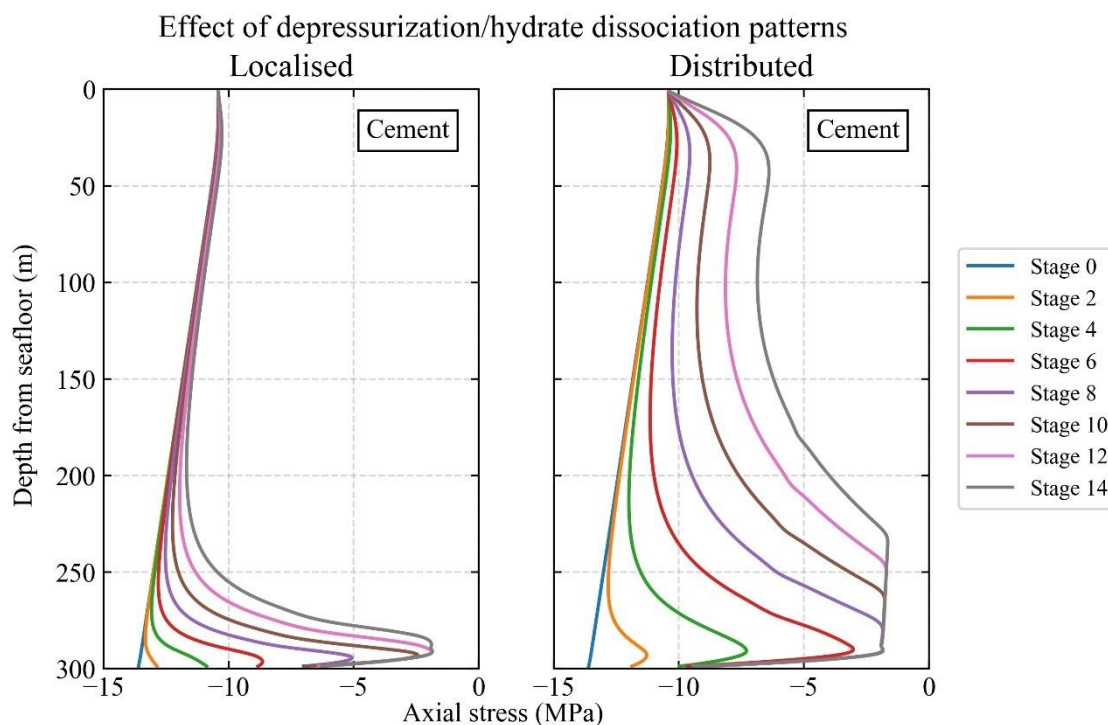
Figure 5-16 Axial stress profiles of the cement (localized dissociation (ΔP_i = -0.3 MPa and Δr_f = 0.5 m) (left) and distributed dissociation (ΔP_i = -0.3 MPa and Δr_f = 3 m) (right)).

Figure 5-16 shows the axial stress development of the cement. Due to the smaller stiffness of the cement than that of the casing, the axial stress increase (in tension) in the cement is found to be much smaller than that in the casing. In fact, the axial stress level in the cement does not become tensile (i.e., positive axial stress values) throughout the simulated depressurization/hydrate dissociation stages. The axial stress plateau is also developed in the cement at the bottom of the overburden layer in compressive axial stress values (approximately -2 MPa). This is because the stress level in the cement in this area has reached its yield stress level governed by the Mohr-Coulomb yield criteria. This indicates that the cement fails in shear but tensile failure is unlikely to occur in the simulated depressurization/hydrate dissociation stages as the axial stress level remains in compression. It is noted, however, that if the depth of the well from the sea surface decreases, the initial compressive axial stress levels in the cement also decrease. This could lead to the development of tensile axial stress with or prior to the shear failure. In such cases, the cement might fail in tension and tensile cracks could develop in the cement. Hence, the consideration of the depth of the well from the sea surface would be important in assessing the cement integrity.

5.3.4. Plastic deviatoric strain development

Figure 5-17 shows the plastic deviatoric strain development of the casing. It is found that the area of the casing plastic deviatoric strain development is greater in the distributed dissociation case than in the localised dissociation case, whereas the magnitude of the maximum plastic deviatoric strain is greater in the letter case than in the former case. The area of plastic deviatoric strain development corresponds to the area of the axial stress plateau (i.e., area of yielding) described earlier. Regarding the magnitude of the maximum plastic deviatoric strain, it is found that the increase in the area of the casing stress plateau (i.e., casing yield) helps distribute the development of plastic deviatoric strain over that area. As a result, smaller levels of the maximum plastic deviatoric strain are developed in the casing in the distributed dissociation case (2,900 $\mu\varepsilon$) than in the localised dissociation case (4,000 $\mu\varepsilon$).
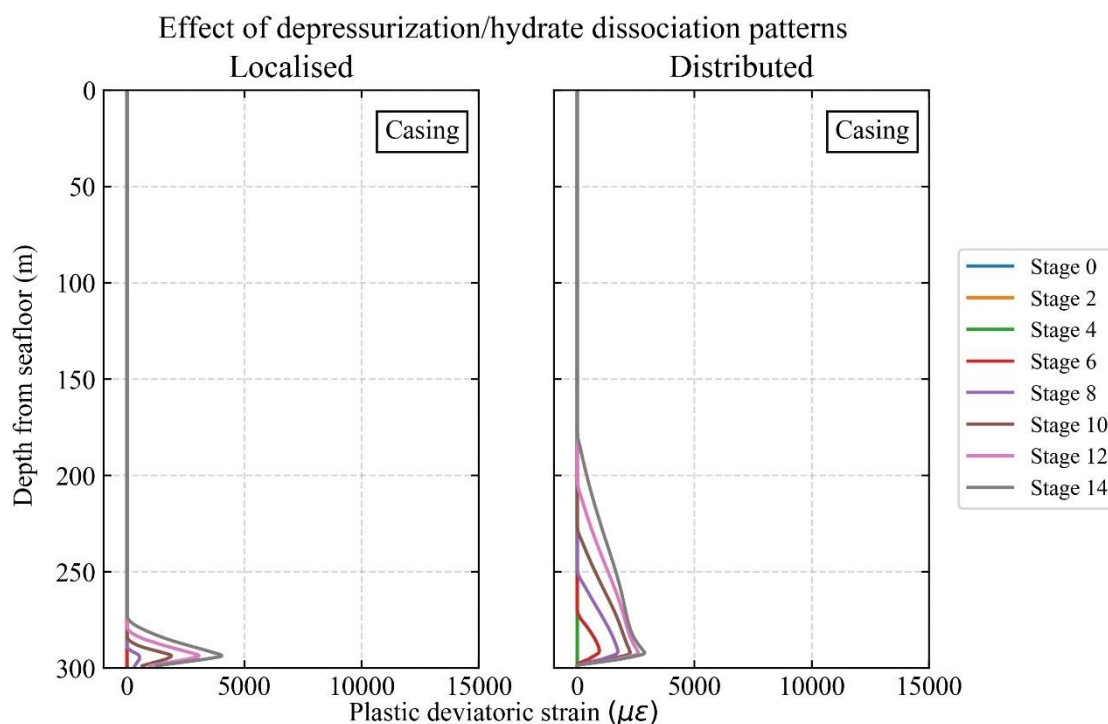
Figure 5-17 Plastic deviatoric stress profiles of the casing (localized dissociation (ΔP_i = -0.3 MPa and Δr_f = 0.5 m) (left) and distributed dissociation (ΔP_i = -0.3 MPa and Δr_f = 3 m) (right)).

The above trends are found to be true in the development of plastic deviatoric strain in the cement as well (Figure 5-18). The difference is that the magnitude of the plastic deviatoric strain is much greater in the cement than in the casing (7,400 $\mu\varepsilon$ in the distributed dissociation case and 13,000 $\mu\varepsilon$ in the localised dissociation case). This is because the area of yielding in the cement is localised within a smaller area than that in the casing. It also indicates that the cement is a brittle material

as opposed to the casing which is ductile.
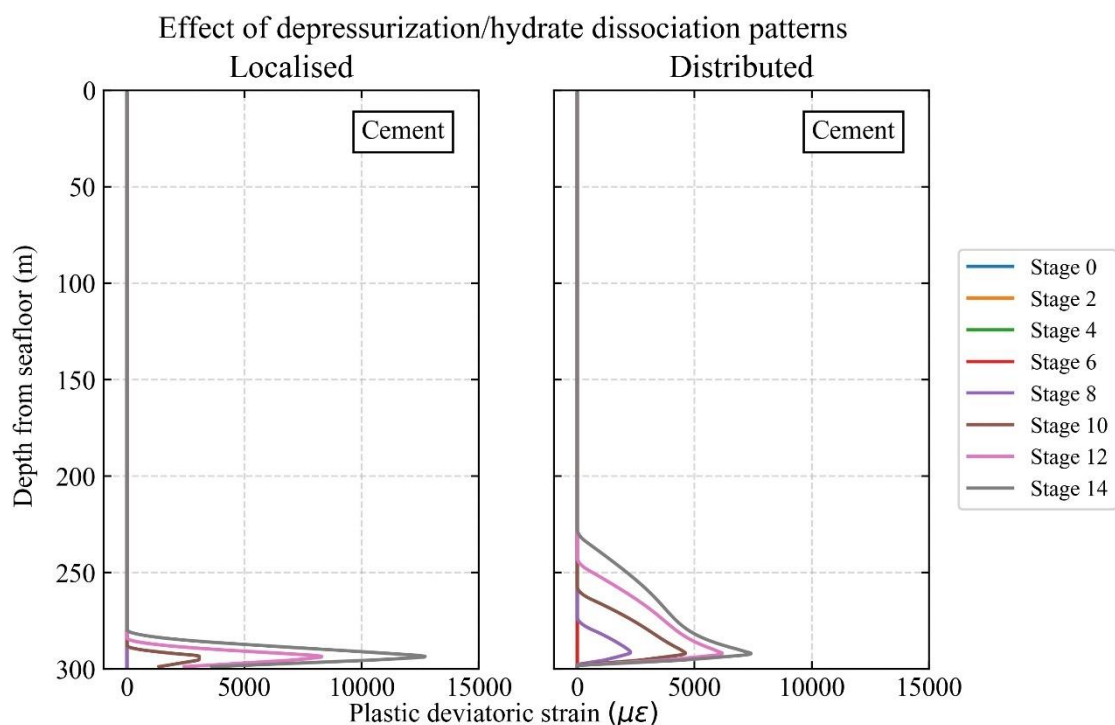
Figure 5-18 Plastic deviatoric stress profiles of the cement (localized dissociation (ΔP_i = -0.3 MPa and Δr_f = 0.5 m) (left) and distributed dissociation (ΔP_i = -0.3 MPa and Δr_f = 3 m) (right)).

5.3.5.   Effect of cement shrinkage

Cement shrinkage occurs due to the capillary pressure development in the cement pores during cement hydration process. In the Nankai Trough formation case, cement shrinkage volume could potentially reach 0.75% (Sasaki et al., 2018). Therefore, the cement shrinkage volume in the cement shrinkage stage is increased from 0% to 0.75% to assess its effect on well integrity.

Figure 5-19 shows the axial stress development of the cement with the cement shrinkage volume of 0% and 0.75%. It is found that the cement has yielded extensively and developed stress plateau over the entire length of the cement prior to the depressurization/hydrate dissociation (i.e., reservoir subsidence) stages in the 0.75% cement shrinkage case. The axial stress level in the cement in the 0.75% shrinkage case remains constant at approximately -2 MPa throughout the reservoir subsidence stages. The negative axial stress value shows that the plastic deformation of the cement occurs in shear but not in tension.
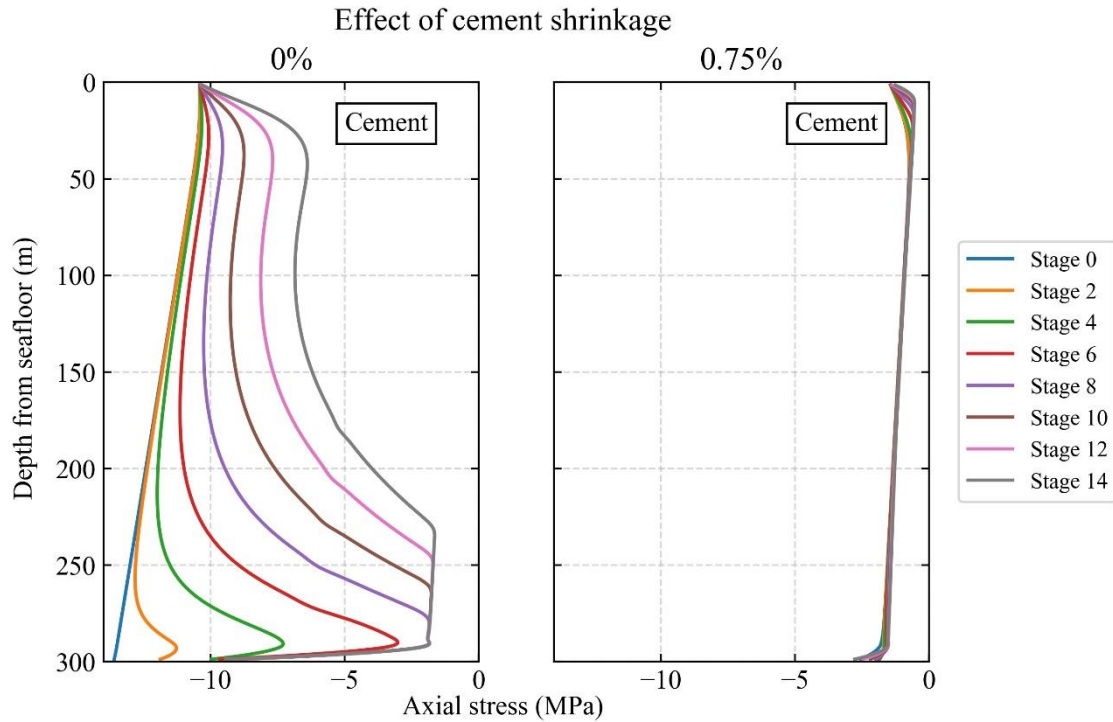
Figure 5-19 Axial stress profiles of the cement with the cement shrinkage volume of 0% and 0.75% (ΔP_i = -0.3 MPa and Δr_f = 3 m).
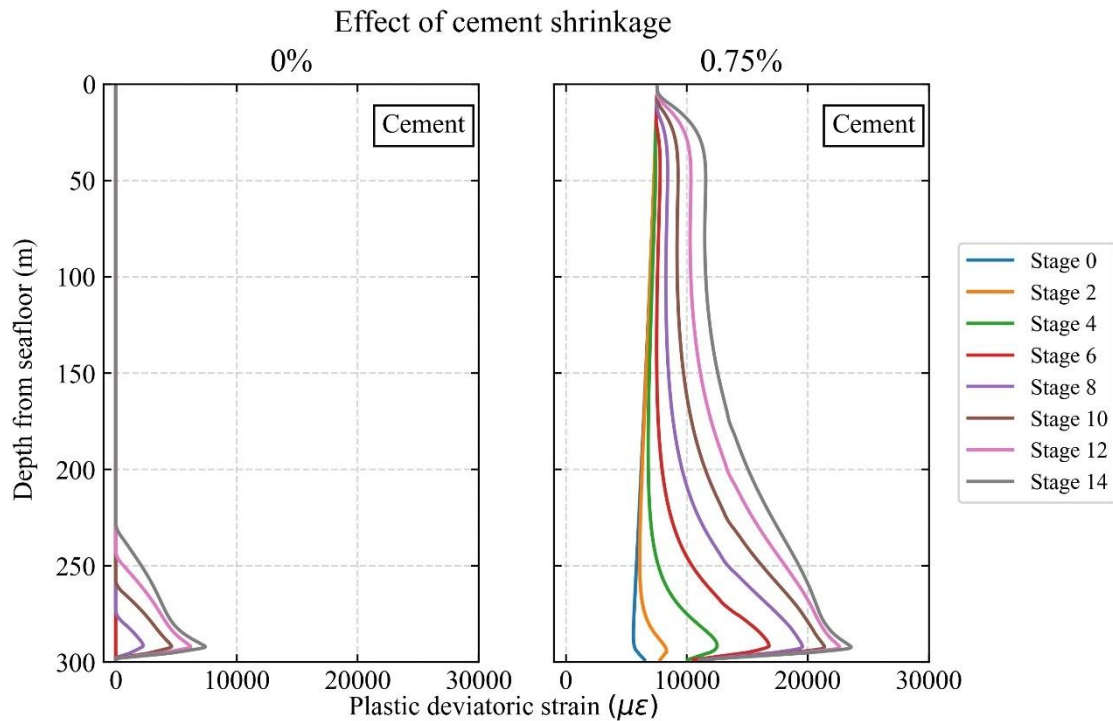
Figure 5-20 Plastic deviatoric strain profiles of the cement with the cement shrinkage volume of 0% and 0.75% (ΔP_i = -0.3 MPa and Δr_f = 3 m).

130

Figure 5-20 shows the corresponding plastic deviatoric strain development of the cement. The average plastic strain level of approximately 6,600 $\mu\varepsilon$ is already developed in the cement due to the cement shrinkage volume of 0.75% prior to reservoir subsidence and it increases with the progress of reservoir subsidence to the maximum value of 24,000 $\mu\varepsilon$ at the bottom part of the well. Compared to the 0% cement shrinkage case, the maximum plastic deviatoric strain in the 0.75% cement shrinkage case is found to increase by more than 200% at the reservoir subsidence stage 14 (7,400 $\mu\varepsilon$ vs. 24,000 $\mu\varepsilon$).

Figure 5-21 shows the axial strain development of the casing and cement with the cement shrinkage volume of 0% and 0.75%. It is found that unlike the axial stress development, the axial strain development of the cement is not affected by the cement shrinkage volume of 0.75%. Also, the axial strain profiles of the casing and cement are found to be identical to each other. These results suggest that the interface slippage at the formation-cemet or cement-casing interface is not induced by the cemet shrinakge volume of 0.75%.

In order to confirm this, a back-of-the-envelope calculation is performed with the analytical solution for the cavity expansion/contraction of an elastic cylinder presented in Section 4.3.4. in Chpter 4. The decrease in the radial effective stress at the cement-formation interface due to cement shrinkage is obtained by substituting Equation 4-8 into 4-7:

$$\Delta\sigma'_r = 2G \left[\sqrt{\left(1 - \left(\frac{r_c}{r_o}\right)^2\right)\left(\frac{100 - \Delta V_{cement}}{100}\right) + \left(\frac{r_c}{r_o}\right)^2} - 1 \right] \tag{5-11}$$

where $\Delta\sigma'_r$ = change in the radial effective stress, G = shear modulus of the formation, r_c = outer radius of the casing, r_o = radius of the wellbore and ΔV_{cement} = volume change of the cement in percent. The value of shear modulus of the overburden layer at 200 m below the seafloor is approximately 40 MPa and the value of r_c/r_o is 0.7857. By setting the value of ΔV_{cement} to 0.75%, the decrease in the radial effective stress is calculated to be $\Delta\sigma'_r$ = -0.115 MPa. The corresponding decrease in the ultimate interface shear stress at the cement-formation interface is $\Delta\tau_{ult} = \mu\Delta\sigma'_r$ = -0.092 MPa (μ = 0.8). This decrease in the interface shear resistance is too small to induce interface slippage. Also, at the casing-cement interface, the radial confining stress increases due to cement shrinkage, which prevents the slipplage from occuring. Therefore, the cement shrinkage volume of 0.75% does not affect the axial strain development of the casing and cement through the reduction in the radial confining stress from the formation.

Effect of cement shrinkage

(a)

Effect of cement shrinkage

(b)
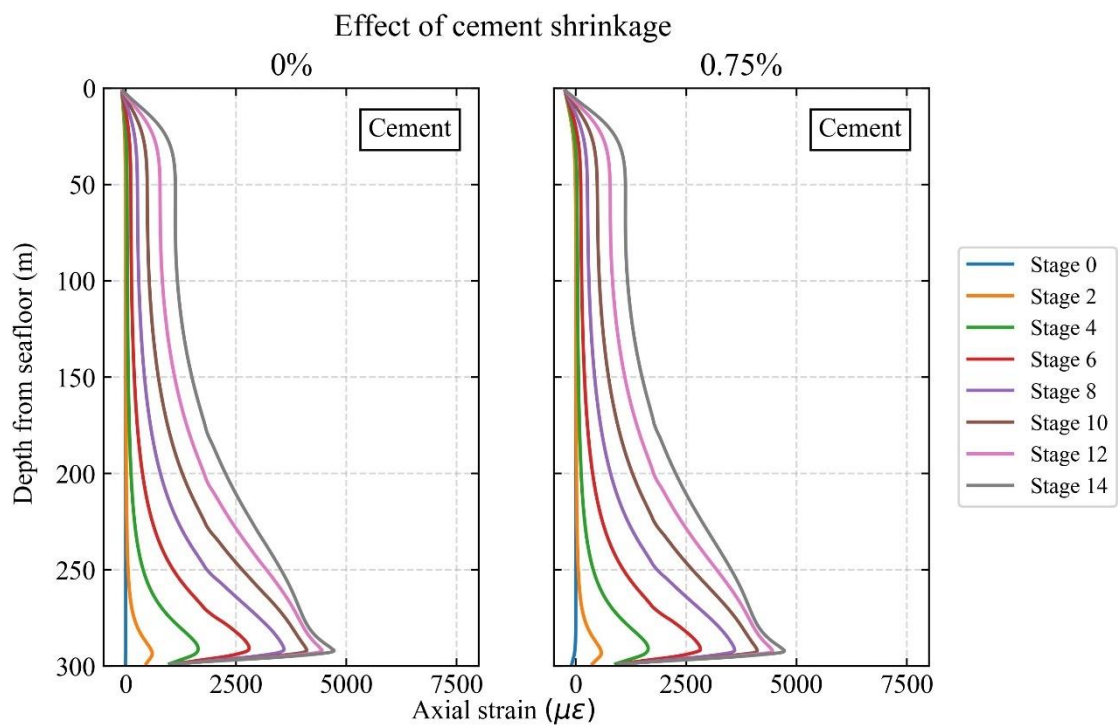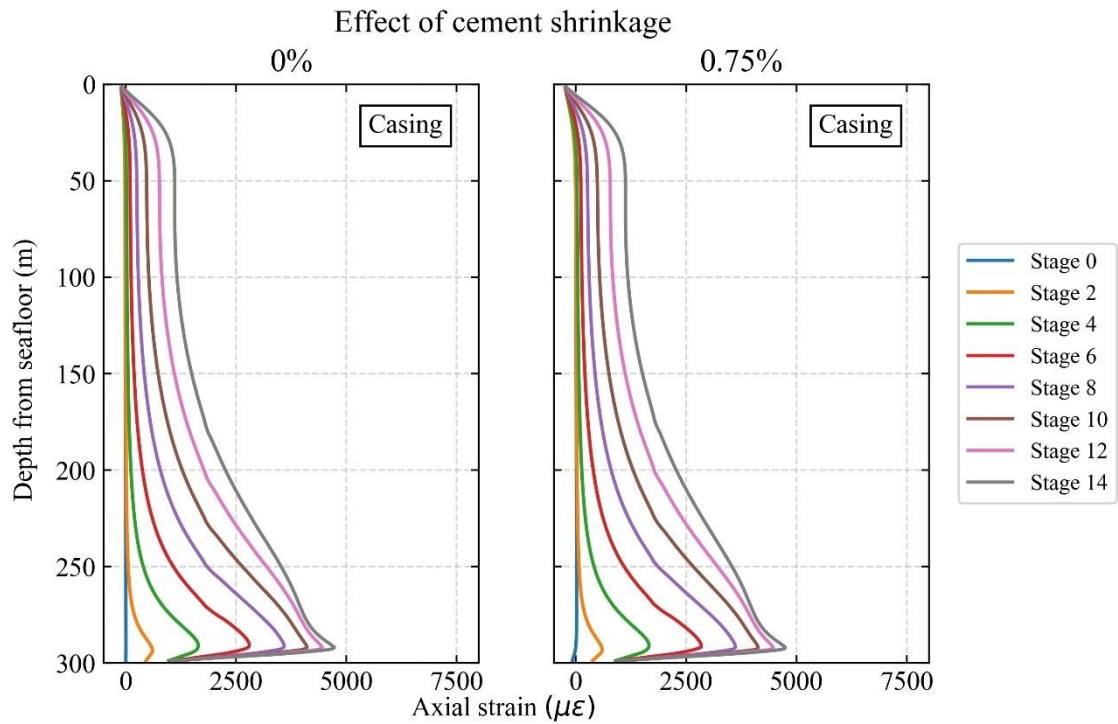
Figure 5-21 Axial strain profiles of (a) the casing and (b) the cement with the cement shrinkage volume of 0% and 0.75% (ΔP_i = -0.3 MPa and Δr_f = 3 m).

5.3.6. Effect of the initial horizontal stress of the formation

The simulation results presented in the earlier sections are computed on the assumption that the formation is initially overconsolidated, because the triaxial tests on the formation samples taken from the Nankai Trough site shows that this is the case (Nishio et al. 2011). However, there are uncertainties over the actual stress state of the Nankai Trough formation due to its complex geologic conditions as it is located near the subduction zone. Also, the formation samples were found to be significantly disturbed prior to the triaxial tests, which decreases the accuracy of the estimation of the stress state of the formation. Therefore, additional simulations for the normally consolidated formation case are conducted. The difference in the horizontal stress profiles of the consolidated and normally consolidated cases are shown earlier in Figure 5-8. It is noted that the cement shrinkage volume is set to 0% in these simulations.
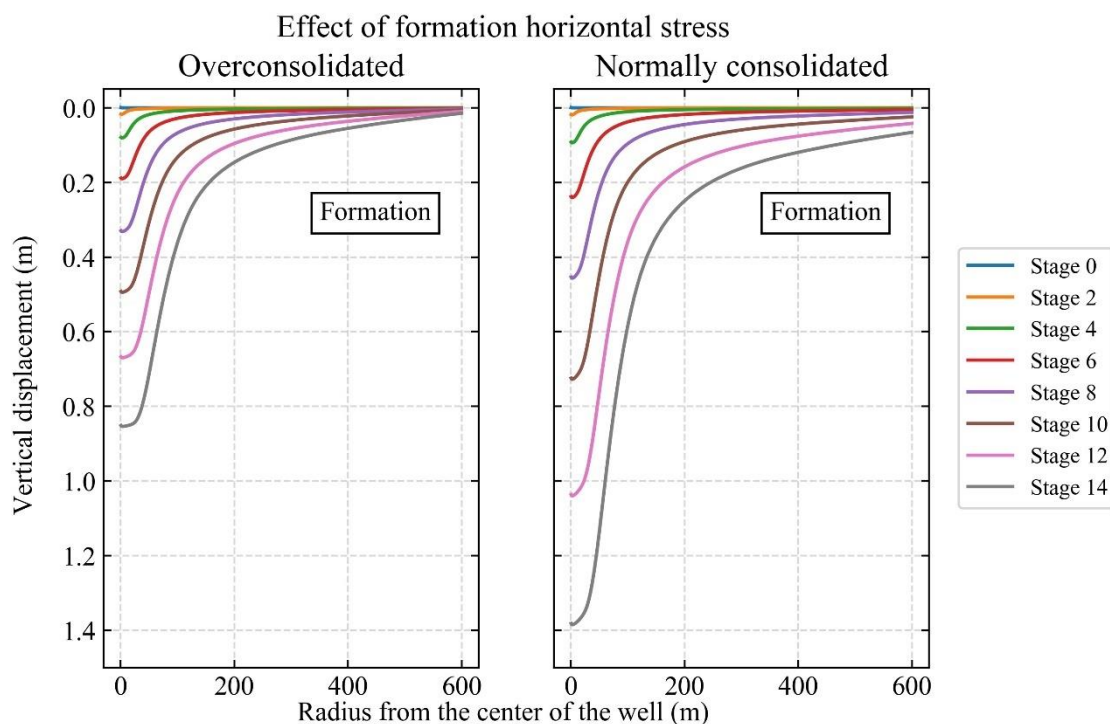
Figure 5-22 Reservoir subsidence along the top of the reservoir layer in the overconsolidated and normally consolidated cases (ΔP_i = -0.3 MPa and Δr_f = 3 m).

Figure 5-22 shows the reservoir subsidence profiles for the overconsolidated and normally consolidated formation cases. It is found that the reservoir subsidence is enhanced if the formation is assumed to be normally consolidated. The maximum reservoir subsidence at the depressurization/hydrate dissociation stage 14 increases from 0.85 m (overconsolidated case) to 1.4 m (normally consolidated case). This is because the ratio of vertical effective stress to horizontal effective stress (i.e., K_0 value) in the reservoir layer is smaller in the normally consolidated formation case (0.40) than in the overconsolidated case (0.44), which increases the magnitude of volumetric compaction per unit increase in mean effective stress in the e-logp' space. In other words, soil becomes stiffer against volumetric compaction with increasing initial mean effective stress level.

The increase in reservoir subsidence due to normally consolidated formation is found to induce increase in the axial and plastic deviatoric strain development of the casing and cement. Figure 5-23 shows the axial strain development of the casing and cement. The maximum axial strain level in the casing increases from approximately 4,700 $\mu\varepsilon$ (overconsolidated formation case) to 7,100 $\mu\varepsilon$ (normally consolidated formation case) and so does the maximum axial strain level in the cement. The axial strain profiles of the casing and cement are identical regardless of the overconsolidated or normally consolidated formation cases, showing that the reduction in the radial effective stress (K_0 value change from 0.44 to 0.40) does not induce interface slippage at the casing-cement interface. Hence, the axial strain development of the casing could still be monitored regardless by measuring the axial strain development of the cement by, for example, fibre optic cables embedded in the cement. Figure 5-24 shows the plastic deviatoric strain development of the casing and cement. It is found that the maximum plastic deviatoric strain levels in the casing and cement (at stage 14) increase from 2,900 $\mu\varepsilon$ (casing) and 7,400 $\mu\varepsilon$ (cement) (overconsolidated formation case) to 5,300 $\mu\varepsilon$ (casing) and 18,000 $\mu\varepsilon$ (cement) (normally consolidated formation case). Therefore, the initial horizontal stress levels of the formation have significant effects on the well integrity during reservoir compaction.

Effect of formation horizontal stress

(a)

Effect of formation horizontal stress

(b)
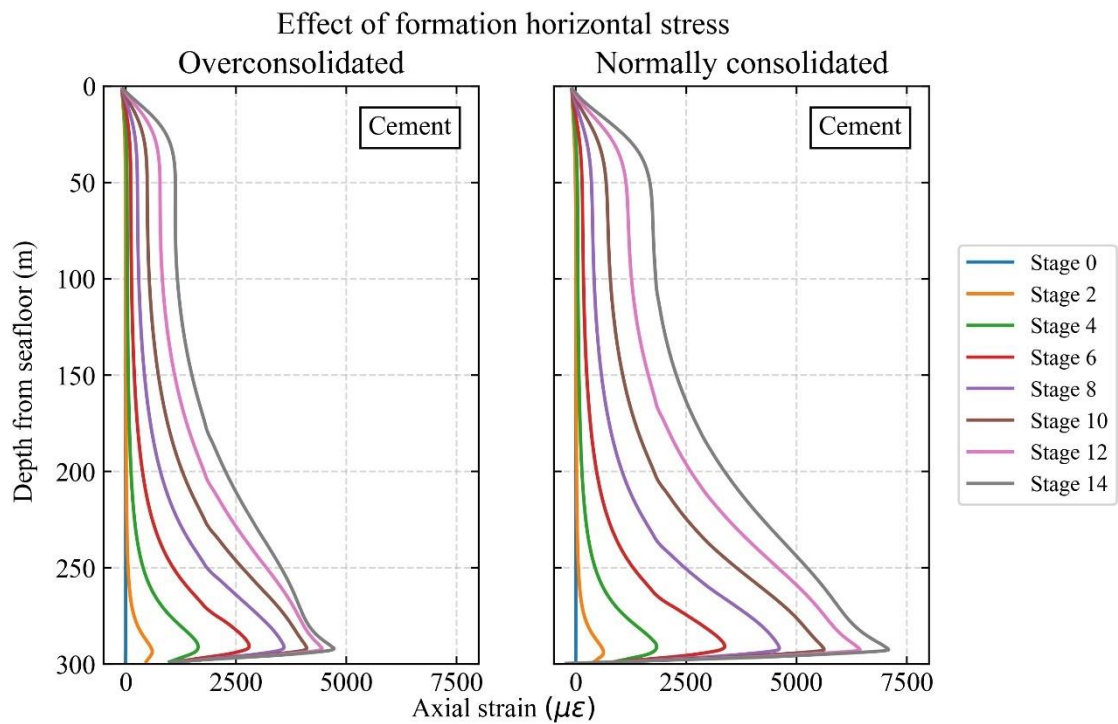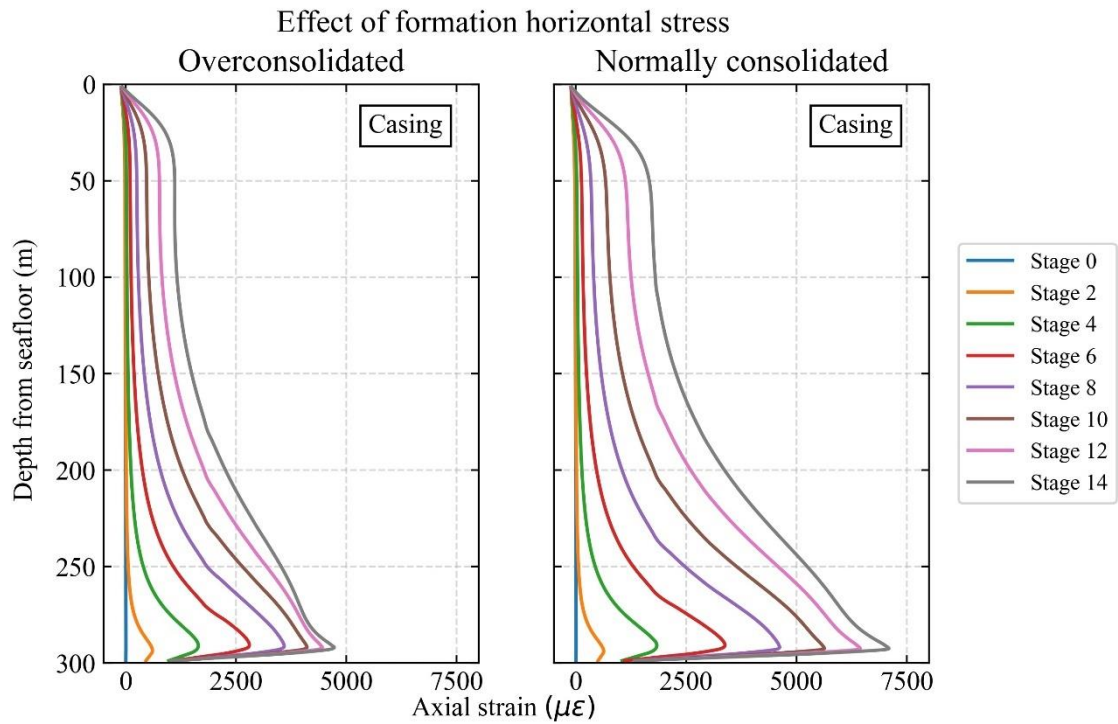
Figure 5-23 Axial strain profiles of (a) the casing and (b) the cement in the overconsolidated and normally consolidated cases (ΔP_i = -0.3 MPa and Δr_f = 3 m).

135

(a)

(b)
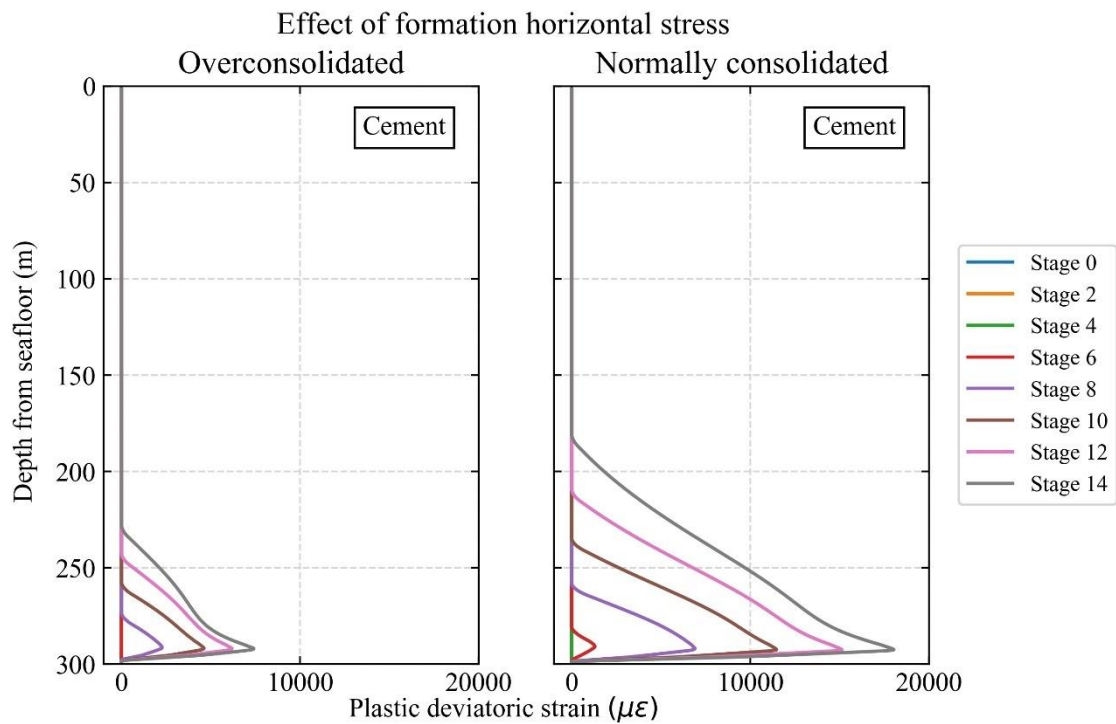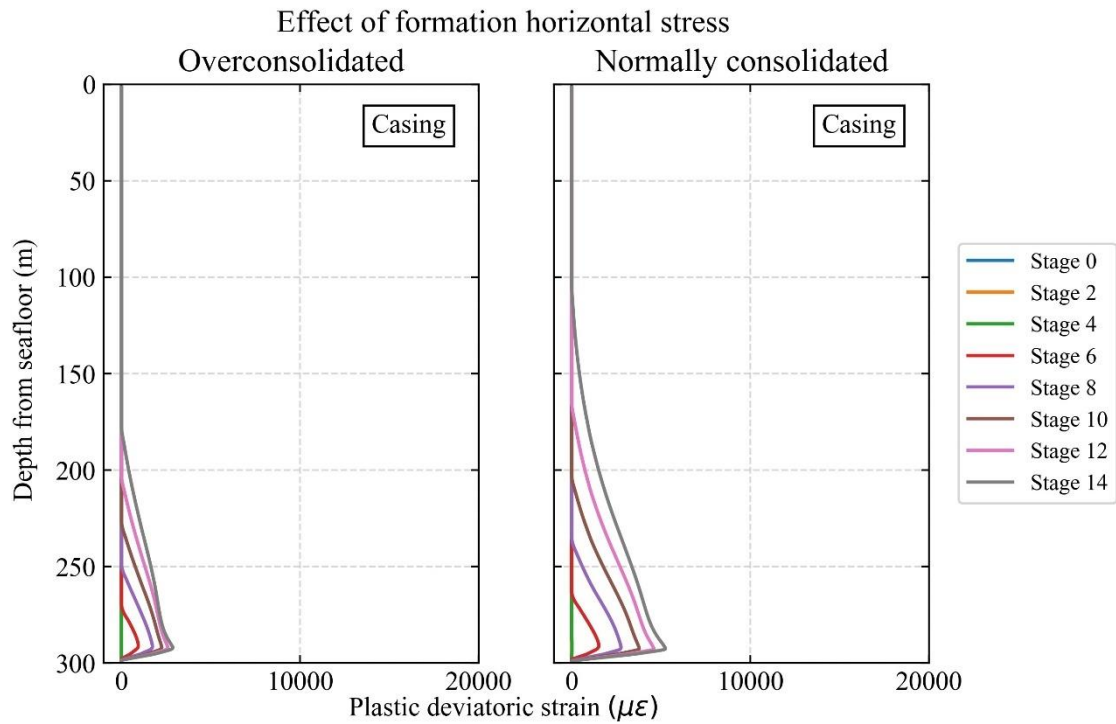
Figure 5-24 Plastic deviatoric strain profiles of (a) the casing and (b) the cement in the overconsolidated and normally consolidated cases (ΔP_i = -0.3 MPa and Δr_f = 3 m).

5.4. Discussion
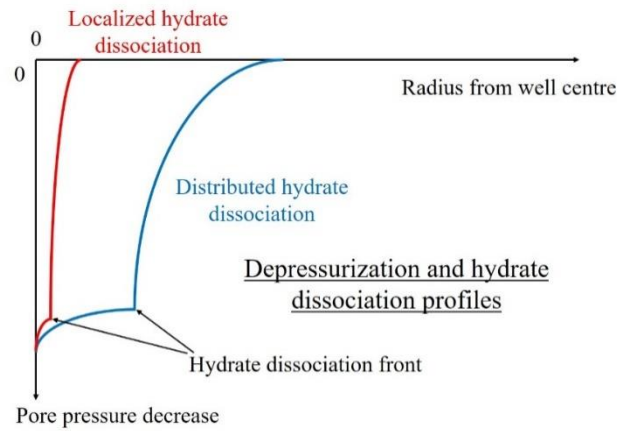
(a)
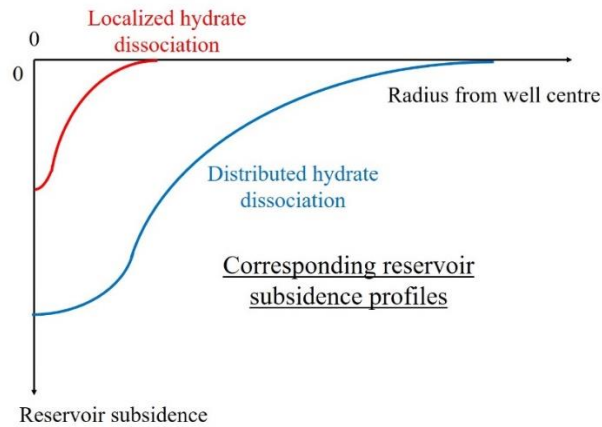
(b)

Figure 5-25 Effect of different depressurization/hydrate dissociation patterns on reservoir subsidence characteristics: (a) simulated pore pressure profiles; (b) consequent reservoir subsidence profiles.

In the preceding sections, well integrity analyses for two depressurization and hydrate dissociation scenarios (i.e., localized and distributed depressurization/hydrate dissociation) are presented to show their effect on the distributions of stresses and strains in the casing and cement. In this section, results from all the simulated 36 depressurization/hydrate dissociation cases are compiled to create the colour maps of maximum axial and plastic deviatoric strains developed in the casing and cement at different pressure drawdown ($\sum \Delta P_i$) and radius of hydrate dissociation front ($\sum \Delta r_f$) values.

It is found that different depressurization/hydrate dissociation patterns create varied reservoir

subsidence profiles. Figure 5-25 shows a schematic diagram depicting how different hydrate dissociation patterns (at the same pressure drawdown) affect the consequent reservoir subsidence profiles. The localized hydrate dissociation induces smaller values of maximum reservoir subsidence and subsidence radius than the distributed hydrate dissociation. This is because when the radius of hydrate dissociation front (r_f) is small, the pressure drawdown does not propagate afar in the reservoir in the radial direction from the centre of the wellbore, resulting in smaller compacted reservoir volume.
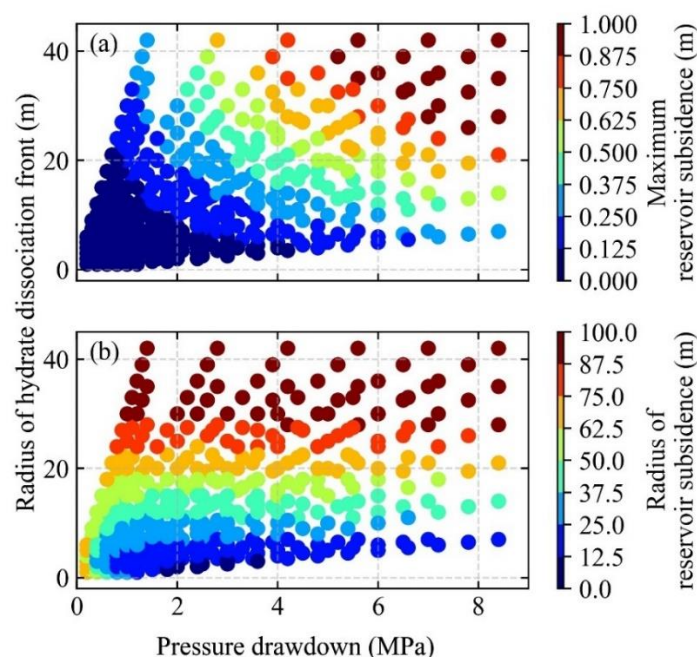
Figure 5-26 Correlations between depressurization/hydrate dissociation patterns and reservoir subsidence characteristics: (a) maximum reservoir subsidence; (b) radius of reservoir subsidence.

Figure 5-26 shows the maximum reservoir subsidence and subsidence radius correlated with pressure drawdown and radius of hydrate dissociation. One data point is extracted from each of the 14 depressurization/hydrate dissociation stages in each of the 36 simulation cases (i.e., 504 data points in total). It is found that the maximum reservoir subsidence increases with increasing pressure drawdown and radius of hydrate dissociation front. For example, if the pressure drawdown is 8 MPa and hydrate dissociation front reaches approximately 25 m from the centre of the wellbore, the maximum reservoir subsidence would approach 1.0 m. It is also found that the reservoir subsidence radius, which indicates the lateral spread of reservoir subsidence, increases with increasing radius of hydrate dissociation front but not with increasing pressure drawdown. This is because when the radius of hydrate dissociation front does not increase, the

pore pressure decrease and compacted volume of the reservoir are localised near the wellbore regardless of the magnitude of pressure drawdown.
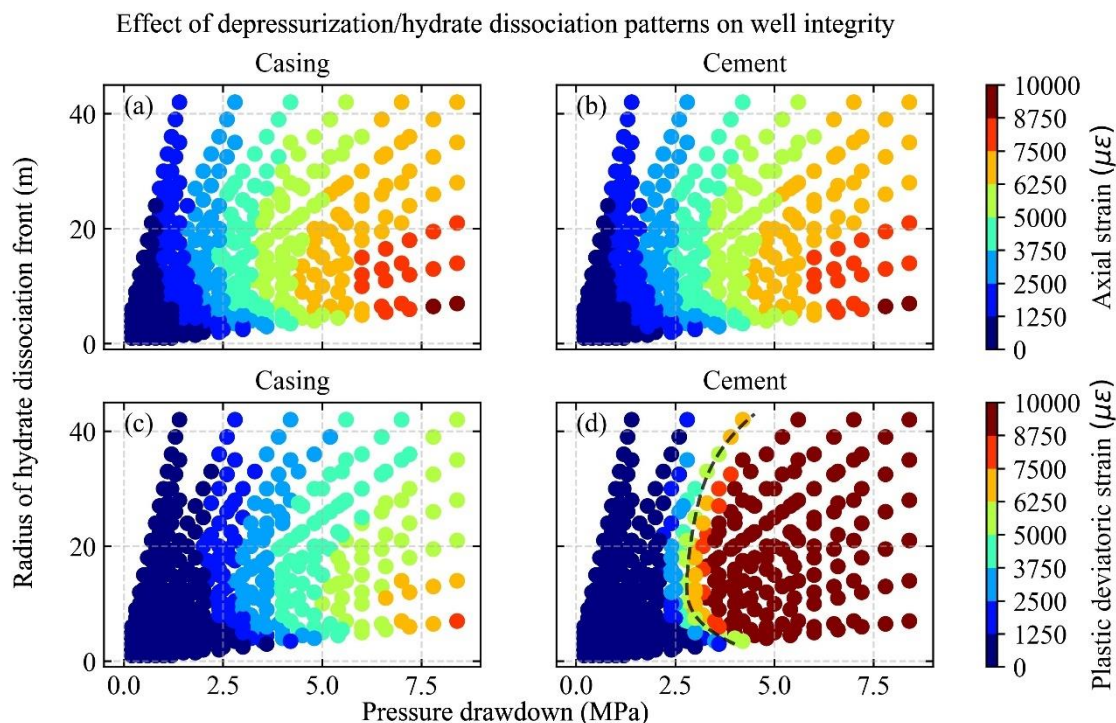
Figure 5-27 The effect of depressurization/hydrate dissociation patterns on well integrity: (a) casing axial strain; (b) cement axial strain; (c) casing plastic deviatoric strain; (d) cement plastic deviatoric strain.

Figure 5-27 shows the change in the maximum axial and plastic deviatoric strain levels in the casing and cement in response to different depressurization/hydrate dissociation patterns. It is found that the larger the pressure drawdown and the smaller the radius of hydrate dissociation front are, the greater the maximum axial strain levels in the casing and cement become (Figure 5-27a and b). For example, if the radius of hydrate dissociation front is only 5 m when the pressure drawdown of 8 MPa is achieved, the maximum axial strain levels in the casing and cement could both reach 10,000 μɛ (i.e., 1%). This level of strain does not cause failure in the casing, which is ductile enough to withstand up to several tens of percent strain, but not in the cement which is a much more brittle material than the casing. Figure 5-27c and d show the maximum plastic deviatoric strain levels in the casing and cement. It is found that the casing develops plastic deviatoric strain gradually due to its ductility. The cement, however, develops large values of plastic deviatoric strain rapidly as the plastic strain level suddenly jumps once the values of pressure drawdown and radius of hydrate dissociation front exceed the dashed line shown in Figure 5-27d. This shows that the cement failure could be localized in the form of, for

example, cracks.

The result also indicates that, in order to avoid the development of high axial strain levels in the casing and cement, pressure drawdown might have to be kept at low levels while the radius of hydrate dissociation front increases above certain values. For instance, if the axial strain level of 10,000 $\mu\varepsilon$ needs to be avoided to ensure that the fibre optic cables installed in the well survive the initial hydrate dissociation process, pressure drawdown could be temporarily stopped and held at 6 MPa until the radius of hydrate dissociation front reaches 25 m. After that, further pressure drawdown could be performed without exceeding the strain limit of the well or instrument installed in the well. It is noted, however, that the simulated pressure drawdown and radius of hydrate dissociation front increase linearly with time simultaneously, which may not be realistic considering that the usual field practice is to perform quick pressure drawdown, which would not cause any increase in the radius of hydrate dissociation front, and maintain the pressure drawdown (i.e., no increase in pressure drawdown) so that the radius of hydrate dissociation front increases to produce gas from the hydrate reservoir. Hence, the effect of the path of pressure drawdown and radius of hydrate dissociation front changes on the stress/strain development in the well has to be examined carefully.
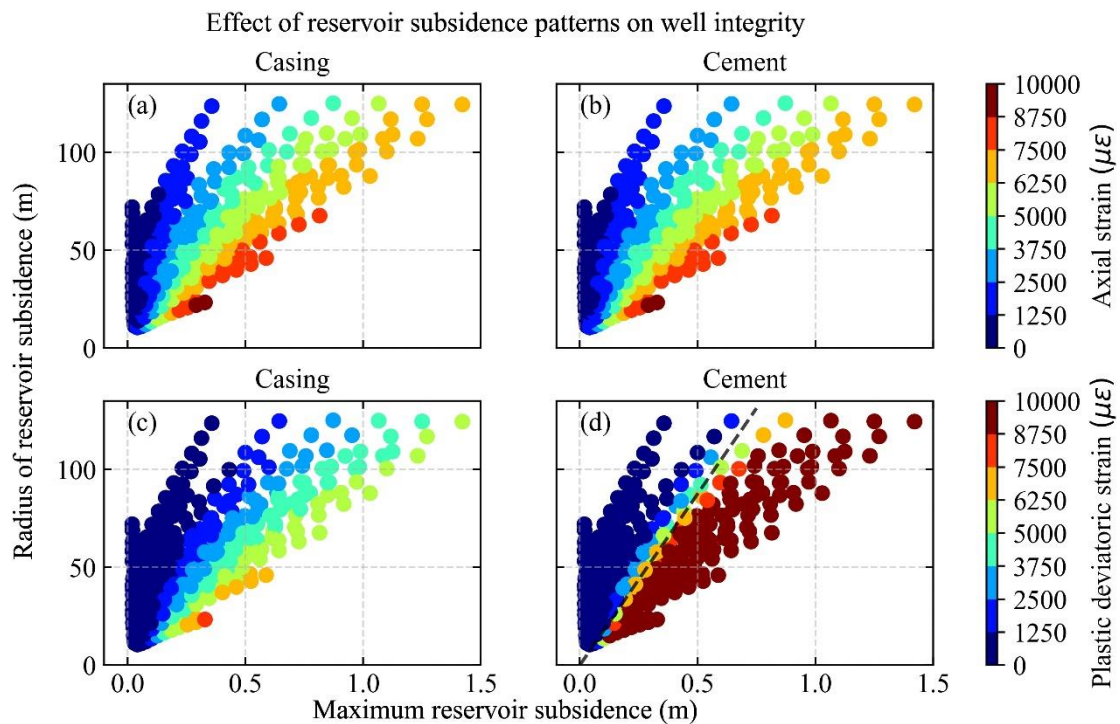
Figure 5-28 The effect of reservoir subsidence characteristics on well integrity: (a) casing axial strain; (b) cement axial strain; (c) casing plastic deviatoric strain; (d) cement plastic deviatoric strain.

Figure 5-28 shows the change in the maximum axial and plastic deviatoric strain levels in the casing and cement with changing reservoir subsidence characteristics. It is found that the larger the maximum reservoir subsidence and the smaller the subsidence radius are, the greater the maximum axial strain levels in the casing and cement become (Figure 5-28a and b). This is because when the subsidence radius is small, the development of overburden layer deformation is localised near the bottom of the overburden layer (see Figure 5-12). As a result, the axial strain development in the casing and cement is concentrated near the bottom of the overburden layer. The maximum plastic deviatoric strain level in the casing changes gradually with changes in the reservoir subsidence characteristics. This is because the casing (i.e., steel) is a ductile material as is mentioned earlier as opposed to the cement which develops large plastic deviatoric strain levels abruptly due to its brittleness. As a result, there are two distinctive areas in Figure 5-28d separated by the dashed line: damaged (below the line) and undamaged (above the line) cement areas. The line can be approximated by the following equation:

$$R_s = 175 \ S_{max} \qquad\qquad (5\text{-}12)$$

where R_s = radius of formation subsidence and S_{max} = maximum formation subsidence. Although the line separates the damaged and undamaged cement areas clearly, the position and shape of the line could be affected significantly by the initial hydrate distribution in the reservoir, which could potentially be highly heterogeneous in the field. In this study, the effect of hydrate saturation distributions on the reservoir behaviour is not considered (i.e., hydrate saturation values in the reservoir are set to zero). This might be acceptable because it is assumed that hydrate saturation has negligible effects on the bulk modulus of the hydrate-bearing soil in the MHCS model employed in this study. However, the shear modulus is enhanced by the presence of hydrate, which helps the reservoir resist inward displacement during depressurization/hydrate dissociation through cavity contraction mechanism. Therefore, the effect of hydrate saturation distributions on the characteristics of reservoir subsidence and well integrity have to be examined carefully. A fully-coupled thermo-hydromechanical simulation would have to be performed to calculate accurate deformations in the reservoir with complex hydrate saturation distributions to assess their effect on well integrity.

5.5. Summary

In this study, a parametric study of well integrity under different reservoir subsidence patterns is

carried out using finite element analysis for the case of the Nankai Trough methane hydrate reservoir. Well construction processes are incorporated prior to the reservoir subsidence stages to investigate the effect of well construction processes, such as cement shrinkage, on well integrity during reservoir compaction. Also, the effect of the initial horizontal stress profile of the formation (i.e., overconsolidated and normally consolidated formation cases) on well integrity is assessed. The MHCS model is used to model the formation behaviour, whereas an interface friction constitutive model is developed to model the behaviour of the casing-cement and cement-formation interfaces. The MHCS and interface friction models are calibrated against relevant laboratory test data. The primary findings of this study are presented below:

(i)   The maximum axial strain and plastic deviatoric strain levels in the casing and cement are found to increase with increasing maximum reservoir subsidence and decreasing radius of formation subsidence (i.e., lateral extent of the subsidence). The computed maximum reservoir subsidence and radius of formation subsidence varies between 0.01 m to 1.42 m and 10.5 m to 125 m, respectively, and the largest maximum axial strain levels developed in the casing and cement are both 9,500 $\mu\varepsilon$, whereas the largest plastic deviatoric strain levels developed in the casing and cement are significantly different (7,700 $\mu\varepsilon$ (casing) vs. 29,000 $\mu\varepsilon$ (cement)). With these levels of strains, the casing is still far from failure (which requires ~30% strain), whereas the cement might already develop localised failures such as cracks.

(ii)   Cement shrinkage volume of 0.75% is found to develop approximately 6,600 $\mu\varepsilon$ plastic deviatoric strain in the cement prior to the reservoir subsidence stages and it increases to the maximum value of 24,000 $\mu\varepsilon$ by the time the reservoir subsidence reaches 0.85 m. Compared to the 0% shrinkage case, the maximum plastic deviatoric strain after the reservoir subsidence of 0.85 m increases by more than 200% (7,400 $\mu\varepsilon$ vs. 24,000 $\mu\varepsilon$) due to the cement shrinkage of 0.75%. The slight change in the initial horizontal stress levels of the formation ($K_0 = 0.40 \sim 0.44$) is also found to affect the maximum plastic deviatoric strain level in the cement by more than 100%. These effects are less pronounced in the casing plastic deviatoric strain development as the casing is ductile whereas the cement is brittle. Therefore, cement shrinkage and initial horizontal stress levels of the formation are both found important in assessing cement integrity and they might have affected the well failure at the Nankai Trough by, for example, inducing fluid flow from the overburden layer through cement cracks.

(iii)   Large pressure drawdown combined with small radius of hydrate dissociation front are

142

found to induce the largest levels of axial and plastic deviatoric strain development in the casing and cement. This indicates that the well integrity would become most vulnerable in the initial stages of hydrate dissociation after rapid depressurization, which is the case in the gas production tests at the Nankai Trough in 2013 and 2017 where the well failure occurred with sand production. In order to circumvent this, the pressure drawdown might have to be kept at a low level (several MPa) until hydrate dissociation front advances to a certain radius.

6. Distributed fibre optic strain monitoring of axial tensile deformation of laboratory-scale well specimens

6.1. Introduction

In the offshore gas production test from methane hydrate reservoirs at the Nankai Trough in 2013, distributed temperature sensing (DTS) with fibre optics was carried out in order to detect the endothermic hydrate dissociation (i.e., temperature decrease is detected if methane hydrate is dissociated). The DTS measurement provided rich datasets for the analysis of flow and hydrate dissociation characteristics of the Nankai Trough formation (Yamamoto et al. 2017). Distributed strain sensing (DSS), however, was not implemented because the risk of well failure during the gas production test was considered insignificant.

However, the gas production test was terminated due to the sand production issue six days after the start of the test. One of the possible causes of the sand production is well failure in the reservoir layer as reservoir compaction, which was described in the previous chapter, might have crashed the screen segment of the well to allow the ingress of formation materials into the well. If DSS had been deployed to monitor the strain development of the well during the gas production test, it could have provided critical information about the initiation of sand production to carry out prompt remedial operations to avert the issue.

In this study, the potential of the BOTDR/A technique to implement the strain monitoring of oil/gas wells was explored in the monitoring of axial tensile deformation of laboratory-scale well specimens. The objectives of this study are as follows:

(i)   to examine the effectiveness of BOTDR/A in detecting axial tensile deformation of the well specimen,

(ii)   to identify key characteristics of fibre optic cables for monitoring the axial strain development of oil/gas wells and

(iii)   to suggest the design of a new fibre optic cable for effective strain BOTDR/A measurements based on (ii).

The tested well specimens consisted of concentric double casings. Fibre optic cables were cemented in the annular gap along the axis of the specimen. The tensile deformation of the specimen was induced by stretching the outer casing, which in turn propagated to the cement and

to the inner casing. A commercial BOTDR/A analyser called Omnisens VISION Dual was employed to carry out BOTDR/A measurements. An FBG analyser from an oil and gas service company was also employed to provide reference strain measurements. Details about the specimen preparation and loading test are provided below.

6.2. Methodology

6.2.1. Design of the specimen

As discussed in the previous chapter, the axial tensile deformation of wells in response to reservoir compaction occurs in the overburden layer of the formation. The overburden layer near the top of the compacting reservoir stretches in the vertical direction while it also compresses toward the well in the horizontal direction (Kristiansen et al. 2005; Li et al. 2003). This overburden movement firmly grabs and pulls the well downward, which gives rise to the tensile strain development of the well, in which the tensile strain propagates from the formation, to the cement and to the casing. To model this axial tensile strain development mechanism of wells, a laboratory-scale specimen was designed as shown in Figure 6-1. The outer casing of the specimen is welded to the top and bottom plate while the inner casing is welded only to the bottom plate. Hence, stretching the specimen results in the tensile strain development first in the outer casing, which then propagates to the cement and to the inner casing, resembling the actual tensile strain development mechanism of wells mentioned earlier. After the design concept of the laboratory-scale specimen was verified by testing of a small-scale specimen of similar design, a 3m-long large-scale specimen was prepared, whose casing diameters corresponded to those of a 9 5/8-in. casing in a 12 1/4-in. borehole, to assess the abovementioned objectives of this study.
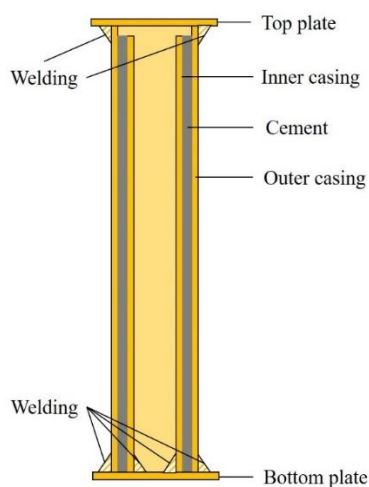
Figure 6-1 A schematic diagram of the configuration of the laboratory-scale specimen.

6.2.2. Fibre optic analysers

The analyser used for the BOTDR/A measurement is shown in Figure 6-2a, which is called Omnisens Vision Dual. The Omnisens analyser is a commercial analyser from a Swiss company of the same name. The analyser employed for the FBG measurement is shown in Figure 6-2b, which is owned and operated by an oil and gas service company. The primary measurement characteristics of the two analysers are provided in Table 6-1.

(a)

(b)

Figure 6-2 The fibre optic analysers employed for the BODTR/A and FBG measurement: (a) Omnisens BOTDR/A analyser; (b) FBG analyser from an oil and gas service company.

Table 6-1 The primary measurement characteristics of the Omnisens (BOTDR) and FBG analysers.

	Omnisens	FBG
Spatial resolution (m)	1.0	0.005
Data sampling interval (m)	0.25	0.02
Axial strain measurement precision ($\mu\varepsilon$)	30	10
Maximum fibre length per channel (km)	15	0.250
Measurement duration per channel (min)	5	3.5

6.3. Tensile loading experiment

6.3.1. Specimen configuration

Figure 6-3 shows the cross section of the large-scale specimen. The outer diameter of the inner casing is 9 5/8 in. (0.24 m) and the inner diameter of the outer casing is 12 1/4 in. (0.31 m). These dimensions corresponds to the diameter of a casing and borehole deployed at the Nankai Trough (Yamamoto et al. 2014). The height of the specimen is approximately 3.0 m, which is three times the spatial resolution of the BOTDR measurement with the Omnisens analyser (BOTDR). To prepare the large-scale specimen, the inner and outer casing subassemblies were first fabricated (Figure 6-4) and they were assembled at the laboratory.
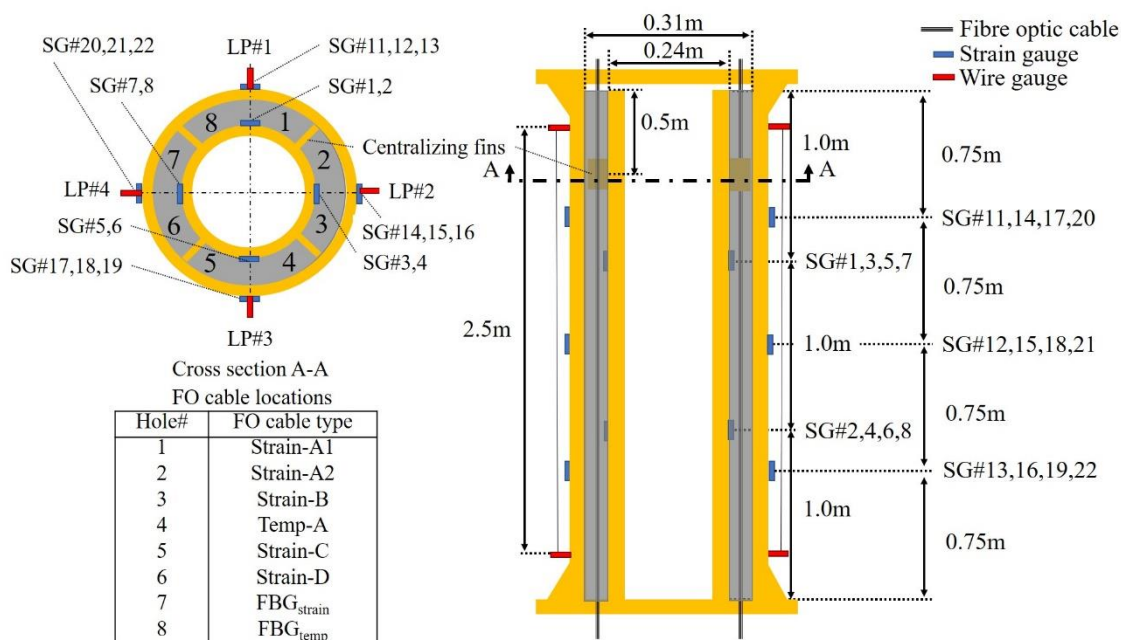
Figure 6-3 The cross sections of the large-scale specimen with types and locations of the instrumented sensors.

Figure 6-4 The inner casing (left) and the outer casing (right) subassemblies of the large-scale specimen.

6.3.2. Sensor instrumentation

The types, locations and number of the instrumented sensors are illustrated in Figure 6-3. Eight strain gauges were attached to the inner casing whereas twelve strain gauges were attached to the outer casing. Wire gauges, which consisted of a piano wire attached to position transducers, were also instrumented on the outer casing.

The fibre optic cables for the BOTDR/A measurement were put through Hole #1 to #6 and they were then spliced with each other to form a connected fibre optic cable (Figure 6-5). The FBG cables were installed in Hole # 7 and #8.

The cross sections of the fibre optic cables employed for the BOTDR/A measurement are illustrated in Figure 6-6. The cables differ significantly in their coating layer characteristics. For example, the Strain-B cable has multiple (excessive) coating layers which makes it robust enough to survive oil and gas well installation. The strain sensitivity of this cable, however, is expected to be low due to increased possibility of slippage between the coating layers. The

Strain-A1, -A2, -C and -D cables, in contrast, have much simpler cross-sections. Therefore, there is in general a trade-off between robustness and strain sensitivity of commercially-available fibre optic cables, which necessitates the identification of key characteristics of fibre optic cables which achieve high robustness and strain sensitivity simultaneously. The values of the strain and temperature coefficients of these cables for BOTDR/A measurements are listed in Table 6-2.

The FBG cable consists of a stainless inner rod and outer tube. Two optical fibres are installed in the gap between the inner rod and outer tube with an adhesive. The Temp-A cable is for temperature measurement as the optical fibres in this cable are encased in a gel-filled tube which isolates the fibres from external strains. The values of the strain and temperature coefficients of the FBG cables are listed in Table 6-3.

Fibre breakage was detected in the BOTDR/A fibre optic cable loop during specimen preparation, which could not be fixed within the timeframe of the test. Therefore, it was decided to employ only BOTDR and to take measurements from both ends of the fibre optic cable loop (i.e., Fibre end 1 and 6 in Figure 6-5).
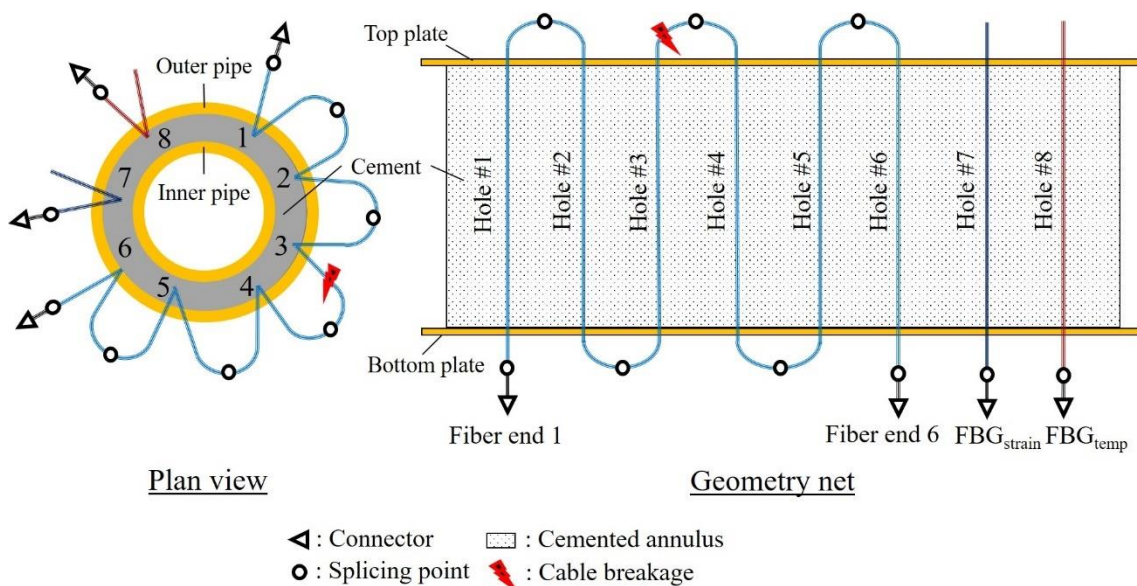
Figure 6-5 The configuration of the fibre optic cables installed in the specimen.
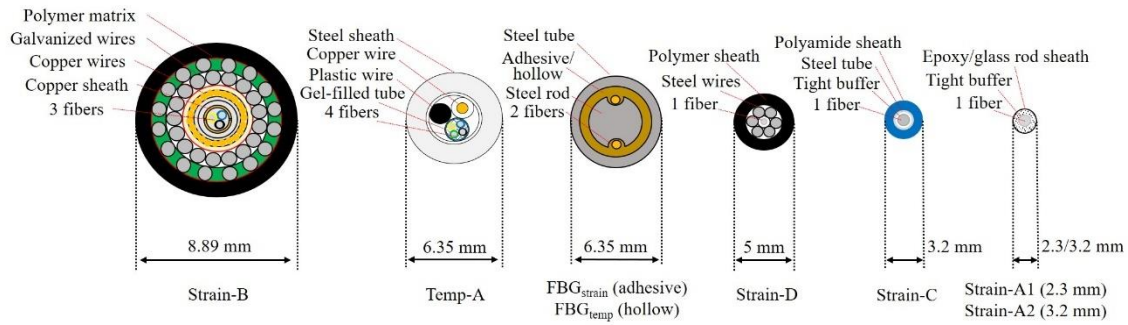
Figure 6-6 The cross sections of the fibre optic cables.

Table 6-2 The values of the BOTDR strain and temperature coefficients of the cables.

	Strain coefficient, C_ε (MHz/%)	Temperature coefficient, C_T (MHz/°C)
Strain-A1	468	1.03
Strain-A2	468	1.03
Strain-B	500	1
Temp-A	N/A	1
Strain-C	450	1.1
Strain-D	499.8	1.775
Strain-E	500	1
Temp-B	N/A	1

Table 6-3 The values of the strain and temperature coefficient of the FBG cables.

	Strain coefficient, $1 - p_e$ (1/µε)	Temperature coefficient, $\alpha_n + \alpha_L$ (1/°C)
FBG$_{strain}$	0.7874×10^{-6}	19.05×10^{-6}
FBG$_{temp}$	0.7874×10^{-6}	9.15×10^{-6}

6.3.3. Monitoring of cement cure process

Class G cement, tap water and the shrinkage reducing admixture (ASTM C494 Type S) were mixed together to prepare cement slurry. The water-to-cement ratio was set to 0.44 and the volume ratio of the admixture was set to 0.75% of the volume of the slurry. The mixing was carried out in four separate batches. The entire cement pour was completed in approximately an hour and the fibre optic monitoring of the temperature change of the cement was initiated with the FBG and Omnisens analyser (BOTDR). Their baseline measurement was taken prior to the cement pour.

Figure 6-7a and b show the temperature change along the Temp-A cable (Hole #4) and FBG$_{temp}$ cable (Hole #8) measured by the BOTDR analyser and FBG analyser, respectively. The averaged nature of the BOTDR measurement can be observed by comparing Figure 6-7a and b. The FBG measurement detected localized high temperature zone between 0 m to 1.0 m whereas it could not be clearly seen in the BOTDR measurement. This is because the BOTDR measurement calculates an average temperature change over the special resolution (i.e., 1 m in this test). The

FBG measurement, in contrast, could capture the localized temperature change with the densely distributed sensing gratings along the FBG cable. The temperature anomaly was generated because the second batch of cement slurry was inadvertently mixed at a lower mixing speed than the other batches. Insufficient mixing resulted in subdued cement hydration reaction and hence the lower temperature increase.
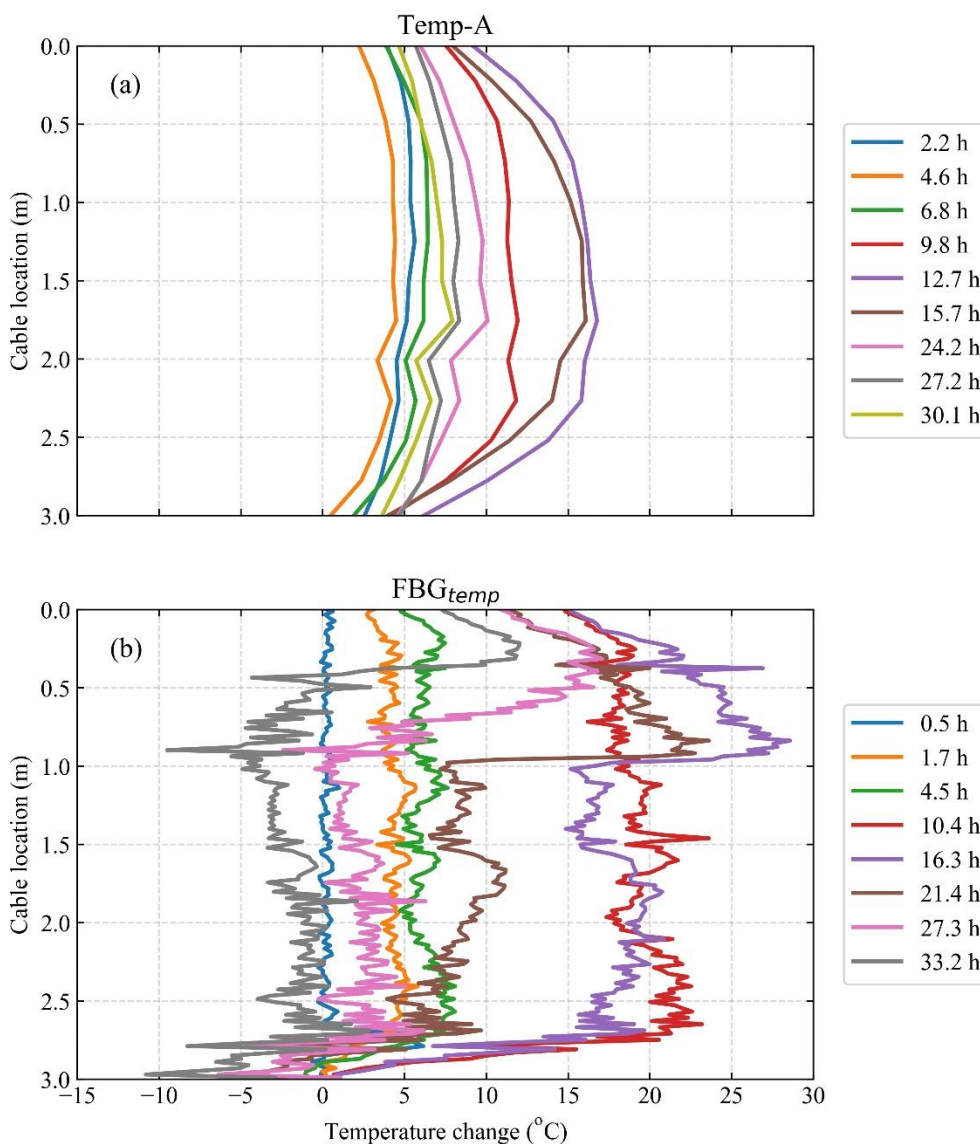
Figure 6-7 Temperature change of the specimen during cement cure: (a) BOTDR measurement; (b) FBG measurement.

6.3.4. Loading test

Six days after the start of cement pour, the tensile loading test was carried out (Figure 6-8). Figure

6-9 shows the time series of the load increments as well as the ambient temperature change during the loading test. Each load increment was held for approximately 15min to allow the period for the BOTDR and FBG measurements. Cyclic loading was carried out to assess potential hysteretic strain transfer characteristics of the fibre optic cables. Before and after the cyclic loading, the load was increased monotonically. The load was increased until the specimen failed at the top part of the outer casing (Figure 6-10)

Figure 6-8 The large-scale specimen set up in a loading frame.
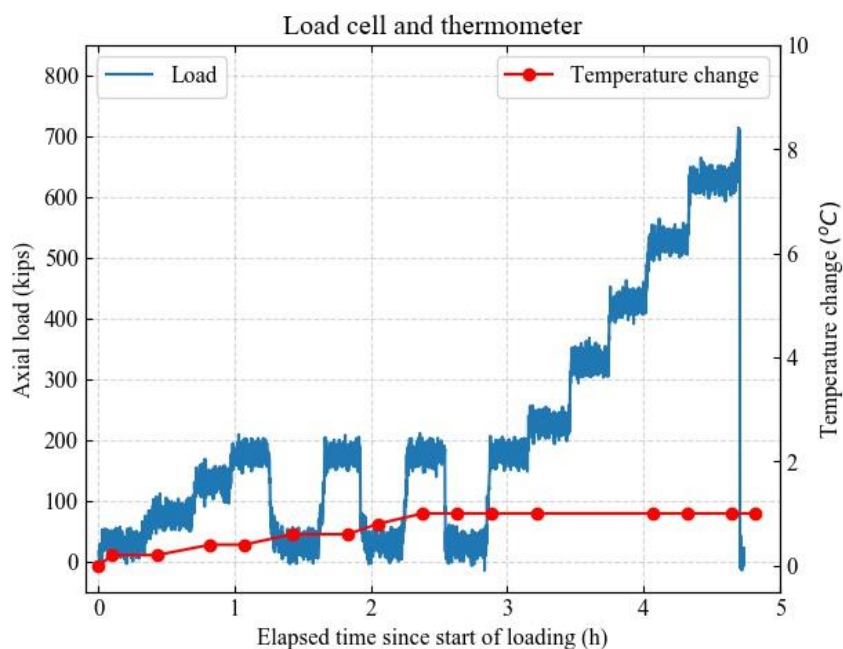
Figure 6-9 The time series of the tensile axial load and temperature change during the loading test.

Figure 6-10 Failure of the specimen at the top part of the outer casing.

Figure 6-11 shows the result of the BOTDR and FBG strain measurement. The effect of temperature change is ignored. It can be seen that the measured strain levels increase with increasing load levels. The strain profiles from the FBG$_{strain}$ cable (Figure 6-11g) shows that the strain distributions from 0.5 m to 2.5 m are relatively uniform. It is assumed that the FBG strain profiles are representative of the real strain profiles of the specimen and they are thus used for the performance evaluation of the fibre optic cables employed for the BOTDR measurement.

Figure 6-11a and b show the strain profiles along the Strain-A1 and Strain-A2 cable, respectively. Similar strain profiles are obtained between the Strain-A cables regardless of the diameter of the cable. The maximum strain magnitude of the Strain-A cables is approximately 1200 με at 625 kips (2,780 kN), which compares favourably with that of the FBG$_{strain}$ cable (i.e., roughly 1100 με at 625 kips). No strain hysteresis is observed in the Strain-A cables during the cyclic loading.

Figure 6-11c shows the strain profiles along the Strain-B cable. The calculated strain magnitudes are slightly smaller than those of the Strain-A cables and FBG$_{strain}$ cable. Also, the strain distributions are not symmetric. This is because of ineffective strain transfer within the coating layers of the Strain-B cable as the number of coating layers of the Strain-B cable are significantly greater than that of the Strain-A cables.
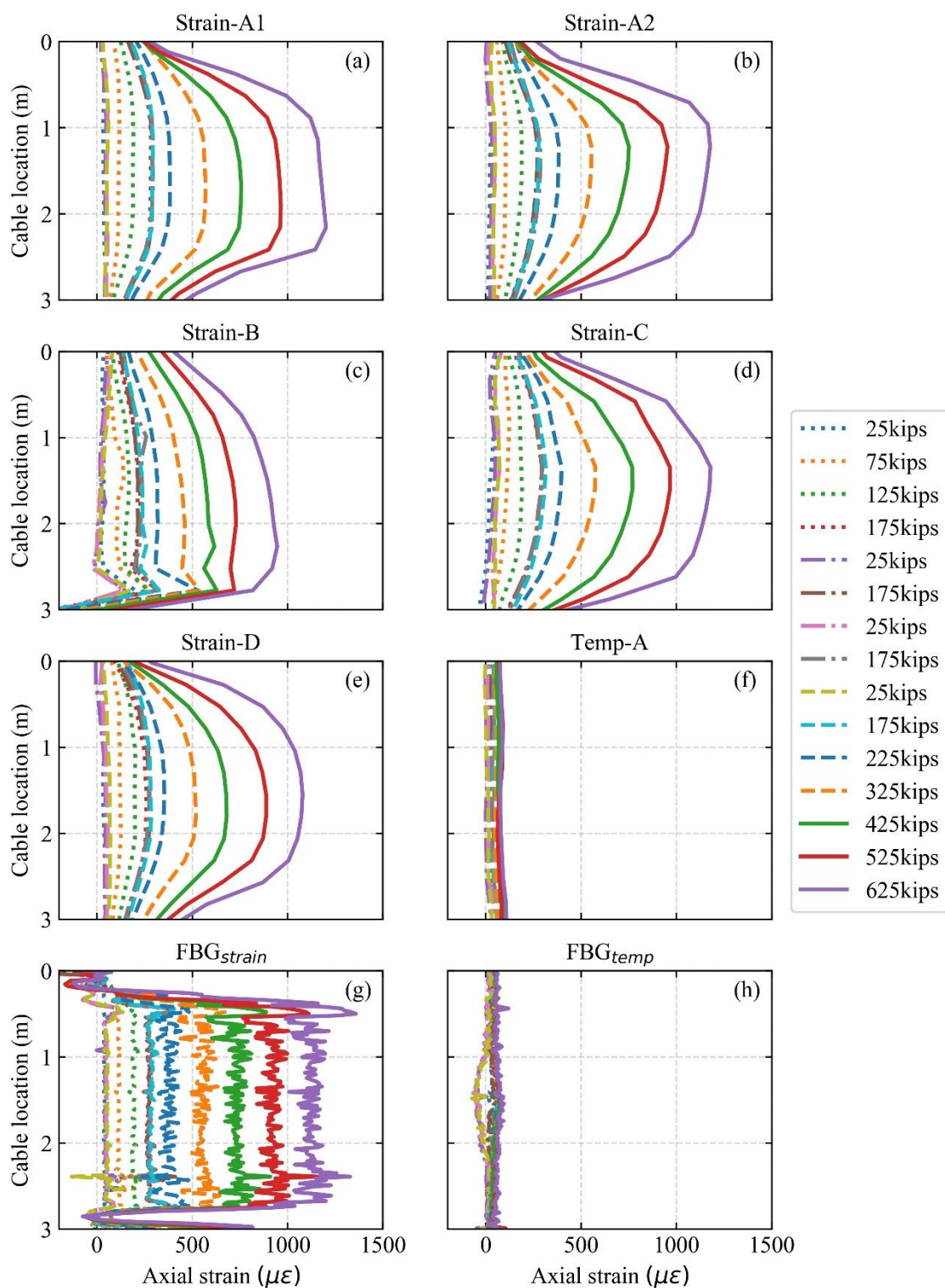
Figure 6-11 Axial strain profiles obtained from the BOTDR and FBG measurements: (a) Strain-A1 (BOTDR); (b) Strain-A2 (BOTDR); (c) Strain-B (BOTDR); (d) Strain-C (BOTDR); (e) Strain-D (BOTDR); (f) Temp-A (BOTDR); (g) FBG$_{strain}$ (FBG); (h) FBG$_{temp}$ (FBG).

Figure 6-11d and e show the strain profiles along the Strain-C and Strain-D cable, respectively. Both profiles are symmetric with the peak strain measured at the centre of the specimen. However, the maximum strain magnitudes at each load increment are larger in the Strain-C cable than in the Strain-D cable. This is mainly because the coating layers of the Strain-C cable are tightly buffered by mechanical compression and chemical adhesion whereas the Strain-D cable relies on the mechanical compression through the steel wire layer which are prone to slippage. As a result, slippage within the coating layers might have accumulated during the cyclic loading in the Strain-D cable. It suggests the importance of tightly buffered coating layers to achieve better strain sensitivity.

It is noted that no axial strain development was detected in the Temp-A and FBG$_{temp}$ cables (Figure 6-11f and h) as the optical fibres in these cables were isolated form external strains by the gel- and air-filled annulus, respectively.

6.4. Discussion

6.4.1. Comparison between BOTDR and FBG measurements

The BOTDR profiles are calculated from the convolution of the real strain profile (ε_{real}) and a convolution function such as the Gaussian function as shown in Equation 6-1:

$$\epsilon_{BOTDR}(x) = \epsilon_{real}(x) \otimes \frac{1}{\sqrt{2\pi\sigma^2}} e^{-\left(\frac{x^2}{2\sigma^2}\right)} \qquad (6\text{-}1)$$

where x = cable distance; $\epsilon_{BOTDR}(x)$ = BOTDR profile; $\epsilon_{real}(x)$ = real strain profile; σ = standard deviation of the Gaussian distribution. The spatial resolution of the BOTDR measurement is defined as the full width at half maximum (FWHM) of the frequency-power spectrum of the incident light pulse, which is assumed to follow the Gaussian distribution herein. The FWHM of the Gaussian distribution is equal to 2.36σ and equating it with the spatial resolution of the BOTDR measurement (i.e., 1.0 m) yields $\sigma = 0.424$ m. This value of the standard deviation was used in Equation 6-1 to convolute the FBG strain profiles (i.e., assumed to be ε_{real}) to produce pseudo BOTDR profiles, which are then compared with the actual BOTDR profiles to evaluate the strain sensitivity of the fibre optic cables.

The comparison between pseudo and actual BOTDR strain profiles are shown in Figure 6-12. The pseudo and actual BOTDR strain profiles are in general in good agreement, which shows that the

strain sensitivity of the fibre optic cables employed for the BOTDR measurement was sufficient. The exception is the Strain-B cable, which highlights the necessity to simplify the coating layers of this cable by, for example, reducing the number of coating layers. Applying mechanical compression and/or chemical adhesion between the coating layers might also improve the strain sensitivity of the Strain-B cable.
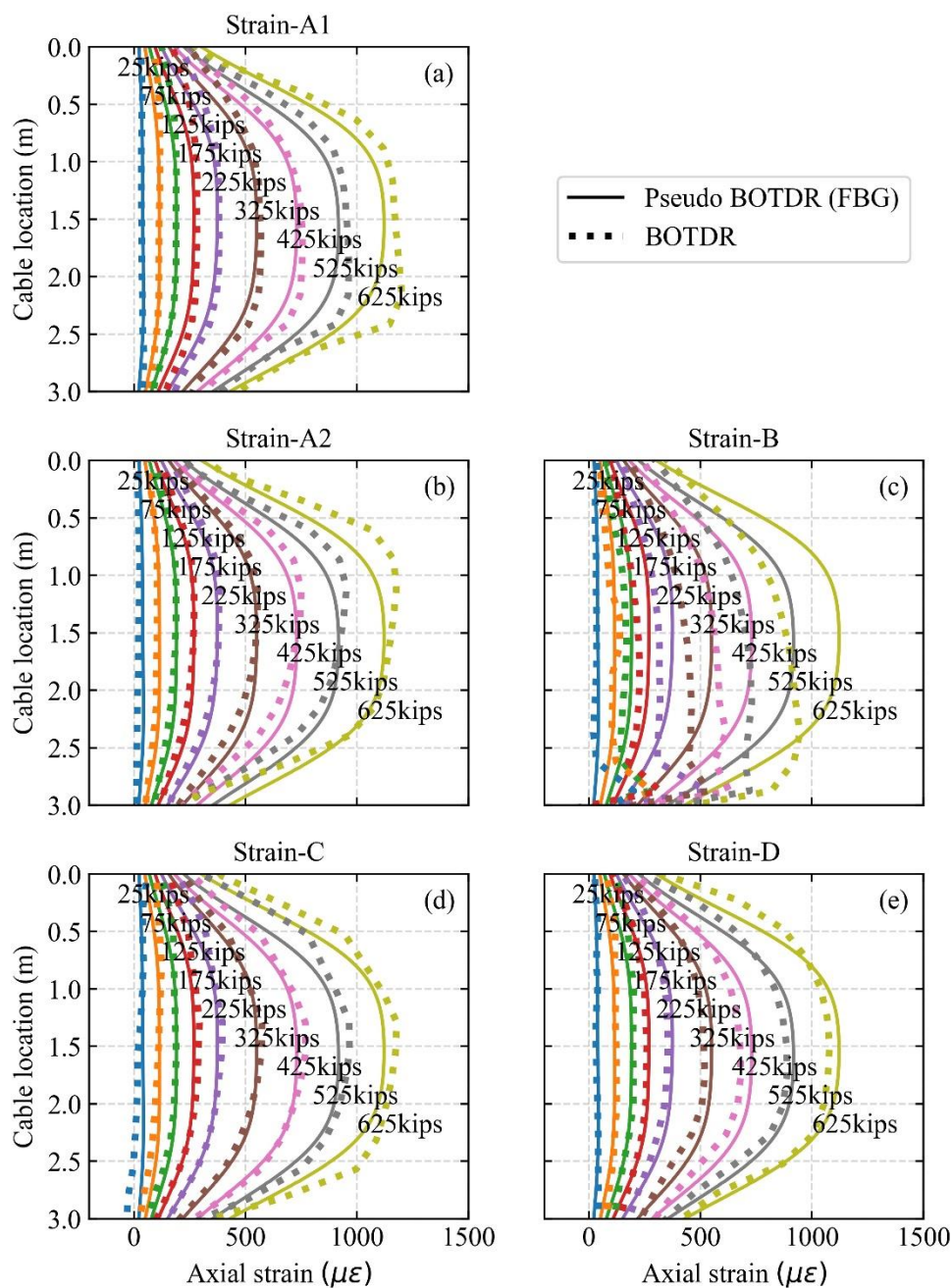
Figure 6-12 Comparison between the strain profiles calculated by the convolution of the FBG strain profiles (i.e., solid lines) and the actual BOTDR strain profiles (i.e., dashed lines): (a) Strain-A1; (b) Strain-A2; (c) Strain-B; (d) Strain-C; (e) Strain-D.

6.4.2. Pipe shaft friction analysis of the specimen

Analytical strain distributions in the outer pipe and cement are derived analytically herein to compare the experimental results against the analytical estimations. Figure 6-13 shows a schematic diagram of a segment of the well model under force equilibrium. The axial stress (σ_a) is applied at the bottom of the outer pipe while the displacement at the top of the outer and inner casing is constrained. The annular cement is constrained only by friction at the interface with the outer pipe. The inner pipe is not applied with any axial load at the bottom.
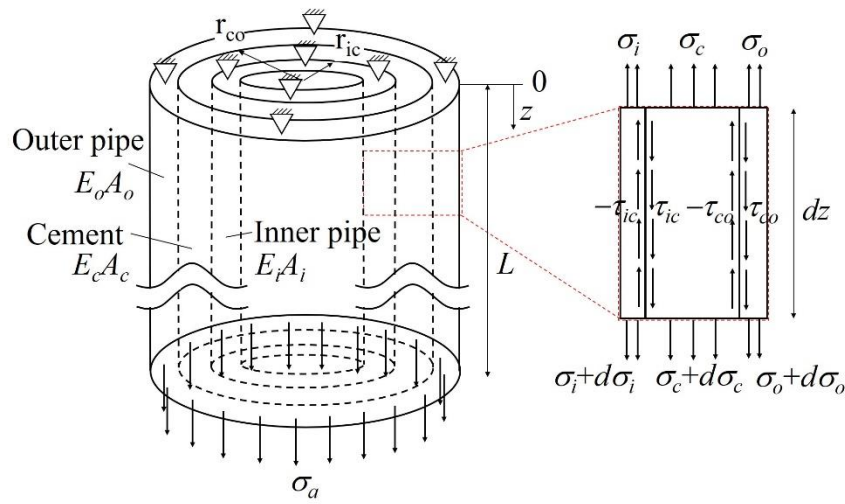
Figure 6-13 The assumed force equilibrium condition of the well specimen under tensile loading for the shaft friction analysis.

The force equilibrium equations for the outer pipe, cement and inner pipe are as follows:

$$\begin{cases} E_o A_o \dfrac{\partial^2 y_o}{\partial z^2} + 2\pi r_{co} k(y_c - y_o) = 0 \\[2mm] E_c A_c \dfrac{\partial^2 y_c}{\partial z^2} - 2\pi r_{co} k(y_c - y_o) + 2\pi r_{ic} k(y_i - y_c) = 0 \\[2mm] E_i A_i \dfrac{\partial^2 y_i}{\partial z^2} - 2\pi r_{ic} k(y_i - y_c) = 0 \end{cases} \tag{6-2}$$

where E_o = Young's modulus of the outer pipe, A_o = cross-sectional area of the outer pipe, E_c = Young's modulus of the cement, A_c = cross-sectional area of the cement, E_i = Young's modulus of the inner pipe, A_i = cross-sectional area of the inner pipe, y_o = axial displacement

157

of the outer pipe, y_c = axial displacement of the cement, y_i = axial displacement of the inner pipe, k = shear stiffness of the cement-steel interface (unit is stress/length), r_{co} = radius from the longitudinal axis of the model to the cement-outer pipe interface, r_{ic} = radius from the longitudinal axis of the model to the inner pipe-cement interface. The above simultaneous equations can be arranged in the matrix form as follows:

$$\frac{\partial^2}{\partial z^2}\begin{bmatrix} y_o \\ y_c \\ y_i \end{bmatrix} = 2\pi k \begin{bmatrix} \dfrac{r_{co}}{E_o A_o} & \dfrac{-r_{co}}{E_o A_o} & 0 \\ \dfrac{-r_{co}}{E_c A_c} & \dfrac{r_{co}+r_{ic}}{E_c A_c} & \dfrac{-r_{ic}}{E_c A_c} \\ 0 & \dfrac{-r_{ic}}{E_i A_i} & \dfrac{r_{ic}}{E_i A_i} \end{bmatrix} \begin{bmatrix} y_o \\ y_c \\ y_i \end{bmatrix} \tag{6-3}$$

Equation 6-3 can be solved via diagonalization of the matrix, which yields the following equations:

$$\frac{\partial^2}{\partial z^2}\begin{bmatrix} Y_o \\ Y_c \\ Y_i \end{bmatrix} = \begin{bmatrix} \lambda_o & 0 & 0 \\ 0 & \lambda_c & 0 \\ 0 & 0 & \lambda_i \end{bmatrix} \begin{bmatrix} Y_o \\ Y_c \\ Y_i \end{bmatrix} \tag{6-4}$$

where $\lambda_o, \lambda_c, \lambda_i$ are the eigenvalues of the matrix and

$$\begin{bmatrix} Y_o \\ Y_c \\ Y_i \end{bmatrix} = \left[\begin{pmatrix} | \\ p_o \\ | \end{pmatrix} \begin{pmatrix} | \\ p_c \\ | \end{pmatrix} \begin{pmatrix} | \\ p_i \\ | \end{pmatrix} \right]^{-1} \begin{bmatrix} y_o \\ y_c \\ y_i \end{bmatrix} = \begin{bmatrix} p_{o1} & p_{c1} & p_{i1} \\ p_{o2} & p_{c2} & p_{i2} \\ p_{o3} & p_{c3} & p_{i3} \end{bmatrix}^{-1} \begin{bmatrix} y_o \\ y_c \\ y_i \end{bmatrix} \tag{6-5}$$

where p_o, p_c, p_i are orthonormal vectors corresponding to the respective eigenvalues. For the parameter values listed in Table 6-4, the eigenvalues of the matrix are calculated to be $\lambda_o = 47.41, \lambda_c = 3.862, \lambda_i = 0$. Therefore, the general solutions for Equation 6-4 are given by the following equations:

$$\begin{bmatrix} Y_o \\ Y_c \\ Y_i \end{bmatrix} = \begin{bmatrix} C_{o1}e^{\sqrt{\lambda_o}z} + C_{o2}e^{-\sqrt{\lambda_o}z} \\ C_{c1}e^{\sqrt{\lambda_c}z} + C_{c2}e^{-\sqrt{\lambda_c}z} \\ C_{i1}z + C_{i2} \end{bmatrix} \tag{6-6}$$

By substituting Equation 6-6 into Equation 6-5, the general solutions are obtained as follows:

$$\begin{bmatrix} y_o \\ y_c \\ y_i \end{bmatrix} = \begin{bmatrix} p_{o1}\left(C_{o1}e^{\sqrt{\lambda_o}z} + C_{o2}e^{-\sqrt{\lambda_o}z}\right) + p_{c1}\left(C_{c1}e^{\sqrt{\lambda_c}z} + C_{c2}e^{-\sqrt{\lambda_c}z}\right) + p_{i1}(C_{i1}z + C_{i2}) \\ p_{o2}\left(C_{o1}e^{\sqrt{\lambda_o}z} + C_{o2}e^{-\sqrt{\lambda_o}z}\right) + p_{c2}\left(C_{c1}e^{\sqrt{\lambda_c}z} + C_{c2}e^{-\sqrt{\lambda_c}z}\right) + p_{i2}(C_{i1}z + C_{i2}) \\ p_{o3}\left(C_{o1}e^{\sqrt{\lambda_o}z} + C_{o2}e^{-\sqrt{\lambda_o}z}\right) + p_{c3}\left(C_{c1}e^{\sqrt{\lambda_c}z} + C_{c2}e^{-\sqrt{\lambda_c}z}\right) + p_{i3}(C_{i1}z + C_{i2}) \end{bmatrix} \quad (6\text{-}7)$$

The boundary conditions of the well model under tensile loading are (i) zero axial displacement in the outer and inner pipes at $z = 0$, (ii) zero axial strain in the cement at $z = 0$, L and in the inner pipe at $z = L$ and (iii) constant axial stress in the outer pipe at $z = L$. The zero strain boundary at $z = 0$ in the cement would be valid assuming that the cohesion at the cement-top plate interface ($z = 0$) in the normal direction is negligible compared to the interface cohesion against shearing at the inner and outer pipe-cement interfaces. The aforementioned boundary conditions are expressed as follows:

$$y_o|_{z=0} = 0, \quad y_i|_{z=0} = 0, \quad \frac{\partial y_c}{\partial z}\bigg|_{z=0} = 0,$$

$$\frac{\partial y_o}{\partial z}\bigg|_{z=L} = \frac{\sigma_a}{E_o}, \quad \frac{\partial y_i}{\partial z}\bigg|_{z=L} = 0, \quad \frac{\partial y_c}{\partial z}\bigg|_{z=L} = 0 \quad (6\text{-}8)$$

By applying these boundary conditions, the coefficients in Equation 6-7 are obtained as follows:

$$\begin{bmatrix} C_{o1} \\ C_{o2} \\ C_{c1} \\ C_{c2} \\ C_{i1} \\ C_{i2} \end{bmatrix} = \begin{bmatrix} p_{o1}e^{\sqrt{\lambda_o}L} & p_{o1}e^{-\sqrt{\lambda_o}L} & p_{c1}e^{\sqrt{\lambda_c}L} & p_{c1}e^{-\sqrt{\lambda_c}L} & p_{i1}L & p_{i1} \\ p_{o3}e^{\sqrt{\lambda_o}L} & p_{o3}e^{-\sqrt{\lambda_o}L} & p_{c3}e^{\sqrt{\lambda_c}L} & p_{c3}e^{-\sqrt{\lambda_c}L} & p_{i3}L & p_{i3} \\ p_{o2}\sqrt{\lambda_o}e^{\sqrt{\lambda_o}L} & -p_{o2}\sqrt{\lambda_o}e^{-\sqrt{\lambda_o}L} & p_{c2}\sqrt{\lambda_c}e^{\sqrt{\lambda_c}L} & -p_{c2}\sqrt{\lambda_c}e^{-\sqrt{\lambda_c}L} & p_{i2} & 0 \\ p_{o1}\sqrt{\lambda_o} & -p_{o1}\sqrt{\lambda_o} & p_{c1}\sqrt{\lambda_c} & -p_{c1}\sqrt{\lambda_c} & p_{i1} & 0 \\ p_{o3}\sqrt{\lambda_o} & -p_{o3}\sqrt{\lambda_o} & p_{c3}\sqrt{\lambda_c} & -p_{c3}\sqrt{\lambda_c} & p_{i3} & 0 \\ p_{o2}\sqrt{\lambda_o} & -p_{o2}\sqrt{\lambda_o} & p_{c2}\sqrt{\lambda_c} & -p_{c2}\sqrt{\lambda_c} & p_{i2} & 0 \end{bmatrix}^{-1} \begin{bmatrix} 0 \\ 0 \\ 0 \\ \frac{\sigma_a}{E_o} \\ 0 \\ 0 \end{bmatrix} \quad (6\text{-}9)$$

Figure 6-14 shows the analytical axial strain distributions of the inner casing, cement and outer pipe obtained from Equation 6 presented earlier, which are compared with the strain distributions obtained from the strain gauges and FBG cable. The values of the parameters used in the equations are listed earlier in Table 6-4. It is found that the match between the analytical and experimental axial strain distributions is satisfactory, proving that the theoretical concept of the tensile axial deformation of the well model is properly implemented in the design of the specimen and loading scheme. This shaft friction analysis has thus verified that the axial tensile deformation of the well is simulated successfully in the laboratory.

The errors between the analytical and experimental strain values in the cement after 225 kips are

caused by plastic deformation of the specimen. In fact, the strain distributions of the FBG cables start to oscillate from this load level. Since the strain distributions of the FBG and other fibre optic cables show larger values than the analytical strain distributions, potential fibre optic cable slippage at the interface between the cables and cement and/or between the fibre core and its coating layers is not induced within the strain range examined in this experiment (~ 1,250 $\mu\varepsilon$).

Table 6-4 The values of the parameters of the shaft friction model.

L (m)	3.1
E_o (GPa)	200
A_o (m^2)	6.334×10^{-3}
E_c (GPa)	8.3
A_c (m^2)	2.910×10^{-2}
E_i (GPa)	200
A_i (m^2)	7.031×10^{-3}
r_{co} (m)	0.1556
r_{ic} (m)	0.1222
k (GPa/m)	6.0
σ_a (MPa)	17.6, 52.7, 87.8, 122.9, 158.0, 228.2, 298.5
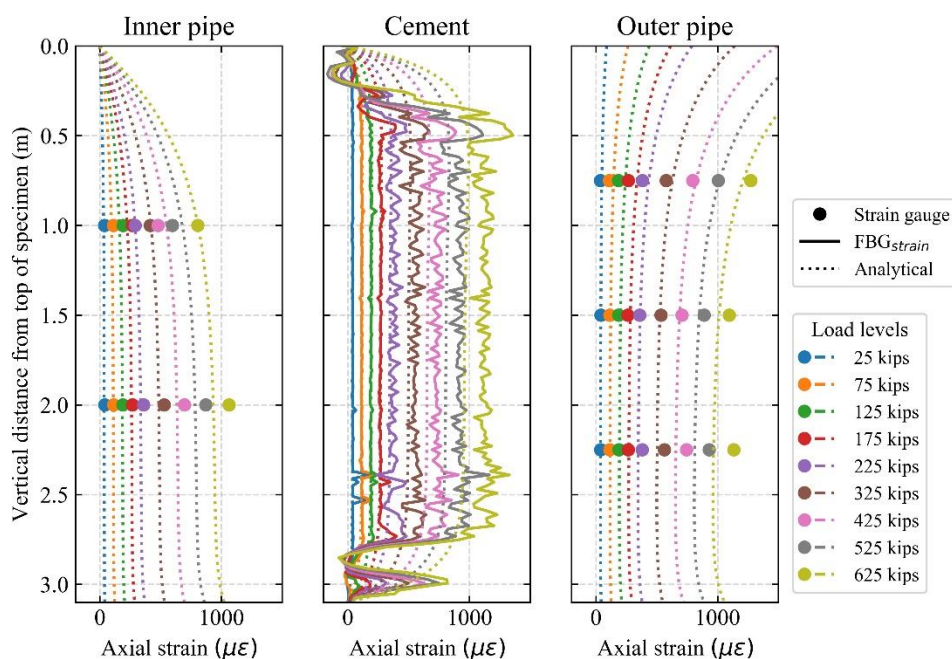
Figure 6-14 Comparison between the analytical solution and experimental result on the axial strain distributions of inner pipe, cement and outer pipe.

In addition, the value of the interface shear stiffness used in the analytical solution to obtain the satisfactory match is 6.0 GPa/m, which is approximately the same value used in the finite element

analysis of the well specimen presented in Chapter 5 ($k = \tau_{ult}/\delta^e_{ult} \sim c'/\delta^e_{ult} = 3.0$ MPa/0.5 mm = 6.0 GPa/m). Therefore, the calibration of the interface shear stiffness performed for the simulation of well integrity during reservoir compaction in Chapter 5 has been validated by this elastic cylindrical shaft friction analysis.

6.4.3. Comparison between BOTDR/FBG and strain gauge measurements

Figure 6-15 show the comparison between the fibre optic (i.e., BOTDR and FBG) and the strain gauge measurements. BOTDR and FBG strain data were extracted from a readout point of the fibre optic cables at approximately middle height of the specimen (i.e., 1.5m). The operational strain gauges located near the readout points were selected for the comparison.
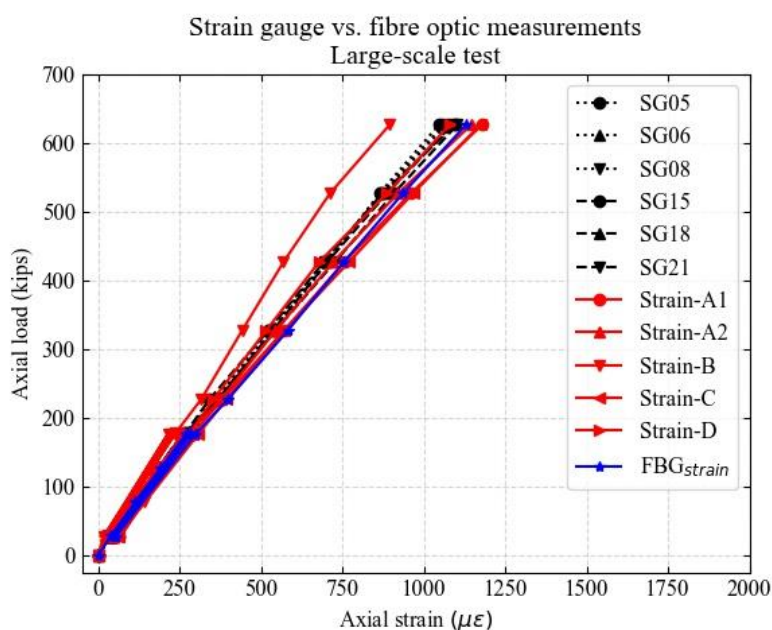
Figure 6-15 Comparison between the fibre optic sand strain gauge measurement.

BOTDR and FBG measurements are in good agreement with the strain gauge data. However, there was discrepancy between the Strain-B cable and the other cables/strain gauges. The difference is again attributed to the ineffective strain transfer between coating layers of the Strain-B cable as the coating layers are not tightly buffered through mechanical compression or chemical adhesion and the number of coating layers was excessive. Therefore, it is argued that key to accurate strain monitoring with BOTDR/A is to employ fibre optic cables which possess a simple yet robust cross-sectional structure with a small number of coating layers that are tightly buffered to each other. One way to achieve such fibre optic cables is to encase an existing tightly buffered strain cable such as the Strain-C cable in a metal tube and fill the gap

with a filler material. The filler material should be chosen such that it does not develop excessive or localized deformation (i.e., too elastic or brittle) in response to external strains as it hinders effective strain transfer to the inner optical fibre cable.

6.5.   Summary

In this study, laboratory-scale well specimens were prepared to simulate compaction-induced tensile strain development of wells in the laboratory. The well specimen consisted of an inner and outer casing with cemented annulus. Different types of fibre optic cables were instrumented in the annulus of the specimens. Strain gauges and wire gauges were also instrumented on the casings to evaluate the accuracy of the BOTDR and FBG measurements. The primary findings form this study with regard to its objectives are as follows:

(i)   The effectiveness of the BOTDR/A measurement was comparable to that of the FBG and strain gauge measurements in detecting the axial strain development of the well specimen subjected to tensile loading.

(ii)   Key to accurate strain measurements by BOTDR/A is to employ fibre optic cables whose cross-sectional structure is simple yet robust with less number of coating layers which are tightly buffered to each other through mechanical compression and/or chemical adhesion.

(iii)   A suggested development strategy of such effective fibre optic cables is to encase a commercially available tightly buffered fibre optic cable (e.g., the Strain-C cable) in a metal tube and fill the gap with an adhesive or polymer which should neither be too brittle or elastic to ensure effective strain transfer from the metal tube to the inner fibre optic cable.

7. Distributed fibre optic strain monitoring of bending deformation of laboratory-scale well specimens

7.1. Introduction

In the previous chapter, the axial tensile strain development of oil and gas wells was modelled through laboratory experiments. This is applicable mainly for the Nankai Trough case where wells were constructed vertical to the formation. In such a configuration, the well is likely to compress in the reservoir layer and elongates in the overburden layer in response to reservoir compaction.

A field test is expected in 2020 in methane hydrate reservoirs in Alaska where wells will be drilled at an angle (e.g., ~30º) to the formation. This is because the drilling equipment has to be set up on existing roads, which are thermally insulated to avoid thawing the permafrost of the Alaska formation, and drill sideways into the formation. The response of deviated wells to reservoir compaction is different from that of vertical wells in that bending deformation occurs. This is due to the vertical gradient of the vertical strain in the overburden layer (e.g., greater tension at the bottom than at the top). Hence, it is important that DAS monitoring system can measure the bending deformation of wells in order to assess the integrity of deviated wells at the Alaska site.

In this study, laboratory monitoring of bending deformation of well specimens was carried out with BOTDR. The objectives of the study are as follows:

(i)   to assess the potential of BOTDR measurements to capture the bending deformation of the well specimen and

(ii)   to investigate the effect of installation location of fibre optic cables on the accuracy of bending curvature distributions measured by BOTDR.

A model well specimen was fabricated with a steel box section and cement sheath. A box section, rather than a circular section, was selected to assure the monitoring of composite bending deformation of the specimen in the laboratory conditions. In other words, the application of the high confining pressure levels of the actual wellbore conditions, which would keep the casing (steel) and cement together during bending, is not feasible at laboratory. As design codes for assuring the composite bending deformation of square-section structures (e.g.,

bridges) are well established in the construction industry, they were referred to for the preparation of the specimen. Details about the specimen preparation, sensor instrumentation and loading test are provided in the following sections.

7.2. Methodology

7.2.1. Specimen design

Figure 7-1 shows the cross-sections of the specimen. The specimen consists of three main components: steel box section, shear studs and cement sheath. The shear studs consist of bolts and nuts which are fixed to the steel box section. The role of shear studs, which is specified in the Eurocode 4 (European Commitee for Standardization 2005), is to prevent slippage at the steel-cement interface so that the specimen bends as a composite material under ambient pressure conditions.
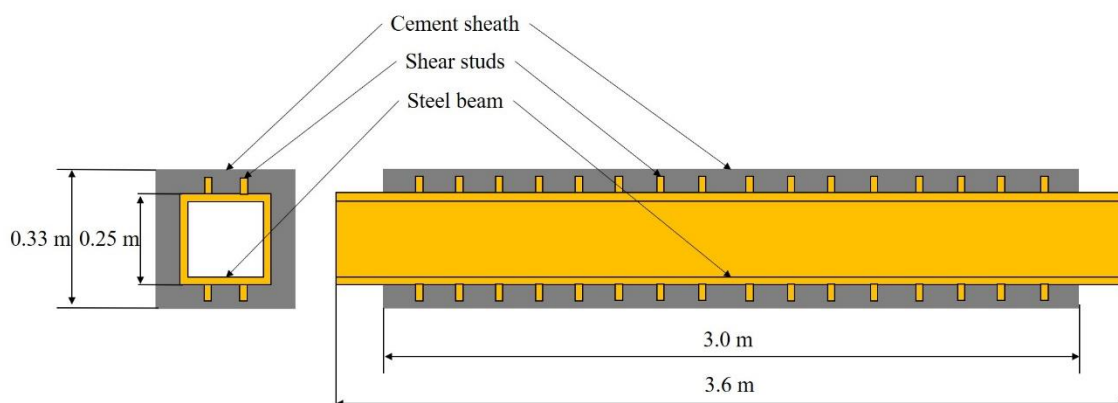
Figure 7-1 Cross-sections of the specimen.

7.2.2. Fibre optic monitoring techniques

Neubrex's NuebreScope NBX-5000 (Figure 7-2) was employed for BOTDR measurements whereas Micron Optics' Optical Sensing Interrogator | sm130 (Figure 7-3) was employed for FBG measurements. The FBG measurement employed in this experiment is different from the one used in the experiment for the axial deformation of the well specimen described in Chapter 6. Hence, the FBG system employed for this experiment (i.e., the Micron Optics' FBG) is referred to as FBGS to distinguish it from the special FBG system offered by an oil and gas service company (see Chapter 6). The main characteristic of the FBGS analyser is that dynamic measurements at hundreds of Hz are feasible. Table 7-1 shows the measurement characteristics of the BOTDR and FBGS analysers.

Figure 7-2 The NeubreScope NBX-5000 analyser for BOTDR measurements [After Chunge (2014)].

Figure 7-3 The Optical Sensing Interrogator | sm130 for FBGS measurements.

Table 7-1 Measurement characteristics of the BOTDR and FBGS analysers.

	BOTDR	FBGS
Spatial resolution (m)	0.5	<0.01
Data sampling interval (m)	0.05	NA
Axial strain measurement precision ($\mu\varepsilon$)	10	1
Measurement duration per channel (min)	5	2×10^{-5}
Measurement frequency (Hz)	3×10^{-3}	1000

7.2.3.   Fibre optic cables

Figure 7-4 shows the cross-section of the fibre optic cables employed for the BOTDR and

FBGS measurements in this experiment. The Excel cable (Figure 7-4a) and Fujikura cable (Figure 7-4b) are used for the BOTDR measurement. The Excel cable is a temperature cable as the fibres are enclosed in a gel-filled tube which insolates the fibres from external strains. The Fujikura cable is a strain cable as the coating layers around the fibres are tightly buffered through mechanical compression. The FBGS cable used for FBGS measurements is also a strain cable as the coating layers are tightly buffered. The strain and temperature coefficients of these fibre optic cables are provided in Table 7-2.
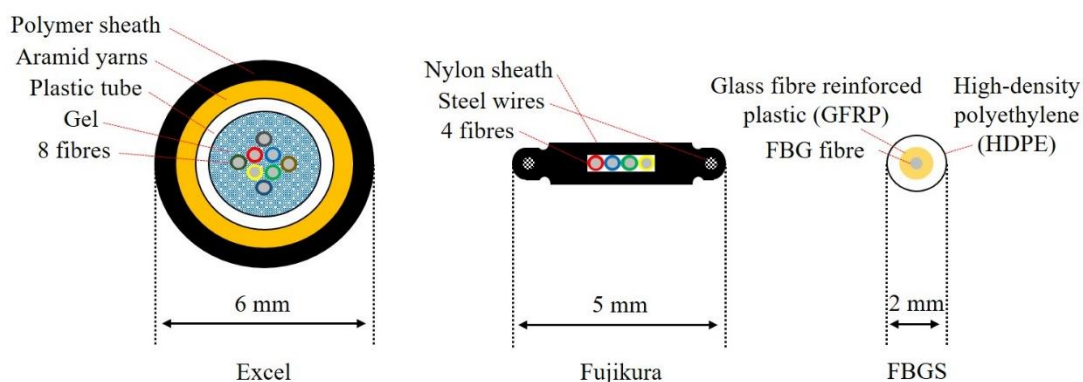
Figure 7-4 The cross-section of the fibre optic cables.

Table 7-2 The strain and temperature coefficients of the fibre optic cables.

	Strain coefficient	Temperature coefficient
	C_ε (MHz/%)	C_T (MHz/°C)
Excel	0	1.17
Fujikura	493	2.10
	1 - p_e (1/με)	$\alpha_n + \alpha_L$ (1/°C)
FBGS	0.7874×10^{-6}	9.15×10^{-6}

.

7.3. Specimen preparation

7.3.1. Steel box section and shear studs

Figure 7-5 shows the steel box section used for the specimen preparation. The length is 3 m and the width is 0.25 m with 8 mm wall thickness. Shear studs were installed in the holes on the steel box section. The number of shear studs, and their length and diameter were determined according to the Eurocode 4 (European Commitee for Standardization 2005).
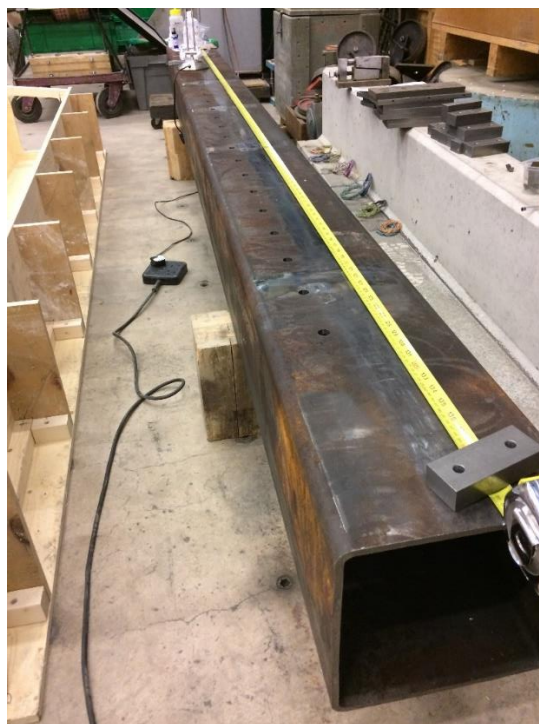
Figure 7-5 The steel box section used for the specimen preparation.

7.3.2. Sensor instrumentation

First, the Fujikura fibre optic cable was installed on the upper and lower surface of the steel box section with glue while the cable was pretensioned by approximately 3000 µε (Figure 7-6). After the steel box section was placed in the mould, additional fibre optic cables (Fujikura and Excel cable) were installed. The fibre optic cables were then spliced for BOTDR measurements. The location and type of fibre optic cables installed to the specimen are shown in Figure 7-7. Strain gauges were also installed on the steel box section. In total, ten strain gauges were attached on the upper and lower surface of the steel box section (Figure 7-7). FBGS cables and wire gauges were also installed on the cement sheath after specimen preparation (Figure 7-8).

In addition, a digital image correlation technique was employed to capture the deformation of the cement sheath. In this technique, a series of photos of the specimen are taken at each load increment. The surface of the cement sheath is painted in plain white background with black dots, of which movement a digital image correlation software tracks to calculate displacement and strain fields. The Optecal software which was developed at the University of California, Berkeley, by Dr Clement B. Barthes, was employed. The test setup for the digital image correlation technique is shown in Figure 7-9.

Figure 7-6 A fibre optic cable (Fujikura cable) and a strain gauge installed to the steel box section.

(a)

(b)
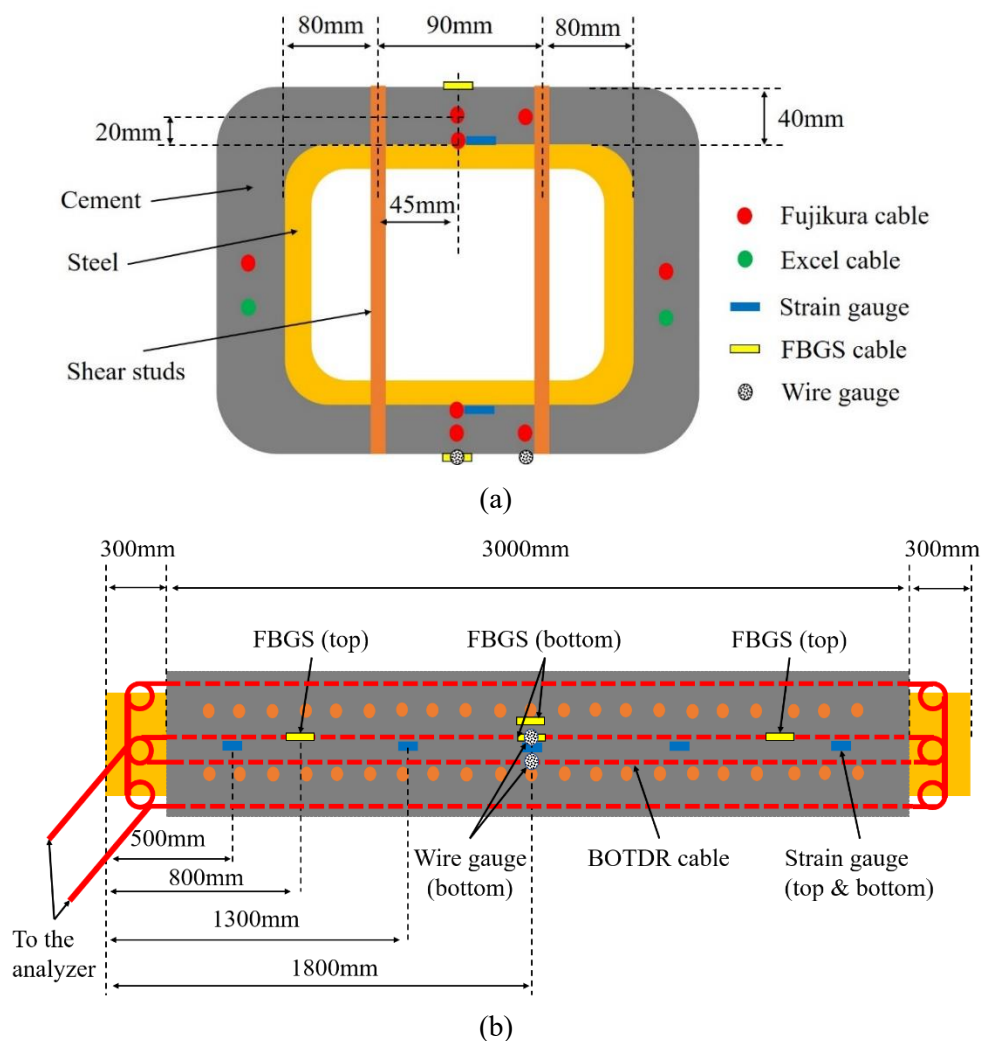
Figure 7-7 The location of fibre optic cables, strain and wire gauges in the specimen: (a) cross-sectional view; (b) plan view from top of specimen.

Figure 7-8 The FBGS cables and wire gauges attached on the cement sheath at the bottom centre part of the specimen.

(a)   (b)

Figure 7-9 The test setup for the digital image correlation technique: (a) overview of the equipment; (b) cement sheath surface painted in white background with black dots.

7.3.3.   Cement pour and cure processes

(a)

(b)
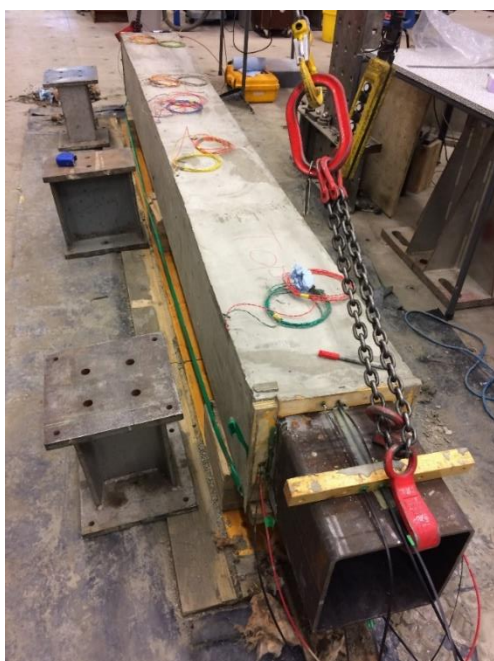
(c)
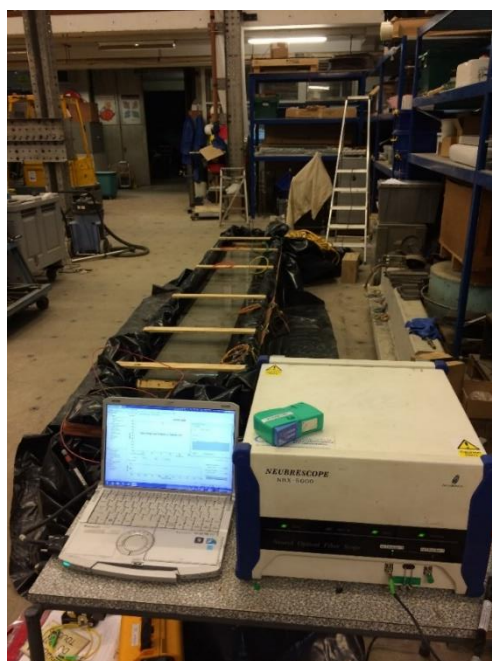
(d)

Figure 7-10 The process of cement pour and cure processes : (a) installation of the steel box section in the mould; (b) cement slurry pour; (c) demoulding after cement set; (d) cement cure in the water bath.

Figure 7-10 shows the process of cement pour and cure during specimen preparation. First, the steel box section was placed in the mould (Figure 7-10a). After installing the rest of the fibre

optic cables, cement slurry was poured into the mould (Figure 7-10b). The cement slurry was prepared by mixing Class G oil well cement with water at the water-to-cement ratio of 0.44. After 48 h the mould was detached from the specimen (Figure 7-10c). The specimen was then placed in a water bath for cement cure (Figure 7-10d). The specimen was cured in the water bath under room temperature and pressure conditions for 20 days. Finally, the specimen was removed from the water bath and set up in the loading apparatus for the loading test.

7.4. Three-point bending test

Three-point bending was implemented on the specimen in the loading apparatus shown in Figure 7-11. Spacer plates were placed between the specimen and loading apparatus to avoid stress concentration and localized failure in the cement sheath. Plaster was applied between the spacer plates and cement sheath to connect them together. The width, length and thickness of the spacer plate were 90 mm, 330 mm and 10 mm, respectively.
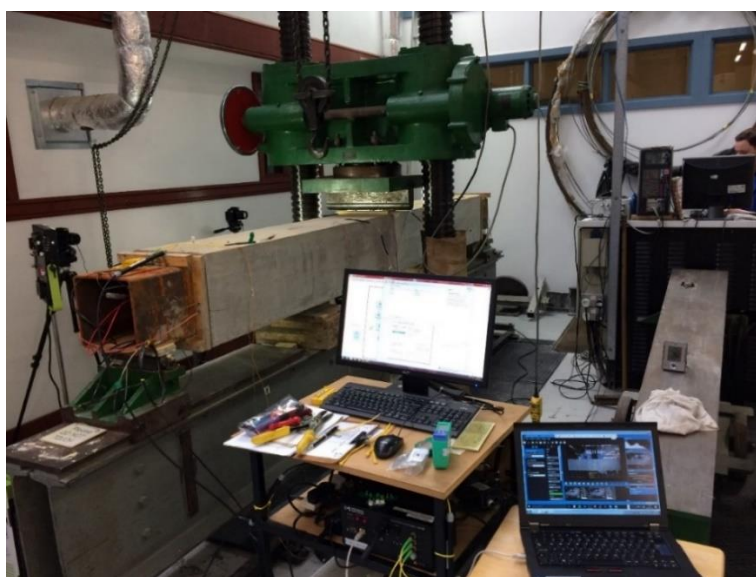
Figure 7-11 An overview of the specimen setup for the three-point bending test.

Figure 7-12a and b show the time series of the loading and the load vs. central deflection diagram, respectively. The step loading was carried out where the load level was held constant at each load increment for approximately 10 min (Figure 7-12a) to allow the period for BOTDR measurements. The load was maintained manually by adjusting the displacement, which resulted in the fluctuation of the load increments. The loading rate between each load increment was set to approximately 10 kN/min.
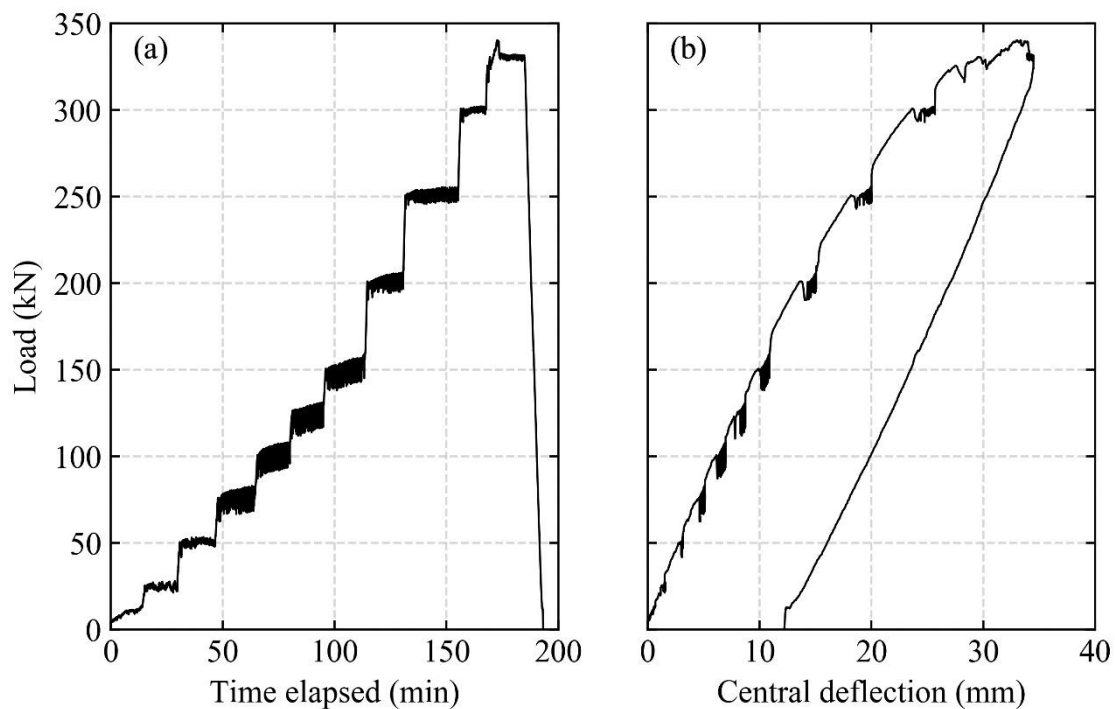
Figure 7-12 The development of load and displacement in the specimen during bending test: (a) time vs. load; (b) central deflection vs. load.

<div align="center">(a)   (b)</div>
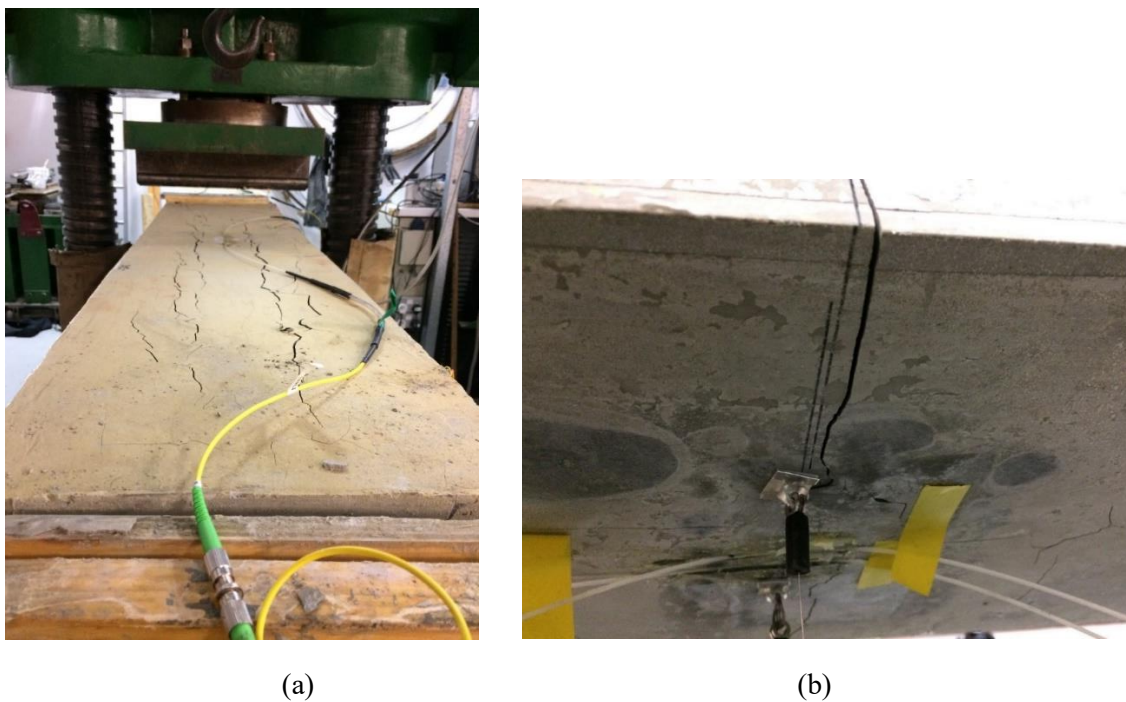
Figure 7-13 Overviews of the specimen after failure: (a) upper right part; (b) lower centre part.

The specimen failed at approximately 330 kN. Overviews of the specimen after the failure are shown in Figure 7-13. The upper section of the specimen developed cracks in the cement sheath in the longitudinal direction. This is because of the compressive stress concentration between the shear studs. In the bottom centre section of the specimen, a major crack was formed in the cement in the transverse direction. This is due to the tensile stress development in this specimen section during bending.

7.4.1. Strain gauge data

Figure 7-14 shows the longitudinal strain development of the steel box section during loading obtained from the strain gauges. The positive values indicate tensile strain. Six of the ten strain gauges were not operational at the time of the loading test. The functional strain gauges were the strain gauge #2 and #3 (i.e., SG2 and SG3), which were attached on the upper part of the steel box section, and the strain gauge #7 and #10 (i.e. SG7 and SG10), which were installed on the lower part of the specimen.
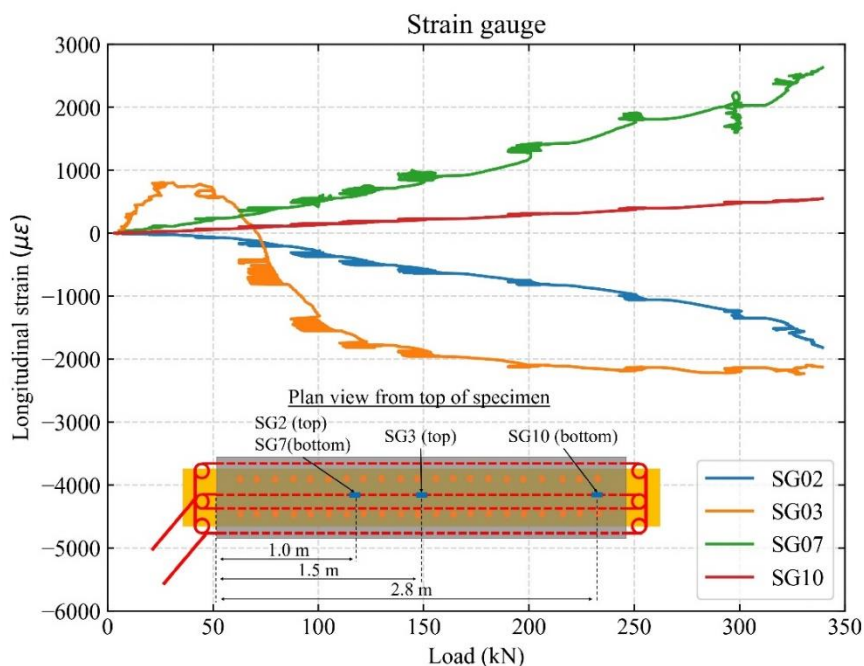
Figure 7-14 Longitudinal strain development of the steel box section during the bending test obtained from the strain gauges.

The response of the strain gauge #2, #7 and #10 was linear with increasing load levels. The strain magnitude became larger toward the centre of the specimen. This is because the maximum bending moment in three-point bending occurs at the centre of beam. The response of the strain gauge #3 at small load levels was not linear. This is because the steel spacer plate,

173

which was placed on the cement surface above this strain gauge, constrained the development of compressive strain. After a certain load level (e.g., 50 kN), slippage occurred between the spacer plate and cement sheath, which reduced the constraining effect and the compressive strain development started to pick up as expected. The strain gauge #2 and #7 were located at the same longitudinal position (i.e., 1.0 m). The magnitude of longitudinal strain from these strain gauges were identical up to a load level of 100 kN, after which the tensile strain from strain gauge #7 became larger than the compressive strain from strain gauge #2. This suggests that the specimen started to fail at 100 kN and the neutral axis of the specimen started to shift upward.
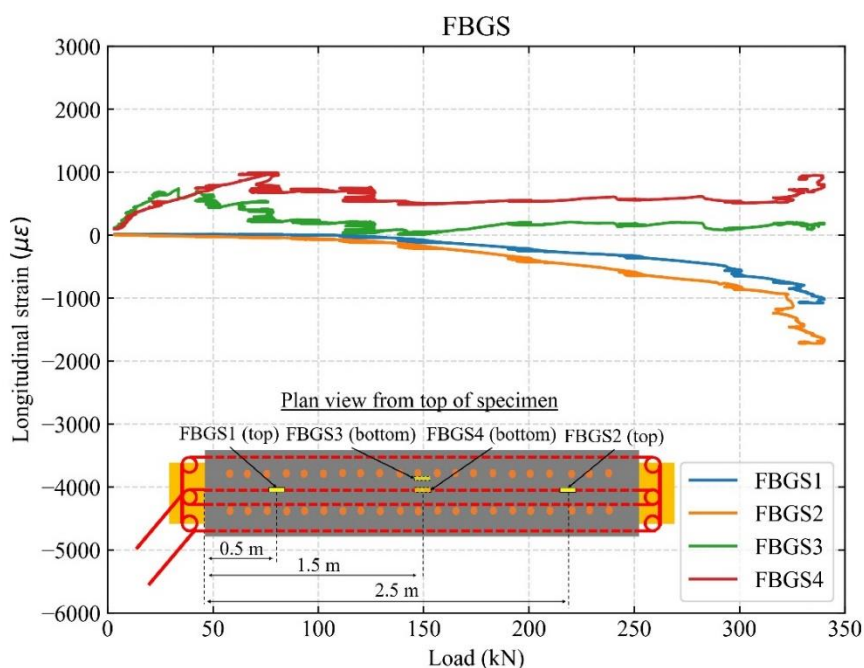
Figure 7-15 Longitudinal strain development of the cement sheath during the bending test obtained from the FBGS measurement.

7.4.2. FBGS

Figure 7-15 shows the development of the longitudinal strain of the cement sheath obtained from the FBGS measurement. The FBGS cables were attached on the cement sheath surface with epoxy and their location is indicated in the insert of the figure. The strain levels of FBGS3 and 4, which were located at the lower centre of the specimen, were smaller than that of the strain gauge #7, which was located near these FBGS cables. A reason why these FBGS cables measured smaller strain levels than the strain gauge is the tensile crack development at the lower centre part of the specimen in the cement sheath (Figure 7-13b). The crack development decreased the tensile strain levels of the nearby cement sections. It seems that the initial crack occurred at a load level of approximately 50 kN where the strain levels measured by FBGS3

and 4 started to decrease. The response of FBGS1 and 2 was more linear than that of FBGS3 and 4 because cracks did not develop near FBGS1 and 2 until the failure load level (330 kN) was reached.
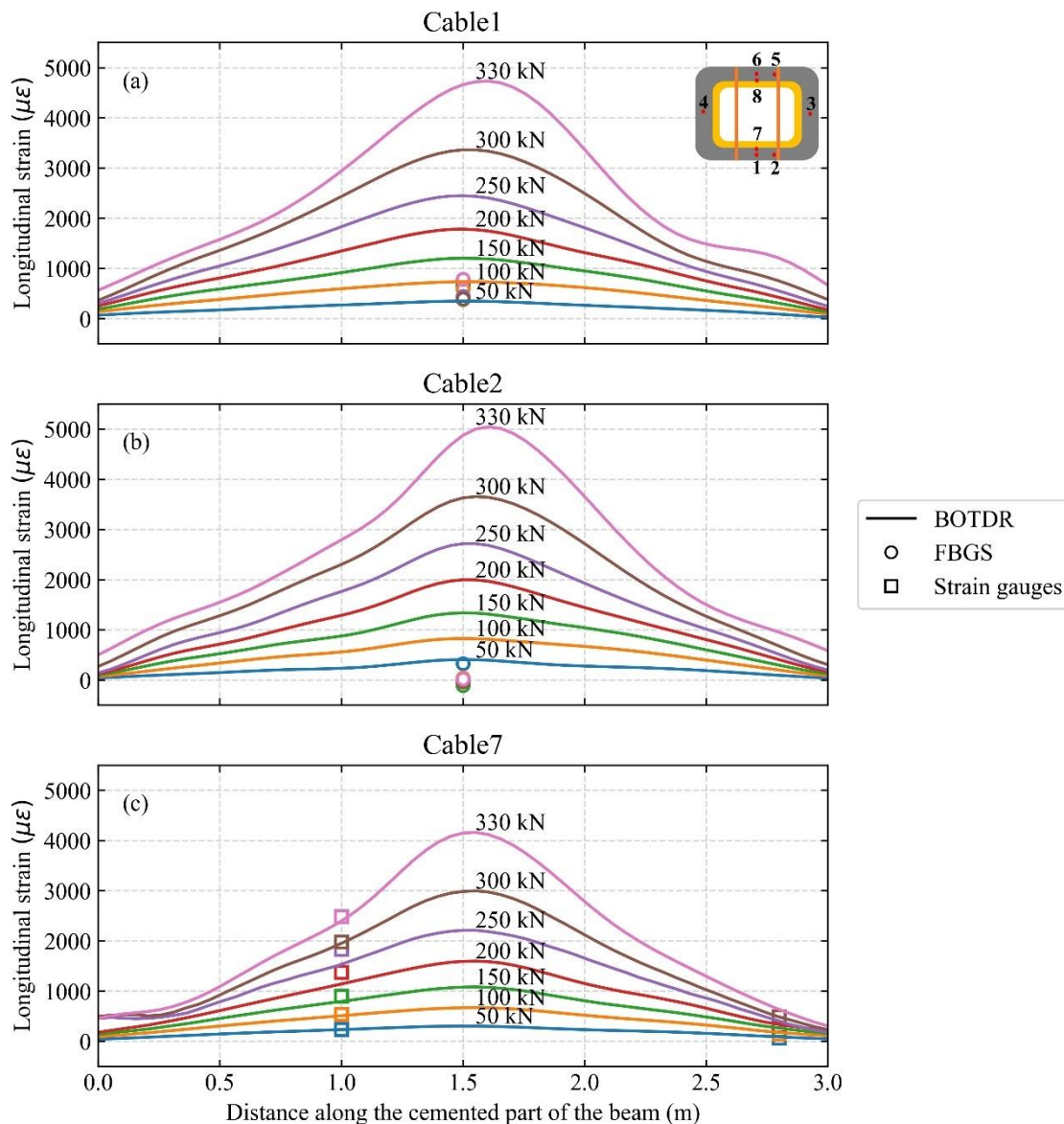
Figure 7-16 Longitudinal strain distributions in the lower section of the specimen obtained from the BOTDR measurement: (a) Cable1; (b) Cable2; (c) Cable7.

7.4.3. BOTDR

Figure 7-16 shows the longitudinal strain distributions at different load levels on the lower section of the specimen obtained from the BOTDR measurement. Cable1 and 2 were embedded in the cement sheath and their strain distributions thus provide those of the cement sheath, whereas the data along Cable7 give strain distributions of the steel box section as Cable7 was

directly attached on it. As such, strain distributions along Cable 1 and 2 were compared with FBGS strain data whereas those along Cable 7 was compared with strain gauge data. The temperature effect was ignored due to the minimal temperature change of less than $\pm 0.5^{\circ}$C during the bending test.
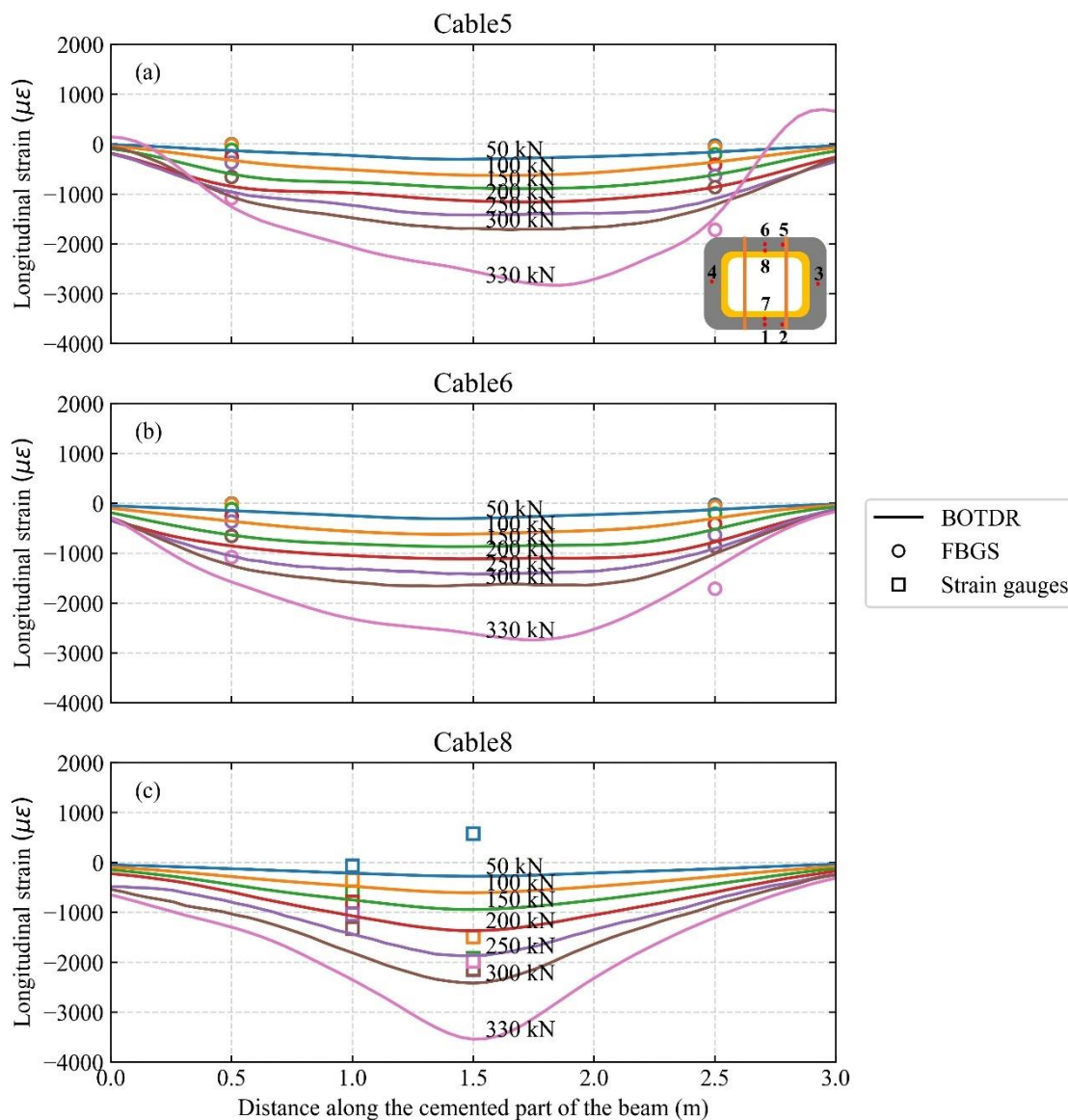
Figure 7-17 Longitudinal strain distributions in the upper section of the specimen obtained from the BOTDR measurement: (a) Cable5; (b) Cable6; (c) Cable8.

Theoretically, three-point bending produces triangular longitudinal strain distributions. This was captured by the BOTDR measurement. The agreement between the BOTDR measurement along Cable 7 and strain gauge measurement was satisfactory (Figure 7-16c) whereas the FBGS measurement did not match well with the BOTDR measurement along Cable 1 and 2 (Figure 7-

16a and b). This indicates the difference between distributed (BOTDR) and localized (FBGS) strain measurements. The FBGS measurements were affected by the stress relaxation induced by cement cracking whereas such localized strain change was averaged out to provide an overall strain distribution in the BOTDR measurement. Although localized and distributed measurements are complementary to each other, localized measurements could be misleading if the number of sensors is insufficient.
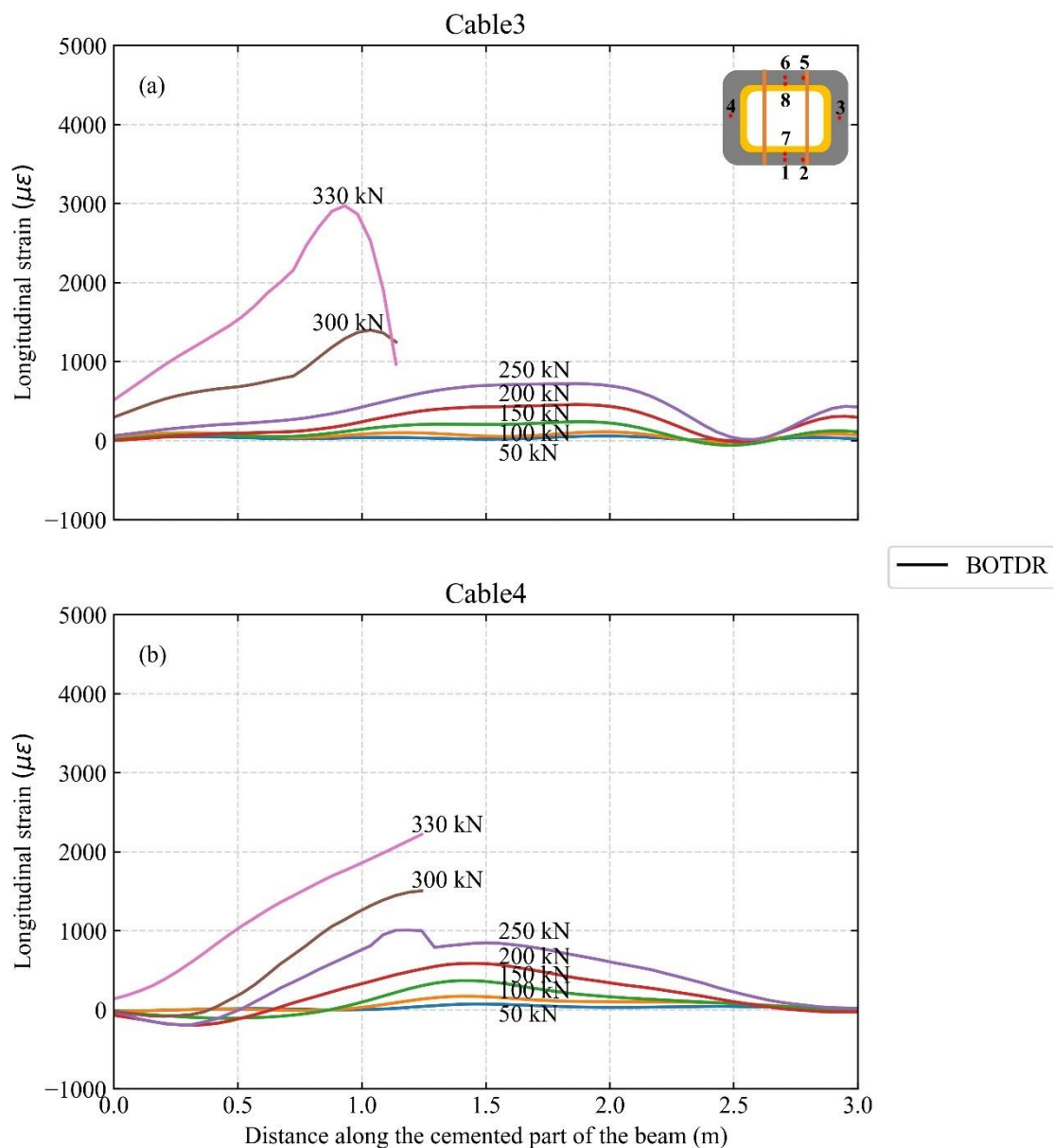
Figure 7-18 Longitudinal strain distributions in the side section of the specimen obtained from the BOTDR measurement: (a) Cable3; (b) Cable4.

Figure 7-17 shows the longitudinal strain distributions in the upper part of the specimen

obtained from the BOTDR measurement. The triangular strain distribution in the compression side (upper part) is captured as was the case for the tension side (lower part) of the specimen. The comparison among BOTDR measurements shows that the cement sheath (Cable5 and 6) developed smaller compressive strain levels than the steel box section (Cable8), which is counterintuitive. This was because the cement around the upper centre part of the specimen elongated laterally due to Poisson's effect by the point loading. Distributed (BOTDR) and localized (FBGS and strain gauges) measurements were in agreement except for the strain gauge attached at the centre of the specimen (Figure 7-17c). The mismatch was probably caused by the point load from the loading apparatus which generated longitudinal elongation of the specimen due to Poisson's effect.

Figure 7-18 shows the longitudinal strain distributions in the side section of the specimen obtained from the BOTDR measurement. As Cable3 and 4 were installed along the neutral axis of the specimen, negligible longitudinal strain levels were measured up to the load level of 100 kN. Above this load level, tensile longitudinal strain started to develop because of the upward shift of the neutral axis following the crack development in the cement sheath at the lower part of the specimen. At the load level of 300 kN, Cable3 and 4 broke at approximately 1.2 m from the left edge of the cement sheath. As a result, strain distributions beyond 1.2 m along Cable3 and 4 could not be obtained.

7.4.4. Digital image correlation

Figure 7-19 shows longitudinal strain distributions of the cement sheath on the right-hand side of the specimen obtained from the digital image correlation technique. The digital image correlation technique shows the locations of cracks propagating in the cement sheath with increasing load levels. It also shows that tensile strain developed at the lower part of the cement whereas compressive strain developed at the upper part, which is consistent with the deformation of the specimen inferred from the BOTDR measurement. It is found that the neutral axis was located in the middle height of the cement sheath at small load levels (Figure 7-19a and b) and it gradually moved upward at higher load levels (Figure 7-19c and d). This is consistent with the BOTDR measurement along Cable3 and 4 (Figure 7-18). It was also found that tensile strain developed at the upper centre part of the specimen, which corroborates the observation from the BOTDR measurement that the lateral elongation of the cement sheath occurred in response to the vertical compressive point load from the loading apparatus due to Poisson's effect (Figure 7-17a and b).
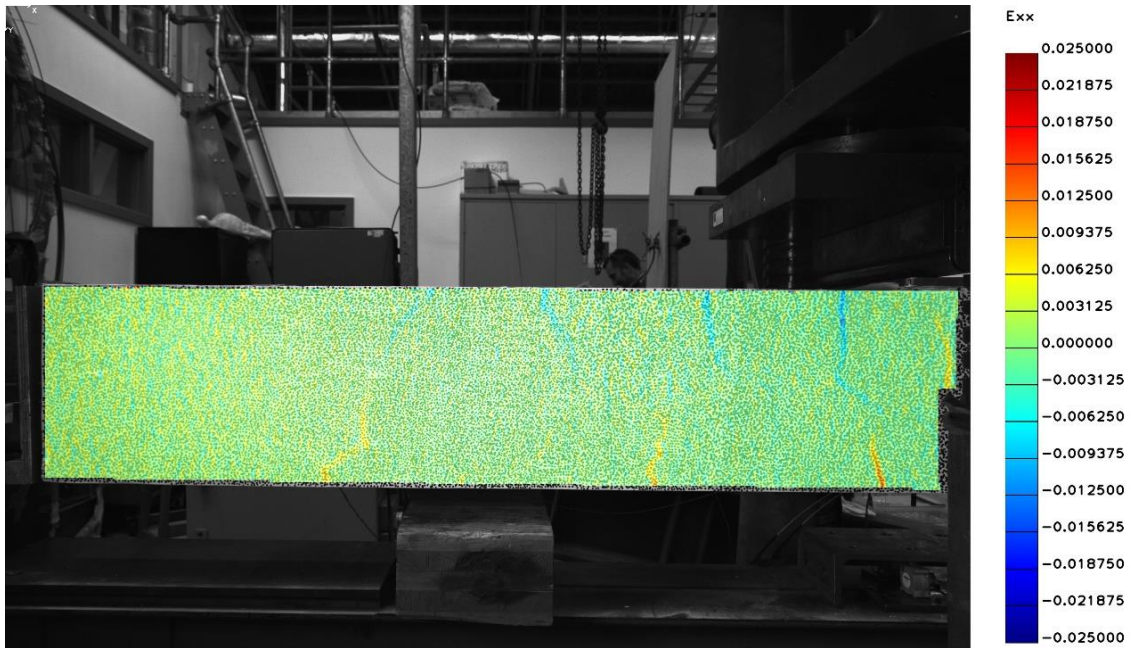
(a)
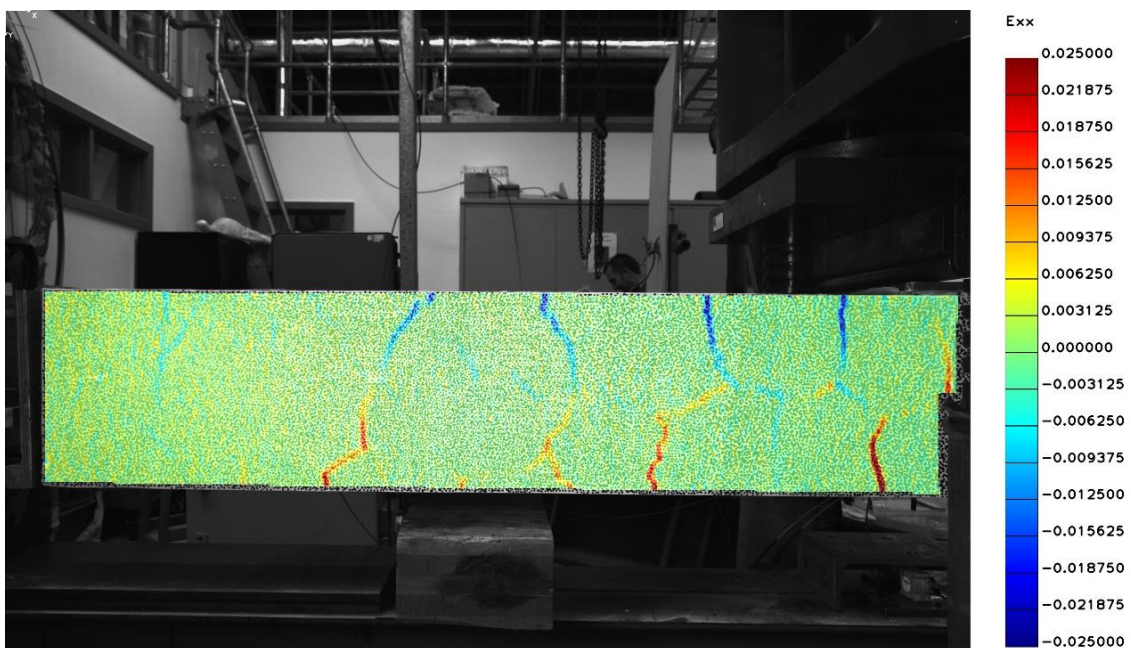
(b)
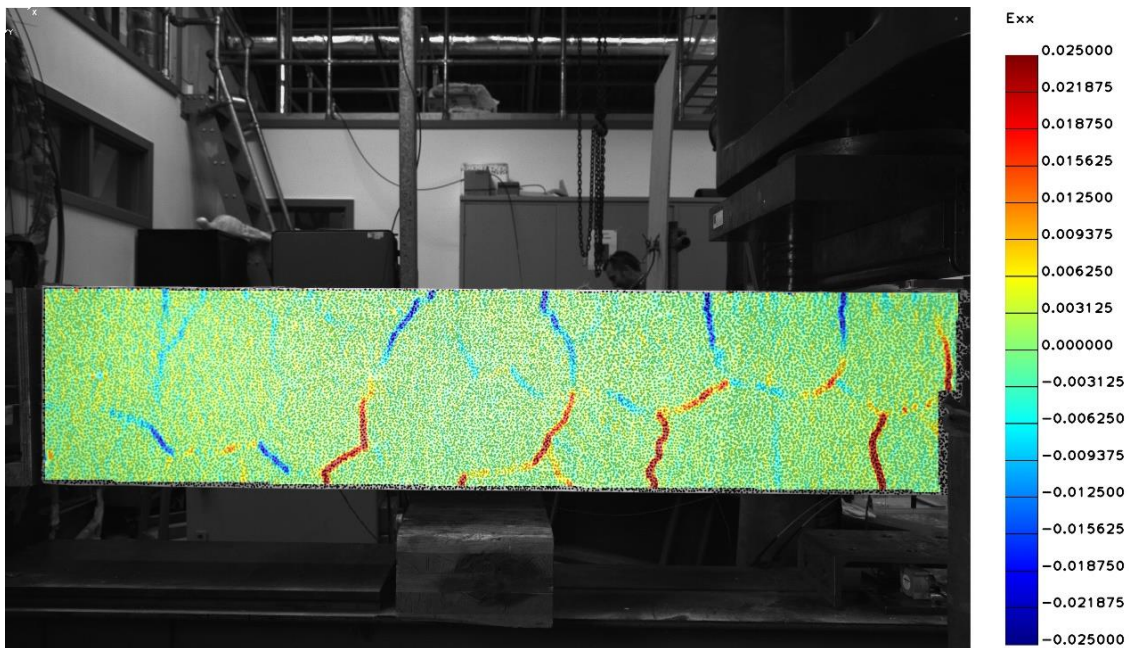
(c)
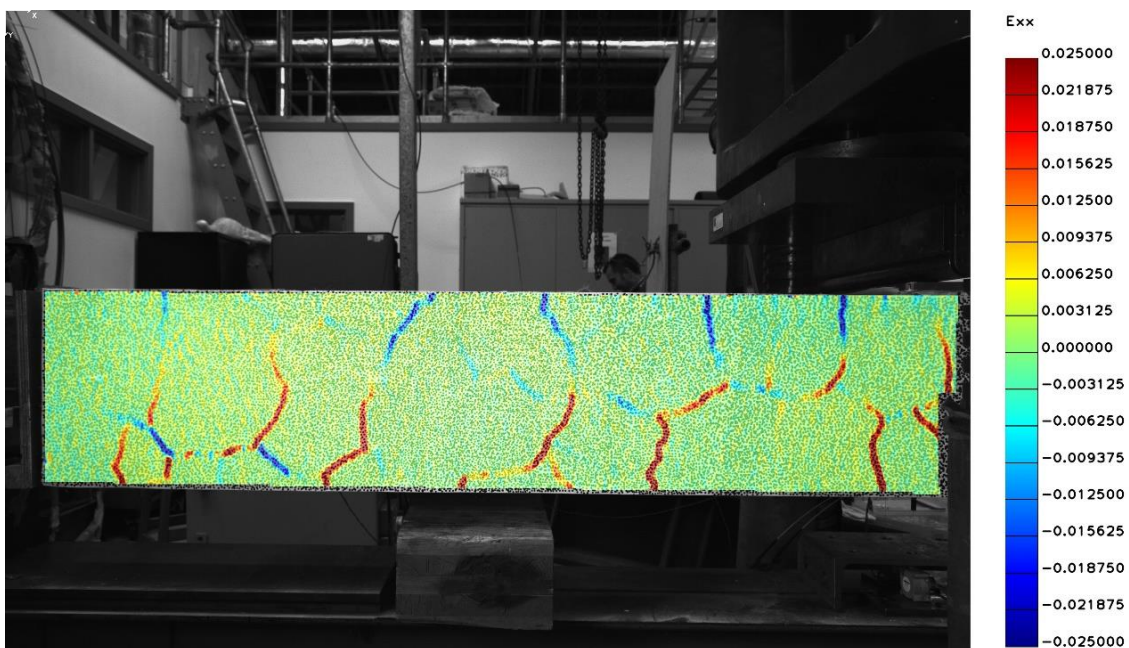
(d)

Figure 7-19 Longitudinal strain distributions in the cement sheath during loading test obtained from the digital image correlation analysis at different load levels: (a) 50 kN; (b) 150 kN; (c) 250 kN; (d) 300 kN.

7.5. Discussion

The potential of BOTDR measurements to monitor the bending curvature development of the well specimen is examined in Figure 7-20. It shows the curvature distributions derived analytically with the central deflection data obtained from the wire gauges (black solid lines) as well as the ones calculated from the BOTDR measurements (red dashed and blue dotted lines).

The analytical curvature distribution was derived in the following manner. First, the flexural rigidity (*EI*) of the specimen under three-point bending was calculated via Equation 7-1:

$$EI = \frac{PL^3}{48\delta_{max}} \tag{7-1}$$

where P = point load at the centre of the specimen; L = distance between the bottom supports; δ_{max} = deflection at the centre of the specimen. The flexural rigidity was updated at each load level with increasing P and δ_{max} values. The value of L was measured as 3.4 m. Second, the bending moment (*M*) was derived via Equation 7-2:

$$M = \frac{P}{2}\langle x \rangle - P\left\langle x - \frac{L}{2}\right\rangle \tag{7-2}$$

where x = distance from the left hand-side support. The $\langle\ \rangle$ operator is the Macaulay brackets which converts negative values into zero and leave positive values unmodified. Finally, the curvature (κ') was derived via Equation 7-3:

$$\kappa' = \frac{M}{EI} \tag{7-3}$$

To calculate empirical curvature from BOTDR measurements, Equation 7-4 was used:

$$\kappa' = \frac{\epsilon}{y} \tag{7-4}$$

where ϵ = longitudinal strain; y = distance from the neutral axis to the location of fibre optic cables in the cross-section. The longitudinal strain was calculated by averaging the absolute difference between strain distributions along pairs of cables embedded at symmetric locations

across the neutral axis (i.e., a cable pair of Cable7 and 8 and of Cable1 and 6) ($\epsilon = (\epsilon_{lower} - \epsilon_{upper})/2$). The values of $y = 0.125$ m and 0.145 m were used for the cable pair of Cable 1 and 6 and of Cable 7 and 8, respectively.
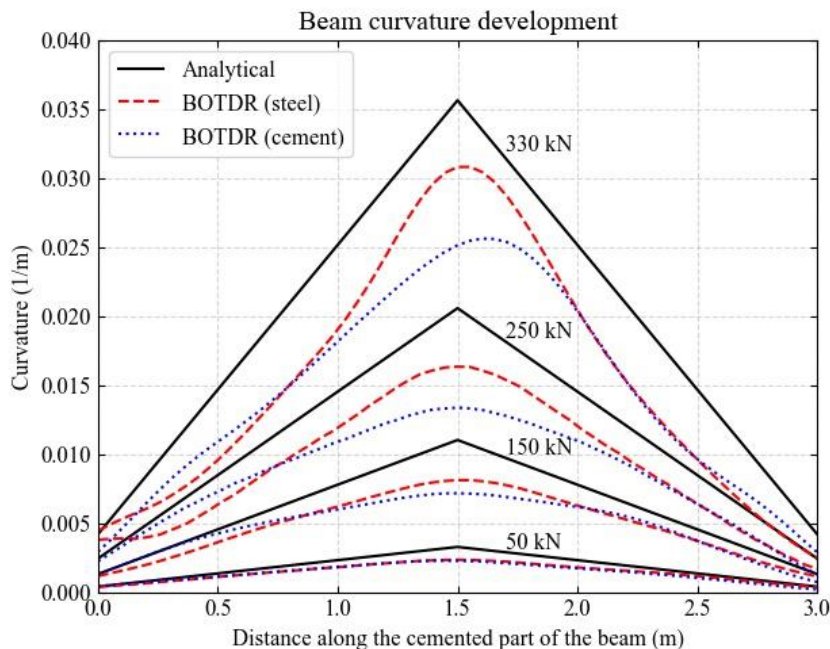
Figure 7-20 Development of bending curvature derived analytically from the central deflection data and calculated empirically from the BOTDR measurement.

It was found that the curvature values estimated from the BOTDR measurement were in good agreement with the analytical values derived with the central deflection data over a wide range of load levels. The values obtained from the BOTDR measurement were smaller than the analytical values. This is mainly due to the averaged nature of BOTDR measurements where the strain values are averaged over the spatial resolution of the BOTDR measurement (i.e., 0.5 m in this test), which makes it difficult to capture the peak value of the curvature distributions. Another reason might be that the specimen was no longer elastic at large load levels as the digital image correlation results showed extensive crack development in the cement sheath. It was also found that the curvature values calculated from the cables embedded in the cement (Cable1 and 6) (blue dotted lines) were smaller than those obtained from the cables attached on the steel box section (Cable7 and 8) (red dashed lines). This is in part caused by the lateral elongation of the cement sheath due to Poisson's effect at the point where the point load was applied from the loading apparatus. The strain distribution along the steel box section was not affected because Poisson's effect (i.e., the effect of the point load) did not propagate to the steel box section. Therefore, the fibre optic cables attached on the steel box section (i.e., on casing surface in the case of oil/gas wells) would be more advantageous than the ones embedded in the

cement in capturing the bending curvature distributions accurately.

7.6. Summary

In this study, distributed fibre optic monitoring of the bending deformation of well specimens was carried out at laboratory. The specimen consisted of a steel box section and cement sheath. To prevent interface slippage between the steel box section and cement sheath at room pressure conditions, shear studs were installed on the steel box section. Fibre optic cables were installed in the longitudinal direction on the steel box section as well as in the cement sheath to measure the longitudinal strain development of the specimen with BOTDR. Localized strain monitoring was performed by the FBGS and strain gauge measurement. The following findings have been obtained from this study:

(i)   BOTDR measurements captured the theoretical triangular longitudinal strain distributions of the specimen under three-point bending. The bending curvature development of the specimen was also captured by BOTDR measurements and it was in good agreement with the analytical bending curvature distributions derived from the central deflection of the specimen measured by the wire gauges.

(ii)   The curvature distributions calculated from BOTDR measurements along fibre optic cables embedded in the cement sheath had smaller peak values than those along cables attached on the steel box section. The longitudinal strain distributions in the cement sheath were significantly affected by Poisson's effect as the cement elongated in the lateral direction near the point load location. Therefore, fibre optic cables attached on the steel (e.g., casing) would produce more accurate bending curvature distributions from BOTDR measurements.

8. Conclusions and recommendations for future work

8.1. Conclusions

The research described in this thesis has contributed to the advancement of well integrity analyses in methane hydrate reservoirs, with particular emphasis on the Nankai Trough case, in the following areas described below.

8.1.1. Cement shrinkage in deepwater well annuli

There are a number of studies on laboratory measurements and numerical simulations of cement shrinkage. However, the inflow of water from the formation to hydrating cement was rarely incorporated. Also, the underlying physics of cement shrinkage (i.e., capillary pressure development) was ignored in the existing numerical simulations.

In the finite element modelling work, cement shrinkage process was modelled through capillary pressure development in a porous material with time-varying pore fluid contraction rate (i.e., sink rate), stiffness and permeability, which accurately represents the underlying physics of the shrinkage behaviour of early-age cement. Also, the simulation was carried out in a hydro-mechanically coupled manner to facilitate the interaction between the cement and formation during cement shrinkage. The model parameters (i.e., sink rate, stiffness and permeability) were calibrated against laboratory cement shrinkage tests performed under the pressure and temperature conditions representative of the Nankai Trough conditions.

Results show that cement shrinkage volume is dependent on the formation permeability because the rate of water supply from the formation to cement controls the negative pore pressure (i.e., capillary pressure) development of the cement. In general, it is found that cement shrinkage volume increases with decreasing formation permeability. However, cement shrinkage volume is also affected by the initial effective stress state of the cement at the initial set (i.e., the time where the phase change from liquid slurry to solid cement occurs). For the Nankai Trough case, it is found that the upper range of cement shrinkage volume is approximately 0.5% to 0.7% for the formation permeability between 0.1 μD to 1 mD.

8.1.2. Well integrity during well construction

Due to the unconsolidated nature of the Nankai Trough formation, well construction process could negatively affect formation integrity prior to gas production. In the previous well

construction modelling work in the literature, only certain construction stages such as drilling and completion stages were modelled. More detailed well construction processes were modelled by Xu (2014). However, the cement shrinkage stage was not modelled appropriately in his work because reasonable values of cement shrinkage volume for the Nankai Trough case were unknown. Therefore, the present work extends the work of Xu (2014) by incorporating the result of the cement shrinkage analysis described earlier.

It is found that the drilling stage has the largest impact among all construction stages on the plastic strain development of the formation around the wellbore. However, when it comes to stress changes of the formation, it is not the drilling stage but the cement shrinkage stage that has significant effects. This is because of the following mechanism (Figure 8-1). First, the drilling stage imposes a constant pressure decrease on the wellbore surface, which generates a larger horizontal strain change in the low stiffness (low hydrate saturation) layer than in the high stiffness (high hydrate saturation) layer (Figure 8-1b). In this process, the low hydrate saturation layer accumulates some plastic strains, which induce vertical stress decrease (stress redistribution) and hence smaller deviator stress changes occur in the low hydrate saturation layer than in the high hydrate saturation layer ($\Delta q \sim \Delta\sigma_v' - \Delta\sigma_h'$). Second, the cementing stage imposes a constant pressure increase on the wellbore surface, which brings the deviator stress levels in each layer back close to their initial levels (Figure 8-1c). It is noted that the deviator stress levels after the cementing process are slightly lower than the initial deviator stress levels due to the aforementioned vertical effective stress decrease in the low hydrate saturation layer. Finally, the cement shrinkage stage imposes a constant radial displacement on the wellbore surface, which generates greater horizontal stress changes in the high stiffness (high hydrate saturation) layer than in the low stiffness (low hydrate saturation) layer (Figure 8-1d). As a result, a significant difference in the final deviator stress levels in each layer is developed due to the cement shrinkage stage. The point is that the cement shrinkage stage imposes displacement boundary conditions on the wellbore surface, whereas the drilling and cementing stages impose pressure boundary conditions. The plastic strain development in the low hydrate saturation layer during the drilling stage contributes to the deviator stress concentration in the high hydrate saturation layer, but the difference in the initial stiffness of each layer has greater impact. This is demonstrated through the elastic cylindrical cavity expansion/contraction analysis described in Chapter 4. Therefore, it is crucial to incorporate the cement shrinkage stage into well construction processes of the well integrity simulation, in order to accurately estimate the stress state of the formation prior to gas production.
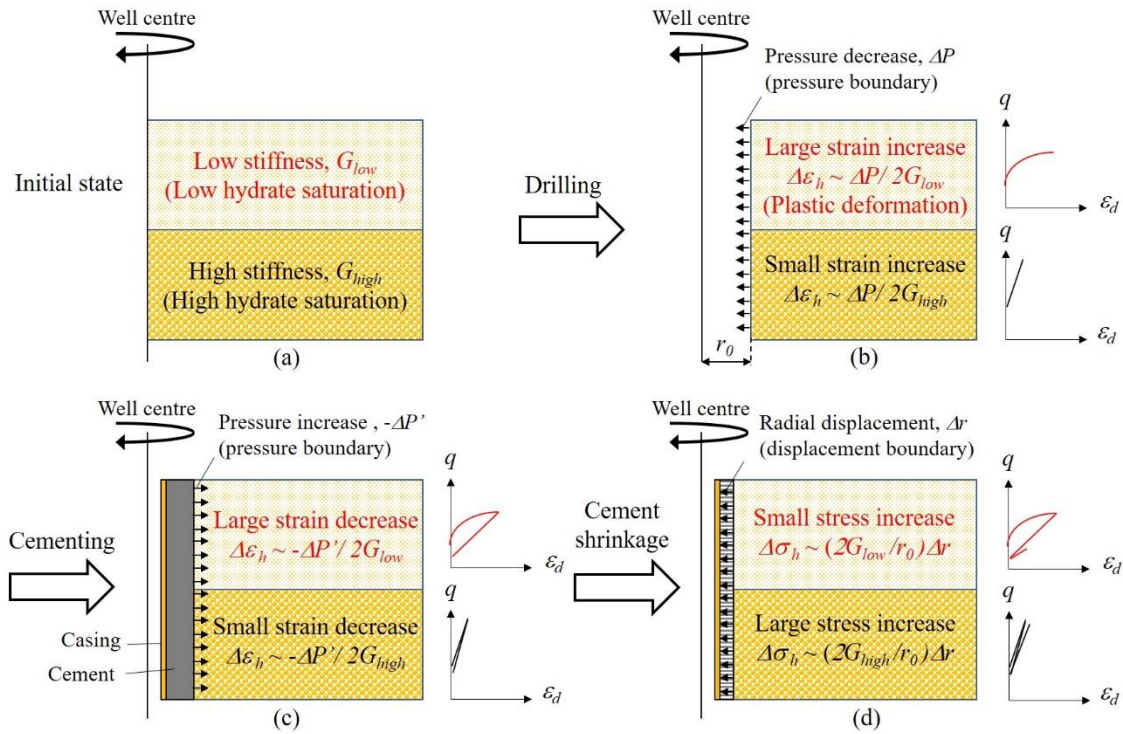
Figure 8-1 Stress and stiffness changes in the formation during well construction processes: (a) initial state; (b) after drilling stage; (c) after cementing stage; (d) after cement shrinkage stage.

8.1.3. Well integrity during reservoir compaction

Well integrity analyses against reservoir compaction is critical for sustainable oil/gas production. Well integrity simulations in the literature typically ignores one or more of the primary model components (i.e., casing, cement and formation). In addition, well construction processes prior to reservoir compaction are usually disregarded. A reservoir compaction model which incorporates all model components as well as well construction process was developed by Xu (2014). The present study extends his work by modelling different reservoir compaction profiles, which vary in their maximum subsidence magnitude and radial extent of subsidence, to assess their effect on the development of well integrity parameters such as axial stress, strain and plastic deviatoric strain of the casing and cement.

Results show that the maximum axial strain and plastic deviatoric strain levels in the casing and cement during reservoir compaction stages develop just above the reservoir layer and their magnitudes increase with increasing maximum reservoir subsidence and decreasing radius of reservoir subsidence. This indicates that the casing and cement are more likely to be damaged if the reservoir subsidence is more radially localised. Cement shrinkage is found to have a significant effect on the plastic deviatoric strain development in the cement as the maximum

plastic deviatoric strain level in the cement developed during reservoir compaction could triple due to the cement shrinkage volume of 0.75%. Also, small changes in the initial horizontal stress levels in the formation ($K_0 = 0.40 \sim 0.44$) (i.e., 10% change in effective stress) are found to cause a twofold increase in the maximum plastic deviatoric strain level in the cement. Therefore, cement shrinkage and the initial horizontal stress levels in the formation are important factors affecting cement integrity during reservoir compaction. The effect of cement shrinkage and initial horizontal stress levels in the formation is not pronounced in the plastic deviatoric strain development in the casing due mainly to its ductility (as oppose to cement's brittleness). Also, the cement shrinkage volume of 0.75% does not induce significant radial stress decrease at the cement-formation interface to induce interface slippage during reservoir compaction, and this is validated by a back-of-the-envelope calculation on the elastic cylindrical cavity contraction of the formation due to cement shrinkage.

Finally, it is found that the maximum axial strain and plastic deviatoric strain levels in the cement and casing increase with increasing pressure drawdown and decreasing radius of hydrate dissociation front. This indicates that the well might become most vulnerable during the initial periods of hydrate dissociation following rapid and large depressurization (~ 8 MPa). In order to maintain well integrity, it would be advisable to keep the depressurization to a low level ($\sim$ several MPa) until hydrate dissociation front advances to a certain radius.

8.1.4. Distributed strain sensing of well integrity with BOTDR/A

In order to accurately assess well integrity, it is imperative to carry out field monitoring. The conventional monitoring techniques typically lack spatial and/or temporal measurement resolutions. Distributed fibre optic monitoring techniques, on the other hand, facilitate real-time distributed monitoring with high spatial resolution and data accuracy. Distributed temperature sensing (DTS) and distributed acoustic sensing (DAS) with fibre optics have been deployed in oil and gas wells for approximately 20 and 10 years, respectively. On the other hand, distributed strain sensing (DSS) has not been utilized as much as DTS and DAS and its application has been limited to pipeline monitoring despite its potential to carry out real-time distributed well integrity monitoring.

The present work employed Brillouin optical time domain reflectometry/analysis (BOTDR/A) in laboratory experiments to evaluate its potential to carry out axial and bending deformation monitoring of well specimens. Results show that BOTDR/A captures the actual axial strain and bending curvature development of the well specimen subjected to axial tensile loading and three-point bending loading, respectively. From the tensile loading test, it is found that fibre

optic cables with a small number of coating layers, which are tightly buffered through mechanical compression and/or chemical bonding, could lead to accurate strain measurement with BOTDR. From the bending test, it is shown that cables attached on the casing would provide more accurate bending curvature distributions than cables embedded in the cement sheath due to cement's deformation in response to bending loads could be significantly affected by Poisson's effect.

8.2. Recommendations for future work

Recommended future work includes, but are not limited to, the ones which could advance the studies presented in this dissertation by addressing their limitations. Therefore, potential future research for the well integrity simulations and monitoring is suggested as below.

8.2.1. Cement shrinkage simulation

In the calibration of the cement shrinkage model, the sink rate, stiffness (Young's modulus) and permeability are assumed to be exponential functions of time since the initial set of cement slurry. As there probably are other combinations of parameter values that match the simulation results with the laboratory cement shrinkage test data, the sink rate, stiffness and permeability changes with time should be directly measured during laboratory shrinkage tests so that the parameter values can be determined without calibration. The sink rate, for example, is the rate of pore water consumption via cement hydration reaction, which generates proportional amounts of hydration heat. Hence, the measurement of heat output from hydrating cement samples should be taken by, for instance, isothermal calorimetry, in order to determine the change in sink rate with time. The rate of change in Young's modulus can be measured by measuring the development of shear wave velocity of hydrating cement samples. As to the measurement of change in permeability values with time, it might be difficult as the permeability of cement is initially low from the start of the hydration process and it decreases to even lower values as the hydration reaction proceeds. However, if changes in the sink rate and stiffness with time are determined through measurements, permeability change can be calibrated to match the pore pressure change of cement samples in an open-valve shrinkage test with pore pressure measurement. This will reduce the uncertainty of the model parameter determination significantly and hence it will lead to more accurate predictions of the behaviour of early-age cement and its interaction with the formation in the well annulus during cement shrinkage process.

In addition, another source of uncertainty in the wellbore cement shrinkage simulation is that the

initial pore pressure level in the cement at the onset of its initial set (i.e., transition from fluid slurry to solid cement) remains unknown. In this thesis, two extreme conditions, where the initial cement pore pressure is set equal to either the slurry pressure or formation pore water pressure, are considered to estimate the upper and lower boundaries of possible cement shrinkage volumes in well annuli. This uncertainty can be eliminated if precise measurements on the pore pressure development of cement samples during their transition period from fluid slurry to solid cement are taken. Therefore, laboratory tests with instrumentation for precise pore pressure measurements of cement samples during their transition from slurry into solid states would have to be carried out in the future.

8.2.2. Well construction simulation

The effect of formation constitutive models on the simulation results needs to be investigated carefully. In this thesis, the MHCS model is primarily used after being calibrated against laboratory triaxial shear test data on *in situ* formation samples. Hence, the simulated formation behaviour would be accurate as long as the loading conditions in the field during well construction processes are identical or similar to those in the laboratory tests. However, the actual loading conditions (e.g., stress paths) could differ between the field and laboratory tests and hence inaccurate prediction of the stress and strain development of the formation could be computed. Therefore, the values of the constitutive model parameters might have to be matched through small-scale laboratory tests, in which well construction processes such as drilling is carried out and the deformation of the formation is monitored by, for example, particle image velocimetry (PIV), to ensure that the parameter values are calibrated for the expected loading conditions in the field during well construction processes. Also, the choice of constitutive models could affect the simulation results. For instance, the Mohr-Coulomb model could be used to simulate the formation behaviour, as the formation compaction process, which is better modelled by critical state soil models such as the MHCS model, would not be the main deformation mechanism during well construction processes.

8.2.3. Well subsidence simulation

In this thesis, the pore pressure change in the reservoir layer is specified directly with the analytical steady-state pore pressure distributions in which the hydrate dissociated (high permeability) and undissociated (low permeability) zones are considered. Although this might be an acceptable approximation of the pore pressure distributions in the hydrate reservoir during hydrate dissociation, the actual pore pressure development is highly complex which involves thermo-hydro-mechanically coupled processes. Therefore, a separate thermo-hydromechanical or thermo-hydro coupled simulation on hydrate dissociation would have to be performed to calculate

accurate pore pressure distributions in the hydrate reservoir layer during hydrate dissociation. The computed pore pressure distributions can then be used as inputs for the hydromechanical simulation specializing in the well-formation interaction analysis. This will add relevant timelines, such as elapsed time since the start of depressurization, to changes in well integrity, which are ignored in the simulation presented in this thesis as steady-state pore pressure distributions are directly applied in arbitrary time intervals.

In addition, the interface friction model, which is employed for the modelling of shaft friction development in the well during reservoir subsidence, should be enhanced by incorporating the interface dilation/contraction. This is because interface dilation/contraction will change the interface pressure, which then changes the interface tangential displacement stiffness as well as the ultimate interface shear stress, affecting the development of shaft friction in the well during reservoir subsidence. Laboratory test data is necessary to validate and calibrate the enhanced interface friction model. Such data should be available in the literature, but for the calibration of specific interfaces, tailored laboratory tests might have to be designed and carried out.
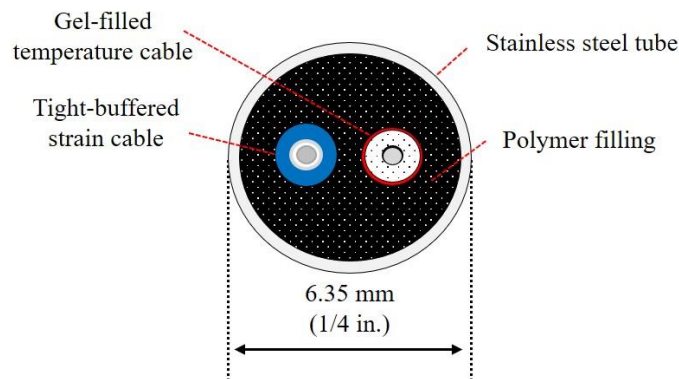
Figure 8-2 The schematic diagram of the cross section of a robust fibre optic cable for in-well distributed strain and temperature monitoring.

8.2.4. Well integrity monitoring

The fibre optic cables examined in the present laboratory tests have been found unsuitable for field deployment in oil and gas wells due to their insufficient robustness and/or low strain sensitivity. Therefore, a new fibre optic cable has been designed so as to achieve high robustness and high strain sensitivity simultaneously (Figure 8-2). The structure of this cable is that one tight-buffered fibre optic strain cable and one gel-filled fibre optic temperature cable, both of which are off-the-shelf products, are encased in a 1/4-in. stainless tube with polymer filling in the gap. The cable robustness is enhanced by the stainless steel coating whereas the strain sensitivity is relied upon the bonding between the polymer layer and the tight-buffered strain cable. The main

concern is that the polymer layer might hinder the strain transfer from the outermost steel coating to the tight-buffered strain cable. Therefore, the performance of the new fibre optic cable needs to be examined in a laboratory test. The polymer material might have to be modified in case the strain sensitivity of the cable is found to be insufficient.

Appendix A

ABAQUS user subroutine codes for the MHCS model

```
c       SDVINI code for Modified Cam Clay
        subroutine sdvini(statev,coords,nstatv,ncrds,noel,npt,layer,kspt)
        include 'aba_param.inc'
        dimension statev(nstatv),coords(ncrds),YR(336),SAT(336)
        double precision rhoB,h
c
        YR=0
        SAT=0
        c1=1
        h=70-coords(2)
c
        do i = 1,150
            statev(i)=0.0
        end do
c
c       Model parameters to get initial values
        if(h.lt.277)then
            statev(113) = 0.18 !cil
            statev(114) = 0.03 !sik
            statev(115) = 1.30 !rM
            statev(116) = 15.0 !u
            statev(117) = 0.25 !pnyu
            statev(118) = 0 !rM2
            statev(119) = 0 !eM
            statev(120) = 0 !a
            statev(121) = 0 !b
            statev(122) = 0 !c
            statev(123) = 0 !d
        else
            statev(113) = 0.10 !cil
            statev(114) = 0.02 !sik
            statev(115) = 1.37 !rM
            statev(116) = 8.0 !u
            statev(117) = 0.35 !pnyu
            statev(118) = 200E3 !rM2
            statev(119) = 2.0 !eM
            statev(120) = 20.0E3 !a
            statev(121) = 1.4 !b
            statev(122) = 0.5E3 !c
            statev(123) = 1.4 !d
        end if
c
c       Initial void ratio
        if(h.lt.277)then
            statev(2)=1.311203320
        elseif(h.ge.277.and. h.lt.339)then
            rhoB=1.750+0.004032258*(h-277)
            statev(2)=(rhoB-2.698)/(1.027-rhoB)
        elseif(h.ge.339)then
            statev(2)=0.717368962
        endif
C
c       Degragation factor
        statev(3)=1.0
c
c       Preconsolidation pressure
        If (h.lt.277) then
            statev(9)=6.8275*h+581.1
        elseif(h.ge.277.and. h.lt.339)then
            statev(9)=632.6*exp(0.0038*h)
        elseif(h.ge.339)then
            statev(9)=8.7514*h-694.7
        end if
C
c       Calculate initial stresses
        if (h.lt.277) then
            ratio=0.40
            porep = ((1030*h*9.81)/1000)+10124.50860
            Total=((1750*h*9.81)/1000)+10124.50860
            statev(102) = Total - porep
            statev(103) = statev(102) * ratio
        elseif(h.ge.277.and. h.lt.339) then
            ratio=0.40
```

```
            porep = ((1030*h*9.81)/1000)+10124.50860
            Total=9.81*(1750+2.016129032*(h-277))*(h-277)/1000+14879.90610
            statev(102) = Total - porep
            statev(103) = statev(102) * ratio
        elseif(h.ge.339) then
            ratio=0.40
            porep = ((1030*h*9.81)/1000)+10124.50860
            Total=((2000*(h-339)*9.81)/1000)+16020.31860
            statev(102) = Total - porep
            statev(103) = statev(102) * ratio
        end if
c
c       Calculate pc and qc
        statev(6)=(statev(102)+2.0*statev(103))/3.0
        statev(7)=statev(102)-statev(103)
c
c
        YR=(/0.0 ,-207.34 ,
     +  -207.51 ,-207.66 ,-208.03,
     +  -208.48 ,-208.67 ,-208.78 ,-208.92 ,-209.1 ,-209.37 ,-209.83 ,
     +  -210.19 ,-210.37 ,-210.49 ,-210.56 ,-210.69 ,-210.87 ,-210.99 ,
     +  -211.12 ,-211.24 ,-211.35 ,-211.47 ,-211.7 ,-211.95 ,-212.06 ,
     +  -212.19 ,-212.4 ,-212.7 ,-213.01 ,-213.17 ,-213.29 ,-213.77 ,
     +  -214.24 ,-214.38 ,-214.54 ,-214.91 ,-215.29 ,-215.41 ,-215.61 ,
     +  -215.81 ,-215.91 ,-216.14 ,-216.45 ,-216.64 ,-216.77 ,-216.87 ,
     +  -216.93 ,-217.01 ,-217.14 ,-217.26 ,-217.38 ,-217.5 ,-217.58 ,
     +  -217.67 ,-217.76 ,-217.84 ,-217.93,-218. ,-218.16,-218.4 ,-218.57
     +   ,-218.74 ,-218.98 ,-219.1 ,-219.2 ,-219.31 ,-219.37 ,-219.44 ,
     +   -219.52 ,-219.6 ,-219.66 ,-219.71 ,-219.75 ,-219.78 ,-219.84 ,
     +  -219.95 ,-220.04 ,-220.12 ,-220.21 ,-220.36 ,-220.48 ,-220.61 ,
     +  -220.77 ,-220.86 ,-220.94 ,-221.16 ,-221.41 ,-221.52 ,-221.57 ,
     +  -221.75 ,-221.95 ,-222.15 ,-222.33 ,-222.45 ,-222.67 ,-222.84 ,
     +  -222.94 ,-223.17 ,-223.37 ,-223.42 ,-223.54 ,-223.84 ,-224.14 ,
     +  -224.33 ,-224.48 ,-224.58 ,-224.68 ,-224.74 ,-224.79 ,-224.86 ,
     +   -224.91 ,-224.98 ,-225.17 ,-225.33 ,-225.45 ,-225.66 ,-225.88,
     +  -226. ,-226.09 ,-226.21 ,-226.3 ,-226.42 ,-226.55 ,-226.61 ,
     +  -226.7 ,-226.82 ,-226.95 ,-227.08 ,-227.14 ,-227.21 ,-227.34 ,
     +  -227.46 ,-227.57 ,-227.73 ,-227.85 ,-227.91 ,-228.03 ,-228.18 ,
     +  -228.34 ,-228.5 ,-228.67 ,-228.97 ,-229.19 ,-229.34 ,-229.64 ,
     +  -229.98 ,-230.32 ,-230.97 ,-231.5 ,-231.64 ,-232.1 ,-232.74 ,
     +  -233.03 ,-233.23 ,-233.49 ,-233.79 ,-234.02 ,-234.12 ,-234.24 ,
     +  -234.41 ,-234.6 ,-234.79 ,-234.9 ,-234.97 ,-235.04 ,-235.11 ,
     +  -235.18 ,-235.39 ,-235.62 ,-235.74 ,-235.82 ,-235.89 ,-236.12 ,
     +  -236.41 ,-236.64 ,-236.85 ,-237.16 ,-237.46 ,-237.58 ,-237.66 ,
     +  -237.76 ,-237.9 ,-238.21 ,-238.48 ,-239.19 ,-240. ,-240.95 ,
     +  -241.81 ,-241.94 ,-242.09 ,-242.17 ,-242.24 ,-242.34 ,-242.46 ,
     +  -242.55 ,-242.7 ,-242.87 ,-242.99 ,-243.12 ,-243.25 ,-243.33 ,
     +  -243.49 ,-243.69 ,-243.81 ,-243.9 ,-243.96 ,-244.06 ,-244.35 ,
     +  -244.77 ,-245.03 ,-245.12 ,-245.27 ,-245.53 ,-245.71 ,-245.8 ,
     +  -245.92 ,-246.01 ,-246.18 ,-246.37 ,-246.43 ,-246.53 ,-246.63 ,
     +  -246.66 ,-246.75 ,-246.87 ,-246.94 ,-247.12 ,-247.34 ,-247.45 ,
     +  -247.51 ,-247.57 ,-247.61 ,-247.7 ,-247.79 ,-247.88 ,-247.96 ,
     +  -248. ,-248.06 ,-248.12,-248.2 ,-248.3 ,-248.49,-248.67,-248.75,
     +  -248.85 ,-248.95 ,-249.06 ,-249.21 ,-249.34 ,-249.46 ,-249.61 ,
     +  -249.87 ,-250.12 ,-250.2 ,-250.26 ,-250.37 ,-250.48 ,-250.53 ,
     +  -250.57 ,-250.85 ,-251.14 ,-251.2 ,-251.27 ,-251.34 ,-251.41 ,
     +  -251.5 ,-251.63 ,-251.78 ,-251.91 ,-252.01 ,-252.17 ,-252.29 ,
     +  -252.42 ,-252.56 ,-252.8 ,-253.02 ,-253.1 ,-253.32 ,-253.49 ,
     +  -253.55 ,-253.72 ,-253.88 ,-254.16 ,-254.45 ,-254.58 ,-254.72 ,
     +  -254.83 ,-255.03 ,-255.21 ,-255.27 ,-255.56 ,-255.95 ,-256.54 ,
     +  -257.04 ,-257.1 ,-257.32 ,-257.59 ,-257.68 ,-257.76 ,-257.86 ,
     +  -258.67 ,-259.43 ,-259.61 ,-259.88 ,-260.05 ,-260.14 ,-260.34 ,
     +  -260.57 ,-260.84 ,-261.06 ,-261.17 ,-261.37 ,-261.53 ,-261.99 ,
     +  -262.46 ,-262.58 ,-262.83 ,-263.06 ,-263.14 ,-263.29 ,-263.43 ,
     +  -264.23 ,-265.07 ,-265.31 ,-265.64 ,-265.88 ,-266.03 ,-266.17 ,
     +  -266.3 ,-266.37 ,-266.46 ,-266.63 ,-266.91 ,-267.22 ,-267.46/)
c
        SAT=(/0.00000 ,0.00000 ,0.14458 ,0.36295 ,0.3418 ,0.61196 ,
     & 0.56277 ,0.00000 ,0.19596 ,0.17561 ,0.00000 ,0.58844 ,0.26251 ,0.00000 ,0.04663,
     & 0.00000,
     & 0.02339 ,0.00000 ,0.3181,0.45953 ,0.33911 ,0.00000 ,0.34258 ,0.00000 ,0.25609 ,
     & 0.00000,
     & 0.10518 ,0.00000 ,0.16705 ,0.05795 ,0.05849 ,0.0812,0.32033 ,0.00000 ,
     & 0.55364 ,0.77874 ,0.37003 ,0.00000 ,0.39255 ,0.00000 ,0.48902 ,0.68256 ,
     & 0.48051 ,0.00000 ,0.56655 ,0.70202 ,0.43452 ,0.00000 ,0.26558 ,0.00000 ,0.38004,
     & 0.71712 ,0.52794 ,0.00000 ,0.45273 ,0.00000 ,0.47713 ,0.76745 ,0.66253 ,0.00000 ,
     & 0.42304 ,0.19709 ,0.00000 ,0.37125 ,0.00000 ,0.27577 ,0.27149 ,0.11948 ,0.00000 ,
     & 0.43313 ,0.73695 ,0.65244 ,0.00000 ,0.18494 ,0.10459 ,0.34962 ,
     & 0.74801 ,0.52668 ,0.00000 ,0.55398 ,0.75093 ,0.47009 ,0.00000 ,0.58854 ,
     & 0.69377 ,0.47352 ,0.00000 ,0.60823 ,0.72542 ,0.64923 ,0.00000 ,0.47925 ,
     & 0.754 ,0.50781 ,0.00000 ,0.50723 ,0.00000 ,0.52267 ,0.74891 ,0.60149 ,0.00000 ,
     & 0.25917 ,0.00000 ,0.50768 ,0.77168 ,0.30597 ,0.00000 ,0.10427 ,0.00000 ,0.55586 ,
```

193

```
     & 0.78226 ,0.77752 ,0.71061 ,0.39131 ,0.5805 ,0.58297 ,0.00000 ,0.45288,
     & 0.75398 ,0.50475 ,0.00000 ,0.70358 ,0.00000 ,0.52833 ,0.69773 ,0.39834 ,0.00000 ,
     & 0.46034 ,0.71502 ,0.50422 ,0.00000 ,0.48412 ,0.60042 ,0.00000 ,0.48005 ,
     & 0.74645 ,0.49663 ,0.00000 ,0.5457 ,0.77428 ,0.60206 ,0.00000 ,0.5045 ,
     & 0.64725 ,0.6294 ,0.66872 ,0.46426 ,0.00000 ,0.58732 ,0.78337 ,0.71101 ,
     & 0.00000 ,0.62937 ,0.00000 ,0.51633 ,0.00000 ,0.61127 ,0.7159 ,0.54398 ,0.00000,
     & 0.41505 ,
     & 0.00000 ,0.51752 ,0.74322 ,0.76902 ,0.76431 ,0.75119 ,0.58331 ,0.00000 ,
     & 0.50445 ,0.65421 ,0.77432 ,0.79747 ,0.83423 ,0.43389 ,0.00000 ,0.41096,
     & 0.00000 ,0.51375 ,0.64605 ,0.6343 ,0.67262 ,0.75764 ,0.76861 ,0.71947 ,
     & 0.41391 ,0.55049 ,0.41993 ,0.34623 ,0.33171 ,0.26036 ,0.00000 ,0.20616,
     & 0.22357 ,0.19394 ,0.77805 ,0.76577 ,0.00000 ,0.55034 ,0.00000 ,0.55567 ,0.00000 ,
     & 0.48432 ,0.00000 ,0.62864 ,0.00000 ,0.46365 ,0.81756 ,0.60301 ,0.77533 ,
     & 0.42136 ,0.66651 ,0.59518 ,0.60866 ,0.67401 ,0.69011 ,0.71775 ,
     & 0.74395 ,0.49358 ,0.5694 ,0.00000 ,0.47692 ,0.52612 ,0.54901 ,0.73134 ,
     & 0.61077 ,0.58083 ,0.51368 ,0.67945 ,0.68911 ,0.76453 ,0.68416 ,
     & 0.52516 ,0.7227 ,0.64475 ,0.72011 ,0.78875 ,0.52931 ,0.68586,
     & 0.50977 ,0.00000 ,0.55483 ,0.00000 ,0.32354 ,0.00000 ,0.693 ,0.72135 ,0.4735,
     & 0.74949,
     & 0.68879 ,0.79019 ,0.59773 ,0.51374 ,0.49226 ,0.00000 ,0.47245 ,0.50104 ,
     & 0.00000 ,0.57874 ,0.48172 ,0.53124 ,0.55259 ,0.45112 ,0.73623 ,0.53675,
     & 0.68487 ,0.7119        ,0.71878 ,0.57726 ,0.70184 ,0.4481 ,0.80921 ,
     & 0.60982 ,0.72346 ,0.40428 ,0.79296 ,0.41893 ,0.73095 ,0.64739 ,
     & 0.77266 ,0.53706 ,0.73922 ,0.58102 ,0.72107 ,0.6254,0.00000 ,0.61026 ,
     & 0.00000 ,0.49962 ,0.62972 ,0.3712 ,0.00000 ,0.57286 ,0.00000 ,0.57 ,0.70676,
     & 0.54237,
     & 0.70601 ,0.44232 ,0.63096 ,0.38387 ,0.77746 ,0.54744 ,0.00000 ,0.51382,
     & 0.67764 ,0.513,0.7292 ,0.48387 ,0.73199 ,0.4716 ,0.44696 ,0.00000 ,
     & 0.42365 ,0.71752 ,0.41728 ,0.68478 ,0.59422 ,0.73123 ,0.50268 ,0.00000 ,0.46104,
     & 0.00000 ,0.51579 ,0.00000 ,0.4612 ,0.00000 ,0.44903 ,0.00000 ,0.46086 ,0.75098,
     & 0.63522,
     & 0.68747 ,0.62945 ,0.73049 ,0.00000/)
c
c     Assign hydrate saturation at each integration point
      do while (c1.LE.335)
          flag1=(COORDS(2)-YR(c1))*(COORDS(2)-YR(c1+1))
          if(flag1.LE.0)then
              statev(112)=(COORDS(2)-YR(c1))*(-SAT(c1)+SAT(c1+1))
              statev(112)=statev(112)/(-YR(c1)+YR(c1+1))+SAT(c1)
          endif
          c1=c1+1
      enddo
c
c     pcd(i.e. 82) and pcc(i.e. 81)
      statev(82)=statev(120)*(statev(3)*statev(112))**statev(121)
      statev(81)=statev(122)*(statev(3)*statev(112))**statev(123)
c
c     Subloading ratio, R
      statev(75)=(statev(7)**2+statev(115)**2*statev(6)*
     1   (statev(6)+statev(81)))/((statev(115)**2)*(statev(6)+
     2   statev(81))*(statev(9)+statev(82)+statev(81)))
c
      return
      end
c
c
c     UMAT code for Cambridge Methane Hydrate Critical Model
      subroutine umat(stress,statev,DDSDDE,sse,spd,scd,
     1 rpl,ddsddt,drplde,drpldt,
     2 stran,dstran,time,dtime,temp,dtemp,predef,dpred,cmname,
     3 ndi,nshr,ntens,nstatev,props,nprops,coords,drot,pnewdt,
     4 celent,dfgrd0,dfgrd1,noel,npt,layer,kspt,kstep,kinc)
      include 'aba_param.inc'
      character*80 cmname
      dimension stress(ntens),statev(nstatev),
     1 DDSDDE(ntens,ntens),ddsddt(ntens),drplde(ntens),
     2 stran(ntens),dstran(ntens),time(2),predef(1),dpred(1),
     3 props(nprops),coords(3),drot(3,3),dfgrd0(3,3),dfgrd1(3,3)
c
c     define internal variables as double precision
      double precision stress1(4,1),strain1(4,1),dstress(4),DeINV(4,4),
     1 dstress1(4,1),dstrain1(4,1),Dsp1(4,1),DShe(4,1),Dsp2(4,1),
     2 dFds(4,1),dFdst(1,4),dlamda0(1,4),dlamda1(1,4),Dp11(4,1),
     3 DHSDDE(4,1),Dp12(4,4),Dp1(4,4),Dp(4,4),ee(4,1),Dhe(4,4),
     4 De(4,4),Dsp(4,1),dstress2(4,1),Dsp22(4,1),DShe1(4,1),Dsp3(4,1),
     5 stress2(4,1),Total,porep,ratio,h,dev,ded,dlamda2,dlamda3,dlamda4,
     6 dlamda5,dlamda6,dlamda7,dlamda,BKS,GS0,GS,depv,depd,void,p1,X,Sh,
     7 pcc,pcd,pc,qc,R,dSh,iter
c
c
      h=70-coords(2)
              iter = 0
```

194

```
c
c
c       Initialise local variables
        dlamda2=0.0
        dlamda3=0.0
        dlamda4=0.0
        dlamda5=0.0
        dlamda6=0.0
        dlamda7=0.0
        dlamda=0.0
        do i=1,4
            stress1(i,1)=0.0
            strain1(i,1)=0.0
            dstress(i)=0.0
            dstress1(i,1)=0.0
            dstress2(i,1)=0.0
            dstrain1(i,1)=0.0
            dFds(i,1)=0.0
            dFdst(1,i)=0.0
            dlamda0(1,i)=0.0
            dlamda1(1,i)=0.0
            Dp11(i,1)=0.0
            ee(i,1)=0.0
            DShe(i,1)=0.0
            DShe1(i,1)=0.0
            DHSDDE(i,1)=0.0
            Dsp(i,1)=0.0
            Dsp1(i,1)=0.0
            Dsp2(i,1)=0.0
            Dsp3(i,1)=0.0
            Dsp22(i,1)=0.0
            stress2(i,1)=0.0
        end do
        do i=1,4
            do j=1,4
                De(i,j)=0.0
                Dp12(i,j)=0.0
                Dp1(i,j)=0.0
                Dp(i,j)=0.0
                Dhe(i,j)=0.0
                DeINV(i,j)=0.0
            end do
        end do
c
c
        do i=1,ntens
c       Get stress tensor from Abaqus
            stress1(i,1)=-stress(i)
        end do
c       stress2 seems to be stress changes from the initial state
            stress2(1,1)=stress1(1,1)-statev(103)
            stress2(2,1)=stress1(2,1)-statev(102)
            stress2(3,1)=stress1(3,1)-statev(103)
            stress2(4,1)=stress1(4,1)
c
c       Get strain tensor from abaqus (change sign)
        do i=1,ntens
            strain1(i,1)=-stran(i)
        end do
c
c       Get strain increment tensor from abaqus (change sign)
        do i=1,ntens
            dstrain1(i,1)=-dstran(i)
        end do
c
c       Calculate dSh
        dSh=0
c
c       Get material parameters
        cil = statev(113)
        sik = statev(114)
        rM = statev(115)
        u = statev(116)
        pnyu = statev(117)
        rM2 = statev(118)
        eM = statev(119)
        a = statev(120)
        b = statev(121)
        c = statev(122)
        d = statev(123)
c
c       Get plastic volumetric strain
```

```
      epv=statev(1)
c
c     Get plastic deviator strain
      epd=statev(4)
c
c     Get void ratio
      void=statev(2)
c
c     Get preconsolidation pressure
      p1=statev(9)
c
c     Get degradation factor
      X=statev(3)
c
c     Get plastic strain
      ep1=statev(89)
      ep2=statev(90)
      ep3=statev(91)
      ep4=statev(92)
c
c     Get total volumetric and deviatoric strain
      ev=statev(100)
      ed=statev(101)
c
c     Get hydrate saturation
      Sh=statev(112)
c
c     Get the enhancement of strength due to hydrate
      pcc=statev(81)
c
c     Get the enhancement of dilatancy  due to hydrate
      pcd=statev(82)
c
c     Get mean and deviator stresses
      pc=statev(6)
      qc=statev(7)
c
c     Get the subloading ratio of R
      R=statev(75)
c
c     Calculate elastic stifness
c     The expressions below are all correct
      BKS=(1.0+void)/sik*pc
      GS0=3.0*BKS/2.0*(1.0-2.0*pnyu)/(1.0+pnyu)
      GS=GS0+rM2*X*Sh
c     The components of the stiffness matrix are all correct
      do i=1,3
          do j=1,3
              if (i==j) then
                  De(i,j)=BKS+4./3.*GS
              else
                  De(i,j)=BKS-2./3.*GS
              end if
          end do
      end do
      De(4,4)=GS
c
      call MATINV(1,4,De,DeINV)
c
c
      do i=1,4
          do j=1,4
c             ee is the elastic strain generated since the initial state
              ee(i,1)=ee(i,1)+DeINV(i,j)*stress2(j,1)
          end do
      end do
c     Calculate elastic stifness changes due to hydrate dissociation
c     The componets of Dhe below are all correct
      do i=1,3
          do j=1,3
              if (i==j) then
                  Dhe(i,j)=4./3.*rM2
              else
                  Dhe(i,j)=-2./3.*rM2
              end if
          end do
      end do
      Dhe(4,4)=rM2
       do i=1,4
          do j=1,4
              DShe1(i,1)=DShe1(i,1)+Dhe(i,j)*ee(j,1)
          end do
```

```
          end do
c
      do i=1,4
          DShe(i,1)=X*DShe1(i,1)
      end do
c
c
c     Update new stresses
      do i=1,4
          do j=1,4
              dstress2(i,1)=dstress2(i,1)+De(i,j)*dstrain1(j,1)
          end do
      end do
c
      do i=1,4
          dstress1(i,1)=dstress2(i,1)+DShe(i,1)*dSh
          dstress2(i,1)=0.0
      end do
c
      do i=1,4
          stress1(i,1)=stress1(i,1)+dstress1(i,1)
          dstress1(i,1)=0.0
      end do
c
c     Update mean stress
      pc=(stress1(1,1)+stress1(2,1)+stress1(3,1))/3.0
c
c     Update deviatoric stress
      qc=sqrt(3.0/2.0)*sqrt((stress1(1,1)-pc)**2+
     1 (stress1(2,1)-pc)**2+(stress1(3,1)-pc)**2+
     2 2.0*stress1(4,1)**2)
c
c
c     Define yield function
      fs=qc**2+(rM**2)*(pc+pcc)*(pc-R*(p1+pcc+pcd))
c
c
c     Judge yielding
      if (fs .le. 0.0) then
          do i=1,4
              do j=1,4
                  DDSDDE(i,j)=De(i,j)
                  DHSDDE(i,1)=DShe(i,1)
                  depv=0.0
                  depd=0.0
                  yjudge=0.0
              end do
          end do
c
c
      do i=1,4
          stress(i)=-stress1(i,1)
      end do
c
c     Update plastic volumetric strain
      epv=epv+depv
c
c     Update plastic deviatoric strain
      epd=epd+depd
c
      dep1=0.0
      dep2=0.0
      dep3=0.0
      dep4=0.0
      ep1=ep1+dep1
      ep2=ep2+dep2
      ep3=ep3+dep3
      ep4=ep4+dep4
c
c     Update the void ratio
      void=void+(dstran(1)+dstran(2)+dstran(3))*(1.0+void)
c
c     Update R
      R=(qc**2+rM**2*pc*(pc+pcc))/((rM**2)*(pc+pcc)*(p1+pcd+pcc))
c
c     Update volmetric strain and deviatoric strain
      dev=dstrain1(1,1)+dstrain1(2,1)+dstrain1(3,1)
      ded=sqrt(2.0/3.0)*sqrt((dstrain1(1,1)-dev/3.0)**2+
     1 (dstrain1(2,1)-dev/3.0)**2+(dstrain1(3,1)-dev/3.0)**2+
     2 0.5*dstrain1(4,1)**2)
      ev=ev+dev
      ed=ed+ded
```

197

```fortran
c
c
c     Judge yielding
      else
c
 800  continue
c     Calulate the dFdq
      dFdq=2.0*qc
c
c     Calculate the dFdS
      do i=1,3
c         ###pc is mean stress and p1 is preconsolidation stress
          dFds(i,1)=(rM**2)*(2.0*pc-R*(pcd+pcc+p1)+pcc)/3.0
     1    +3.0*(stress1(i,1)-pc)
      end do
      dFds(4,1)=6.0*stress1(4,1)
c
c     Calculate the dFdPcc and dFdPcd
      dFdPcc=(rM**2)*(pc-R*(pc+pcc+pcd+p1+pcc))
      dFdPcd=-R*(rM**2)*(pc+pcc)
c
c     Calculate the dlamdah
      dlamdah=dFdPcd*a*b*(X*Sh)**b+dFdPcc*c*d*(X*Sh)**d
c
c
c     Calculate plastic stiffness matrix
      dFdsii=dFds(1,1)+dFds(2,1)+dFds(3,1)
c
      do i=1,4
          dFdst(1,i)=dFds(i,1)
      end do
      do i=1,4
          do j=1,4
              dlamda1(1,i)=dlamda1(1,i)+dFdst(1,j)*De(j,i)
          end do
      end do
c
c
      rMODU=sqrt(dFds(1,1)**2+dFds(2,1)**2+dFds(3,1)**2+dFds(4,1)**2)
c
c
      dlamda2=-R*(rM**2)*(pc+pcc)*(1+void)*p1/(cil-sik)*dFdsii
     1     +rM**2*(pc+pcc)*(p1+pcd+pcc)*u*(1+(pcc+pcd)/p1)
     2      *log(R)*rMODU-eM*dlamdah*dFdq
c
      do i=1,4
          dlamda3=dlamda3+dlamda1(1,i)*dFds(i,1)
      end do
c
      do i=1,4
          dlamda0(1,i)=dlamda1(1,i)
      end do
c
c
      do i=1,4
          dlamda4=dlamda4+dfdst(1,i)*DShe(i,1)
      end do
c
c     Calculate the dfdsh
      dpcddsh=X*a*b*(X*Sh)**(b-1)
      dpccdsh=X*c*d*(X*Sh)**(d-1)
      dfdsh=dfdpcd*dpcddsh+dfdpcc*dpccdsh
      do i=1,4
          do j=1,4
              Dsp22(i,1)=Dsp22(i,1)+De(i,j)*dFds(j,1)
          end do
      end do
c
      do i=1,4
          Dsp2(i,1)=dfdsh*Dsp22(i,1)
      end do
c
c
      dlamda6=dSh*dfdsh
      dlamda=(dlamda6+fs)/(-dlamda2+dlamda3)
c
      do i=1,4
          do j=1,4
              Dp11(i,1)=Dp11(i,1)+De(i,j)*dFds(j,1)
          end do
      end do
c
```

```
        do i=1,4
            do j=1,4
                Dp12(i,j)=Dp12(i,j)+Dp11(i,1)*dFdst(1,j)
            end do
        end do
c
        do i=1,4
            do j=1,4
                do k=1,4
                    Dp1(i,j)=Dp1(i,j)+Dp12(i,k)*De(k,j)
                end do
            end do
        end do
c
        do i=1,4
            do k=1,4
                Dsp1(i,1)=Dsp1(i,1)+Dp12(i,k)*DShe(k,1)
            end do
        end do
c
c
        do i=1,4
            do j=1,4
                Dp(i,j)=Dp1(i,j)/(-dlamda2+dlamda3)
            end do
        end do
c
c
        do i=1,4
c           Dsp is plastic stiffness for the hydrate term
            Dsp(i,1)=Dsp2(i,1)/(-dlamda2+dlamda3)
        end do
c
c
        do i=1,4
            do j=1,4
                DDSDDE(i,j)=De(i,j)-Dp(i,j)
                DHSDDE(i,1)=DShe(i,1)-Dsp(i,1)
                depv=dlamda*dFdsii
                depd=dlamda*dFdq
                yjudge=1.0
            end do
        end do
c
        if (abs(fs) .le. 0.001 .and. iter .gt. 0) goto 810
c
c     Update new stresses
        do i=1,4
            stress1(i,1)=stress1(i,1)-dlamda*Dp11(i,1)
            stress(i)=-stress1(i,1)
        end do
c
c     Update mean stress
        pc=(stress1(1,1)+stress1(2,1)+stress1(3,1))/3.0
c
c     Update deviatoric stress
        qc=sqrt(3.0/2.0)*sqrt((stress1(1,1)-pc)**2+
     1  (stress1(2,1)-pc)**2+(stress1(3,1)-pc)**2+
     2  2.0*stress1(4,1)**2)
c
c     Update plastic volumetric strain
        epv=epv+depv
c
c     Update plastic deviatoric strain
        epd=epd+depd
c
c     Update plastic strain
        dep1=dlamda*dFds(1,1)
        dep2=dlamda*dFds(2,1)
        dep3=dlamda*dFds(3,1)
        dep4=dlamda*dFds(4,1)
        ep1=ep1+dep1
        ep2=ep2+dep2
        ep3=ep3+dep3
        ep4=ep4+dep4
c
c
c
c     Update preconsolidation pressure
        p1=p1+(1+void)*p1/(cil-sik)*depv
        if (p1.le.0) p1=0
c
```

```
c
c       Update degradation factor
        dX=-eM*X*depd
        X=X+dX
        if (X.le.0) X=0
c
c
c       Update pcc and pcd
        pcc=c*(X*Sh)**d
        pcd=a*(X*Sh)**b
c
c       Update R
        dR=-u*(1+(pcd+pcc)/p1)*log(R)*
     1      sqrt(dep1**2+dep2**2+dep3**2+dep4**2)
        R=R+dR
        if (R .gt. 1.0) R=1.0
c
c       Define yield function
        fs=qc**2+(rM**2)*(pc+pcc)*(pc-R*(p1+pcc+pcd))
c
c!      Initialize variables for next iteration
        dlamda3 = 0.0
        dlamda4 = 0.0
        do i=1,4
            dlamda1(1,i) = 0.0
            Dsp22(i,1) = 0.0
            Dp11(i,1) = 0.0
            Dsp1(i,1) = 0.0
        enddo
        do i=1,4
            do j=1,4
                Dp12(i,j) = 0.0
                Dp1(i,j) = 0.0
            enddo
        enddo
c
        iter = iter + 1
        goto 800
c
 810    continue
c       Update hydrate saturation
        Sh=Sh+dSh
        if (Sh.le.0) Sh=0
c
c       Update the void ratio
        void=void+(dstran(1)+dstran(2)+dstran(3))*(1.0+void)
c
c       Update volmetric strain and deviatoric strain
        dev=dstrain1(1,1)+dstrain1(2,1)+dstrain1(3,1)
        ded=sqrt(2.0/3.0)*sqrt((dstrain1(1,1)-dev/3.0)**2+
     1    (dstrain1(2,1)-dev/3.0)**2+(dstrain1(3,1)-dev/3.0)**2+
     2    0.5*dstrain1(4,1)**2)
        ev=ev+dev
        ed=ed+ded
c
        endif
c
c
c       Update solution dependent state variable (SDV)
        statev(1)=epv
        statev(2)=void
        statev(3)=X
        statev(4)=epd
        statev(5)=dX
        statev(6)=pc
        statev(7)=qc
        statev(8)=GS
        statev(9)=p1
        statev(10)=yjudge
        statev(11)=dlamda
        statev(12)=fs
        statev(13)=dFdsii
        statev(14)=dFdq
        statev(15)=De(1,1)
        statev(16)=De(2,2)
        statev(17)=De(3,3)
        statev(18)=De(1,2)
        statev(19)=De(1,3)
        statev(20)=De(2,3)
        statev(21)=De(4,4)
        statev(22)=De(5,5)
        statev(23)=De(6,6)
```

```
      statev(24)=Dp(1,1)
      statev(25)=Dp(2,2)
      statev(26)=Dp(3,3)
      statev(27)=Dp(1,2)
      statev(28)=Dp(1,3)
      statev(29)=Dp(2,3)
      statev(30)=Dp(4,4)
      statev(31)=Dp(5,5)
      statev(32)=Dp(6,6)
      statev(33)=DDSDDE(1,1)
      statev(34)=DDSDDE(2,2)
      statev(35)=DDSDDE(3,3)
      statev(36)=DDSDDE(1,2)
      statev(37)=DDSDDE(1,3)
      statev(38)=DDSDDE(2,3)
      statev(39)=DDSDDE(4,4)
      statev(42)=Dp1(1,1)
      statev(43)=Dp1(2,2)
      statev(44)=Dp1(3,3)
      statev(45)=Dp1(1,2)
      statev(46)=Dp1(1,3)
      statev(47)=Dp1(2,3)
      statev(48)=Dp1(4,4)
      statev(49)=Dp1(5,5)
      statev(50)=Dp1(6,6)
      statev(51)=Dp11(1,1)
      statev(52)=Dp11(2,2)
      statev(53)=Dp11(3,3)
      statev(54)=Dp11(1,2)
      statev(55)=Dp11(1,3)
      statev(56)=Dp11(2,3)
      statev(57)=Dp11(4,4)
      statev(58)=Dp11(5,5)
      statev(59)=Dp11(6,6)
      statev(60)=Dp12(1,1)
      statev(61)=Dp12(2,2)
      statev(62)=Dp12(3,3)
      statev(63)=Dp12(1,2)
      statev(64)=Dp12(1,3)
      statev(65)=Dp12(2,3)
      statev(66)=Dp12(4,4)
      statev(67)=Dp12(5,5)
      statev(68)=Dp12(6,6)
      statev(69)=dstran(1)
      statev(70)=dstran(2)
      statev(71)=dstran(3)
      statev(72)=dstran(4)
      statev(75)=R
      statev(76)=depv
      statev(77)=depd
      statev(78)=dFds(1,1)
      statev(79)=dFds(2,1)
      statev(80)=dFds(3,1)
      statev(81)=pcc
      statev(82)=pcd
      statev(83)=dlamda2
      statev(84)=dlamda3
      statev(85)=dlamda4
      statev(86)=dlamdah
      statev(87)=dFdPcc
      statev(88)=dFdPcd
      statev(89)=ep1
      statev(90)=ep2
      statev(91)=ep3
      statev(92)=ep4
      statev(93)=ep5
      statev(94)=ep6
      statev(96)=MODI
      statev(97)=dFds(4,1)
      statev(98)=dFds(5,1)
      statev(99)=dFds(6,1)
      statev(100)=ev
      statev(101)=ed
      statev(111)=iter
      statev(112)=Sh
c
      return
      end
c
c
```

Appendix B

ABAQUS user subroutine codes for the interface friction model

```fortran
      subroutine sdvini(statev,coords,nstatv,ncrds,noel,npt,layer,kspt)
      include 'aba_param.inc'
      dimension statev(nstatv),coords(ncrds)
      double precision rhoB,h
!
      statev(201)=0   !frictional stiffness (MPa/mm)
      statev(202)=0   !initial cohesion(MPa)
      statev(203)=0   !initial friction coefficient(-)
      statev(204)=0   !storage for cohesion
      statev(205)=0   !storage for friction coefficient
      statev(206)=0   !softening scaler for cohesion
      statev(207)=0   !softening scaler for friction coefficient
      statev(208)=0   !cumulative dlamda
      statev(209)=0   !the numerator for dlamda
      statev(210)=0   !the denominator for dlamda
      statev(211)=0   !directionless cumulative plastic slip
      statev(212)=0   !residual cohesion flag
      statev(213)=0   !residual friction coefficient flag
      statev(214)=0   !the alpha coefficient for cohesion softening(positive value for softening)
      statev(215)=0   !the beta coefficient for cohesion softening(positive value for softening)
      statev(216)=0   !residual cohesion
      statev(217)=0   !residual friction coefficient
      statev(218)=0   !shear stress increment, dtau=slipstiffness*dgamma
      statev(219)=0   !temporary updated shear stress
      statev(220)=0   !value of yield function
      statev(221)=0   !value of the PRESS
      statev(222)=0   !value of (PRESS + DPRESS)
      statev(223)=0   !storage for cumulative dlamda up to the previous iteration
      statev(224)=0   !the alpha coefficient for friction softening(positive value for softening)
      statev(225)=0   !the beta coefficient for friction softening(positive value for softening)
!
      return
      end
!
!
!    ###Constitutive model for interfacial frictional behaviour###
!    #######Don't use this subroutine with the small sliding method!#######
      SUBROUTINE FRIC(LM,TAU,DDTDDG,DDTDDP,DSLIP,SED,SFD,
     +DDTDDT,PNEWDT,STATEV,DGAM,TAULM,PRESS,DPRESS,DDPDDH,SLIP,
     +KSTEP,KINC,TIME,DTIME,NOEL,CINAME,SLNAME,MSNAME,NPT,NODE,
     +NPATCH,COORDS,RCOORD,DROT,TEMP,PREDEF,NFDIR,MCRD,NPRED,
     +NSTATV,CHRLNGTH,PROPS,NPROPS)
C
      INCLUDE 'ABA_PARAM.INC'
C
      CHARACTER*80 CINAME,SLNAME,MSNAME
C
      dimension TAU(NFDIR),DDTDDG(NFDIR,NFDIR),DDTDDP(NFDIR),
     +DSLIP(NFDIR),DDTDDT(NFDIR,2),STATEV(*),DGAM(NFDIR),
     +TAULM(NFDIR),SLIP(NFDIR),TIME(2),COORDS(MCRD),
     +RCOORD(MCRD),DROT(2,2),TEMP(2),PREDEF(2,*),PROPS(NPROPS)
!
      IF (CINAME == 'GENERAL-1') THEN !CINAME needs to be given in capital letters.
          statev(202)=3.0
          statev(203)=0.8
          statev(201)=(statev(203)*(PRESS+DPRESS)+statev(202))/(0.5*1E-3)
          statev(204)=0
          statev(205)=0
          statev(206)=0
          statev(207)=0
          statev(208)=0
          statev(209)=0
          statev(210)=0
          statev(211)=0
          statev(212)=0
          statev(213)=0
          statev(214)=0
          statev(215)=0
          statev(216)=3.0
          statev(217)=0.8
          statev(218)=0
          statev(219)=0
          statev(220)=0
```

```
                  statev(221)=0
                  statev(222)=0
                  statev(223)=0
                  statev(224)=0
                  statev(225)=0
            ELSE
                  statev(202)=0.0
                  statev(203)=0.65
                  statev(201)=(statev(203)*(PRESS+DPRESS)+statev(202))/(0.25*1E-3)
                  statev(204)=0
                  statev(205)=0
                  statev(206)=0
                  statev(207)=0
                  statev(208)=0
                  statev(209)=0
                  statev(210)=0
                  statev(211)=0
                  statev(212)=0
                  statev(213)=0
                  statev(214)=0
                  statev(215)=0
                  statev(216)=0.0
                  statev(217)=0.65
                  statev(218)=0
                  statev(219)=0
                  statev(220)=0
                  statev(221)=0
                  statev(222)=0
                  statev(223)=0
                  statev(224)=0
                  statev(225)=0
            END IF
!
!     Initialize cumulative dlamda
            statev(223)=0.0
!     Get the trial contact shear stress
            statev(219) = TAU(1) + statev(201)*DGAM(1)
!     Get the current and trial contact pressure
            statev(221) = PRESS
            statev(222) = PRESS + DPRESS
!     Duplicate the current cohesion and friction coefficient
            statev(204) = statev(202)
            statev(205) = statev(203)

!     Assign the softening scalar for cohesion
            IF(statev(212).EQ.1)THEN  !check the residual cohesion flag
                  statev(206) = 0   !if yes set the scalar to zero
            ELSE
                  statev(206) = statev(214)*(1+statev(211))**(-statev(215))
            End IF

!     Assign the softening scalar for friction coefficient
            IF(statev(213).EQ.1)THEN  !check the residual friction coefficient flag
                  statev(207) = 0   !if yes set the scalar to zero
            ELSE
                  IF(statev(221).LE.1.0)THEN
                        statev(207) = statev(224)*(1+statev(211))**(-statev(225))
                  ELSE
                        statev(207) = statev(224)*(1+statev(211))**(-statev(225))
                        statev(207) = statev(207)/statev(221)
                  ENDIF
            End IF
C
!     Check if contact pressure is negative
            IF(statev(222).LT.0.0)THEN
                  statev(203)=0.0    !eliminate friction coefficient from yield function, dlamda, and
Jacobians
                  statev(221)=0.0    !eliminate current contact pressure from yield function, dlamda, and
Jacobians
                  statev(222)=0.0    !eliminate updated contact pressure from yield function, dlamda, and
Jacobians
            END IF
C
!     Calculate the current value of yield function
            statev(220) = abs(statev(219))-statev(203)*statev(222)-statev(202)
C
!     Judge yielding
            IF(statev(220).LE.0.0)THEN  !In case the stress is within yield surface
                  TAU(1) = statev(219)
                  DDTDDG(1,1) = statev(201)
                  DDTDDP(1) = 0
                  DSLIP(1) = 0
```

```
                statev(202)=statev(204)   !cohesion
                statev(203)=statev(205)   !friction coefficient
                LM = 0   !set LM to zero to allow the call for this subroutine in the next increment
          ELSE   !In case the stress is outside the yield surface
!         Check the direction of contact shear stress
                IF(statev(219).LT.0.0)THEN   !If negative, use negative cohesion and friction coefficient
                    statev(202)=-statev(202)
                    statev(203)=-statev(203)
                    statev(204)=-statev(204)
                    statev(205)=-statev(205)
                    statev(216)=-statev(216)
                    statev(217)=-statev(217)
                ENDIF

!         Backward Euler method with Newton iteration
                DO WHILE (abs(statev(220)).GT.0.001)   !check if the gap is within tolerance (i.e. 1kPa)
                    statev(210) = statev(201)-statev(206)-statev(207)*statev(222)
                    statev(209) = statev(219)-statev(205)*statev(222)-statev(204)
                    statev(208) = statev(209)/statev(210)   !calculate dlamda
                    statev(223) = statev(223)+statev(208)   !update cumulative dlamda
                    statev(204) = statev(204)-statev(206)*statev(208) !updated cohesion
                    statev(205) = statev(205)-statev(207)*statev(208) !updated friction coefficient
!         Check if updated cohesion and friction coefficient is less than the respective residual
values
                    IF(abs(statev(204)).LT.abs(statev(216)))THEN
                        statev(204) = statev(216)
                        statev(206) = 0.0
                        statev(212) = 1
                    ENDIF

                    IF(abs(statev(205)).LT.abs(statev(217)))THEN
                        statev(205) = statev(217)
                        statev(207) = 0.0
                        statev(213) = 1
                    ENDIF
                    statev(219) = statev(219)-statev(201)*statev(208)   !update contact shear stress
                    statev(220) = statev(219)-statev(205)*statev(222)-statev(204)   !get the gap from the
updated yield surface
                ENDDO

!         Update shear stress, cohesion, friction coefficient, and Jacobians
                TAU(1) = statev(219)   !contact shear stress
                DDTDDG(1,1) = -statev(201)*(statev(206)+statev(207)*statev(221))
                DDTDDG(1,1) = DDTDDG(1,1)/(statev(201)-statev(206)-statev(207)*statev(221))   !Jacobian
                DDTDDP(1) = statev(201)*statev(203)
                DDTDDP(1) = DDTDDP(1)/(statev(201)-statev(206)-statev(207)*statev(221))   !Jacobian
                DSLIP(1) = statev(223)   !plactic cumulative slip
                statev(211) = statev(211)+abs(statev(223))   !absolute plastic cumulative slip
                statev(202)=abs(statev(204))   !cohesion
                statev(203)=abs(statev(205))   !friction coefficient
                statev(216)=abs(statev(216))   !residual cohesion
                statev(217)=abs(statev(217))   !residual friction coefficient
            LM = 0   !set LM to zero to allow the call for this subroutine in the next increment
          End IF
C
C
C
C
      RETURN
      END
!
```

References

Appleby, S. & Wilson, A., 1996. Permeability and suction in setting cement. *Chemical Engineering Science*, 51(2), pp.251–267. Available at: https://doi.org/10.1016/0009-2509(95)00260-x.

Backe, K.R. et al., 1999. Characterizing Curing-Cement Slurries by Permeability, Tensile Strength, and Shrinkage. *SPE Drilling & Completion*, 14(3), pp.162–167. Available at: https://doi.org/10.2118/57712-PA.

Backe, K.R. et al., 1998. Shrinkage of Oil Well Cement Slurries. *The Journal of Cannadian Petroleum Technology*, 37(9), pp.63–67. Available at: https://doi.org/10.2118/98-09-06.

Badakhshan Raz, S. & Ghassemi, A., 2011. Stresses Around a Production Well In Gas Hydrate-Bearing Formation. In *Proceedings of the 45th U.S. Rock Mechanics / Geomechanics Symposium*. San Francisco, California, USA, pp. 1–7. Available at: https://www.onepetro.org/conference-paper/ARMA-11-540.

Baldwin, C., 2018. Fiber Optic Sensors in the Oil and Gas Industry: Current and Future Applications. In *Opto-Mechanical Fiber Optic Sensors: Research, Technology, and Applications in Mechanical Sensing*. Elsevier Inc., pp. 211–236. Available at: http://dx.doi.org/10.1016/B978-0-12-803131-5.00008-8.

Baldwin, C.S., 2015. Applications for fiber optic sensing in the upstream oil and gas industry. In *Proceedings of Fiber Optic Sensors and Applications XII*. Baltimore, Maryland, USA, pp. 1–10. Available at: https://doi.org/10.1117/12.2176226.

Berger, A. et al., 2004. Effect of Eccentricity, Voids, Cement Channels, and Pore Pressure Decline on Collapse Resistance of Casing. In *Proceedings of SPE Annual Technical Conference and Exhibition*. Houston, Texas, USA, pp. 1–8. Available at: https://doi.org/10.2118/90045-ms.

Biot, M.A., 1962. Mechanics of deformation and acoustic propagation in porous media. *Journal of Applied Physics*, 33(4), pp.1482–1498. Available at: https://doi.rog/10.1063.1.1728759.

Biot, M.A. & Willis, D.G., 1957. The elastic coefficients of the theory of consolidation. *J. Appl. Mech*, 24, pp.594–601. Available at: https://doi.org/10.2118/139668-PA.

Bois, A.-P. et al., 2011. How to prevent loss of zonal isolation through a comprehensive analysis of microannulus formation. *SPE Drilling & Completion*, 26(1), pp.4–7. Available at: https://doi.org/10.2118/124719-PA.

Bois, A. et al., 2012. Use of a Mechanistic Model To Forecast Cement-Sheath Integrity. *SPE Drilling & Completion*, 27(2), pp.303–314. Available at: https://doi.org/10.2118/139668-PA.

Bosma, M. et al., 1999. Design Approach to Sealant Selection for the Life of the Well. In *Proceedings of the 1999 SPE Annual Technical Conference and Exhibition*. Houston, Texas, USA, pp. 1–14. Available at: https://doi.org/10.2523/56536-ms.

Boswell, R., 2013. Japan completes first offshore methane hydrate production test - methane successfully produced from deepwater hydrate layers. *Fire in the Ice*, 13(2), pp.1–2. Available at: https://www.netl.doe.gov/research/oil-and-gas/methane-hydrates/fire-in-the-ice.

Bourne-Webb, P.J. et al., 2009. Energy pile test at Lambeth College, London: geotechnical and thermodynamic aspects of pile response to heat cycles. *Géotechnique*, 59(3), pp.237–248. Available at: https://doi.org/10.1680/geot.2009.59.3.237.

Bruno, M.S. & Bovberg, C.A., 1992. Reservoir compaction and surface subsidence above the Lost Hills Field, California. *International Journal of Rock Mechanics and Mining Sciences & Geomechanics Abstracts*, 30(2), p.A136. Available at: https://doi.org/10.1016/0148-9062(93)91213-3.

Bui, B.T. & Tutuncu, A.N., 2013. Modeling the Failure of Cement Sheath in Anisotropic Stress Field. In *Proceedings of SPE Unconventional Resources Conference-Canada*. Calgary, Alberta, Canada, pp. 1–11. Available at: https://doi.org/10.2118/167178-ms.

Butler, L.J. et al., 2016. Evaluating the early-age behaviour of full-scale prestressed concrete beams using distributed and discrete fibre optic sensors. *Construction and Building Materials*, 126, pp.894–912. Available at: http://dx.doi.org/10.1016/j.conbuildmat.2016.09.086.

Chen, L., Feng, Y., Kogawa, T., et al., 2018. Construction and simulation of reservoir scale layered model for production and utilization of methane hydrate: The case of Nankai Trough Japan. *Energy*, 143, pp.128–140. Available at: https://doi.org/10.1016/j.energy.2017.10.108.

Chen, L., Feng, Y., Okajima, J., et al., 2018. Production behavior and numerical analysis for 2017 methane hydrate extraction test of Shenhu, South China Sea. *Journal of Natural Gas Science and Engineering*, 53, pp.55–66. Available at: https://doi.org/10.1016/j.jngse.2018.02.029.

Chenevert, M.E. & Jin, L., 1989. Model for Predicting Wellbore Pressures in Cement Columns. In *Proceedings of the 64th Annual Technical Conference and Exhibition of the Society of Petroleum Engineers*. San Antonio, Texas, USA, pp. 35–47. Available at: https://doi.org/10.2118/spe-19521-ms.

Chenevert, M.E. & Shrestha, B.K., 1991. Chemical Shrinkage Properties of Oilfield Cements. *SPE Drilling Engineering*, 6(1), pp.37–43. Available at: https://doi.org/16654-PA.

Chenevert, M.E. & Shrestha, B.K., 1987. Shrinkage Properties of Cement. In *Proceedings of the*

62nd Annual Technical Conference and Exhibition of the Society of Petroleum Engineers. Dallas, Texas, USA, pp. 49–57. Available at: https://doi.org/10.2118/16654-MS.

Chia, Y.P. & Bradley, D.A., 1988. Effects of Nonlinear Reservoir Compaction on Casing Behavior. *SPE Production Engineering*, 3(03), pp.333–338. Available at: https://doi.org/10.2118/15469-pa.

Chia, Y.P. & Bradley, D.A., 1989. Evaluation of Reservoir Compaction and Its Effects on Casing Behavior. *SPE Production Engineering*, 4(02), pp.167–172. Available at: https://doi.org/10.2118/14985-pa.

Choi, K.N. & Taylor, H.F., 2003. Spectrally stable Er-fiber laser for application in phase-sensitive optical time-domain reflectometry. *IEEE Photonics Technology Letters*, 15(3), pp.386–388. Available at: https://doi.org/10.1109/lpt.2003.807905.

Chunge, M.P.M., 2014. *Monitoring the Integrity of Bored Concrete Piles using Distributed Fibre Optic Sensors*. Master's thesis. University of Cambridge.

Coussy, O. et al., 2004. The equivalent pore pressure and the swelling and shrinkage of cement-based materials. *Materials and Structures*, 37(265), pp.15–20. Available at: https://doi.org/10.1007/bf02481623.

Cruz, C.R. & Gillen, M., 1980. Thermal Expansion of Portland Cement Paste, Mortar and Concrete at High Temperatures. *Fire and Materials*, 4(2), pp.66–70. Available at: https://doi.org/10.1002/fam.810040203.

Dale, B.A., Narahara, G.M. & Stevens, R.M., 1996. A Case History of Reservoir Subsidence and Wellbore Damage Management in the South Belridge Diatomite Field. In *Proceedings of the SPE Western Regional Meeting*. Anchorage, Alaska, USA, pp. 101–113. Available at: https://doi.org/10.2118/35658-ms.

Delli, M.L. & Grozic, J.L.H., 2014. Experimental determination of permeability of porous media in the presence of gas hydrates. *Journal of Petroleum Science and Engineering*, 120, pp.1–9. Available at: http://dx.doi.org/10.1016/j.petrol.2014.05.011.

DeMerchant, M. et al., 1999. Structural Monitoring by Use of a Brillouin Distributed Sensor. *Applied Optics*, 38(13), p.2755. Available at: https://doi.org/10.1364/ao.38.002755.

Doornhof, D. et al., 2006. Compaction and subsidence. *Oilfield Review - Schlumberger*, pp.50–68. Available at: https://www.slb.com/~/media/Files/resources/oilfield_review/ors06/aut06/compaction_and_subsidence.pdf.

Earles, D.M. et al., 2010. Real-Time Monitoring of Sand Control Completions. In *Proceedings of the SPE Annual Technical Conference and Exhibition*. Florence, Italy, pp. 19–22. Available at: https://doi.org/10.2118/134555-ms.

European Commitee for Standardization, 2005. *BS EN 1994-2:2005 Eurocode 4. Design of*

composite steel and concrete structures. General rules and rules for bridges, Available at: https://doi.org/10.3403/30117101.

Farrell, H. et al., 2012. IġnIk SIkumI GaS Hydrate FIeld trIal Completed. *Fire in the Ice*, 12(1), pp.1–3. Available at:
https://www.netl.doe.gov/sites/default/files/publication/MHNews_2012_June.pdf.

Fredrich, J.T. et al., 2000. Geomechanical Modeling of Reservoir Compaction, Surface Subsidence, and Casing Damage at the Belridge Diatomite Field. *SPE Reservoir Evaluation & Engineering*, 3(4), pp.8–10. Available at: https://doi.org/10.2118/65354-pa.

Freij-Ayoub, R., Tan, C., et al., 2007. A wellbore stability model for hydrate bearing sediments. *Journal of Petroleum Science and Engineering*, 57, pp.209–220. Available at: https://doi.org/10.1016/j.petrol.2005.10.011.

Freij-Ayoub, R., Clennell, B., et al., 2007. Casing integrity in hydrate bearing sediments. In *Proceedings of the 6th International Offshore Site Investigation and Geotechnics Conference*. London, UK, pp. 103–112. Available at: https://www.onepetro.org/download/conference-paper/ARMA-09-138?id=conference-paper%2FARMA-09-138.

Froggatt, M. & Moore, J., 1998. High-spatial-resolution distributed strain measurement in optical fiber with Rayleigh scatter. *Applied Optics*, 37(10), p.1735. Available at: https://www.osapublishing.org/abstract.cfm?URI=ao-37-10-1735.

Fujii, T. et al., 2015. Geological setting and characterization of a methane hydrate reservoir distributed at the first offshore production test site on the Daini-Atsumi Knoll in the eastern Nankai Trough, Japan. *Marine and Petroleum Geology*, 66, pp.310–322. Available at: https://doi.org/10.1016/j.marpetgeo.2015.02.037.

Furui, K., Fuh, G.-F. & Morita, N., 2011. Casing and Screen Failure Analysis in Highly Compacting Sandstone Fields. In *Proceedings of the SPE Annual Technical Conference and Exhibition*. Denver, Colorado, USA, pp. 1–17. Available at: https://doi.org/10.2118/146231-ms.

Garg, S.K. & Nur, A., 1973. Effective Stress Laws for Fluid-Saturated Porous Rocks. *Journal of Geophysical Research*, 78(26), pp.5911–5921. Available at: https://doi.org/10.1029/jb078i026p05911.

Gebremichael, Y.M. et al., 2005. Integration and assessment of fibre Bragg grating sensors in an all-fibre reinforced polymer composite road bridge. *Sensors and Actuators, A: Physical*, 118(1), pp.78–85. Available at: https://doi.org/10.1016/j.sna.2004.08.005.

Goboncan, V.C. & Dillenbeck, R.L., 2003. Real-Time Cement Expansion / Shrinkage Testing Under Downhole Conditions For Enhanced Annular Isolation. In *Proceedings of the SPE/IADC Drilling Conference*. Amsterdam, The Netherlands, pp. 1–9. Available at:

https://doi.org/10.2118/79911-ms.

Gray, K.E. et al., 2007. Finite Element Studies of Near-Wellbore Region During Cementing Operations : Part I. In *Proceedings of the SPE Production and Operations Symposium*. Oklahoma City, Oklahoma, USA, pp. 1–15. Available at: https://doi.org/10.2118/106998-MS.

Großwig, S., Hurtig, E. & Kühn, K., 1996. Fibre optic temperature sensing : A new tool for temperature measurements in boreholes. *GEOPHYSICS*, 61(4), pp.1065–1067. Available at: https://doi.org/10.1190/1.1444027.

Gue, C.Y. et al., 2015. The monitoring of an existing cast iron tunnel with distributed fibre optic sensing (DFOS). *Journal of Civil Structural Health Monitoring*, 5(5), pp.573–586. Available at: https://doi.org/10.1007/s13349-015-0109-8.

Gupta, S. et al., 2017. Testing a thermo-chemo-hydro-geomechanical model for gas hydrate-bearing sediments using triaxial compression laboratory experiments. *Geochemistry, Geophysics, Geosystems*, 18(9), pp.3419–3437. Available at: https://doi.org/10.1002/2017gc006901.

Hamilton, J.M., Maller, A.V. & Prins, M.D., 1993. Subsidence-Induced Shear Failures Above Oil and Gas Reservoirs. *International Journal of Rock Mechanics and Mining Sciences & Geomechanics Abstracts*, 30(2), p.A136. Available at: https://doi.org/10.1016/0148-9062(93)91214-4.

Hashiguchi, K., 1989. Subloading surface model in unconventional plasticity. *International Journal of Solids and Structures*, 25(8), pp.917–945. Available at: https://doi.org/10.1016/0020-7683(89)90038-3.

Hauswirth, D. et al., 2014. Use of fibre-optic sensors for simple assessment of ground surface displacements during tunnelling. *Géotechnique*, 64(10), pp.837–842. Available at: http://www.icevirtuallibrary.com.libproxy1.nus.edu.sg/content/article/10.1680/geot.14.T.009.

Heathman, J. & Beck, F.E., 2006. Finite Element Analysis Couples Casing and Cement Designs for HP/HT Wells in East Texas. In *Proceedings of the IADC/SPE Drilling Conference*. Miami, Florida, USA, pp. 1–23. Available at: https://doi.org/10.2118/98869-ms.

Hodge, M. et al., 2006. Analysis of Time-Dependent Wellbore Stability of Underbalanced Wells Using a Fully Coupled Poroelastic Model. In *Proceedings of the SPE Annual Technical Conference and Exhibition*. San Antonio, Texas, USA, pp. 1–5. Available at: https://doi.org/10.2118/102873-ms.

Horiguchi, T. et al., 1995. Development of a Distributed Sensing Technique Using Brillouin Scattering. *Journal of Lightwave Technology*, 13(7), pp.1296–1302. Available at: https://doi.org/10.1109/50.400684.

Horiguchi, T., Kurashima, T. & Tateda, M., 1989. Tensile strain dependence of Brillouin frequency shift in silica optical fibers. *Photonics Technology Letters*, 1(5), pp.107–108. Available at: https://doi.org/10.1109/68.34756.

Horiguchi, T. & Tateda, M., 1989. BOTDA—Nondestructive Measurement of Single-Mode Optical Fiber Attenuation Characteristics Using Brillouin Interaction: Theory. *Journal of Lightwave Technology*, 7(8), pp.1170–1176. Available at: https://doi.org/10.1109/50.32378.

Hou, J. et al., 2018. Effect of hydrate on permeability in porous media: Pore-scale micro-simulation. *International Journal of Heat and Mass Transfer*, 126, pp.416–424. Available at: https://doi.org/10.1016/j.ijheatmasstransfer.2018.05.156.

Hua, C., Acker, P. & Ehrlacher, A., 1995. Analyses and models of the autogenous shrinkage of hardening cement paste. I. Modelling at macroscopic scale. *Cement and Concrete Research*, 25(7), pp.1457–1468. Available at: https://doi.org/10.1016/0008-8846(95)00140-8.

Hurtig, E. et al., 1994. Fibre-optic temperature measurements in shallow boreholes: experimental application for fluid logging. *Geothermics*, 23(4), pp.355–364. Available at: https://doi.org/10.1016/0375-6505(94)90030-2.

Hveding, F., Bukhamsin, A. & Aramco, S., 2018. Distributed Fiber Optic Sensing – A Technology Review for Upstream Oil and Gas Applications. In *Proceedings of the SPE Kingdom of Saudi Arabia Annual Technical Symposium and Exhibition*. Dammam, Saudi Arabia, pp. 1–15. Available at: https://doi.org/10.2118/192323-ms.

Hveding, F. & Porturas, F., 2015. Integrated Applications of Fiber-Optic Distributed Acoustic and Temperature Sensing. In *Proceedings of the SPE Latin American and Caribbean Petroleum Engineering Conference*. Quito, Ecuador, pp. 1–16. Available at: https://doi.org/10.2118/177222-ms.

Hyodo, M. et al., 2014. Effects of dissociation on the shear strength and deformation behavior of methane hydrate-bearing sediments. *Marine and Petroleum Geology*, 51, pp.52–62. Available at: https://doi.org/10.1016/j.marpetgeo.2013.11.015.

Hyodo, M. et al., 2013. Mechanical and dissociation properties of methane hydrate-bearing sand in deep seabed. *Soils and Foundations*, 53(2), pp.299–314. Available at: https://doi.org/10.1016/j.sandf.2013.02.010.

Jammer, P., Hariharan, H. & Klever, F.J., 2015. Casing Collapse Strength Enhancement Due to Cement and Pipe Support via Modelling and Testing. In *Proceedings of the SPE/IADC Drilling Conference and Exhibition*. London, UK, pp. 1–19. Available at: https://doi.org/10.2118/173069-ms.

Jandhyala, S. et al., 2013. Cement sheath integrity in fast creeping salts: Effect of well

operations. In *Proceedings of the SPE Offshore Europe Oil and Gas Conference and Exhibition*. Aberdeen, UK, pp. 1–10. Available at: https://doi.org/10.2118/166622-ms.

Jinnai, Y. & Morita, N., 2009. Analysis of Casing-Shift Problems in Compacting Reservoirs. *SPE Drilling & Completion*, 24(02), pp.332–345. Available at: https://doi.org/10.2118/111243-pa.

Justnes, H. et al., 1995. Chemical shrinkage of oil well cement slurries. *Advance in Cement Research*, 7(26), pp.85–90. Available at: https://doi.org/10.1680/adcr.1995.7.26.85.

Kakumoto, M. et al., 2011. Development of the Geo-mechanical simulation code COTHMA. In *Proceedings of the Ninth (2011) ISOPE Ocean Mining Symposium*. Maui, Hawaii, USA, pp. 3–6. Available at: https://doi.org/10.1201/b17435-306.

Kakumoto, M. et al., 2012. Frictional Strength between Casing and Cement under Confining Pressure. In *Proceedings of the Twenty-second (2012) International Offshore and Polar Engineering Conference*. Rhodes, Greece, pp. 77–82. Available at: https://www.onepetro.org/conference-paper/ISOPE-I-12-043.

Kalil, I.A. & Mcspadden, A.R., 2012. Casing Burst Stresses in Particulate-Filled Annuli : Where Is the Cement ? *SPE Drilling & Completion*, 27(04), pp.473–485. Available at: https://doi.org/10.2118/139766-pa.

Kimoto, S. et al., 2007. A chemo-thermo-mechanically coupled numerical simulation of the subsurface ground deformations due to methane hydrate dissociation. *Computers and Geotechnics*, 34(4), pp.216–228. Available at: https://doi.org/10.1016/j.compgeo.2007.02.006.

Klar, A. et al., 2006. Distributed strain measurement for pile foundations. *Proceedings of the ICE - Geotechnical Engineering*, 159(3), pp.135–144. Available at: https://doi.org/10.1680/geng.2006.159.3.135.

Klar, A. et al., 2019. Marine gas hydrate technology : State of the art and future possibilities for Europe. *Marine gas hydrate – an indigenous resource of natural gas for Europe (MIGRATE)*, p.54. Available at: https://www.migrate-cost.eu/documents/1134909/1134981/WG2+COST+Action+ES+1405+2019+Report.pdf/6fa77840-a4d0-4c4e-a9aa-6b5e29e2d4c2.

Klar, A. et al., 2013. Thermo-hydro-mechanical Sand Production Model in Hydrate-bearing Sediments. In *Proceedings of the International Workshop on Geomechanics and Energy – The Ground as Energy Source and Storage*. Lausanne, Switzerland, pp. 1–5. Available at: https://doi.org/10.3997/2214-4609.20131988.

Klar, A., Goldfeld, Y. & Charas, Z., 2010. Measures for identifying cracks within reinforced concrete beams using BOTDR. In *Proceedings of the SPIE Smart Structures and Materials + Nondestructive Evaluation and Health Monitoring, 2010*. San Diego,

California, USA, pp. 1–9. Available at: https://doi.org/10.1117/12.848578.

Klar, A. & Linker, R., 2010. Feasibility study of automated detection of tunnel excavation by Brillouin optical time domain reflectometry. *Tunnelling and Underground Space Technology*, 25(5), pp.575–586. Available at: https://doi.org/10.1016/j.tust.2010.04.003.

Klar, A., Soga, K. & Ng, M.Y.A., 2010. Coupled deformation–flow analysis for methane hydrate extraction. *Géotechnique*, 60(10), pp.765–776. Available at: https://doi.org/10.1680/geot.9.p.079-3799.

Konno, Y. et al., 2015. Permeability of sediment cores from methane hydrate deposit in the Eastern Nankai Trough. *Marine and Petroleum Geology*, 66, pp.487–495. Available at: https://doi.org/10.1016/J.marpetgeo.2015.02.020.

Kreger, S.T. et al., 2016. Optical frequency domain reflectometry: principles and applications in fiber optic sensing. In *Proceedings of the SPIE Commercial + Scientific Sensing and Imaging*. Baltimore, Maryland, USA, pp. 1–10. Available at: https://doi.org/10.1117/12.2229057.

Kristiansen, T.G. et al., 2005. Production-Induced Deformations Outside the Reservoir and Their Impact on 4D Seisimic. In *Proceedings of the International Petroleum Technology Conference*. Doha, Qatar, pp. 1–12. Available at: http://www.onepetro.org/doi/10.2523/10818-MS.

Kumar, A. et al., 2010. Experimental determination of permeability in the presence of hydrates and its effect on the dissociation characteristics of gas hydrates in porous media. *Journal of Petroleum Science and Engineering*, 70, pp.114–122. Available at: http://dx.doi.org/10.1016/j.petrol.2009.10.005.

Kurashima, T. et al., 1993. Brillouin optical-fiber time domain reflectometry. *IEICE transactions on communications*, 76(4), pp.382–390. Available at: https://search.ieice.org/bin/summary.php?id=e76-b_4_382.

Kvenvolden, K.A., 1993. Gas hydrates—geological perspective and global change. *Reviews of Geophysics*, 31(2), pp.173–187. Available at: https://doi.org/10.1029/93rg00268.

Li, X. et al., 2003. Compaction, Subsidence, and Associated Casing Damage and Well Failure Assessment for the Gulf of Mexico Shelf Matagorda Island 623 Field. In *Proceedings of the SPE Annual Technical Conference and Exhibition*. Denver, Colorado, USA, pp. 1–15. Available at: https://doi.org/10.2118/84553-ms.

Li, X. et al., 2005. Compaction Considerations for the Gulf of Mexico Deepwater King West Field Completion Design. In *Proceedings of the SPE/IADC Drilling Conference*. Amsterdam, The Netherlands, pp. 1–14. Available at: http://www.onepetro.org/doi/10.2118/92652-MS.

Linker, R. & Klar, A., 2015. Detection of Sinkhole Formation by Strain Profile Measurements

Using BOTDR: Simulation Study. *Journal of Engineering Mechanics*, 143(3), pp.1–10. Available at: https://doi.org/10.1061/(asce)em.1943-7889.0000963.

Liu, H.B. et al., 2003. Strain and temperature sensor using a combination of polymer and silica fibre Bragg gratings. *Optics Communications*, 219, pp.139–142. Available at: https://doi.org/10.1016/s0030-4018(03)01313-0.

Loiseau, A., 2014. Thermal Expansion of Cement and Well Integrity of Heavy Oil Wells. In *Proceedings of the SPE Heavy and Extra Heavy Oil Conference*. Medillin, Columbia, pp. 1–13. Available at: https://doi.org/10.2118/171066-MS.

Lu, Y. et al., 2010. Distributed Vibration Sensor Based on Coherent Detection of Phase-OTDR. *Journal of Lightwave Technology*, 28(22), pp.3243–3249. Available at: https://doi.org/10.1109/jlt.2010.2078798.

Lura, P., Jensen, O.M. & Van Breugel, K., 2003. Autogenous shrinkage in high-performance cement paste: An evaluation of basic mechanisms. *Cement and Concrete Research*, 33(2), pp.223–232. Available at: https://doi.org/10.1016/s0008-8846(02)00890-6.

Lyomov, S.K. et al., 1997. Shrinkage of oil well cement slurries. *Advances in Cement Research*, 7(26), pp.85–90. Available at: https://doi.org/10.2118/97-77.

Maaskant, R. et al., 1997. Fiber-optic Bragg grating sensors for bridge monitoring. *Cement and Concrete Composites*, 19(1), pp.21–33. Available at: https://doi.org/10.1016/s0958-9465(96)00040-6.

Maharidge, R. et al., 2016. Development of Permeability and Mechanical Properties of Class G Cement from Slurry to Set. In *Proceedings of the SPE Annual Technical Conference and Exhibition, 26-28 September, Dubai, UAE*. Dubai, UAE, pp. 26–28. Available at: https://doi.org/10.2118/181512-MS.

Majumder, M. et al., 2008. Fibre Bragg gratings in structural health monitoring-Present status and applications. *Sensors and Actuators A: Physical*, 147(1), pp.150–164. Available at: https://doi.org/10.1016/j.sna.2008.04.008.

Maslin, M. et al., 2010. Gas hydrates: past and future geohazard? *Philosophical Transactions of the Royal Society A: Mathematical, Physical and Engineering Sciences*, 368, pp.2369–2393. Available at: https://doi.org/10.1098/rsta.2010.0065.

Masoudi, A., Belal, M. & Newson, T.P., 2013. A distributed optical fibre dynamic strain sensor based on phase-OTDR. *Measurement Science and Technology*, 24(8), pp.1–7. Available at: https://doi.org/10.1088/0957-0233/24/8/085204.

Masui, A. et al., 2005. Effects of Methane Hydrate Formation on Shear Strength of Synthetic Methane Hydrate Sediments. In *Proceedings of the Fifteenth International Offshore and Polar Engineering Conference*. Seoul, South Korea, pp. 364–369. Available at: https://www.onepetro.org/conference-paper/ISOPE-I-05-056.

Masui, A. et al., 2007. Mechanical Properties of Sandy Sediment Containing Marine Gas Hydrates in Deep Sea Offshore Japan. In *Proceedings of the Seventh (2007) ISOPE Ocean Mining Symposium*. Lisbon, Portugal, pp. 53–56. Available at: https://www.onepetro.org/conference-paper/ISOPE-M-07-015.

Matsuzawa, M., Umezu, S. & Yamamoto, K., 2006. Evaluation of experiment program 2004: Natural hydrate exploration campaign in the Nankai-Trough offshore Japan. In *Proceedings of the IADC/SPE Drilling Conference*. Miami, Florida, USA, pp. 1–13. Available at: https://doi.org/10.2118/98960-ms.

Mayuga, M.N. & Allen, D.R., 1969. Subsidence in the Wilmington oil field, Long Beach, California, U.S.A. In *Proceedings of the Tokyo Symposium on Land Subsidence, International Association of Scientific Hydrology, Studies and reports in hydrology, IASH-UNESCO*. Tokyo, Japan, pp. 66–79. Available at: http://www.saveballona.org/gasoilfields/WilmSubGC.pdf.

Miyazaki, K. et al., 2011. Triaxial compressive properties of artificial methane-hydrate-bearing sediment. *Journal of Geophysical Research: Solid Earth*, 116(B6), pp.1–11. Available at: https://doi.org/10.1029/2010jb008049.

Miyazaki, K. et al., 2007. Variable-Compliance-Type Constitutive Model for Toyoura Sand Containing Methane Hydrate. In *Proceedings of the Seventh (2007) ISOPE Ocean Mining Symposium*. Lisbon, Portugal, pp. 57–62. Available at: https://www.onepetro.org/conference-paper/ISOPE-M-07-017.

Mohamad, H. et al., 2011. Performance Monitoring of a Secant-Piled Wall Using Distributed Fiber Optic Strain Sensing. *Journal of Geotechnical and Geoenvironmental Engineering*, 137(12), pp.1236–1243. Available at: https://doi.org/10.1061/(asce)gt.1943-5606.0000543.

Molenaar, M.M. et al., 2012. First Downhole Application of Distributed Acoustic Sensing for Hydraulic-Fracturing Monitoring and Diagnostics. *SPE Drilling & Completio*, 27(1), pp.32–38. Available at: https://doi.org/10.2118/140561-pa.

Moridis, G.J. et al., 2008. Toward Production From Gas Hydrates: Current Status, Assessment of Resources, and Simulation-Based Evaluation of Technology and Potential. In *Proceedings of the SPE Unconventional Reservoirs Conference*. Keystone, Colorado, USA, pp. 1–43. Available at: https://doi.org/10.2118/114163-ms.

Moridis, G.J., Kowalsky, M.B. & Pruess, K., 2012. *TOUGH+HYDRATE v1.2 User's Manual: A Code for the Simulation of System Behavior in Hydrate-Bearing Geologic Media*, Available at: https://doi.org/10.2172/1173164.

Nagano, Y., Lin, W. & Yamamoto, K., 2015. In-situ stress analysis using the anelastic strain recovery (ASR) method at the first offshore gas production test site in the eastern Nankai

214

Trough, Japan. *Marine and Petroleum Geology*, 66, pp.418–424. Available at: https://doi.org/10.1016/j.marpetgeo.2015.02.027.

Nagel, N.B., 2001. Compaction and subsidence issues within the petroleum industry: From Wilmington to Ekofisk and beyond. *Physics and Chemistry of the Earth, Part A: Solid Earth and Geodesy*, 26(1–2), pp.3–14. Available at: https://doi.org/10.1016/s1464-1895(01)00015-1.

Nikles, M. et al., 2004. Leakage detection using fiber optics distributed temperature monitoring. In *Proceedings of the SPIE Smart Structures and Materials 2004: Smart Sensor Technology and Measurement Systems*. San Diego, California, USA, pp. 18–25. Available at: https://doi.org/10.1117/12.540270.

Nishio, S., Ogisako, E. & Denda, A., 2009. Geotechnical Properties of Core Samples Recovered from Seabed Ground in East Nankai Trough. *Journal of Geography*, 118(5), pp.955–968. Available at: https://doi.org/10.5026/jgeography.118.955.

Nishio, S., Ogisako, E. & Denda, A., 2011. Geotechnical Properties of Seabed Ground in East Nankai Trough. In *Proceedings of the 7th International Conference on Gas Hydrates (ICGH 2011)*. Edinburgh, UK, pp. 1–4. Available at: https://doi.org/10.5026/jgeography.118.955.

Nur, A. & Byerlee, J.D., 1971. An exact effective stress law for elastic deformation of rock with fluids. *Journal of Geophysical Research*, 76(26), pp.6414–6419. Available at: https://doi.org/10.1029/jb076i026p06414.

Othonos, A., 1997. Fiber Bragg gratings. *Review of Scientific Instruments*, 68(12), pp.4309–4341. Available at: https://doi.org/10.1063/1.1148392.

Oyarhossein, M. & Dusseault, M.B., 2015. Wellbore Stress Changes and Microannulus Development Because of Cement Shrinkage. In *Proceedings of the 49th US Rock Mechanics / Geomechanics Symposium*. San Francisco, California, USA, pp. 1–7. Available at: https://www.onepetro.org/conference-paper/ARMA-2015-118.

Parcevaux, P.A. & Sault, P.H., 1984. Cement Shrinkage and Elasticity: A New Approach for a Good Zonal Isolation. In *Proceedings of the SPE Annual Technical Conference and Exhibition*. Houston, Texas, USA, pp. 1–12. Available at: https://doi.org/10.2118/13176-MS.

Pearce, J. & Legrand, P., 2009. Real-time compaction monitoring with fiber-optic distributed strain sensing (DSS). In *Proceedings of the SPWLA 50th Annual Logging Symposium*. The Woodlands, Texas, USA, pp. 1–11. Available at: https://www.onepetro.org/conference-paper/SPWLA-2009-85310.

Pearce, J.G. & Rambow, F.H.K., 2009. High Resolution, Real-Time Casing Strain Imaging for Reservoir and Well Integrity Monitoring: Demonstration of Monitoring Capability in a

Field Installation. In *Proceedings of the 2009 SPE Annual Technical Conference and Exhibition*. New Orleans, Louisiana, USA, pp. 1–15. Available at: https://doi.org/10.2118/124932-ms.

Pelecanos, L. et al., 2018. Distributed Fiber Optic Sensing of Axially Loaded Bored Piles. *Journal of Geotechnical and Geoenvironmental Engineering*, 144(3), pp.1–16. Available at: https://doi.org/10.1061/(asce)gt.1943-5606.0001843.

Pelecanos, L. et al., 2017. Distributed fibre-optic monitoring of an Osterberg-cell pile test in London. *Géotechnique Letters*, 7(2), pp.1–9. Available at: https://doi.org/10.1680/jgele.16.00081.

Philippacopoulos, A.J. & Berndt, M.L., 2002. Mechanical Response and Characterization of Well Cements. In *Proceedings of the SPE Annual Technical Conference and Exhibition*. San Antonio, Texas, USA, pp. 1–8. Available at: https://doi.org/10.2523/77755-ms.

Qiu, K. et al., 2015. Well Integrity Evaluation for Methane Hydrate Production in the Deepwater Nankai Trough. *SPE Drilling & Completion*, 30(1), pp.52–67. Available at: https://doi.org/10.2118/174081-PA.

Ravi, K., Bosma, M. & Gastebled, O., 2002a. Improve the Economics of Oil and Gas Wells by Reducing the Risk of Cement Failure. In *Proceedings of IADC/SPE Drilling Conference*. Dallas, Texas, USA, pp. 1–13. Available at: https://doi.org/10.2118/74497-MS.

Ravi, K., Bosma, M. & Gastebled, O., 2002b. Safe and Economic Gas Wells through Cement Design for Life of the Well. In *Proceedings of the SPE Gas Technology Symposium*. Calgary, Alberta, Canada, pp. 1–15. Available at: https://doi.org/10.2523/75700-ms.

Reddy, B. et al., 2009. Cement-Shrinkage Measurement in Oilwell Cementing--A Comparative Study of Laboratory Methods and Procedures. *SPE Drilling & Completion*, 24(1), pp.104–114. Available at: https://doi.org/10.2118/103610-PA.

Roberts, D., 1953. Shear prevention in the Wilmington Field. , pp.146–155. Available at: https://www.onepetro.org/conference-paper/API-53-146.

Rodriguez, W.J., Fleckenstein, W.W. & Eustes, A.W., 2003. Simulation of collapse loads on cemented casing using finite element analysis. In *Proceedings of the SPE Annual Technical Conference and Exhibition*. Denver, Colorado, USA, pp. 1–9. Available at: https://doi.org/10.2118/84566-ms.

Rougelot, T., Skoczylas, F. & Burlion, N., 2009. Water desorption and shrinkage in mortars and cement pastes: Experimental study and poromechanical model. *Cement and Concrete Research*, 39(1), pp.36–44. Available at: https://doi.org/10.1016/j.cemconres.2008.10.005.

Rutqvist, J. et al., 2012. Coupled multiphase fluid flow and wellbore stability analysis associated with gas production from oceanic hydrate-bearing sediments. *Journal of Petroleum Science and Engineering*, 92–93, pp.65–81. Available at:

https://doi.org/10.1016/j.petrol.2012.06.004.

Saint-Marc, J., Garnier, A. & Bois, A.-P., 2008. Initial State of Stress: The Key to Achieving Long-Term Cement-Sheath Integrity. In *Proceedings of the SPE Annual Technical Conference and Exhibition*. Denver, Colorado, USA, pp. 1–15. Available at: https://doi.org/10.2118/116651-MS.

Salehabadi, M., Jin, M. & Yang, J., 2008. Finite Element Modelling of Casing in Gas Hydrate Bearing Sediments. In *Proceedings of the 2008 SPE Europec/EAGE Annual Conference and Exhibition*. Rome, Italy, pp. 1–13. Available at: https://doi.org/10.2118/113819-ms.

Sang, A.K. et al., 2008. One Centimeter Spatial Resolution Temperature Measurements in a Nuclear Reactor Using Rayleigh Scatter in Optical Fiber. *IEEE Sensors Journal*, 8(7), pp.1375–1380. Available at: https://doi.org/10.1109/jsen.2008.927247.

Sasaki, T., Soga, K. & Abuhaikal, M., 2018. Water absorption and shrinkage behaviour of early-age cement in wellbore annulus. *Journal of Petroleum Science and Engineering*, 169, pp.205–219. Available at: https://doi.org/10.1016/j.petrol.2018.05.065.

Sasaki, T., Soga, K. & Elshafie, M., 2018. Simulation of wellbore construction in offshore unconsolidated methane hydrate-bearing formation. *Journal of Natural Gas Science and Engineering*, 60, pp.312–326. Available at: https://doi.org/10.1016/j.jngse.2018.10.019.

Sayers, C.M. et al., 2006. Predicting Reservoir Compaction and Casing Deformation in Deepwater Turbidites using a 3D Mechanical Earth Model. In *Proceedings of the First International Oil Conference and Exhibition*. Cancun, Mexico, pp. 1–7. Available at: http://www.onepetro.org/doi/10.2118/103926-MS.

Schofield, A.N. & Wroth, C.P., 1968. *Critical State Soil Mechanics*. University of Cambridge. Available at: http://www-civ.eng.cam.ac.uk/geotech_new/publications/schofield_wroth_1968.pdf.

Schulz, W.L. et al., 2000. Static and dynamic testing of bridges and highways using long-gage fiber Bragg grating based strain sensors. In *Proceedings of the SPIE Industrial Sensing Systems*. Boston, Massachusetts, USA, pp. 1–9. Available at: https://doi.org/10.1117/12.411730.

Schwall, G.M. & Denney, C.A., 1994. Subsidence Induced Casing Deformation Mechanisms in the Ekofisk field. In *Proceedings of the 1994 Eurock SPE/ISRM Rock Mechanics in Petroleum Engineering Conference*. Delft, The Netherlands, pp. 507–515. Available at: https://doi.org/10.2523/28091-ms.

Sellevold, E.J. & Bjøntegaard, Ø., 2006. Coefficient of thermal expansion of cement paste and concrete: Mechanisms of moisture interaction. *Materials and Structures*, 39(9), pp.809–815. Available at: https://doi.org/10.1617/s11527-006-9086-z.

Shin, H. & Santamarina, J.C., 2016. Sediment-well interaction during depressurization. *Acta*

Geotechnica, 12(4), pp.883–895. Available at: https://doi.org/10.1007/s11440-016-0493-1.

Soga, K. & Schooling, J., 2016. Infrastructure sensing. *Interface Focus*, 6(4), pp.1–17. Available at: https://doi.org/10.1098/rsfs.2016.0023.

Sun, J. et al., 2016. Numerical simulation on gas production from hydrate reservoir at the 1st offshore test site in the eastern Nankai Trough. *Journal of Natural Gas Science and Engineering*, 30, pp.64–76. Available at: http://dx.doi.org/10.1016/j.jngse.2016.01.036.

Sun, X., Lua, H. & Soga, K., 2018. A coupled thermal–hydraulic–mechanical–chemical (THMC) model for methane hydrate bearing sediments using COMSOL Multiphysics. *Journal of Zhejiang University-SCIENCE (Applied Physics & Engineering)*, 19(8), pp.600–623. Available at: https://doi.org/10.1631/jzus.a1700464.

Sun, X., Nanchary, N. & Mohanty, K.K., 2005. 1-D modeling of hydrate depressurization in porous media. *Transport in Porous Media*, 58(3), pp.315–338. Available at: https://doi.org/10.1007/s11242-004-1410-x.

Suzuki, K., Takayama, T. & Fujii, T., 2015. Density structure report from logging-while-drilling data and core data at the first offshore gas production test site on Daini-Atsumi Knoll around eastern Nankai Trough. *Marine and Petroleum Geology*, 66, pp.388–395. Available at: https://doi.org/10.1016/j.marpetgeo.2015.02.026.

Takahashi, H. & Tsuji, Y., 2005. Multi-Well Exploration Program in 2004 for Natural Hydrate in the Nankai-Trough Offshore Japan. In *Proceedings of the 2005 Offshore Technology Conference*. Houston, Texas, USA, pp. 1–10. Available at: https://www.onepetro.org/conference-paper/OTC-17162-MS.

Taoutaou, S. et al., 2014. Implementation of a Fit-for-Purpose Cementing Technology for the First Gas Hydrate Production in Japan. In *Proceedings of the International Petroleum Technology Conference*. Kuala Lumpur, Malaysia, pp. 1–15. Available at: https://doi.org/10.2523/iptc-17991-ms.

Teodoriu, C. et al., 2012. Experimental Measurements of Mechanical Parameters of Class G Cement. In *Proceedings of the SPE/EAGE European Unconventional Resources Conference and Exhibition*. Vienna, Austria, pp. 1–7. Available at: https://doi.org/10.2118/153007-MS.

Thiercelin, M., Baumgarte, C. & Guillot, D., 1998. A Soil Mechanics Approach To Predict Cement Sheath Behavior. In *Proceedings of the SPE/ISRM Eurock '98*. Trondheim, Norway, pp. 329–337. Available at: https://doi.org/10.2118/14375-MS.

Thiruvenkatanathan, P. et al., 2016. Downhole Sand Ingress Detection Using Fibre-Optic Distributed Acoustic Sensors. In *Proceedings of the Abu Dhabi International Petroleum Exhibition & Conference*. Abu Dhabi, UAE, pp. 1–9. Available at: https://doi.org/10.2118/183329-ms.

Thomas, J., Miller, J. & Musso, S., 2015. *Shrinkage Behavior during Early Hydration and Setting of DeepCRETE Lightweight Cement for Methane Hydrate Wells*. Schlumberger-Doll Research.

U.S. Geological Survey, 2012. An Estimate of Undiscovered Conventional Oil and Gas Resources of the World, 2012. , pp.1–5. Available at: https://doi.org/10.3133/fs20123042.

Uchida, S., 2012. *Numerical investigation of geomechanical behaviour of hydrate-bearing sediments*. PhD thesis. University of Cambridge.

Uchida, S., Soga, K. & Yamamoto, K., 2012. Critical state soil constitutive model for methane hydrate soil. *Journal of Geophysical Research: Solid Earth*, 117(B3), pp.1–13. Available at: https://doi.org/10.1029/2011jb008661.

Uesugi, M., Kishida, H. & Uchikawa, Y., 1990. Friction between dry sand and concrete under monotonic and repeated loading. *Soil Science Society of America Journal*, 30(1), pp.115–128. Available at: https://doi.org/10.3208/sandf1972.30.115.

Ulm, F.J., Constantinides, G. & Heukamp, F.H., 2004. Is concrete a poromechanics materials?-A multiscale investigation of poroelastic properties. *Materials and Structures*, 37(1), pp.43–58. Available at: https://doi.org/10.1007.bf02481626.

Vu, M.H. et al., 2012. Time-dependent behaviour of hardened cement paste under isotropic loading. *Cement and Concrete Research*, 42(6), pp.789–797. Available at: https://doi.org/10.1016/j.cemconres.2012.03.002.

Williams, G.R. et al., 2000. Distributed temperature sensing (DTS) to characterize the performance of producing oil wells. In *Proceedings of SPIE Industrial Sensing Systems*. Boston, Massachusetts, USA, pp. 39–54. Available at: https://doi.org/10.1117/12.411726.

Wood, D.M., 2004. *Geotechnical Modelling*, Abingdon on Themes, Oxfordshire: Spon Press.

Xu, D.S., Borana, L. & Yin, J.H., 2013. Measurement of small strain behavior of a local soil by fiber Bragg grating-based local displacement transducers. *Acta Geotechnica*, 9(6), pp.935–943. Available at: https://doi.org/10.1007/s11440-013-0267-y.

Xu, E., 2014. *Numerical Analysis of Wellbore Behaviour during Methane Gas Recovery from Hydrate Bearing Sediments*. PhD thesis. University of Cambridge.

Yamamoto, K. et al., 2005. Application of Wireline Conveyed Through Casing Formation Tester to Methane Hydrate Research in Japan. In *Proceedings of the 11th Formation Evaluation Symposium of Japan*. Chiba, Japan, pp. 1–12. Available at: https://ci.nii.ac.jp/naid/10025875980/.

Yamamoto, K. et al., 2006. Geomechanics data acquisition techniques used in the METI Tokai-oki to Kumano-nada drilling campaign. In *Proceedings of the 12th Formation Evaluation Symposium of Japan*. Chiba, Japan, pp. 1–6. Available at: https://scholar.google.com/scholar_lookup?title=Geomechanics data acquisition

techniques used in the METI Tokai-oki to Kumano-nada drilling campaign&publication_year=2006&author=K. Yamamoto&author=D. Murray&author=C.-K. Khong&author=M. Yasuda&author=M. Na.

Yamamoto, K. et al., 2014. Operational overview of the first offshore production test of methane hydrates in the Eastern Nankai Trough. In *Proceedings of the Offshore Technology Conference*. Houston, Texas, USA, pp. 1–11. Available at: https://doi.org/10.4043/25243-MS.

Yamamoto, K., 2015. Overview and introduction: Pressure core-sampling and analyses in the 2012-2013 MH21 offshore test of gas production from methane hydrates in the eastern Nankai Trough. *Marine and Petroleum Geology*, 66, pp.296–309. Available at: https://doi.org/10.1016/j.marpetgeo.2015.02.024.

Yamamoto, K. et al., 2017. Thermal responses of a gas hydrate-bearing sediment to a depressurization operation. *RSC Advances*, 7(10), pp.5554–5577. Available at: https://doi.org/10.1039/c6ra26487e.

Yamamoto, K. & Dallimore, S.R., 2008. Aurora-JOGMEC-NRCan Mallik 2006-2008 gas hydrate research project progress. *Fire in the Ice*, Summer, pp.1–5. Available at: https://www.netl.doe.gov/research/oil-and-gas/methane-hydrates/fire-in-the-ice.

Yeo, T.L. et al., 2005. Polymer-coated fiber Bragg grating for relative humidity sensing. *IEEE Sensors Journal*, 5(5), pp.1082–1088. Available at: https://doi.org/10.1109/jsen.2005.847935.

Yoneda, J. et al., 2014. Evaluation of Frictional Properties for Methane-Hydrate-Well Completion and Production. *SPE Drilling & Completion*, 29(01), pp.115–124. Available at: https://doi.org/10.2118/169897-pa.

Yoneda, J. et al., 2015. Mechanical properties of hydrate-bearing turbidite reservoir in the first gas production test site of the Eastern Nankai Trough. *Marine and Petroleum Geology*, 66, pp.471–486. Available at: https://doi.org/10.1016/j.marpetgeo.2015.02.029.

Yoneda, J. et al., 2018. Mechanical Response of Reservoir and Well Completion of the First Offshore Methane-Hydrate Production Test at the Eastern Nankai Trough: A Coupled Thermo-Hydromechanical Analysis. *SPE Journal*, 24(02), pp.531–546. Available at: https://doi.org/10.2118/191145-pa.

Yudovich, A., Chin, L. V & Morgan, D.R., 1988. Casing Deformation in Ekofisk. In *Proceedings of the Offshore Technology Conference*. Houston, Texas, USA, pp. 63–72. Available at: https://doi.org/10.4043/5623-ms.

Zhang, C., Kishi, M. & Hotate, K., 2015. 5,000 points/s high-speed random accessibility for dynamic strain measurement at arbitrary multiple points along a fiber by Brillouin optical correlation domain analysis. *Applied Physics Express*, 8(4), pp.1–3. Available at:

https://doi.org/10.7567/apex.8.042501.

Zhen, L. & Xiong, Y., 2013. Multiscale Chemico-Thermo-Hydro-Mechanical Modeling of Early-Stage Hydration and Shrinkage of Cement Compounds. *Journal of Materials in Civil Engineering*, 25(9), pp.1239–1247. Available at: https://doi.org/10.1061/(asce)mt.1943-5533.0000754.

Zhou, D. & Wojtanowicz, A.K., 2000. New Model of Pressure Reduction to Annulus During Primary Cementing. In *Proceedings of the 2000 IADC/SPE Drilling Conference*. New Orleans, Louisiana, USA, pp. 1–10. Available at: https://www.onepetro.org/conference-paper/SPE-59137-MS.

Zhou, M.C., 2015. *Geomechanical study of hydrate-bearing sediments with turbidite formation and hydrate heterogeneity*. PhD thesis. University of Cambridge.

Zou, L. et al., 2006. Distributed Brillouin fiber sensor for detecting pipeline buckling in an energy pipe under internal pressure. *Applied optics*, 45(14), pp.3372–3377. Available at: https://doi.org/10.1364/ao.45.003372.

Zou, L. et al., 2004. Distributed Brillouin Scattering Sensor for Discrimination of Wall-Thinning Defects in Steel Pipe under Internal Pressure. *Applied Optics*, 43(7), pp.1583–1588. Available at: https://doi.org/10.1364/ao.43.001583.